Investigation of Brain Tissue Water NMR Response by Optimised Quantitative Single-voxel Proton Magnetic Resonance Spectroscopy

Abdul Nashirudeen Mumuni

B.Sc, M.Sc

A thesis submitted in partial fulfilment of the requirements for the Degree of Doctor of Philosophy

Department of Clinical Physics

College of Medical, Veterinary and Life Sciences

University of Glasgow

University of Glasgow

June 2013

Abstract

Nuclear Magnetic Resonance (NMR) is a phenomenon in which certain nuclei in the presence of a magnetic field and radiofrequency (RF) radiation emit a certain amount of signal at a frequency equal to that of the RF radiation. Proton Magnetic Resonance Spectroscopy (^{1}H-MRS) is an NMR technique capable of measuring the chemical composition, often referred to as metabolites, of the human body non-invasively and *in vivo*. It is commonly used as a research tool in the investigation of neurological disorders such as multiple sclerosis, brain tumors, stroke, clinical depression, and schizophrenia. Accurate quantification of the metabolites of interest requires a reference standard of known and fixed concentration.

Brain tissue water has been previously reported to have a fairly constant and known concentration, and so has been suggested to be a suitable reference concentration in absolute quantitative ^{1}H-MRS of the human brain. In practice, however, it is challenging to measure the actual tissue water concentration; hence, some studies choose to use estimates of tissue water concentration from the literature. These literature values are usually averages from a healthy study group. There are however indications that brain tissue water content could vary widely in certain disease conditions such as in brain tumors and inflammation. In such situations, absolute metabolite quantification using the literature estimates of tissue water content will be inaccurate while the measurement of cerebral water content using the available techniques will be impractical for the patients due to scanning time considerations. It is therefore necessary to develop a technique that can be used to quantify both the reference water and metabolite concentrations, simultaneously without subject tolerance issues.

The main objective of this thesis was to investigate the response of water NMR signal from human brain tissue under various measurement conditions using the single-voxel ^{1}H-MRS technique. As part of the investigation, the thesis also focused on the development of methods for the absolute quantification of cerebral water and metabolite concentrations.

A standard ^{1}H-MRS water-suppressed acquisition on the General Electric (GE) MR scanner acquires some unsuppressed-water spectra at the beginning of the PRESS pulse sequence. Using the Spectroscopy Analysis by GE (SAGE) software package (version 7), this thesis developed methods to optimise the unsuppressed-water and suppressed-water signals from which, respectively, cerebral water and metabolite concentrations were estimated.

The unsuppressed-water signal response characteristics were investigated in experiments at 3 T that involved: 1) variation of the MRS voxel position over a three-dimensional RF field within an eight-channel head coil; 2) measurement of the relaxation times of brain tissue water using standard saturation recovery and multi spin-echo MRS techniques; 3) measurement of brain tissue water content in peripheral inflammation; and 4) estimation of the BOLD effect on the water spectral peak.

The stability of the MR scanner used for all the investigations was assessed. Over the project period, the worst precision measurements of the scanner (for both water and metabolite signals) were observed to be about 12 % and 26 % in serial phantom and human studies, respectively. The MRI/MRS scanner was therefore found to measure water and metabolite signals with good precision, both *in vivo* and *in vitro*.

By recording the water NMR signal responses at various locations within the phased-array head coil, RF sensitivity profile (voxel position-dependent) equations of the head coil were obtained. The coordinates of any *in vivo* voxel could be substituted into an appropriate profile equation to estimate an unsuppressed-water signal area that could be used as a reference signal to quantify brain tissue water content. This novel technique of quantifying cerebral water content is superior to the previous techniques of performing multi-echo unsuppressed-water signal acquisitions. The method does not require extra unsuppressed-water acquisitions, or corrections for variations in the sensitivity of the eight-channel head coil as both the *in vivo* and reference signals are acquired from the same voxel position.

Brain tissue water content was subsequently quantified accurately using the newly developed method of referencing. In frontal brain voxels, the average water content, WC of grey matter, GM was found to be higher than that of white matter, WM (GM/WM WC ± SE = 46.37 ± 2.58/42.86 ± 2.46 mol/kg; p = 0.02); parietal voxels also showed a similar comparison (GM/WM WC ± SE = 37.23 ± 1.70/34.14 ± 2.02 mol/kg; p = 0.03). These findings were consistent with previous reports of cerebral water content. For regions of mixed proportions of grey and white matter tissues, the average water contents of each tissue type considered separately (by voxel segmentation) and together were found to compare with literature estimates. Using data from five voxel positions, average brain tissue water content was observed to be uniformly distributed across the human brain by one-way ANOVA (p = 0.60), and did not vary significantly with gender (p > 0.05) and age (p > 0.05).

For the first time, cerebral water content was observed in this thesis to remain fairly constant in psoriatic arthritis, a peripheral inflammatory condition (one-way ANOVA, p = 0.63). Among five brain metabolites quantified in the psoriasis patients, only the mean concentration of creatine, Cr was found to be significantly lower in the frontal grey matter voxels of the patients, PsA compared to healthy controls, HC at baseline (PsA/HC ± SE = 6.34 ± 0.38/7.78 ± 0.38 mM/kg; p = 0.01) and post-TNF-α blockade medication (PsA/HC ± SE = 6.69 ± 0.25/7.78 ± 0.38 mM/kg; p = 0.03). None of the metabolite concentrations, including Cr (p = 0.27), changed significantly with medication. The condition of PsA was not observed to affect the mood of the patients, as indicated by their BDI scores. The significant finding of Cr concentration alteration in psoriatic arthritis thus suggests that Cr may not be a reliable denominator in studies of psoriasis that express the metabolite levels as ratios.

The T_1 and T_2 relaxation times of water and the metabolites were measured in the prefrontal grey matter (T_1/T_2 ± SE = 1574 ± 61/147 ± 6 ms) and bilateral Hippocampi (T_1/T_2 ± SE; left = 1475 ± 68/178 ± 83 ms, right = 1389 ± 58/273 ± 98 ms). The relaxation time estimates for the metabolites were in agreement with literature values; relaxation times for water however were measured for the first time in those regions and at 3 T. The measured relaxation times were used to correct the water and metabolite signals for relaxation effects during

their absolute quantification, and could as well serve the same purpose in future studies.

There is increasing interest in the BOLD response of cerebral metabolites and water during tasks. This thesis thus also assessed changes in brain tissue metabolite and water contents while a subject experienced a visual stimulus. In the presence of the visual stimulus, the BOLD effects on the metabolite and water spectral peaks were found to be comparable, as has been observed in previous studies. For the first time, this thesis further investigated the impact of temporal resolution (determined by NEX) on the amount of the BOLD signal acquired from cerebral water and metabolites. In a single visual activation paradigm, the BOLD effect resulted in increased water peak area which differed significantly between NEX values of 2 and 8 ($p < 0.01$); this observation also was true for NAA and Glu. The findings thus suggest that temporal resolution of the MRS data could result in significant differences in the results of functional MRS studies.

In conclusion, by its detailed investigations of the water signal characteristics and newly developed methods for the absolute quantification of cerebral water and metabolite concentrations, this thesis has corroborated the suitability of the brain tissue water signal as a reference and has also improved on the accuracy of quantitative MRS using the endogenous water signal as a reference standard. The techniques presented in this thesis can thus be applied in future ^{1}H-MRS brain studies where the endogenous unsuppressed-water signal is required.

Table of Contents

List of Tables

List of Figures

Acknowledgements

I would like to thank my supervisory team, Prof. Barrie Condon, Drs. Jonathan Cavanagh, John McLean, Maria del Rosario Lopez-Gonzalez and Gordon Waiter, for their continual advice and valuable support over the last 3 years. I am very grateful to them for trusting in my abilities and ideas, for providing me with invaluable research training, for being generous with their time for guidance and discussions about my project, and for providing very helpful comments on the draft copies of this thesis. I wish to also give a special thank you to Prof. Barrie Condon, Dr. Jonathan Cavanagh and Dr. John McLean for providing me with extra funding during the last 6 months of the project.

I am also grateful to Scottish Imaging Network: A Platform for Scientific Excellence (SINAPSE) Collaboration, a Pooling Initiative funded by the Scottish Funding Council and the Chief Scientist Office of the Scottish Executive, for my PhD studentship and for the partial sponsorship of my research. My PhD studentship was also partly funded by the College of Medicine, University of Glasgow, through the Overseas Studentship Award. Many thanks go to the University of Glasgow for the partial scholarship and to Miss Audrey Hillis for believing in my ability to pursue this project and recommending me for the Scholarship Award.

I would like to acknowledge the use of MRS data previously acquired by Miss Lorna Harper for 'Study 6A' in chapter six of this thesis. I thank her for acquiring those high quality spectra that served a very useful purpose in my research. Many thanks also go to the Sackler Lab Group for providing good quality data for 'Study 6B' in chapter 6 of this thesis.

Dr. John McLean provided me with a depth of practical experience on the use of the MR scanner for both MRI and MRS acquisitions. Dr. Maria del Rosario Lopez-Gonzalez introduced me to the Image-J software package which was used in analysing the data on MT imaging and MRI relaxation times. Dr. David Brennan introduced me to the analysis tools of the FSL software package for the fMRI data analysis in chapter eight. Dr. Rajeev Krishnadas received ethical approval (Appendix 2.4) and recruited the patient group for the study in

chapter seven. Drs. McLean and Brennan helped with scanning the psoriatic arthritis patients for the TNF-α study in chapter seven. I thank these four people for their individual contributions to the success of my research as mentioned above, and for their persistent encouragement, for their help in keeping me mentally sane, and for making me feel so much closer to home during the research period.

My sincere thanks also go to Drs. Timo Schirmer and Ralph Noeske of General Electric Global Research Lab, Germany for their prompt responses, via email correspondence, to all my questions regarding the use of the SAGE software package. Many thanks go to Prof. Donald Hadley for reporting all the MRI brain scans in the various human studies presented in this thesis.

The following people also deserve to be acknowledged for providing advice, both research and non-research, over the project period: Prof. Ian Marshall, Dr. Mary McLean, Dr. Matthew Taylor, Dr. Nigel Davies, Dr. William Holmes, Dr. Deborah Dewar, Dr. Sue Champion, Dr. Santosh Celestine, Dr. Mahsa Shokouhi, Dr. Aaron Sam, and Prof. David Wyper.

I wish to also thank all the staff of the Institute of Neurological Sciences, Southern General Hospital of Glasgow, especially the radiographers for their patience in sharing their work space with me in the MR scanner room, and for making my experience as a learner radiographer an exciting one.

I also owe a debt of gratitude to Dr. Frankie Zhang and Mr. Wenbo Rong for introducing me to some of the healthy subjects who later volunteered in my research. I'm very grateful to all those participants in the various human studies reported in this thesis.

Finally, I wish to thank my parents, Mr. and Mrs. Mahama Mumuni, my wife, Mrs. Fatahiya Abdul-Nasir, my siblings, Abdallah and Jamal Mumuni, and my closest friends, Abdul-Mumin M. Amin, Shurehu Munkaila, Bawa Mahi, Katara Salifu, Julius Mngumi, Mohammed Gaali Jibriel, and Shaibu Abdul-Wahab for their love, care, understanding, support and encouragement during the difficult moments of my research.

Author's Declaration

This thesis has been composed and documents the original work carried out by Abdul Nashirudeen Mumuni.

All data were originally acquired and analysed by the author of this thesis unless explicitly stated otherwise in the text.

This thesis has not been previously submitted in any form to any institution or University. However, sections of the work described herein have been presented elsewhere by the author as listed below.

Signature: _____

Abdul Nashirudeen Mumuni
June 2013

List of Abstracts

1. **Mumuni A.**, McLean J., Brennan D., Lopez R., Waiter G., Cavanagh J., and Condon B. "Comparison of the BOLD Responses of Brain Tissue Water and Creatine during a Sustained Visual Stimulation." Proc. BC-Intl. Soc. Mag. Reson. Med. Cambridge, UK; Sept 11-13, 2012; pp. 109

2. **Mumuni, A.**, Krishnadas, R., McLean, J., Lopez, R., Waiter, G., Cavanagh, J., and Condon, B. "Single-voxel ^{1}H-MRS Study of the impact of Peripheral inflammation on Brain Metabolism and Mood". Annual Scientific Meeting of the Scottish Imaging Network – A Platform for Scientific Excellence (SINAPSE), Glasgow, Scotland, May 30, (2012).

3. **Mumuni, A.**, McLean, J., Lopez, R., Waiter, G., Cavanagh, J., and Condon, B. "MRS and Inflammation". Abstracts Meeting of the Sackler Institute of Psychological Medicine, Glasgow, Scotland, October 29, (2011).

4. **Mumuni, A.**, McLean, J., Brennan, D., Lopez, R., Waiter, G., Cavanagh, J., and Condon, B. "Estimation of the BOLD Effect on Cerebral Water Content: Implication for Referencing in Absolute Quantitative MRS". Abstracts Meeting of the Sackler Institute of Psychological Medicine, Glasgow, Scotland, September 23, (2011).

5. **Mumuni, A.**, McLean, J., Lopez, R., Cavanagh, J., Waiter, G., Condon, B. "Towards Optimised ^{1}H-MRS Acquisition and Absolute Quantification of the Brain Water Signal". Annual Scientific Meeting of the Scottish Imaging Network – A Platform for Scientific Excellence (SINAPSE), Dundee, Scotland, June 16, (2011).

6. **Mumuni, A.**, McLean, J., Lopez, R., Waiter, G., Cavanagh, J., and Condon, B. "Application of MRI and Proton Spectroscopy in Brain Tissue Water Estimation". Ghana Atomic Energy Commission (GAEC), Accra, Ghana, March 23, (2011).

7. **Mumuni, A.**, McLean, J., Lopez, R., Cavanagh, J., Krishnadas, R., Waiter, G., and Condon, B. "Proton MR Spectroscopy of the Frontal Brain in Psoriatic Arthritis". Glasgow Neuroscience Day, Glasgow, Scotland, January 12, (2011).

8. **Mumuni, A.**, McLean, J., Lopez, R., Cavanagh, J., Krishnadas, R., Waiter, G., and Condon, B. "Peripheral inflammation influences Brain Chemistry: A ^{1}H-MR Spectroscopy Study". Postgraduate Open Day of the College of Medical, Veterinary and Life Sciences (MVLS) of the University of Glasgow, Glasgow, Scotland, December 2, (2010).

9. **Mumuni, A.**, McLean, J., Lopez, R., Cavanagh, J., Krishnadas, R., Waiter, G., and Condon, B. "Absolute Quantitative ^{1}H-MRS in Depression". Annual Scientific Meeting of the Scottish Imaging Network – A Platform for Scientific Excellence (SINAPSE), Edinburgh, Scotland, June 16, (2010).

List of Abbreviations/Definitions

^{13}C	Carbon-13 atom
^{14}N, ^{15}N	Nitrogen-14 and 15 atoms
^{17}O	Oxygen-17 atom
180^{o}	Inversion radiofrequency pulse
^{19}F	Flourine-19 atom
^{1}H	Hydrogen-1 atom or proton
^{1}H-MRS	Proton Magnetic Resonance Spectroscopy
^{23}Na	Sodium-23 atom
2D or 3D	2- or 3-dimensional
^{31}P	Phosphorus-31 atom
^{35}Cl	chlorine-35 atom
^{39}K	Potassium-39 atom
^{6}Li, ^{7}Li	Lithium-6 and 7 atoms
90^{o}	Excitation radiofrequency pulse
a. u.	Arbitrary unit
ACC	Anterior cingulate cortex
AC-PC	Anterior commissure-posterior commissure
ADP	Adenosine diphosphate
A_{fit}	Reference signal area derived from a polynomial equation
ANOVA	Analysis of variance
AP	Anterior-Posterior direction
A_{phan}	T_1, T_2 and TG corrected phantom unsuppressed-water peak area
A_u	Unsuppressed-water spectral peak area
B_0	External magnetic field
B_1	Radiofrequency pulse or field
BDI	Beck's Depression Inventory
BET	Brain Extraction Tool
Block	Interleaved rest-visual stimulation periods
BOLD	Blood Oxygen Level Dependent contrast or effect
CHESS	CHEmical Shift Selective preparation
Cho	Free choline
CI	Confidence interval

cm^3	Cubic centimetre
CNS	Central nervous system
CoV	Coefficient of variation
Cr	Creatine
CSF	Cerebrospinal fluid
CSI	Chemical Shift Imaging
dB	decibel unit
DC	Direct current
DRESS	Depth-REsolved Surface-coil Spectroscopy
exp or e	Exponential
FAST	FMRIB's Automated Segmentation Tool
FEAT	FMRI Expert Analysis Tool
FID	Free induction decay
FILM	FMRIB's Improved Linear Model
FLAIR	FLuid Attenuated Inversion Recovery pulse sequence
FLIRT	FMRIB's Linear Image Registration Tool
fMRI	Functional Magnetic Resonance Imaging
FMRIB	Functional MRI of the Brain Analysis Group
fMRS	Functional Magnetic Resonance Spectroscopy
FOV	Field-of-view
FSE	Fast Spin Echo pulse sequence
FSL	FMRIB's Software Library
FSPGR	Fast SPoiled GRadient echo pulse sequence
FT	Fourier transform
f_{tissue}	Fraction of solid brain tissue within a voxel
FWHM	Full-width at half-maximum
g/mL	gram per millilitre
GABA	Gamma-aminobutyric acid
GDP	Guanosine diphosphate
GE	General Electric Company Ltd.
GHQ	General Health Questionnaire
Gln	Glutamine
Glu	Glutamate
Glx	Glutamate-Glutamine Complex
GM	Grey matter tissue

GPC	Glycerophosphorylcholine
GRE-EPI	Gradient echo-planar imaging
H_2O	Water
IL-1/IL-6	Interleukin-1 or 6
Image-J	Java-based image processing program
INTERPRET	INTERnational network for Pattern REcognition of Tumors
IR	Inversion Recovery
IR-FSPGR	Inversion Recovery-Fast SPin GRadient echo pulse sequence
K	kelvin temperature
kHz	kilo-heartz
k_{pr}	Lost fraction of *in vivo* unsuppressed-water signal
Lac	Lactate
LC Model	Linear Combination Model
M/F	Numbers of males and females in sample
MATLAB	MATrix LABoratory
MCFLIRT	Motion Correction tool of FLIRT
MHz	Mega-heartz
m-Ins/Ins/mI	myo-inositol
mM	millimoles
mm^3	cubic millimetre
M_o	Equilibrium or net spin longitudinal magnetisation
mol/kg	moles per kilogram wet weight of brain tissue
mol/L	moles per litre
MR	Magnetic Resonance
MRI	Magnetic Resonance Imaging
MRS	Magnetic Resonance Spectroscopy
MRSI	Magnetic Resonance Spectroscopic Imaging
ms	millisecond
MS	Multiple sclerosis
MT	Magnetisation Transfer
MTC	Magnetisation Transfer Contrast
MTR	Magnetisation Transfer Ratio
M_{xy}	Transverse magnetisation
M_z	Recovered longitudinal magnetisation along the z-axis
NAA	N-Acetyl Aspartate

NAAG	N-Acetyl-aspartyl-glutamate
NEX	Number of phase cycles
NH_4^+	Ammonium ion
NHS	National Health Service
NMR	Nuclear Magnetic Resonance
NSA	Number of signal averages or acquisitions
^oC	degree celsius
OFF-ON	rest-visual stimulation period
PCh	Phosphorylcholine
PCr	Phosphocreatine
PD	Proton density
PET	Positron Emission Tomography
PRESS	Point-RESolved Spectroscopy
PsA	Psoriatic arthritis
p-value	Significance level
PVE	Partial volume effect
PVEC	Partial volume effect correction
RA	Rheumatoid arthritis
rad/T sec	radians per tesla-second
REC	Relaxation effect correction
RF	Radiofrequency
RL	Right-Left direction
ROC	Receiver Operating Characteristic
ROI	Region of interest
SAGE	Spectroscopy Analysis by General Electric
SD	Standard deviation
SE	Standard error
SI	Superior-Inferior direction
SNR	Signal-to-Noise Ratio
SPECT	Single Photon Emission Computed Tomography
SPGR	SPoiled GRadient echo pulse sequence
STEAM	Stimulated Echo Acquisition Mode
SV-MRS	Single-voxel Magnetic Resonance Spectroscopy
T	Tesla (e.g. 1.5 T, 3 T, 4 T as in text)
T/F	True/False

T_1	Longitudinal relaxation time constant
T_2	Transverse relaxation time constant
T_2^*	Relaxation time constant due to susceptibility effects
tCho	Total free choline
tCr	Total creatine
TE	Echo time
TG	Transmitter gain
TI	Inversion time
TM	Mixing time
tNAA	Total N-Acetyl Aspartate
TNF-α	Tumor necrosis factor-alpha
TR	Repetition time
US	United States (of America)
VOI	Volume of interest
WC	Cerebral water content
WM	White matter tissue
WoSREC	West of Scotland Research Ethics Committee
ΔAs	Change in spectral peak area
ΔH	Change in spectral peak height
$\Delta\upsilon_{1/2}$	Change in spectral linewidth at half peak height
ω	Larmor frequency

Chapter 1: Introduction

1.1 Overview of MR Spectroscopy as Applied in this Thesis

1.1.1 Advances in MR Spectroscopy

Historically, Magnetic Resonance Spectroscopy (MRS) was an analytical method in Chemistry that was used for the identification and quantification of chemical species in samples. In clinical practice, presently, it is a non-invasive research tool that provides *in vivo* information about the chemical composition and metabolism of a part of the human body under investigation. *In vivo* MRS is basically a complementary method to diagnostic imaging and can be used, for example, in the detailed analysis of primary and secondary brain tumours and metabolic diseases [1]. Clinical MRS is a relatively new and advanced technique of *in vivo* Nuclear Magnetic Resonance (NMR).

The NMR effect of a nucleus was discovered in 1938 by Isidor Isaac Rabi (Nobel Prize 1944) [2]. NMR in condensed matter was first achieved in 1946 simultaneously by two independent groups led by Felix Bloch of Stanford University [3] and Edward Mills Purcell of Harvard University [4] (Nobel Prize 1952). At this time, NMR was only experimental until in the 1950s when the creation of a one-dimensional NMR image was first described by Herman Carr [5]. The application of Fourier analysis to NMR by Richard Ernst in 1966 (Nobel Prize 1991) [6] dramatically improved the efficiency of NMR imaging. In 1973, Paul Lauterbur (Nobel Prize 2003) expanded on Carr's technique and generated the first NMR images (of water filled tubes) in 2D and 3D using gradients [7]. Lauterbur later published the first cross-sectional NMR image of a living mouse in 1974 [8]. The first NMR image of a human body part (the finger) was acquired by Peter Mansfield of the University of Nottingham, England in 1976 [9]. During his research on the analytical properties of NMR, Raymond Damadian created the world's first whole-body NMR imaging machine in 1972 [10]. Damadian and his colleagues subsequently performed the first whole-body

NMR imaging scan of a human being in 1977 [11]. Peter Mansfield and his team again developed a mathematical technique to speed up NMR imaging scan times and to also improve the NMR image quality in 1978 [12].

The first NMR Spectroscopy experiments, observing the ^{31}P nucleus, were reported in 1973 by Moon and Richards [13] who determined intact red blood intracellular pH from chemical shift differences and in 1974 by Hoult and colleagues [14] who first studied intact, excised rat hind leg. NMR Spectroscopy at this time was originally concerned with identifying chemical compounds in samples and there was no spatial information contained in the data (i.e. it was not associated with NMR imaging) [1]. NMR Spectroscopy therefore developed separately from NMR imaging on different machines at that time. During the 1980s, Paul Bottomley of General Electric (GE) research centre, New York developed the first whole-body clinical NMR imaging and spectroscopy scanner at 1.5T. In 1985, Bottomley performed the first localised *in vivo* proton (^{1}H) NMR Spectroscopy in the human brain on their 1.5T NMR imaging/spectroscopy scanner [15].

Despite its high natural abundance of 99.985 % and having the greatest NMR-sensitivity [16, 17], previous NMR Spectroscopy experiments could not study the ^{1}H nucleus because its presence *in vivo* is predominantly in water whose concentration is in the order of about 10^4 larger than the concentrations of the metabolites of interest. Suppression of the solvent, including lipid, signal thus became essential but remained a challenge [15]; consequently limiting the early *in vivo* NMR Spectroscopy studies to the ^{31}P nucleus when, in practice, it is the ^{1}H NMR spectrum that is altered in almost all neurological disorders [18].

The 1985 pioneering ^{1}H-NMR Spectroscopy study by Bottomley et al was further refined by Frahm et al in 1987 who published [19] the various metabolites detected *in vivo* with ^{1}H-NMR Spectroscopy; this was then followed by the work of Narayana and colleagues who in 1989 also published the first paper [20] on quantification of the metabolites detected by ^{1}H-NMR Spectroscopy in the human brain.

Since these studies, improvements have been made in modern clinical NMR imaging/spectroscopy scanners especially related to higher field strengths for imaging and spectral localisation. These advances have aided the proliferation of the use of ^{1}H-NMR Spectroscopy in examining various pathologies in the human body. In particular, neurological pathologies that have been studied with ^{1}H-NMR Spectroscopy include stroke [21], multiple sclerosis [22], brain tumours [23], Alzheimer's disease [24], dementia [25], schizophrenia [26], bipolar disorders [27], and major depression [28]. Later on, *in vivo* NMR imaging was renamed MRI (Magnetic Resonance Imaging) whereas *in vivo* NMR Spectroscopy was renamed MRS (Magnetic Resonance Spectroscopy) by US radiologists to prevent the public being alarmed with the term "nuclear" [1]. The term "nuclear" was also reported to be constantly and erroneously associated with Nuclear Medicine. Thus, in subsequent discussions in this thesis, MRI and MRS will be used for NMR imaging and NMR Spectroscopy respectively.

1.1.2 MR Spectroscopy in Practice

MRI provides anatomical information by using pulsed static magnetic fields to record spatially encoded signals from protons in a localised region of the body while MRS uses magnetic field gradients to gain information on the spatial distribution of nuclei within a specific anatomical region of the body. In practice, MRS is guided by an MRI localised anatomical region to acquire signals from chemical species (usually called metabolites) which contain either protons (^{1}H) or any one of the other NMR-sensitive nuclei such as ^{13}C, ^{31}P and ^{19}F. Thus, a typical MRS examination of any anatomical region is preceded by the MRI acquisition of that region using the MR scanner (Figure 1.1a). For instance, all the *in vivo* experiments in this thesis were performed in the human brain, and so MRI of the brain was acquired in each case before MRS localisation; all MRS localisations were performed using the phased-array head coil (Figure 1.1b). The MRS localised region is called a volume element or voxel. Two MRS localisation techniques are available: single-voxel MRS (SV-MRS) and MRS imaging (MRSI). Both techniques are discussed in detail in section 2.2.4. MRS data may be evaluated either by visual inspection [29] or

quantification [1] of the spectra. This thesis will however focus on quantitative SV ^{1}H-MRS examination of the human brain.

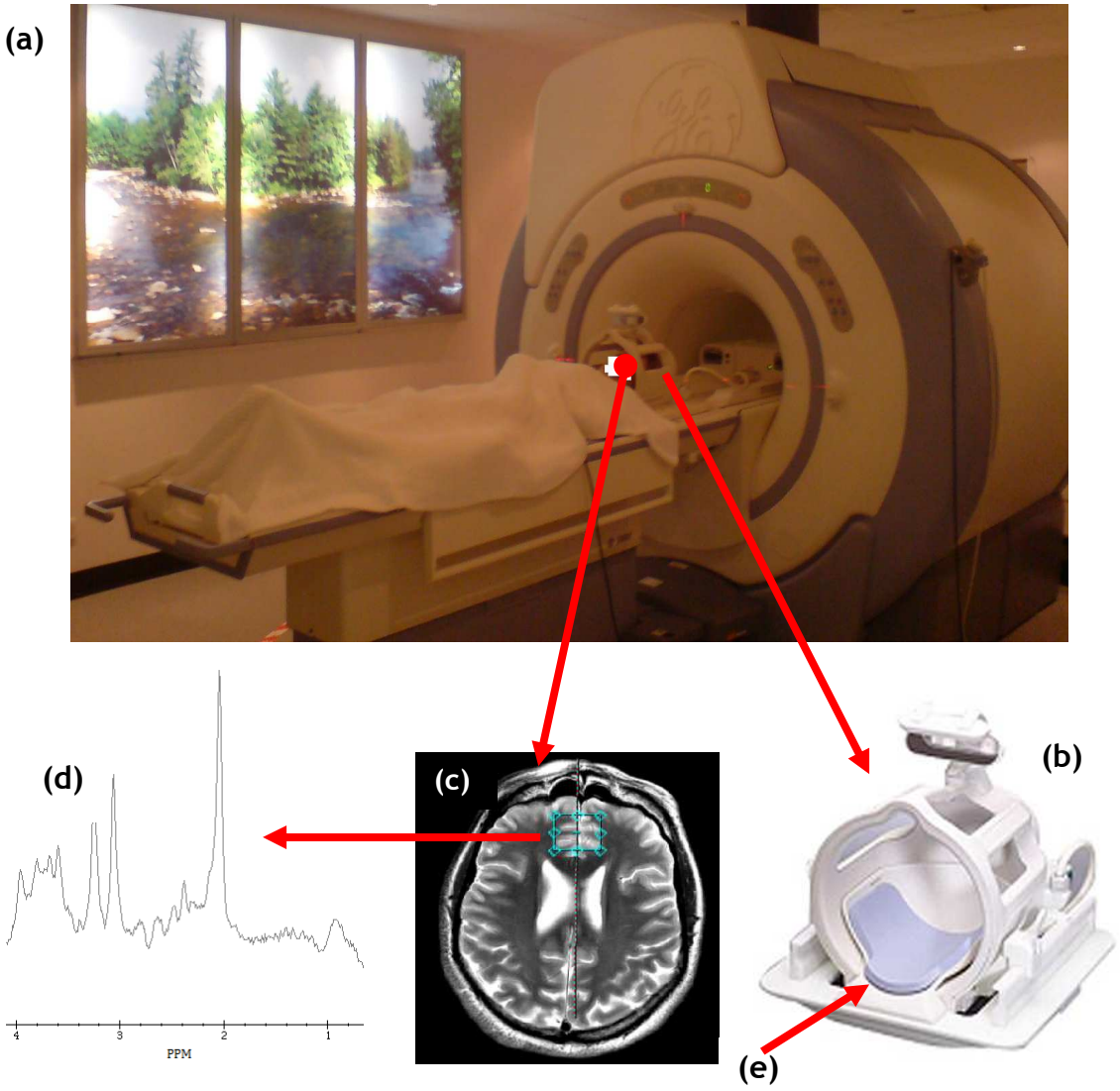

Figure 1.1: A clinical whole-body MRI scanner(a) equipped with a phased-array head coil (b) used to acquire MRI of the brain (c) and to localise spectra to the frontal region of the brain (d). The patient rests their head on the padding in the head coil (e).

1.1.3 Overview and Objective of this Thesis

The utility of MRS lies in the accurate quantification of the metabolite spectra. Quantified spectrum in this sense will make it possible for MRS data interpretation to be objective, reproducible and comparable between studies. In addition, spectral quantification will enhance the reliability of MRS and

enable the direct evaluation of biological changes in disease progression and recovery following treatment [1, 30].

In brain studies, most of the regions of interest are commonly small and curved. This means that in SV-MRS, spectra will have to be localised to smaller voxels (typically 1 cm^3 cuboid or cube) at the expense of poorer signal-to-noise ratio (SNR). The use of larger voxel sizes to increase SNR on the other hand will mean that spectra will be contaminated by signals originating from outside the region of interest and/or cerebrospinal fluid (CSF). Signal contribution to the acquired MRS signal by CSF is usually referred to as the partial volume effect (PVE). The use of larger voxel sizes without PVE correction (PVEC) will result in inaccuracies of the quantified concentrations [1].

In quantitative MRS, the area under each spectral peak is proportional to the concentration of the metabolite they represent [31]. However, these spectral areas largely depend on the T_2 relaxation times of protons in the chemical structures of the metabolites. Depending on the spectral acquisition parameters used, the spectral areas (and hence the calculated concentrations) could be over- or underestimated. To minimise this error arising from relaxation effects, the relaxation times for the respective metabolites are used to deduce correction factors for relaxation effect correction (REC). The final result of the REC method is that each spectral peak area is appropriately adjusted for signal losses it might have suffered due to the relaxation effects.

Concentration estimates in quantitative MRS can be expressed in two ways: ratio and absolute units (details in section 4.1.1). In either units of expression, a standard concentration is required. The absolute quantification method was implemented in this thesis. In the absolute unit expression, the standard concentration is usually known (either by assumption or from a separate measurement). This known standard concentration in millimolar (mM) units is then used to convert the metabolite peak area unit from arbitrary to concentration units. The unit conversion process is usually in two stages (see equation 1.4): firstly, the ratio of the spectral peak areas (after PVEC and REC) of the metabolite and the standard solution is evaluated; secondly, this ratio is multiplied by the mM standard concentration. Thus, after the second step, the

concentration of the metabolite is obtained in mM units. The rationale for this thesis was the practical assessment of a chosen standard concentration for its suitability in absolute quantitative SV-MRS.

The requirement of the standard concentration is that its value should remain fairly constant over time. Such a standard concentration could either be an external solution or an internal metabolite within brain tissue (details in section 4.1.2). Water within brain tissue was used as the reference concentration in this thesis (chapter 7). However, the focus of this thesis was not only on the development of methods of absolute quantification of cerebral water content (chapter 6) and metabolite concentrations (chapter 7). The main focus, and theme, of this thesis was the investigation of the NMR response characteristics of cerebral water under different experimental situations: RF coil sensitivity profiling (chapter 4), relaxation time measurements (chapter 5), assessment of regional distribution of cerebral water content (chapter 6), peripheral inflammation (chapter 7), and visual stimulation (chapter 8). These experimental conditions were chosen for two reasons: firstly, they represent some of the most common clinical situations encountered in human MRS studies. Secondly, they were thought to be potential ways by which substantial changes in the cerebral water signal could be obtained (i.e. the water NMR signal was likely to be more sensitive, or respond, to how those conditions changed in the experiments).

The development of absolute quantitative methods (for cerebral water and metabolites) aspects of this thesis also involved the use of the water signal, measured *in vitro* and *in vivo*. All experiments in this thesis were performed using the phased-array coil (Figure 1.1b). Most of the recent clinical MRI scanners are equipped with this type of head coil to improve signal-to-noise ratio of MRI [32]. However, the implication of these coils for SV-MRS is that metabolite signal intensities are affected by the relative position of each receiver coil element from the SV-MRS localised region [1]. This RF coil response characteristics was made use of in this thesis: the RF response profiles (plots of the water spectral peak areas) for various voxel positions were deduced mathematically from *in vitro* experiments (chapter 4) such that each profile equation was a function of voxel position.

The RF response profiles provided information on the NMR response characteristics of water, *in vitro* and at the same time were used to calculate reference water signal areas for *in vivo* acquisitions (by substitution of the *in vivo* voxel coordinates into the deduced RF profile equations). The calculated *in vivo* water signal area (from the equations) was then used as a reference signal in the quantification of cerebral water content (chapters 6 and 7).

From the same acquisition and voxel position, metabolite and water signal areas were obtained *in vivo*. Using the water signal as a reference concentration, the concentrations of the metabolites were calculated (chapter 7). Such an absolute quantitative method was not affected by the non-uniform RF response characteristics of the phased-array coil, circumventing the need for signal non-uniformity correction.

The objective of this thesis was to investigate how cerebral water NMR signal varies in response to various experimental conditions in order to ascertain its suitability as a reference concentration in novel absolute quantitative methods developed herein. This thesis therefore is a cohesive body of work that seeks to corroborate or otherwise previous studies that have suggested the use of cerebral water as a suitable standard concentration.

Since this thesis focuses on brain tissue water content, it is necessary to discuss the biological significance of water in cellular tissue function (section 1.2) and its relevance in MRI (section 1.3) and quantitative MRS (section 1.4).

1.2 The Role of Water in Neurophysiology

This section aims to discuss only the role of water in tissue function, focusing on the human brain. Even though the emphasis is on the brain, the underlining role played by water discussed here is not limited to only brain tissues but is applicable to the whole body.

Water is the most abundant substance in, and the most important component of, the human body. It comprises about three quarters of the human mass and is a major component in every cell. The unique structure of water (i.e. its

bipolar ends) gives it properties that enable it to play many biological roles. Primarily, the presence of water is that which provides life for cells and consequently living organisms. This is because its involvement in photosynthesis produces oxygen that we breathe and utilise for all life sustaining processes that occur at the cellular level. Water within cells plays important roles in metabolism, excretion, temperature regulation and structural support. It is therefore an element of extreme importance supporting all physiological activities of living cells. For this reason, the body has an adaptive mechanism (involving the secretion of hormones by the pituitary glands that signal the kidneys to reabsorb water) to maintain constant cellular tissue water content so that too much water does not leave the body. When the body lacks water, brain cells and other neurons shrink and biochemical processes involved in cellular communication slow down. A constant tissue water content is thus critical because dehydration, even as little as 2 % loss of body weight, results in impaired physiological (e.g. visuomotor tracking, psychomotor speed and thermoregulatory responses) and performance (e.g. mood, cognition and physical activity level) responses; and the body can collapse when water loss approaches 7 % [33-37]. However, the lowest levels of dehydration that produce significant effects on cognitive performance and mood have not been established [25].

The human brain is about 77-78 % water [38] which is distributed within the brain cells and also bathes the cells. This intra and extra cellular water distribution provides a medium for communication among all the brain cells and also gives structure and shape to the cells. Nutrients and other important substances required for cell function are then transported in the water medium by diffusion or osmosis between the cells. This process of communication between the cells is only possible when what is being transported is water soluble [39].

Within the water molecule, the charge distribution is such that one end of the molecule is slightly negative while the other end is slightly positive (section 2.2.6.1); water is therefore said to be polarised. This charge distribution within the water molecule gives it an electrical conducting property. Thus, the electrical potential of water makes it a reactant in intracellular reactions.

Being a reactant in this case, it helps in the formation of electrical pathways through which signals and other ions are conducted between the brain neurons. The electrical pathway further links the various parts of the body to the central nervous system (which includes the brain) through nerve formations. This link provides a communication channel to conduct impulses between the brain and other parts of the body.

The energy required for the normal functioning of the brain comes from nutrients that are dissolved in water first, before being transported by blood to the brain tissue. Enzymes, hormones and coenzymes that aid the breakdown process of the nutrients (i.e. amino acids, carbohydrates, vitamins and minerals) are also dissolved in water. By the process of hydrolysis, the cells then use water to separate a phosphate group from adenosine triphosphate (ATP) or an analogue of ATP such as guanosine triphosphate (GTP) in the nutrients to produce energy [40] as illustrated by the following equations:

$$ATP + H_2O = Energy + ADP + Inorganic\ Phosphate \quad \text{(Eq. 1.1)}$$

$$GTP + H_2O = Energy + GDP + Inorganic\ Phosphate \quad \text{(Eq. 1.2)}$$

This is the same mechanism by which the major excitatory neurotransmitter called glutamate is produced:

$$Glutamine + H_2O = Glutamate + NH_{4+} \quad \text{(Eq. 1.3)}$$

Glutamate is considered to be the major mediator of excitatory signals in the central nervous system and is involved in most aspects of normal brain function including cognition, memory and learning [41].

As the energy is utilised by the brain, heat and other waste products (such as carbon dioxide) are produced. The presence of water within and around the brain cells provides a ‘heat sink’ or cooling medium to help (the hypothalamus/pituitary gland) in the regulation of the core brain temperature; and to also serve as a solvent for the waste products. As a solvent containing the waste substances, water is directly or indirectly involved in their transport to their points of excretion.

1.3 The Relevance of Tissue Water in MRI

MRI produces images whose intensities reflect the intrinsic NMR characteristics of tissues. The NMR characteristics of tissues that define contrast in the MR image are related to proton density, relaxation (T_1 and T_2), flow and diffusion of tissue water. It is the amount of binding of tissue water that produces the differences in T_1 and T_2 relaxation times between tissues [1]. By manipulating these characteristics of tissue water in a desired way (using the MR scanner), various contrasts can be produced in MR imaging as discussed in the following subsections. All the contrast types discussed in these subsections were produced in the MRI acquisitions of this thesis.

1.3.1 Proton Density

Proton density MRI relies mainly on protons (i.e. ^{1}H atoms) in free water within tissue. This is because these are the only protons that contribute to the MR signal. The concentration of MRI-visible protons in a tissue, relative to that in the same volume of water at the same temperature is referred to as the proton density (PD) of the tissue [1]. By using a short echo time (*TE*) and a long repetition time (*TR*), a PD-weighted MR image (Figure 1.2) can be generated, with intensity related to tissue water content. In the brain, where most mobile protons are in water, the PD image provides a direct measure of tissue water content [1]. PD-weighted image intensity thus increases with oedema, inflammation or demyelinating disease since any one of these conditions increases tissue water content within the affected location [42].

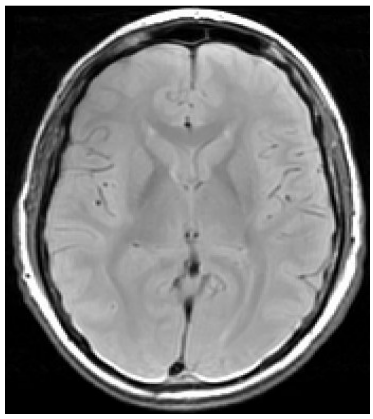

Figure 1.2: A PD-weighted axial MR image of the brain

1.3.2 Proton Relaxation

Free water protons are in constant random motion and in the process may either lose energy to their surroundings or change their interactions with one another. The energy loss process is measured by a time-constant called T_1 relaxation time (section 2.1.2.1), whereas the change in interaction process is measured by a time-constant called T_2 relaxation time (section 2.1.2.2). Both processes occur simultaneously but independently of each other. The T_1 and T_2 relaxation times of tissue water protons are very essential to MRI. This is because both relaxation times help define contrast in MRI: for example, using particular values of *TE* and *TR*, increased MR signal will be acquired from tissues with longer T_2 relaxation times; decreased signal will be acquired from those tissues with longer T_1 relaxation times. An MR image may thus be T_2-weighted, T_1-weighted or it may have a contrast generally defined by a combination of the two with other tissue NMR characteristics such as proton cross-relaxation, flow or diffusion. When both *TR* and *TE* are short, a T_1-weighted contrast (Figure 7.1a) is produced, whereas both long *TR* and *TE* will produce a T_2-weighted contrast (Figure 7.1b).

1.3.3 Tissue-bound Protons

In addition to the free water protons, biological tissues also contain a specific pool of protons bound in macromolecules (usually proteins). These macromolecular protons however cannot directly contribute to the MR signal

because they have very short T_1 relaxation times due to their constrained motion – i.e. the protons have a short relaxation time compared to the time required to make an NMR measurement. They have a wider range of Larmor frequencies than free water protons. Therefore MRI of a tissue with a large pool of these bound water protons could involve exciting only the tissue at a frequency slightly greater or lesser than the Larmor frequency of the free protons; the excitation pulse does not directly affect those protons in free water. Repeated delivery of the off-resonant radiofrequency pulses to the tissue saturates the magnetization of the bound protons from where it (i.e. the magnetisation) is transferred to free protons nearby by a cross-relaxation process. The free water protons then mirror, in magnitude, the macromolecular content of the tissue being studied. This process by which water serves as a 'transcription medium' for MR imaging of macromolecules is called Magnetisation Transfer (MT) imaging (Figure 1.3). The concentration of macromolecules and their interaction with free water defines the contrast in MT imaging (Figures 1.4a-b).

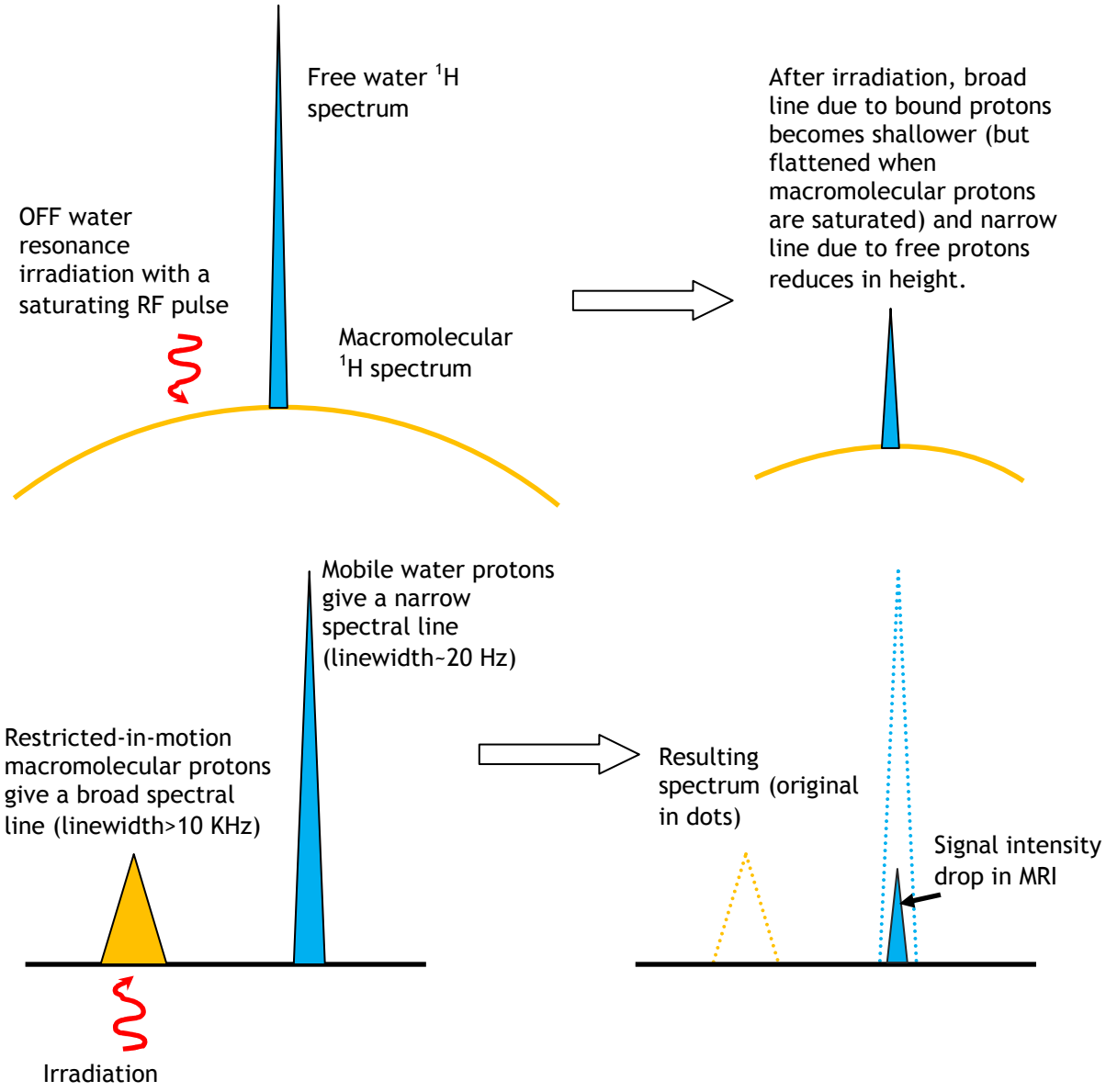

Figure 1.3: Generation of magnetisation transfer contrast (MTC) in MT Imaging

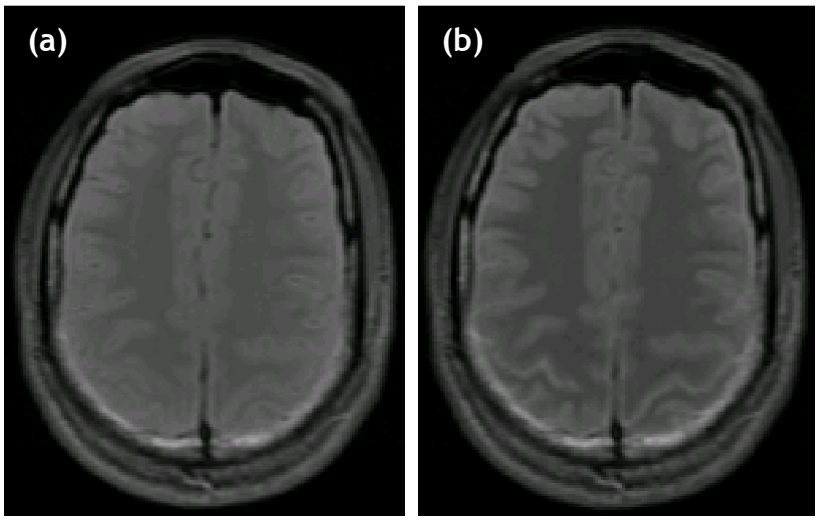

Figure 1.4: Axial MRI of the same subject acquired with the MT pulse switched OFF (a) and ON (b)
Note that white matter (WM) tissue is brighter in the MT OFF than in the MT ON image. This is because WM tissue is made up mainly of myelin which has a lot of water trapped in sheaths. It is this bound water content of the WM tissue that makes it respond more to the MT effect compared to grey matter tissue.

1.3.4 BOLD Contrast

Blood plasma is the component of blood that normally holds the blood cells. It is almost 92 % water by volume and 8 % of proteins, metabolites and ions. It serves as the main medium for transportation of materials including oxygenated blood in the body [40]. Blood flow could therefore be seen as being due to plasma, which is water. Regional blood flow is closely related to neural activity, and produces a sensitive MR imaging contrast mechanism which dependends on blood oxygen level, known as blood oxygen level dependent (BOLD) contrast. Neural activity causes blood to become deoxygenated; this creates a susceptibility difference between vessels carrying this blood and their surrounding tissue. Such susceptibility differences cause a decrease in the MR proton signal due mainly to pseudo-relaxation (dephasing) process measured by a time constant denoted by T_2^*(more in section 8.1.1). Thus in a T_2^*-weighted MR image, the presence of deoxygenated blood (which is paramagnetic) in vessels causes pixels containing those vessels to appear darker. Upon neural activity, there is an increased supply or flow of oxygenated blood (which is diamagnetic) to vessels and so the T_2^*-weighted image becomes brighter in

those pixels containing these vessels (Figure 8.3a-b). This type of MR imaging that relies on the BOLD contrast mechanism is called functional MRI (fMRI).

1.4 The Relevance of Tissue Water in MRS

For *in vivo* MRS, water provides the medium for all the biochemical reactions involving the metabolites being studied. Mobility of the metabolite molecules makes MRS feasible, and these molecules are mobilised by water (section 1.2). The mobility of the metabolite molecules depends on the nature of their chemical bonds; the relative mobility in turn influences how the molecules interact with one another. For a given metabolite, its position on the frequency axis is determined by the degree of shielding of its protons by neighbouring atoms; whereas the interaction of its molecules determines the splitting of its spectral peak. A certain number of protons in the molecular structure of each metabolite determines the intensity of the spectral peak of that metabolite (details in sections 2.2.1-2). In particular, the frequency positions of the spectral peaks are unique and specific to each metabolite, and are therefore used in the identification of the metabolites.

Aside from the major role water plays in MR spectral peak characterisation and identification as mentioned above, it is also relevant mostly in spectral processing and quantification in MRS. In the following subsections, the relevance of water in MRS that have been applied in this thesis are discussed; only MRS thermometry (section 1.4.2) has not been applied in this thesis but has been discussed in order to introduce the concept of brain temperature measurements using the MRS technique. This would then make it clearer when MRS thermometry is suggested as one of the possible research areas where the methods developed in this thesis could be applied (see section 9.3.2).

1.4.1 Reference Standard

Tissue water contributes a large quantifiable peak in the MR spectrum (Figure1.5) that can be used as an internal reference standard to quantify the metabolites. In most MRS studies, the unsuppressed-water signal is acquired

separately (from the metabolite spectra) for this purpose. However, as in this thesis, it is also possible to acquire both the reference water and metabolite spectra at the same time (section 2.3.1.3). These two acquisition methods use the water peak area together with the molar concentration of tissue water (~55.51 mol/L) in a model to estimate the metabolite concentrations. Generally, such models take the form:

$$[\text{Metabolite}] = A_{\text{metabolite}}/A_{\text{standard}} \times (\text{Correction factors}) \times [\text{Standard}] \quad \text{(Eq. 1.4)}$$

In this model, [Metabolite] is the estimated metabolite concentration, $A_{\text{metabolite}}$ is the area under the metabolite peak whose concentration is to be estimated, A_{standard} is the area under the water peak which is the reference standard and [Standard] is the concentration in molar units of pure water which is approximately 55.6 mol/L [31]. The correction factors may vary depending on the errors that are more likely to affect the measurements and so these may vary depending on the study.

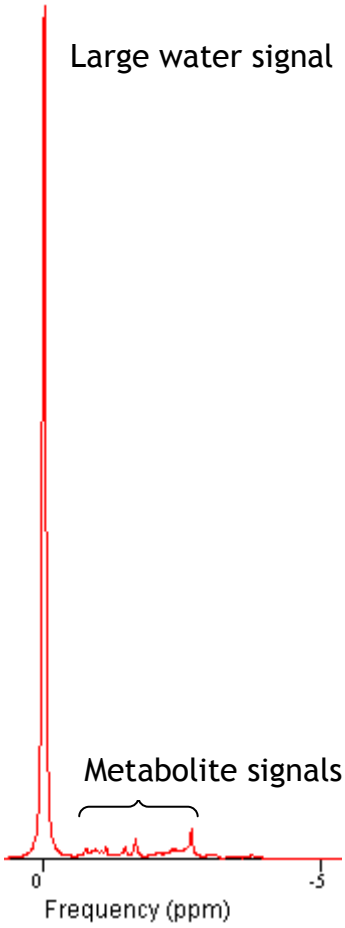

Figure 1.5: MR Spectrum showing the large residual water peak after its suppression
The figure also illustrates the importance of suppressing the water signal: the metabolites of interest have a signal more than one hundred times smaller than that of the water peak, and without water suppression will be poorly resolved.

1.4.2 MRS Thermometry

The water peak is relevant in non-invasive and *in vivo* brain temperature measurement using MR Spectroscopy. This technique depends on the effect of temperature on the water proton chemical shift [43, 44].Temperature drifts affect the local magnetic field strength experienced by the water protons in their chemical environment. A change in magnetic field strength local to the water protons results in a shift in the water peak resonance frequency. This is manifested in a 'displacement' of the water peak from its normal position on the frequency axis of the MR spectrum (Figure 1.6). Cady et al [43] investigated this temperature-dependent frequency shift in the brains of anaethetised, ventilated new-born piglets, and subsequently estimated the

brain temperature in six new-born human infants using the NAA peak as a reference in the following equation:

$$T = 286.9 - 94(\Delta H_2O - \delta_{NAA}) \quad \text{(Eq. 1.5)}$$

In equation 1.5, T is the estimated temperature in degree Celsius, ΔH_2O is the measured frequency offset of the water peak and δ_{NAA} is the chemical shift of the reference NAA peak, which is 2.01 ppm.

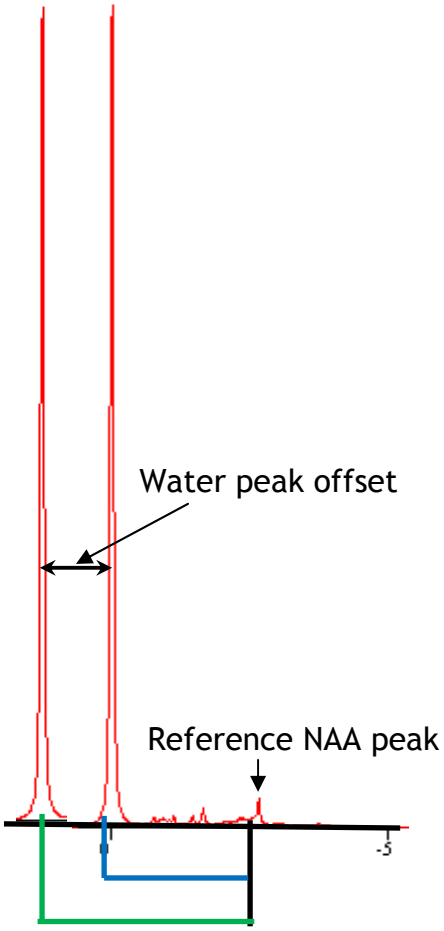

Figure 1.6: Temperature-dependent frequency shift of the water peak
Blue line: normal chemical shift of the water peak relative to the NAA peak; green line: frequency offset from the reference NAA peak. The new frequency of the water resonance peak (green line) is denoted by ΔH_2O, and the chemical shift of NAA denoted by δ_{NAA}

1.4.3 Eddy current correction

MR Spectroscopy uses magnetic field gradients to spatially define a voxel to which spectra are localised (sections 2.2.3.2-3). Rapid switching of the magnetic field gradients (which occurs in every localisation pulse sequence)

induces eddy currents in the magnetic cryostat. This causes a transient distortion of the magnetic field which consequently causes time-dependent shifts of the resonance frequency in the selected volume. The effect of eddy currents on MRS is that they result in a distorted or poorly resolved spectrum in the frequency domain [45, 46].

The eddy current correction procedure involves the use of the unsuppressed-water signal as a reference for the water-suppressed signals (i.e. the metabolites). Usually, the unsuppressed-water peak is acquired by using the same spoiler gradients as the metabolite spectrum and so will be affected by the same distortions. Practically, the metabolite signal is divided by the phase factor of the water signal for each data point in the time-domain by the following derivation [46]:

The received signal, $A(t)$ after phase-sensitive detection, can be described as a complex parameter with real part $A_R(t)$ and imaginary part $A_I(t)$, and phase $\Phi(t)$. The real and imaginary entities can be described together as a magnitude $A_M(t)$ as shown in the following equations:

$$A(t) = [A_R(t) + iA_I(t)]\, e^{i\Phi(t)} = A_M(t)\, e^{i\Phi(t)} \qquad \text{(Eq. 1.6)}$$

The transmitter frequency on the MR scanner is tuned to the water resonance frequency. Therefore, the time-dependent phase component of the water signal (w) is only caused by eddy currents as follows (i.e. modifying equation 1.6):

$$A_w = A_{M,w}(t)\, e^{i\Phi_w(t)}, \text{ where } \Phi_w(t) = \Phi_{eddy}(t) \qquad \text{(Eq. 1.7)}$$

The metabolite spectra are water-suppressed. Therefore, the phase of their signal, $\Phi_s(t)$ is the sum of the required spectral information, $\Phi_{req}(t)$ and the effect of eddy currents, $\Phi_{eddy}(t)$:

$$A_{suppressed} = A_{M,s}(t)\, e^{i\Phi_s(t)}, \text{ where } \Phi_s(t) = \Phi_{req}(t) + \Phi_{eddy}(t) \qquad \text{(Eq. 1.8)}$$

Dividing the suppressed signal (i.e. equation 1.8) by the phase factor of the water signal (in equation 1.7) results in the cancellation of the effect of eddy currents as shown in the following equation:

$$A_{corrected} = A_{M,s}(t)\, e^{i\Phi_s(t)} / e^{i\Phi_w(t)} \quad \text{(Eq. 1.9)}$$

Hence $A_{corrected} = A_{M,s}(t)\, e^{i\Phi req(t)}$, the Fourier transform of which yields a spectrum without eddy current effects in the frequency domain. The resulting spectrum is also simultaneously phase-corrected with good spectral resolution.

1.4.4 Signal Weighting in Phased-Array Coil Data Combination

Further to eddy current and phase correction, the unsuppressed-water is also of relevance in the determination of signal weights for signal combination in phased-array head coils. In an N-channel head coil, the weighting factors are determined by [46-48]:

$$W_k = A_{w.\,k} / \sum_{l=1}^{N} A_{w.\,l} \quad \text{(Eq. 1.10)}$$

where $A_{w,k}$ is the maximum amplitude of the time-domain unsuppressed-water signal (obtained by fitting an exponential decay to the data) and $A_{w,l}$ is the unsuppressed-water signal from the individual coil elements.

The subsequent summation procedure used by the N-channel head coil combines the individual phase-corrected spectra, $A_{corrected}$ by using the weighted sum in equation 1.9:

$$A_{sum}(t) = \sum_{k=1}^{N} W_k \cdot A_{corrected,\,k}\,(t) \quad \text{(Eq. 1.11)}$$

A_{sum} therefore becomes the amplitude of the localised metabolite signals recorded from the MRS voxel. In this thesis, an 8-channel head coil was used; therefore N = 8 in equations 1.10 and 1.11.

1.5 Structure and Outline of this Thesis

The body of this thesis is structured into nine chapters under three main sections: background to MRS with regards to the study theme (chapters 1-2), experimental results (chapters 3-8), and general conclusions (chapter 9). The six results chapters are presented in the format of a typical peer reviewed scientific paper (i.e. introduction, methods, results and discussion, and summary/conclusions).

An outline, with brief descriptions, of each chapter contained in this thesis is as follows:

- Chapter 1; Overview of *in vivo* MR Spectroscopy, theme of this thesis, its objective, structure, and chapter outline.

- Chapter 2; Principles of NMR as applied to MRS, biological significance of the MR spectra, analysis of the MR spectra, statistical methods used in this thesis, and ethical issues in the human studies of this thesis.

- Chapter 3; Longitudinal reproducibility MRS studies measuring the precision of the ^{1}H-MRS signal area estimates, *in vitro* and *in vivo*.

- Chapter 4; RF coil sensitivity mapping using the unsuppressed-water signal acquired from a phantom.

- Chapter 5; Measurement of brain tissue, metabolite and water relaxation times; partial volume correction by voxel localisation, registration and segmentation.

- Chapter 6; Quantification of cerebral water content, its assessment by brain region, tissue type, gender and age; comparison between MT ratios (as measured by MT imaging) and water content (as measured by MRS) of the same brain regions.

- Chapter 7; Assessment of the changes (compared to controls) in cerebral water and metabolite concentrations in psoriatic arthritis.

- Chapter 8; Study of the BOLD changes in cerebral water and metabolite resonances during sustained visual stimulation of the visual cortex.

- Chapter 9; Novel contributions of this thesis, methodological limitations, and some suggested extensions of this work.

Chapter 2: Background

This chapter introduces the fundamental concepts of Nuclear Magnetic Resonance and their application to Magnetic Resonance Spectroscopy (MRS). The chapter aims to provide an explanation of: MRS data acquisition, interpretation and biological significance of the MR spectra. The chapter therefore is of relevance to the understanding of the MRS results presented in the subsequent chapters of this thesis.

2.1 Principles of Nuclear Magnetic Resonance

Nuclear Magnetic Resonance (NMR) is a physical phenomenon that depends on a property called spin, which is possessed by some atomic nuclei. Atomic nuclei that contain odd number of protons and/or of neutrons have an intrinsic spin. Examples of such nuclei are ^{1}H, ^{6}Li, ^{7}Li, ^{13}C, ^{14}N, ^{15}N, ^{17}O, ^{19}F, ^{23}Na, ^{31}P, ^{35}Cl, and ^{39}K. Any such nucleus with an intrinsic spin also has a magnetic property and is theoretically NMR-sensitive: it is affected by external magnetic fields and electromagnetic waves. Such a nucleus must also have a high natural abundance and gyromagnetic ratio to generate a large NMR signal. Hydrogen-1 (^{1}H) is the most commonly studied NMR nucleus due to its high natural abundance (99.984 %), high NMR-sensitivity (100 %) and high gyromagnetic ratio (26.75×10^{-7} rad/T sec)[17].The ^{1}H atom has only one proton but no neutrons, and so is often simply referred to as a "proton".

The principle of NMR usually involves two sequential steps:

1. The alignment of the magnetic nuclear spins in an external, static magnetic field, B_0

2. The perturbation of this alignment of the nuclear spins by the use of an electromagnetic radiofrequency (RF) pulse. The frequency of the RF pulse depends on the nucleus being studied and the strength of B_0.

The resulting response to these two sequential steps by the nuclear spins, $\underline{\mu}_i$ is the phenomenon that is exploited in Magnetic Resonance Imaging (MRI) and Spectroscopy (MRS).

2.1.1 Origin of the NMR Signal

2.1.1.1 Alignment of Magnetic Spins in B_0

A proton has a positive charge and also rotates about its axis. As a rotating mass with an electrical charge, it has magnetic moment and angular momentum.

In the presence of an external magnetic field B_0, the magnetic moment experiences a torque. At the same time, it tries to align with or against the direction of B_0 (in the case of spin, $\boldsymbol{I}$ = 1/2). As a result, it precesses about the axis of $\boldsymbol{B}_0$ at a rate that is proportional to the strength of the applied magnetic field. The rate of precession is called the Larmor frequency, which is given by the Larmor equation:

$$\omega = \gamma B_0 \qquad \text{(Eq. 2.1)}$$

where ω is the Larmor frequency in megahertz (MHz), B_0 is the strength of the applied magnetic field in tesla (T) and γ is the gyromagnetic ratio, a constant specific to a particular nucleus.

In the absence of an external magnetic field however, a population of protons are randomly oriented and there is no net magnetisation (Figure 2.1(A)). When exposed to a strong magnetic field $\boldsymbol{B}_0$, the protons tend to align parallel or anti-parallel to $\boldsymbol{B}_0$ [for $\boldsymbol{I}$=1/2, where $\boldsymbol{I}$ is the intrinsic spin of the nucleus] (Figure 2.1(B)). The parallel alignment is slightly preferred as it is equivalent to spins residing in a lower energy level.

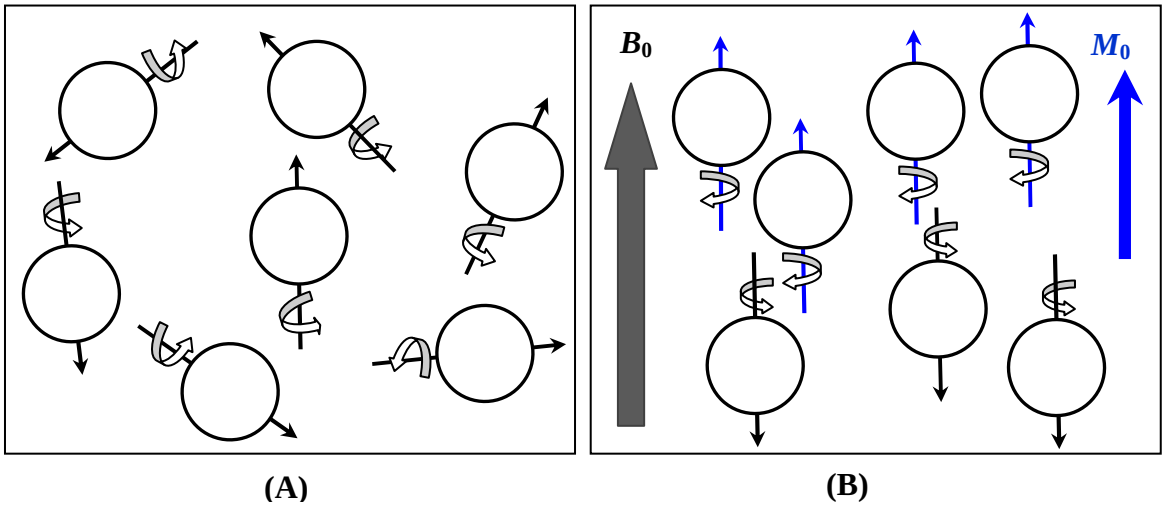

Figure 2.1: Alignment of NMR-sensitive spins in the case of I = 1/2
(A) Spins are randomly aligned in the absence of an external magnetic field but each precesses about its axis; (B) When an external magnetic field, B_0 is applied, some spins align parallel while others align antiparallel to the field. Spins in each alignment resonate in phase with each other. Those spins aligned parallel to the field create a net magnetisation, M_0.

If N_P and N_A are respectively the numbers of protons in the parallel and anti-parallel orientations, then the equilibrium populations are given by the Boltzmann distribution:

$$N_P/N_A = \exp(\hbar\omega/kT) \approx 1 + \hbar\omega/kT \qquad \text{(Eq. 2.2)}$$

where k is Boltzmann's constant, ħ is Plank's constant and T is absolute temperature. The fractional excess of protons aligned with $\boldsymbol{B}_0$ is then given by:

$$(N_P\text{-}N_A)/N_A \approx \hbar\omega/kT = \hbar\gamma B_0/kT \qquad \text{(Eq. 2.3)}$$

This fractional excess of protons creates a small collective net equilibrium magnetisation $\boldsymbol{M}_0$ which points along the axis of $\boldsymbol{B}_0$. $\boldsymbol{M}_0$ is called the longitudinal magnetisation and is the source of the NMR signal. As it has both magnitude and direction, the longitudinal magnetisation is considered to be a vector visualised in a rotating frame of reference (Figure 2.2). This frame of reference has three mutually orthogonal axes, represented by x', y' and z'. $\boldsymbol{B}_0$ points in the z'-direction and so the longitudinal magnetisation $\boldsymbol{M}_0$ being parallel to $\boldsymbol{B}_0$ also points in the z'-direction while precessing at a frequency of ω.

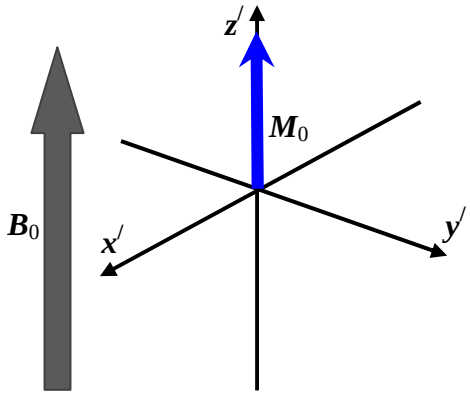

Figure 2.2: Equilibrium magnetisation, M_0 aligned parallel to the B_0 field in the rotating frame of reference

2.1.1.2 Irradiation of the B_0-aligned Spins with an RF Pulse

In order to measure M_0, a radiofrequency (RF) field of amplitude B_1 is applied perpendicularly to B_0 (Figure 2.3). The applied RF field oscillates in phase with, and at the same rate ω as, the precessing nuclear magnetic moments, $\underline{\mu}_i$ and introduces energy into the spin system. Viewed from the laboratory frame, the equilibrium magnetisation, M_0 (i.e. the total of the individual $\underline{\mu}_i$) lies along the +z-axis parallel to B_0 in the Cartesian coordinate system. B_1 on the other hand could be aligned with the laboratory x-axis and can be resolved into two components rotating in opposite directions about the z-axis: one of these becomes the required B_1 field, in phase with the precessing magnetisation, while the other appears to rotate at 2ω relative to the magnetisation, and can usually be ignored.

The required B_1 field causes M_0 to tip away from its parallel position with B_0 toward the transverse plane, and to execute a spiral path, as shown in Figure 2.3; this is known as excitation. The excitation energy of B_1 required to cause the tipping of each $\underline{\mu}_i$ (making up M_0) is given by:

$$\Delta E = \hbar\gamma B_0 \qquad \text{(Eq. 2.4)}$$

If the duration and strength of B_1 are sufficient to tip M_0 through 90°, a transverse magnetisation will be created and M_0 will now lie in the xy-plane where it will be denoted by M_{xy}. This is known as a 90° or $\pi/2$ pulse. Alternatively, if M_0 is tipped right over onto the -z direction, this is called a 180°, π or inversion pulse. Generally, the RF pulse which rotates the longitudinal magnetisation, M_0 by an angle of α^o is called a α^o RF pulse. The RF pulse angle is normally 90° or 180° in most conventional pulses. Nonetheless, low flip angle gradient echo techniques, such as SPGR, are becoming common.

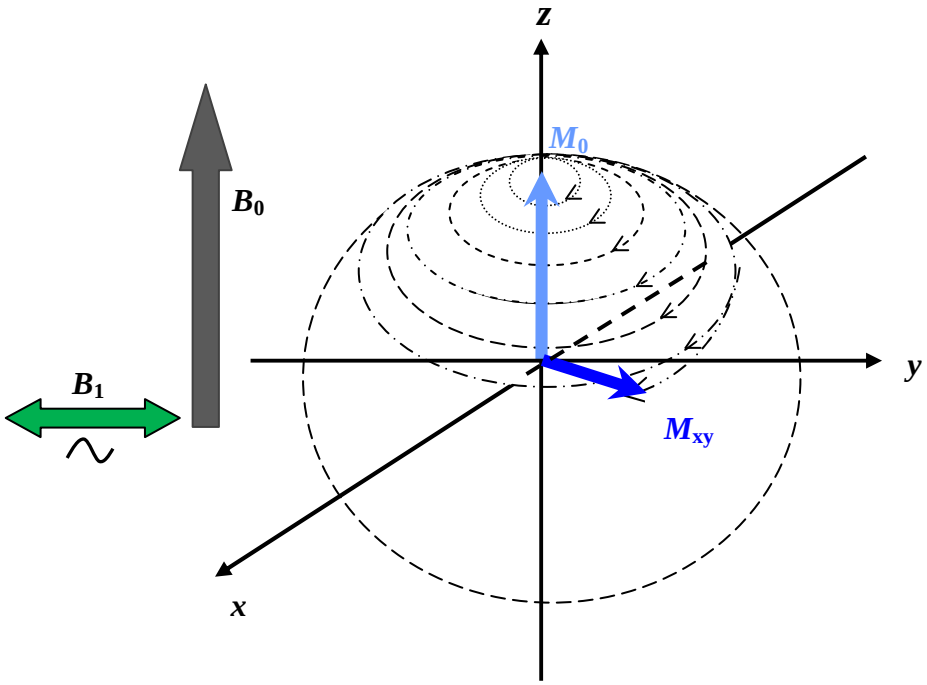

Figure 2.3: The B_1 field oscillates at the same Larmor frequency as the protons and tips the longitudinal magnetisation, M_0 into the transverse plane, causing it to execute a spiral path.
M_0 is denoted by M_{xy} in the transverse or xy-plane. This is illustrated in the laboratory frame of reference where the three axes are x, y and z and not x', y' and z'.

When the RF pulse is switched off, M_0 continues to precess about B_0, describing a cone of half-angle α, called the flip angle, as shown in Figure 2.4. For any RF pulse, B_1 of duration t_p, the flip angle is described as:

$$\alpha = \gamma B_1 t_p \qquad \text{(Eq. 2.5)}$$

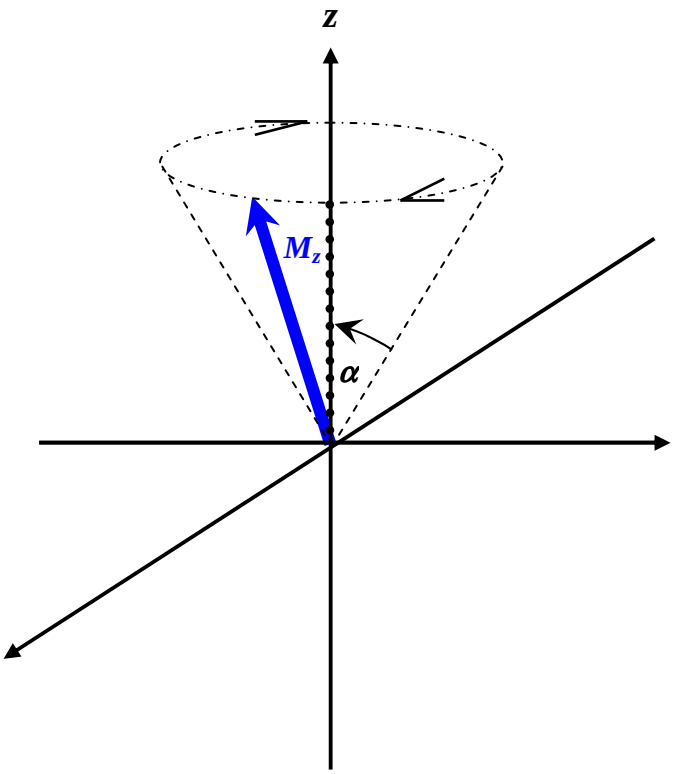

Figure 2.4: The longitudinal magnetisation in the absence of B_1 describes a cone of half-angle, α along the z-axis and is now denoted by M_z in the laboratory frame of reference.

2.1.1.3 Generation of the NMR Signal

B_1 is often called the radiofrequency (RF) field because $\omega/2\pi$ normally lies between 1 MHz and 500 MHz. The B_1 field for NMR experiments is generated by applying a voltage, oscillating at ω, to the terminals of a suitable RF coil surrounding the sample. Whenever the transverse magnetisation M_{xy} is created by the application of B_1, it rotates about the z-axis (Figures 2.3-4). This has the effect of an electrical generator and induces an alternating voltage of the same frequency as the Larmor frequency, ω in a receiver coil. This induced voltage is the NMR signal. The strength of this resulting NMR signal can be increased by decreasing the temperature T of the study sample (though impractical in humans) or increasing the applied magnetic field strength B_0 (equation 2.3) or increasing the flip angle of the RF pulse up to 90^{o}. The NMR signal is then collected and processed with sensitive receivers and computers to generate an MR image or spectrum.

2.1.2 Relaxation of the NMR Signal

The applied RF field normally disturbs the equilibrium state of the spin system. However, as soon as the RF pulse is switched off, the spin system tries to re-establish equilibrium. The return to equilibrium of the spin system causes the NMR signal to gradually decay (Figure 2.5) due to the loss of transverse magnetisation with time. This type of decaying signal obtained in the absence of the B_1 field is called a Free Induction Decay (FID). The processes that determine the return to equilibrium of both longitudinal and transverse magnetisation are called "spin-lattice" and "spin-spin" interactions, respectively. These two processes cause T_1 (or spin-lattice) relaxation and T_2 (or spin-spin) relaxation respectively, and are exponential in nature with time constants T_1 and T_2. These two time constants are important for tissue and spectral characterisation in MRI and MRS.

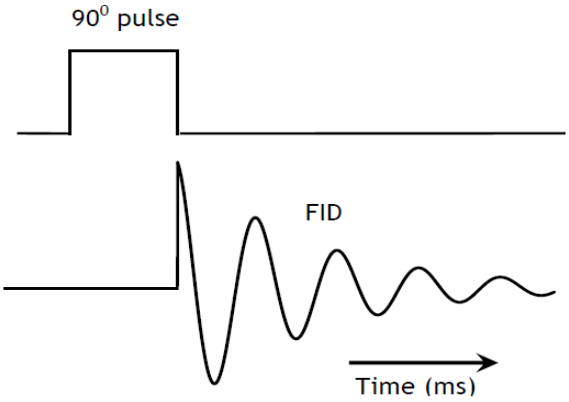

Figure 2.5: Free induction decay (FID) following a 90° excitation pulse

2.1.2.1 T_1 Relaxation

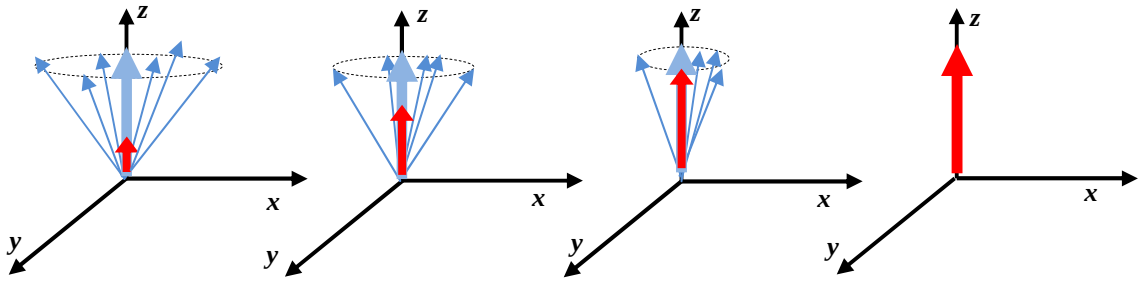

Figure 2.6: Return of the bulk magnetisation to its equilibrium magnetisation, M_0 due to spin-lattice relaxation with time constant T_1.
The thin blue arrows represent the individual spins, $\underline{\mu}_i$ making up the equilibrium magnetisation, M_o (thick blue arrow). The thick red arrow represents the longitudinal magnetisation, M_z recovering monoexponentially towards its initial equilibrium value of M_o (from left to right). The last diagram on the right shows the point at which M_z has recovered fully to M_o (i.e. Mz = Mo).

Spin-lattice or T_1 relaxation describes the transfer of energy from the spin system to its surroundings, otherwise known as the lattice [32]. The energy transfer process causes the longitudinal magnetisation, $\boldsymbol{M}_z$ to gradually recover exponentially towards its initial equilibrium value $\boldsymbol{M}_o$ (Figure 2.6). Thus T_1 relaxation is also known as longitudinal relaxation or T_1 recovery, described by the monoexponential equation:

$$M_z(t) = M_0[1 - \exp(-t/T_1)] \qquad \text{(Eq. 2.6)}$$

where $M_z(t)$ is the longitudinal magnetisation at time t, M_0 is the equilibrium magnetisation and T_1 is the longitudinal relaxation time.

The T_1 rate constant depends on the strength of the applied magnetic field B_0, tissue composition, structure, molecular motion and surroundings. Protons in different tissues and metabolites therefore have different T_1 recovery rates. For instance, at 1.5 T, the T_1 relaxation time of grey matter tissue is about 1138 ms whereas that of white matter tissue is about 649 ms [49].

2.1.2.2 T_2 Relaxation

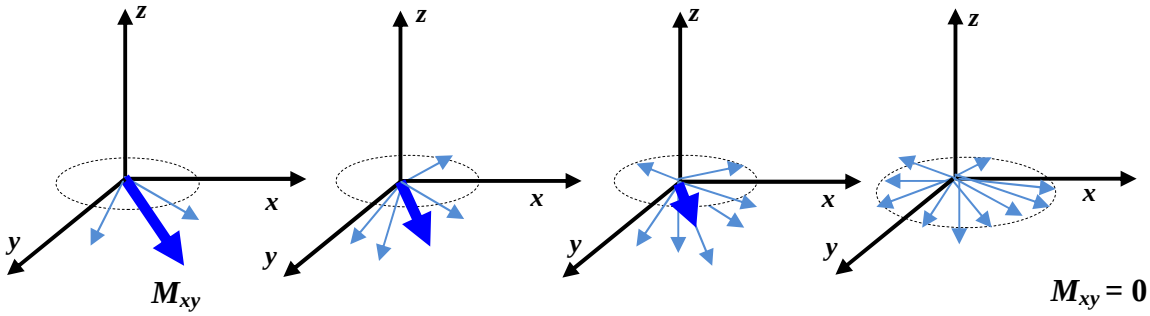

Figure 2.7: Loss of phase coherence between neighbouring magnetic moments, μ_i due to spin-spin relaxation causes an exponential decay of the transverse magnetisation, M_{xy} with time constant T_2.
The thick blue arrow represents the transverse magnetisation, M_{xy} which, due to the T_2 relaxation effect, experiences loss in phase coherence among its component spins, μ_i (light blue arrows); this results in the fanning out of the individual spins, μ_i while M_{xy} decays exponentially to zero (from left to right).

T_2 relaxation describes the loss in phase coherence between neighbouring spins with time. Each spin experiences the external magnetic field, B_0. However, one spin affects the other by slightly altering the magnetic field experienced by the second spin. The precession rate of the second spin will change slightly, causing an increase or decrease in its phase relative to the first spin. Thus, these dipole-dipole interactions cause the precession rates of the individual spins to vary slightly. The result is that they lose phase coherence (i.e. they no longer precess at the same rate as before) and the resultant transverse magnetisation M_{xy} decays gradually to zero as shown in Figure 2.7. The relaxation process can be described by the exponential equation:

$$M_{xy}(t) = M_{0,xy} \exp(-t/T_2) \qquad \text{(Eq. 2.7)}$$

where $M_{xy}(t)$ is the transverse magnetisation at time t, $M_{0,xy}$ is the initial transverse magnetisation (immediately after the RF pulse) and T_2 is the transverse relaxation time.

This type of relaxation involves energy exchange among only the spins and so is called spin-spin relaxation.

Spin-spin relaxation time depends on the molecular environment of the spins, and so T_2 varies between tissues. Free molecules (i.e. spins) in fluids influence the phase of each other less than if they were close to one another as in solids. Thus, spins in fluids take longer to dephase than those in solids. Fluids therefore mostly have longer T_2 relaxation times than solids. For instance, in tumours where there is more unbound water than in normal tissues, spins take longer to dephase. Therefore at 1.5 T, in white matter tissue, lesions have longer T_2 relaxation times (e.g. 165 ms) compared to normal tissue (98 ms) [49].

T_1 and T_2 relaxation occur simultaneously but are independent of each other. Nonetheless, the dephasing of the spins occurs much faster than the recovery of longitudinal magnetisation. For this reason, longitudinal magnetisation can never be re-established until all the transverse magnetisation has decayed away [32]. Hence for a given tissue, T_2 is usually about a tenth of T_1.The T_1 and T_2 values of CSF however are close at a given field strength: for example, T_1 = 3302 ms and T_2 = 2269 ms at 0.15 T [50].

2.1.2.3 T_2* Relaxation

Intrinsic inhomogeneities caused by the magnetic field generator and by the person being examined also contribute to dephasing of the spins [32]. The rate of the signal decay caused by these field inhomogeneities is even faster than that caused by T_2. This second type of decay (or "pseudo-relaxation") occurs with the time constant T_2*, which is typically always shorter than T_2. The observed rate of decay of the NMR signal due to T_2* is described as:

$$1/T_2^* = 1/T_2 + \gamma\Delta B_0 \qquad \text{(Eq. 2.8)}$$

where ΔB_0 is the amount of variation of the applied magnetic field strength over the region occupied by the study sample.

The T_2* effect is more pronounced at tissue borders, particularly at air-tissue interfaces, or may be induced by local magnetic fields (e.g. from iron particles).

2.1.3 Methods of Measuring Relaxation

Measurement of the T_1 and T_2 relaxation times involves the use of a series of RF pulses. These pulses are applied sequentially at predefined time intervals in order to produce varying signal intensities with respect to the time intervals. Such a group of applied RF pulses is known as a "pulse sequence". The most common pulse sequences for measuring T_1 and T_2 relaxation times are described in the following subsections. These sequences have been used in this thesis for the estimation of relaxation times of brain tissue and metabolites (chapter 5).

2.1.3.1 Measurement of T_1 Relaxation Time

The inversion recovery pulse sequence (Figure 2.8) is used for measuring T_1 relaxation time. It comprises of a 180^o pulse, followed after an inversion time, *TI* by a 90^o pulse.

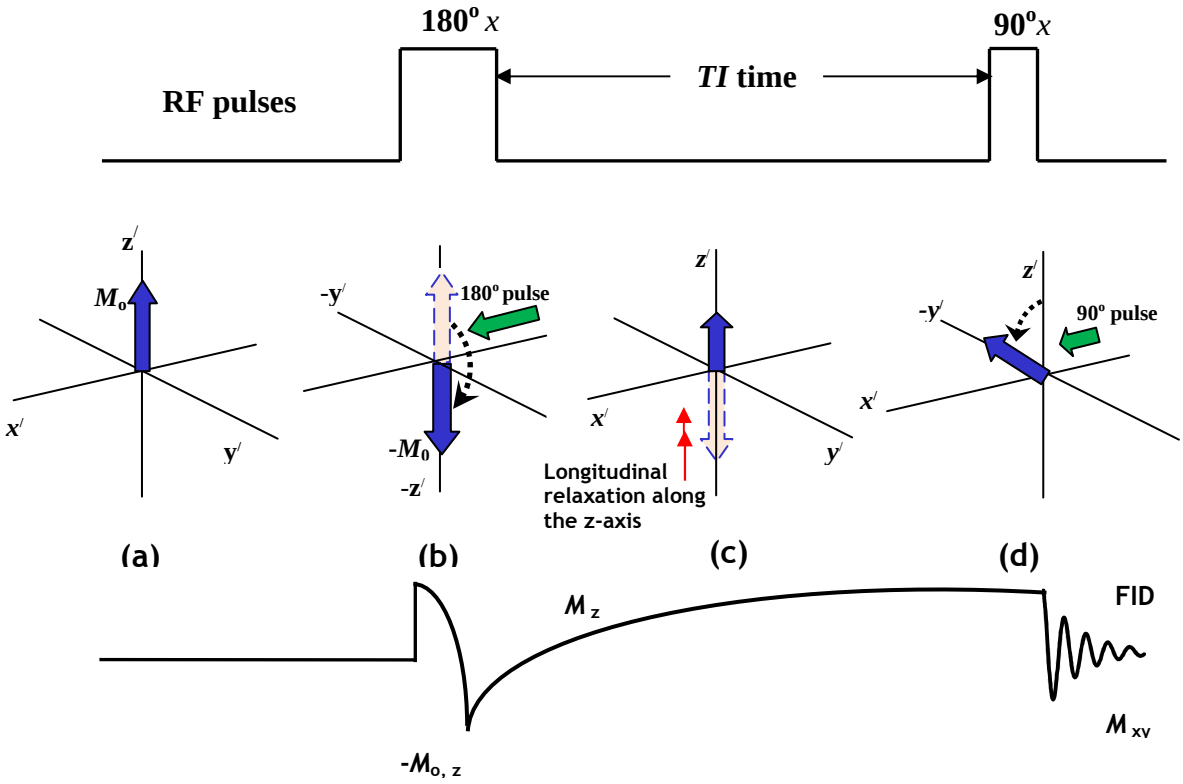

Figure 2.8: The inversion recovery experiment viewed from the rotating frame of reference, x', y', z'.
A 180^0 pulse inverts the equilibrium magnetisation into the $-z'$ plane (a-b). After a time delay called the inversion time, *TI* some amount of signal recovers along the $+z'$-axis by the T_1 recovery process (c). At the end of the *TI* time, a 90^0 pulse is applied to tip any recovered longitudinal magnetisation, M_z into the transverse plane; precession of this transverse magnetisation, M_{xy} generates an FID which is the measurable NMR signal (d).

The 180^o pulse inverts the longitudinal magnetisation onto the $-z'$ axis such that its $\boldsymbol{M}_z$ component has an initial value of $-\boldsymbol{M}_0$ (b). During the inversion time, *TI* the magnetisation recovers towards its equilibrium value of $+\boldsymbol{M}_0$ along the z' axis (c). After the application of the 90^o pulse, any $\boldsymbol{M}_z$ component recovered (along the z' axis) is converted into transverse magnetisation, $\boldsymbol{M}_{xy}$ (d). The magnitude and sign of the resulting FID indicates how far the magnetisation had recovered along the z' axis during the *TI* time (Figure 2.9).

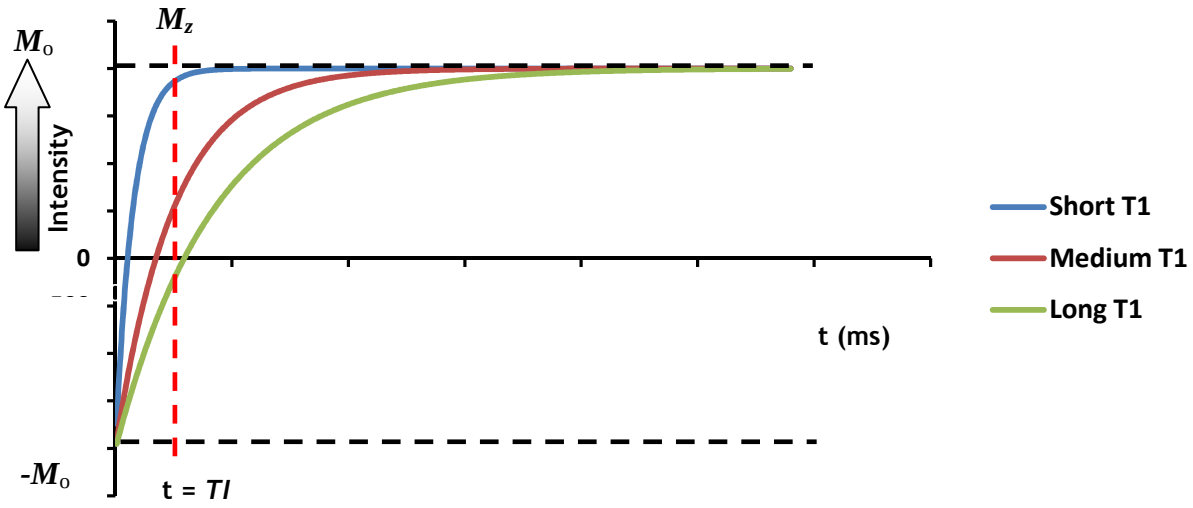

Figure 2.9: A plot of the intensity of the recovered magnetisation, M_z versus time, t in the inversion recovery experiment.
At t = 0, the 180^0 inversion pulse ends; at $t = TI$ following the inversion pulse, the 90^o excitation pulse is applied, converting M_z into a transverse magnetisation and generating an FID whose intensity is proportional to $M_z(TI)$. Three curves are shown for samples with different T_1 relaxation times: the sample with the shortest T_1 (blue line) will appear brightest in an MR image because its magnetisation recovers fastest to a large, positive value at $t = TI$.

By a least-square curve fit (similar to those of Figure 2.9) of the signal intensities, S versus their corresponding TI times, T_1 can be estimated from the exponential equation:

$$S \propto M_z(TI) = M_0\ [1 - 2\exp(-TI/T_1)] \qquad \text{(Eq. 2.9)}$$

where M_0 is the equilibrium magnetisation equivalent to the proton density of the sample.

For the T_1 measurements in this thesis, the inversion recovery experiment was implementable on the MR scanner by varying the repetition time (TR). Signal intensity, M_z was therefore a function of TR as follows:

$$M_z(TR) = M_\infty \times [1 - \exp(-TR/T_1)] \qquad \text{(Eq. 2.10)}$$

where M_∞ is the signal intensity at the longest possible TR time.

2.1.3.2 Measurement of T_2 Relaxation Time

The spin echo pulse sequence (Figure 2.10) is used to measure T_2 relaxation time. It comprises a 90° pulse, followed after a time delay of $TE/2$ by a 180° pulse.

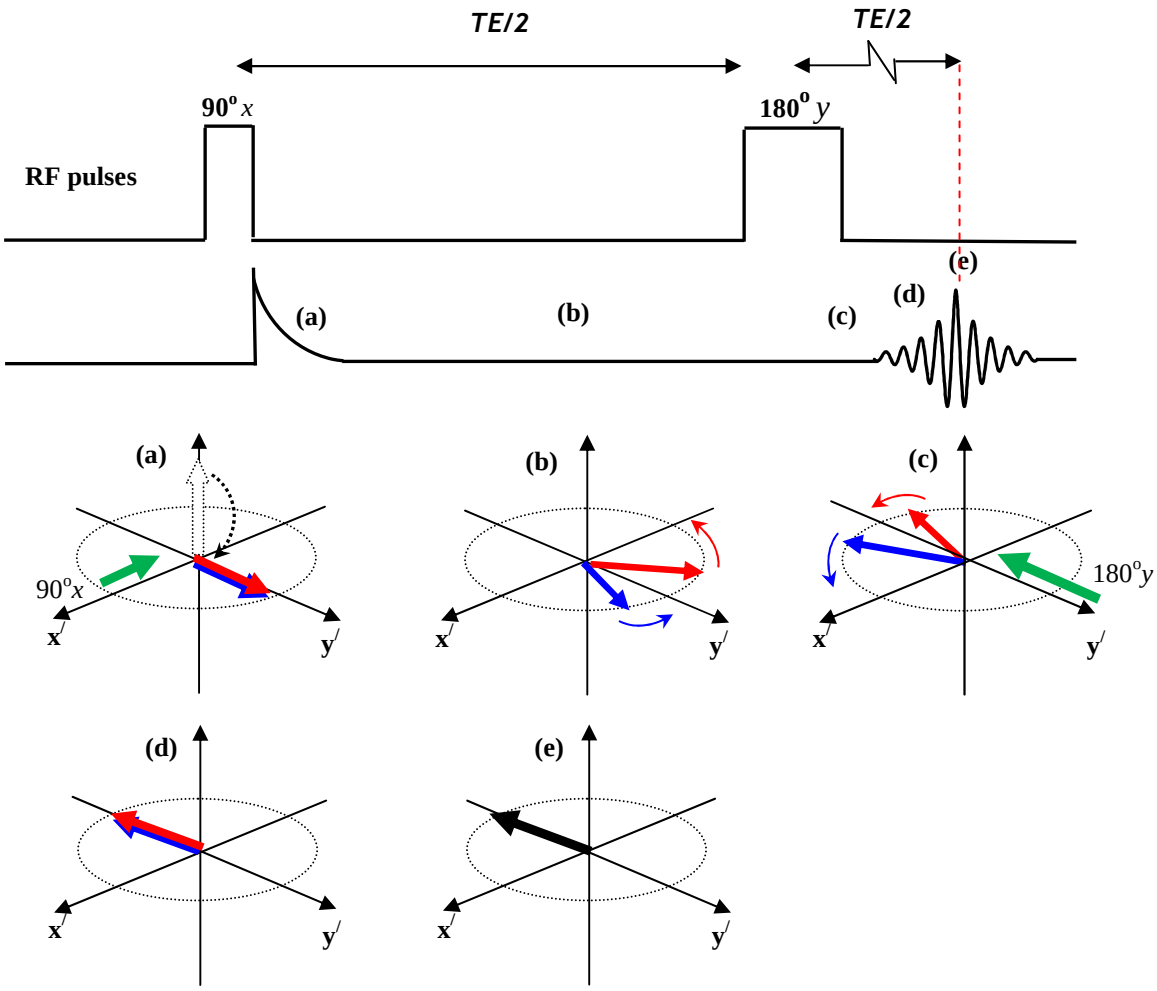

Figure 2.10: The spin-echo experiment viewed from a rotating frame of reference
A 90° excitation pulse (in the x′-direction) generates an FID in the transverse plane at time $TE/2$ (a). Some spins precess faster (red arrow) than others (blue arrow); this creates a phase difference between them (b). After another time delay of $TE/2$, a 180° inversion pulse (in the y′-direction) inverts the spins (c) such that the faster precessing spins catch up with the slower precessing spins (d). The spins intersect (black arrow) at time *TE (i.e. TE/2 + TE/2)* where the maximum spin echo signal is recorded (e).

The 90° pulse flips the magnetisation vector, $\boldsymbol{M}_0$ onto the y' axis (a), where the component vectors making up $\boldsymbol{M}_0$ are caused to dephase with respect to one another by spin-spin interaction (b). Following the application of the 180° pulse, after the waiting time of $TE/2$, the "fan" of magnetisation vectors is

flipped over along the $-y'$ axis (c). The initial dephasing process after the 90° pulse is now exactly reversed and the vector sum of the rephrasing magnetisation vectors reaches a maximum at time *TE*, at the centre of an echo signal (d). In this case, instead of the initial FID after the 90° pulse, it is rather the spin echo signal after the 180° pulse that is acquired (e), the amplitude, *S* of which is given by:

$$S = S_0 \exp(-TE/T_2) \qquad \text{(Eq. 2.11)}$$

where S_0 is the initial amplitude of the FID generated by the 90° pulse at $TE \approx 0$.

The T_2 relaxation time can then be estimated from equation 2.11 by performing a least-square fit to a few sampled points (at least five) for the different echo times used in the experiment. The fit to the data usually takes the form of a monoexponential decay curve as shown in Figure 2.11.

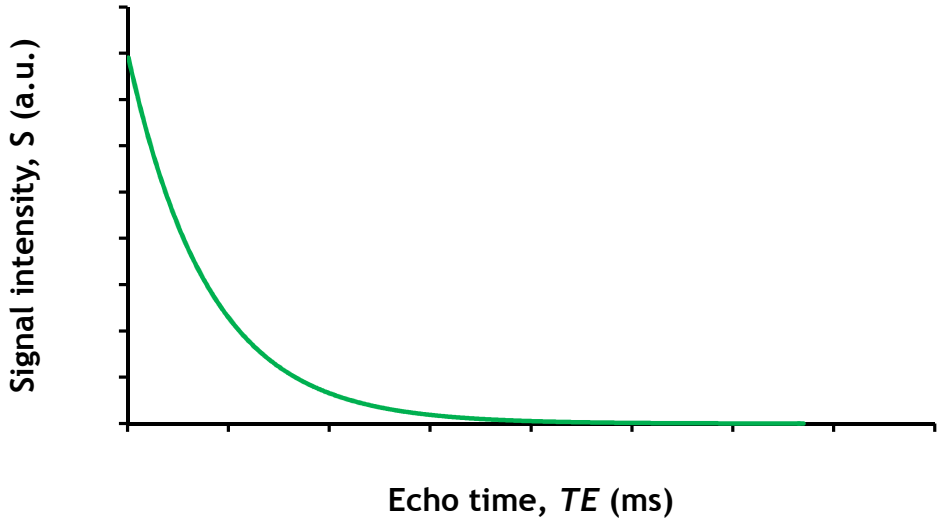

Figure 2.11: A typical T_2 decay curve showing a plot of spin echo signal intensity, S versus echo time, *TE*

In section 5.2.1.4, the T_2 relaxation time of brain tissue was measured using a multi spin-echo pulse sequence commercially available on the GE MR scanner used for all the experiments of this thesis. The main advantage of the multi spin-echo acquisition is that several echoes can be measured within a reasonable experimental time. The technique could, however, measure T_2 inaccurately due to stimulated echoes arising from RF pulse imperfections [51-

53]. Imperfect 180^o pulses do not refocus all the magnetisation in the selected slice, thus converting part of the transverse magnetisation into longitudinal magnetisation, which is subject to T_1 relaxation. The longitudinal components are later refocused by the subsequent 180^o pulses, resulting in unwanted T_1 relaxation time-dependent echoes [54]. However, the pulse sequence used in the acquisitions applies crusher gradients in the slice direction during each echo acquisition to reduce the effects of T_1 contamination in the image.

The principles of NMR discussed in the preceding sections form the bases of MR imaging and spectroscopy. However, further discussion on MR imaging is beyond the scope of this thesis; Weishaupt et al [32] provides a good background to MR hardware and imaging. Subsequent sections of this chapter will discuss the principles of NMR applicable to MR spectroscopy.

2.2 Principles of MR Spectroscopy

MR Spectroscopy can also be performed with nuclei that are NMR-sensitive (due to their magnetic spin properties) and abundant in a given sample. Examples of these nuclei are mentioned in section 2.1.

This section discusses the theory of MR Spectroscopy and its application in spectral generation and characterisation. The section concludes with a discussion on other factors that can affect the quality of the spectra and techniques of minimising them, some of which have been utilised in this thesis.

2.2.1. Chemical Shift

When a nucleus is placed in a magnetic field, $\boldsymbol{B}_0$, its electrons circulate in such a manner that there is an induced magnetic field, $\boldsymbol{B}_i$, aligned opposite to the main field. This is known as the shielding effect. The effective field, $\boldsymbol{B}_{eff}$, experienced by the nucleus is then reduced by a fraction, δ of $\boldsymbol{B}_0$ given by:
$\boldsymbol{B}_{eff} = \boldsymbol{B}_0(1-\delta)$, so that the Larmor frequency (equation 2.1) now becomes:

$$\omega = \gamma \boldsymbol{B}_0(1-\delta) \qquad \text{(Eq. 2.12)}$$

A nucleus with a greater electron cloud density experiences a greater shielding effect and thus has a lower Larmor frequency at a given field. In a chemical bond, nuclei share their electron clouds and the more electronegative of the pair tends to 'steal' charge from around the other one. In this case, the nucleus whose charge density is reduced by the more electronegative one is said to be deshielded. The deshielded nucleus experiences a higher $\boldsymbol{B}_{eff}$ value and so resonates at a higher frequency than its unbound state. Hence, the chemical environment of a given nucleus affects its resonance frequency.

The shielding effect is expressed in terms of the chemical shift, δ_{cs}. This is the fractional difference, in parts per million (ppm), between the Larmor frequency, ω_s of a nucleus in a particular chemical bond and the frequency, ω_{ref} of the same nucleus in a standard reference compound, expressed as:

$$\delta_{cs} = \frac{\omega_s - \omega_{ref}}{\omega_{ref} \times 10^{-6}} \qquad \text{(Eq. 2.13)}$$

The ppm scale is independent of $\boldsymbol{B}_0$. For *in vitro* ^{1}H-MRS, the reference compound is usually tetramethyl-silane, TMS [$(CH_3)_4Si$)], chosen because it contains almost a totally shielded nucleus. Its single peak is assigned a chemical shift of 0.0 ppm. TMS is toxic [31] and so in *in vivo* ^{1}H brain MRS, the CH_3 peak of N-acetyl aspartate (NAA) is usually the reference standard and δ_{cs} is expressed in this case as:

$$\delta_{cs} = \frac{\omega_s}{\omega_{transmitter} \times 10^{-6}} + \textit{offset} \qquad \text{(Eq. 2.14)}$$

where ω_s is the frequency of the sample, $\omega_{transmitter}$ is the frequency of the transmitter and *offset* is a constant that references the ppm scale to the *in vivo* standard (whose chemical shift value is 2.01 ppm).

The chemical shift phenomenon makes it possible for metabolites and other resonances to be distinguishable in a spectrum.

2.2.2 Spin-Spin Coupling

In the presence of a magnetic field, B_0, a bond between two nuclei 'A' and 'X' where for instance 'X' has an equal chance of being aligned with or against B_0, nucleus 'A' will be split into two equal spectral peaks. The spectral peak of nucleus 'A' that is coupled to 'X' aligned with B_0 will have a higher frequency; the peak coupled to 'X' aligned against B_0 will have a lower frequency. This frequency modification process by neighbouring nuclei is called spin-spin coupling. The *J*-coupling constant expresses the numerical difference (in hertz) between the two resulting frequencies from the same nucleus. It is a unique value for every molecule but unlike the chemical shift, it remains constant with B_0.

Generally, if nucleus 'A' is coupled to 'n' chemically equivalent 'X' nuclei, the spectral line of nucleus 'A' will be split into 'n+1' multiplet peaks. For instance, in the spectrum of ethanol, CH_3-CH_2-OH, the spectral line of the CH_3 group is split into a triplet by its interaction with the CH_2 protons while there is a reciprocal splitting of the CH_2 line into a quartet by its interaction with CH_3 protons. The OH line is split into a triplet by the CH_2 protons and each component of the CH_2 quartet is sub-split into a doublet by the OH proton. However, chemically equivalent nuclei (e.g. the three CH_3 protons) do not produce an observable splitting with each other. The C-C bond here contributes to the covalent bond electrons through which these spin-spin interactions take place.

2.2.3 Water Suppression and MRS Pulse Sequences

In the simplest form, such as in analytical chemistry, the MR spectrum from an entire uniform sample is collected without any form of spatial information [1]. However, in *in vivo* MR spectroscopy, other techniques are required to isolate the spectroscopic signals of interest from those generated by surrounding tissues. Early *in vivo* spectroscopy used a surface coil to restrict the volume of tissue from which signal was effectively collected. Signal strength was related to distance from the coil but with a limited spatial range [1]. Surface coils

were later used with a single slice-select gradient in a sequence known as Depth-Resolved Surface-coil Spectroscopy or DRESS [55]. Signals were collected from a whole slice with DRESS and so volume selection was poorly defined due to the non-uniform RF field distribution of the surface coil. Another disadvantage of the use of surface coils for spatial localisation was that it was more difficult to localise signal originating from a given volume deep within an organ. The technique was therefore limited to signal localisation from superficial organs.

Current methods rely on rapidly switched magnetic gradients to achieve spatial localisation. A voxel is defined by the intersection of three mutually orthogonal slabs, each slab being excited by a spatially selective pulse applied in the presence of a gradient (as in the case of slice selection in conventional MRI). The water, and sometimes fat, signals are several orders of magnitude larger than the signals of interest. The large spectral peak from the unwanted water/fat signal can cause distortion of nearby metabolite peaks and so it is necessary to suppress the solvent peak. The commonly used water suppression and spatial localisation techniques in ^{1}H-MRS are discussed in the following subsections. CHESS water suppression and PRESS localisation have been used in this thesis.

2.2.3.1 CHEmical Shift Selective (CHESS) Preparation

CHESS (Figure 2.12) uses a highly frequency selective 90^{o} pulse to excite only those spins present in free water or fat, and a high intensity ‘crusher’ gradient to dephase the spins; this process is known as “spoiling”. The RF pulse tips the spins through 90^{o} so that at the start of the MRS sequence, the dephased water or fat magnetisation lies on the transverse plane and hence has no net z-component (i.e. T_1 recovery is absent).

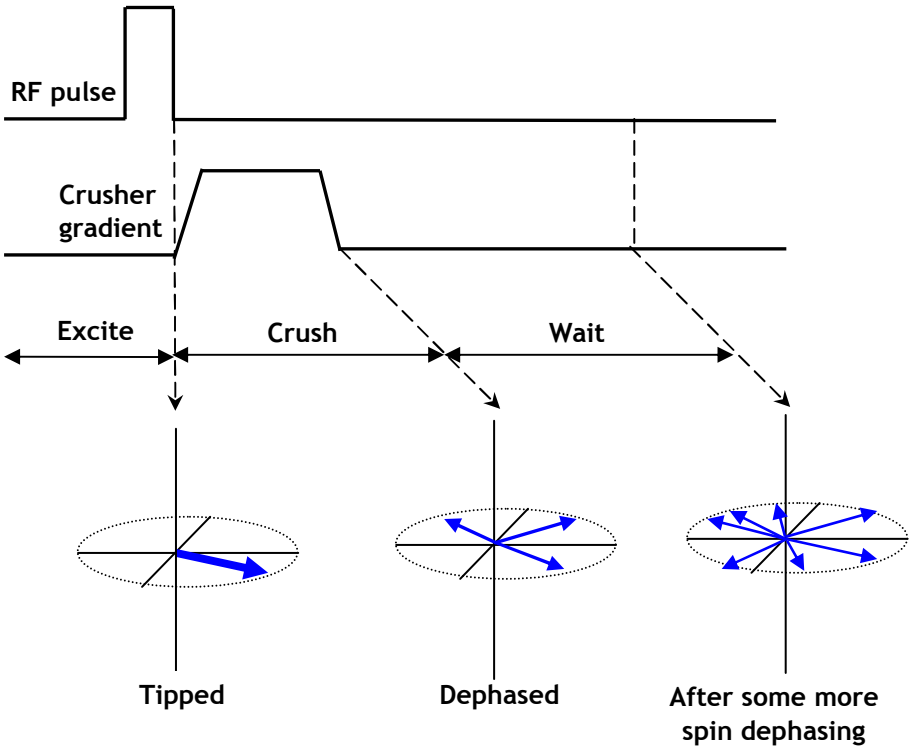

Figure 2.12: The CHESS water/fat suppression module prior to MRS localisation

2.2.3.2 Point-RESolved Spectroscopy (PRESS)

PRESS uses a 90^{o} slice selective excitation pulse together with two 180^{o} slice selective refocusing pulses (Figure 2.13).

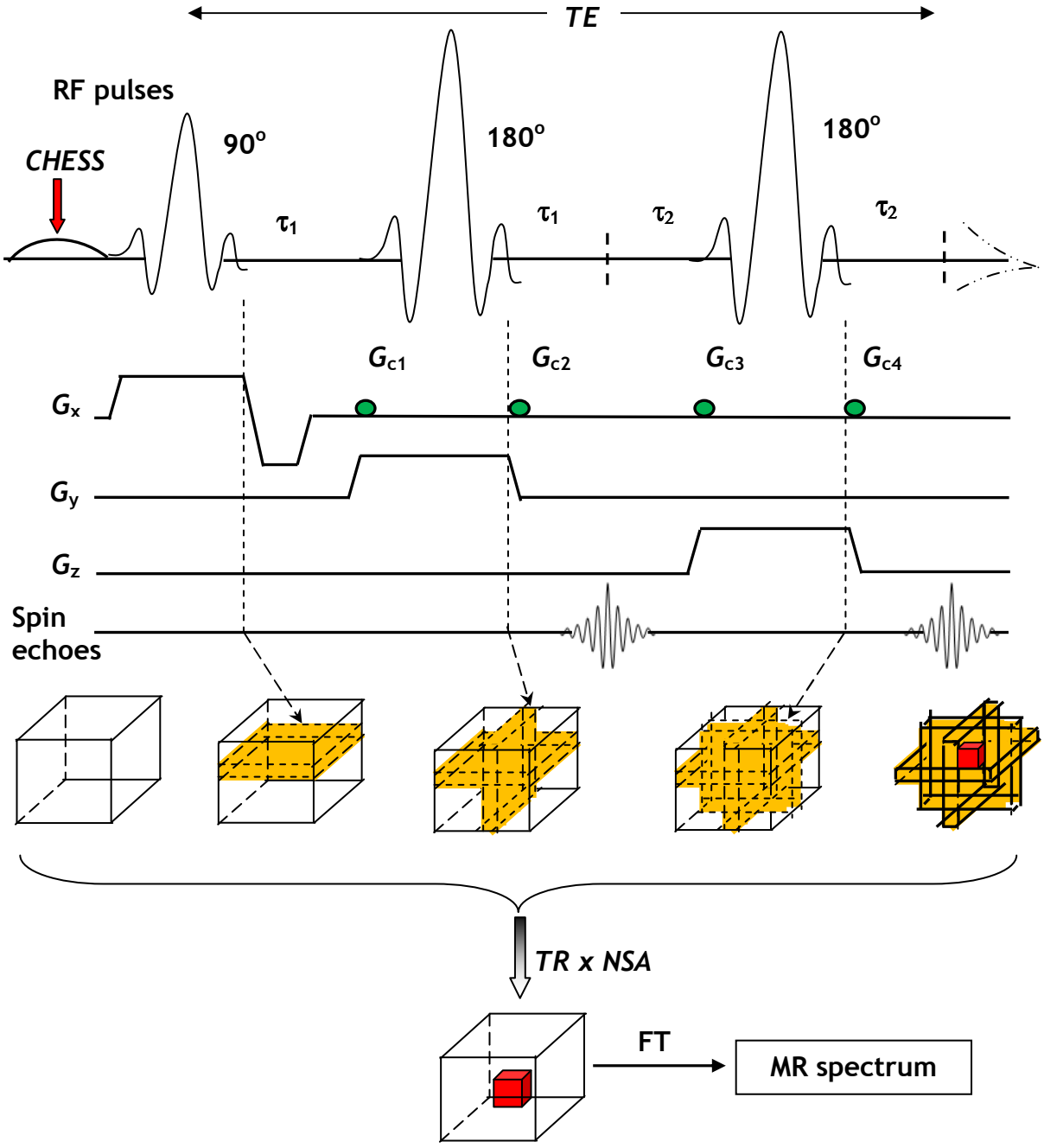

Figure 2.13: A schematic diagram of the PRESS localisation sequence.
The large box represents a region of interest on an MR image. Gradient coils (G_x, G_y and G_z) generate magnetic fields that vary B_0 experienced by spins linearly along the x, y and z directions. The RF pulses are applied in the presence of slice selection gradients. Crusher gradients (G_{c1}-G_{c4}) on each side of the 180° refocusing pulses are used to ensure that only spins within the selected voxel (red box) contribute to the final spin echo while destroying those spins outside the voxel. The sequence is repeated at certain intervals, *TR* so that a number of signals can be averaged (NSA). A Fourier transform (FT) of the raw data in the time domain gives the spectra in the frequency domain. The actual number of spectral lines stored in the MRS data of the above PRESS acquisition is given by NSA/NEX. Thus in a given MRS acquisition, while NSA is the number of echoes sampled, NEX determines the number of spectral lines (from these echoes) that are stored over a given *TR* time. These stored spectral lines are those processed and quantified to represent the peak parameters (i.e. area, intensity and FWHM) using MRS processing software packages.

The initial 90° pulse is followed after a time period τ_1 by a 180° refocusing pulse. A spin-echo is generated at time $2\tau_1$. A second 180° pulse is applied to refocus this spin-echo at a time delay $2\tau_2$. This produces the final spin-echo after time $2\tau_1 + 2\tau_2$, referred to as the echo time (*TE*) of the sequence. The first spin-echo contains signal originating only from the column that is the intersection between the two orthogonal slices selected by the 90° and the first 180° pulses. The second spin-echo contains signal only from the intersection of the three planes selected by the three pulses. This results in the selection of the desired volume (red box). Spins outside of the voxel are dephased by large 'crusher' gradients (G_{c1}-G_{c4}) on each side of the 180° refocusing pulses [31, 56], as shown in Figure 2.13. The block of three pulses (90°-180°-180°) is successively repeated to increase the SNR by averaging spectra. The number of acquisitions (NSA) is the number of times the sequence is repeated (typically 128). The repetition time (*TR*) is the time interval between repetitions of the entire pulse sequence (i.e. between the first 90° and the subsequent 90°). The echo time (*TE*) is the time between the 90° pulse and the appearance of the sampled echo signal.

2.2.3.3 STimulated Echo Acquisition Mode (STEAM)

STEAM (Figure 2.14) uses three 90° pulses to generate the signal as a stimulated echo rather than a spin-echo. The times between the pulses are τ_1, τ_2 and τ_3. The echo time (*TE*) is given by $\tau_1 + \tau_3$ and $\tau_1 = \tau_2$. The mixing time (*TM*) is the time, τ_2 between the second and the third pulses.

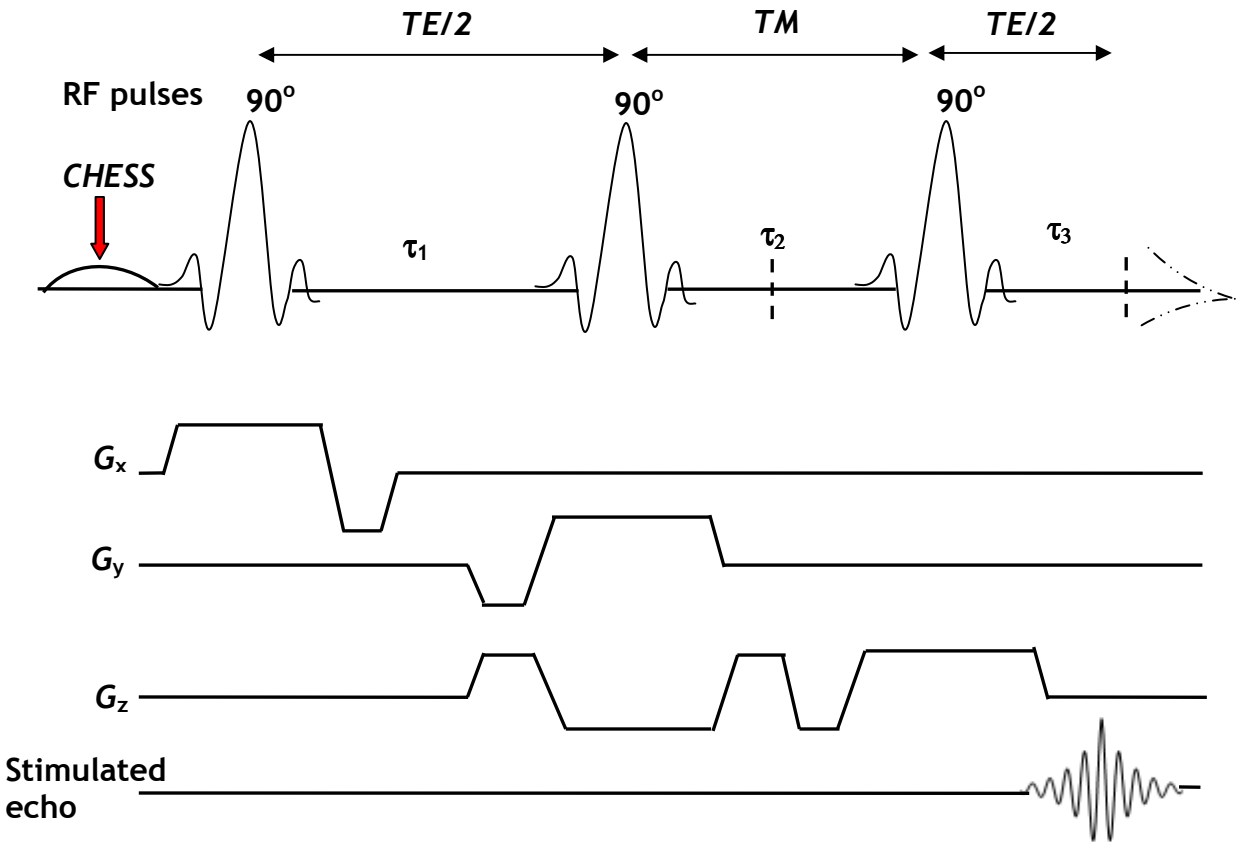

Figure 2.14: A schematic diagram of the STEAM localisation sequence

In the STEAM sequence, only half of the transverse magnetisation produced by the first 90° pulse is converted into longitudinal magnetisation by the second 90° pulse; this reduces SNR by a factor of 2 [31]. Typically, the *TE* time in STEAM is shorter, and so during the *TM* period, longitudinal magnetisation decays with T_1 rather than T_2. The third RF pulse flips the longitudinal magnetisation stored by the second RF pulse back into the transverse plane to form the stimulated echo.

Both PRESS and STEAM have advantages and disadvantages: In a PRESS sequence, the selective pulses are relatively long and time may also be required for eddy currents to die away after gradient switching. This could result in significant T_2 decay accompanied by loss of SNR [1]. However, STEAM has a shorter minimum *TE* and so the stimulated echo has almost no T_2 decay. The shorter acquisition time of the STEAM sequence allows more averages to be collected in a given time. STEAM also deposits less radiofrequency energy into

the subject as it does not use 180° pulses. PRESS depends on the scanner generating two accurate 180° pulses which may be difficult depending on local field homogeneities. The sequence timing of the 180° sinc pulses used in PRESS causes a fall off in flip angles and so the slice profile is not rectangular even for perfect homogeneity of the B_0 field and uniformity of the RF coil sensitivity. Consequently, PRESS localisation causes spectral distortion near the edges of the voxel [57]. PRESS has the advantage that it is inherently a factor of two more sensitive than STEAM (section 3.3.1). This is because a stimulated echo is only half the amplitude of a conventional spin-echo. PRESS therefore is the sequence of choice for measuring signals with long T_2 values.

Improvements in selective pulses and gradient switching have now allowed for shorter *TE* times with PRESS, and so it is now more widely used as it does not have the intrinsic 50 % loss of STEAM [1]. For all the experiments reported in this thesis, the PRESS sequence was used because of its high SNR.

2.2.4 Types of MRS Localisation

Using PRESS or STEAM, MRS data can be collected by two main approaches: single-voxel spectroscopy (SVS) and multivoxel spectroscopy (also known as magnetic resonance spectroscopic imaging, MRSI). The most common form of MRSI is chemical shift imaging (CSI). In SVS, a region of interest is selected and one voxel is placed in this region. In CSI, a grid of voxels is placed over the region of interest. The CSI data can then be viewed as a matrix of spectra or as a colour map of the metabolite concentrations (or metabolite ratios).

Practical disadvantages associated with CSI include adjacent voxel contamination and inefficiencies with shimming, water suppression and slice selection [31]. The advantage of CSI over SVS, however, is that it allows spectral acquisition from many locations simultaneously without prior knowledge of the location of any abnormality. Secondly, the CSI grid can be shifted to a precise location during post-processing [1, 31]. Nonetheless, consistently high quality short *TE* spectra *in vivo* are best acquired with SVS. All spectra in this thesis were collected using the SVS technique.

2.2.5 Echo Times

The various metabolites (section 2.2.6) have different molecular structures and so their protons are said to reside in different chemical environments. MRS signals from the metabolites therefore have different recovery (or T_1 relaxation) and decay (or T_2 relaxation) rates. Collecting MRS data at different echo times provides information from different number of metabolites. Figures 2.15 and 2.16 show spectrum collected from an MRS brain phantom (Figure 2.26) at the same repetition time (*TR* = 1500 ms), signal averages (NSA = 64) but different echo times (*TE* = 35 ms in Figure 2.15; *TE* = 144 ms in Figure 2.16).

A shorter echo time (*TE*) acquisition, typically 20-40 ms, will produce more information in the spectrum because less metabolite signals will have decayed. The spectrum will therefore contain more peaks (Figure 2.15). For *in vivo* acquisition, the problem with short *TE* spectra is that they overlap and contain contributions from lipids and macromolecules. A longer *TE* acquisition (typically *TE* ≥135ms) on the other hand will result in significant signal decay, resulting in fewer peaks in the spectrum (Figure 2.16). Lipids and macromolecules have short T_2 relaxation times; their signals will therefore decay, eliminating their contribution in the spectrum. However, potentially interesting metabolite peaks are lost from the spectrum. These metabolites often have strongly *J*-coupled spins which undergo destructive interactions so that at the *TE* time, their signals have decayed.

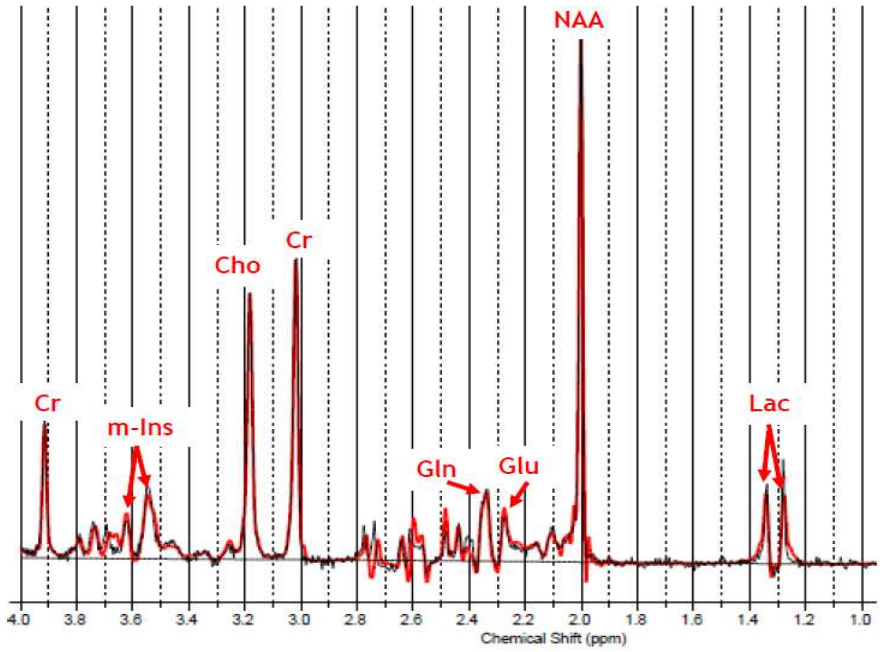

Figure 2.15: MR spectrum collected at a short *TE*

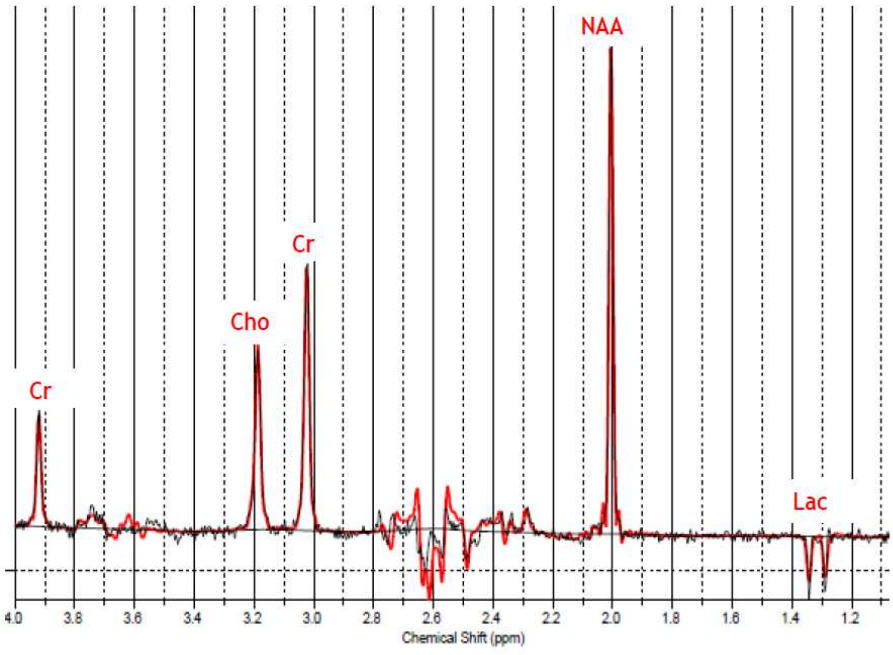

Figure 2.16: MR spectrum collected at a long *TE*
The above spectra were collected using a *TE* of 144 ms; the lactate doublet is inverted at this *TE* time

The choice of *TE* time in an acquisition therefore depends on the aim of the examination. In some cases, it may be beneficial to use both long and short *TE* times in the same examination. Both *TE* times have been used in this thesis.

2.2.6 Neurohistology, Brain Tissue Water and Metabolites

Before describing the location and biological significance of each brain metabolite detected *in vivo* by ^{1}H-MRS, it is appropriate to briefly discuss the cells that make up the central nervous system (CNS).

The CNS is made up of neurons and glial cells. While the neurons transmit electrochemical signals through the CNS, glial cells provide support for the CNS.

The neuron has three main parts: the cell body, the axons and the dendrites. The neuronal cell bodies constitute the grey matter in the brain and the axons are projections from each cell body. Signals from the cell body are transmitted through the axons. To enhance signal transmission, the axons are wrapped in layers of lipid called myelin. The tracts of myelinated axons constitute the white matter in the brain and spinal cord. The dendrites are nerve endings that receive signals from the axons through synapses.

There are three types of CNS glial cells: astrocytes, oligodendrocytes and microglia. Astrocytes provide physical support to the neurons, nourish them, regulate the chemicals surrounding them and clean up dead neurons. There are more astrocytes in grey matter than there are in white matter. Oligodendrites make up the myelin sheath surrounding the axons and so provide physical support to the axons. The oligodendrites are therefore predominant in white matter. The microglia are the smallest of the CNS glial cells and they clean up debris from the CNS.

The following subsections discuss the most ^{1}H-MRS visible brain metabolites *in vivo* using a standard short echo MRS sequence, stating whether they are predominantly found in neurons or glia. They are discussed in order of their positions on the frequency axis (from left to right) as shown in Figure 2.15. There are many other chemicals but due to their low concentrations and substantial *J*-coupling, they contribute MR signals of low SNR and so it is

difficult to accurately measure them. Some of these chemicals include N-Acetyl-aspartyl-glutamate (NAAG), γ-Aminobutyric acid (GABA), glucose and taurine. The unsuppressed or residual water peak is usually not shown in the spectral display window because its appearance dominates the metabolite peaks (Figure 1.10). However, since the focus of this thesis is on brain tissue water, it is necessary to mention it here as part of the MR spectrum.

2.2.6.1 Water

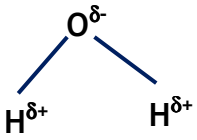

Figure 2.17: Chemical structure of water showing two polar ends: one end is slightly negative whereas the other end is slightly positive

Water (Figure 2.17) provides the largest peak at 4.70 ppm in the ^{1}H spectrum. It is present in all cells and its presence provides a medium for most biochemical reactions in the CNS. Brain water is uniformly distributed but slightly greater in grey matter than in white matter both *in vivo* [49, 58, 59] and *in vitro* [60]. Reported brain tissue water content is about 36 moles/kg [31, 61]. Due to its abundance and uniform distribution, brain water has been suggested to be a reference concentration in absolute metabolite quantification [62-64].

Brain water content is increased in inflammation and tumours [1]. In healthy tissue, water content could decrease in severe dehydration but this is often less than 2 % because water loss above this estimate could be fatal [33-37].

2.2.6.2 myo-Inositol

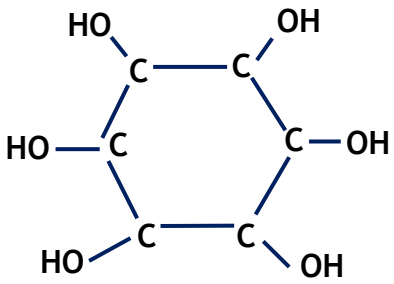

Figure 2.18: Chemical structure of myo-inositol

Among the nine isomers of inositol, myo-inositol, m-Ins (Figure 2.18) is the predominant form found in tissue. Often visible in a spectrum acquired at a shorter *TE*, its signal may contain smaller contributions from inositol monophosphate, inositol polyphosphates and glycine. Myo-inositol shows four resonances in the spectrum, two of which are prominent: a doublet-of-doublets at 3.52 ppm and a triplet at 3.61 ppm. The other two include a triplet at 3.27 ppm usually obscured by choline, and another at 4.05 ppm which is usually not observed due to water suppression [65].

The function of m-Ins is unclear but it is believed to play a role in various neuronal signalling systems [66, 67], metabolism of membrane-bound inositol phospholipids [66], cell growth [31], an osmolite (particularly in the cerebellum)[66, 68], and a storage form of glucose [68]. It is not present in neurons and has been proposed as a glial cell marker [69].

Brain m-Ins varies regionally, being lowest in white matter, slightly higher in cortical grey matter and highest in the cerebellum [70, 71]. Normal brain m-Ins concentrations range from 3.8-8.1 mM [72, 73]. Increased levels have been associated with diffuse pontine gliomas, diabetes and Alzheimer's disease, and decreased levels with malignant tumours [74] and stroke [1].

2.2.6.3 Choline-Containing Compounds

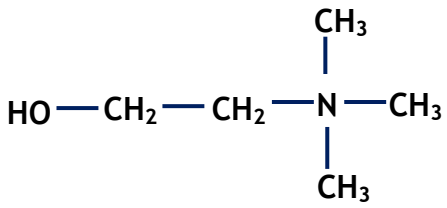

Figure 2.19: Chemical structure of choline

The choline-containing metabolites include glycerophosphorylcholine (GPC), phosphorylcholine (PCh) and free choline. They contribute to a prominent peak at 3.2 ppm and secondary peaks at 3.5 and 4.0 ppm. It is often not possible to separate their contributions with ^{1}H spectroscopy but they are distinguishable with ^{31}P spectroscopy [75]. The combined resonance of the choline-containing compounds is therefore often reported as total choline (tCho). However, GPC and PCh contribute more to the tCho signal than free choline as it is present in smaller amounts (< 0.03 mM) in the brain but could increase significantly in tumours [65]. Brain tCho concentration is about 0.9-2.5 mM [73], and is reported to vary significantly across the brain and increase with age [1, 65]. Because there is more Cho (Figure 2.19) in white matter than in grey matter, the level of Cho correlates with the degree of myelination [66, 70], and is considered to be a marker of membrane turnover and glial cell integrity.

There are uncertainties associated with the metabolites contributing to the tCho signal. Interpretation of alterations in the tCho peak is thus difficult. Nonetheless, changes are commonly associated with alterations in membrane composition, with increased levels in tumours [74, 76-78], ischemia, head trauma, inflammation, multiple sclerosis, Alzheimer's disease, and decreased levels in liver disease [1, 79].

2.2.6.4 Creatine

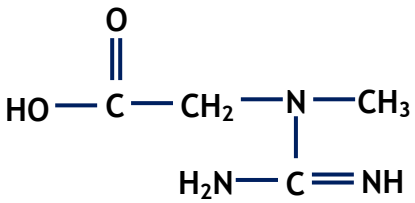

Figure 2.20: Chemical structure of creatine

The creatine signal arises from two chemicals: creatine (Cr) and phosphocreatine (PCr), both contributing overlapping signals to the resonances at 3.03 and 3.93 ppm. Cr (Figure 2.20) synthesis occurs in the kidney and liver. It plays a role in the anaerobic storage and production of energy in cells. During the energy production process, creatine kinase catalyses the reversible transfer of inorganic phosphate (P_i) from PCr and ADP to Cr and ATP. This Cr/PCr reaction sustains energy consumption in cells and facilitates ATP transfer from the mitochondria to sites where energy is needed. Total Cr is therefore thought to be a marker of the energetic status of cells. Regions with greater amounts of the creatine kinase enzymes also have high concentrations of Cr and PCr. Higher concentrations of these enzymes have been reported in cell preparations of astrocytes and oligodendrocytes than in neurons [80, 81]. Indeed, the total Cr signal has been reported to be higher in grey matter, at 6.4-9.7 mM, than in white matter, at 5.2-5.7mM [66, 82]. The total Cr content of the human brain ranges from 5.1-10.6 mM [72, 73]. It is low in infants and increases with age [1].

It is reported that the Cr peak is relatively stable with no age- [83] or disease-related changes. For this reason, it is commonly used as the concentration standard in quantifying the other metabolites. However, this assumption is not always true: decreased Cr levels have been observed in hypoxia, tumours [78, 84] and stroke [21], and increased levels in trauma and myotonic dystrophy [85].

2.2.6.5 Glutamate and Glutamine

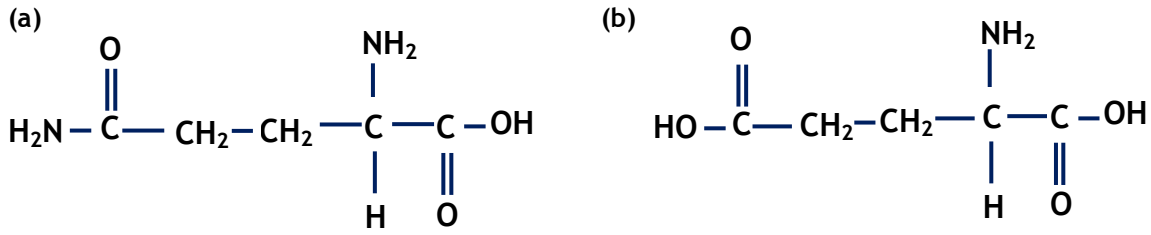

Figure 2.21: Chemical structures of glutamine (a) and glutamate (b)

The chemical structures of glutamine (Gln) and glutamate (Glu) are shown in Figures 2.21a and 2.21b respectively. At clinical field strengths (typically 1.5-3.0 T), Glu and Gln signals overlap and are difficult to be distinguished and quantified *in vivo* due to strong *J*-coupling effects [1, 65]. They are usually observed as a complex overlapping resonance called Glx. The Glx signal also contains contributions from GABA, and is only observed at shorter *TE* acquisitions. The Glx complex can be separated by spectral editing or homonuclear decoupling techniques [86, 87]. It is also possible to separate the resonances at 4 T [88, 89] and when this is possible, the resonance of Glu occurs within 2.04-2.35 ppm and that of Gln within 2.12-2.46 ppm [65].

Glu is present in all cells and is synthesised from the precursor α-ketoglutarate in the citric acid cycle in mitochondria. Glu acts as the major excitatory neurotransmitter in the CNS and so is found in higher concentrations in neurons than in glia. Its concentration in grey matter is thus reported to be higher than in white matter [66, 70], with brain concentration of 6.0-12.5 mM [70, 72, 73]. Gln on the other hand is an inhibitory neurotransmitter predominantly found in astrocytes which contain Gln ligase. Due to the larger population of CNS astrocytes, Gln concentration in grey matter is higher than in white matter [70] and ranges in concentration from 3.0-5.8 mM in the brain [72, 90].

The Glu/Gln pathway is essential for ammonia detoxification in the liver; they are therefore together regarded as amino acid neurotransmitters. If the liver is compromised, ammonia detoxification is carried out in the astrocytes by the

enzyme glutamine synthetase which combines ammonia and Glu to produce Gln [91]. Gln therefore is a storage form of Glu. When the Glu/Gln cycle is altered with hyperammonemia, Gln increases significantly. Gln thus acts as a biomarker of liver disease and its levels can be monitored in the brain [68, 92]. Increased Glu and Gln concentrations have been observed in severe ischaemia, hypoxia and hepatic encephalopathy [1, 93, 94], and could both possibly be decreased in Alzheimer's disease [1].

2.2.6.6 N-Acetyl Aspartate

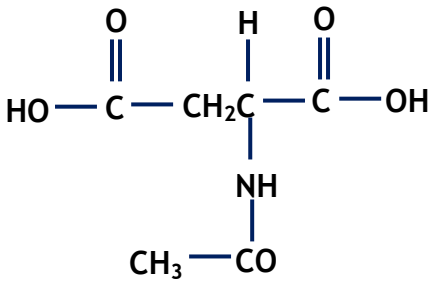

Figure 2.22: Chemical structure of N-Acetyl Aspartate

N-Acetyl Aspartate or NAA (Figure 2.22) is a free amino acid relatively abundant in the human brain and contributes the most prominent peak in the ^{1}H spectrum at 2.01 ppm. NAA also has smaller resonances arising from the aspartate CH and CH_2 groups contributing doublet-of-doublets at 2.49, 2.67 and 4.38 ppm plus an amide temperature-dependent doublet at 7.82 ppm. Confined to the fluid portion of the cytoplasm [95, 96], it is primarily localised in the neurons and dendrites of the central and peripheral nervous system [65]. NAA concentration in grey matter is reported to be higher than in white matter [70]. Even though its exact function is unclear, brain NAA is believed to act as an osmolite in the nerve cell, a storage form of aspartate, a precursor of N-acetyl-apartyl-glutamate (NAAG) and an acetyl donor for myelin synthesis [95, 97]. Brain NAA concentration ranges from 7.9-16.6 mM [65, 72] but is low in infants and its increase coincides with myelination [95].

The NAA group contains at least two chemical moieties: NAA and NAAG. NAAG is predominant in the nerve cell but varies regionally within the brain with a concentration range of 0.6-2.7 mM [98]. It is suggested to be involved in excitatory neurotransmission and also acts as a source of glutamate [31, 65]. Its peak occurs at 2.10 ppm but mostly overlaps with the large NAA peak particularly at lower field strengths. The NAA peak thus contains contributions from NAAG, which can be separated at higher field strengths or by using 2-dimensional MRS [65]. Unresolved NAA and NAAG are usually reported as the total NAA (tNAA).

Because of its specificity to neurons, NAA is commonly considered to be a marker of healthy neuronal density [1]. NAA levels may also reflect reversible neuronal dysfunction rather than irreversible neuronal loss [31]. A decrease in the NAA peak intensity has been reported in a number of neurological disorders including multiple sclerosis [99], ischaemia [100], acute head injury [101], schizophrenia [102-104], inflammation [1] and tumours [74, 105]. Increased NAA has also been reported in Canavan's disease [99, 106].

2.2.6.7 Lactate

Figure 2.23: Chemical structure of lactate

Lactate (Figure 2.23) is an end product of anaerobic glycolysis, exhibiting a doublet at 1.31 ppm which becomes inverted at *TE* = 144 ms (Figure 2.16). In shorter *TE* acquisitions *in vivo*, it may be difficult to distinguish the lactate resonance from that of lipids and macromolecules [107] and so lactate is commonly studied at longer *TE* times. Brain tissue lactate content is low (about 0.4 mM [73]) and only becomes MRS-visible in diseased tissue undergoing anaerobic respiration. It is thus suggested to be a marker of anaerobic metabolism. Even though its presence can be highly variable, lactate

concentration increases rapidly following hypoxia and cases of blood flow impairment such as stroke, trauma, tumour, necrotic tissue and cystic masses [79, 108, 109]. Functional activation and hyperventilation have also been suggested to cause small increases of brain lactate content [110, 111].

2.2.6.8 Lipids and Macromolecules

In most cases, lipid and macromolecular resonances occur at various regions of the spectrum: around 0.9, 1.3-1.4 and 2.0-2.6 ppm. They could sometimes be more pronounced particularly at shorter *TE* times and in the presence of tumours. Their signals may also arise from a healthy brain if the voxel is placed close to the skull [45, 65]. Macromolecular/lipid spectra usually occur as broad singlet and/or multiplet peaks in the MR spectrum. These unwanted resonances could be reduced by planning acquisitions with longer *TE* times, placing the voxel away from the skull or using saturation bands to eliminate signals from outside the voxel [31].

2.2.7 Challenges of *in vivo* MRS

Apart from relaxation and partial volume effects (chapter 5), in practice, the quality of MRS data can be affected by a number of factors which could be subject, operator or equipment dependent. However, strategies are available to minimise the errors introduced into the data by these factors. These strategies have been used in this thesis. The most common factors that can possibly affect the spectral quality and how to minimise them are presented in the following subsections.

2.2.7.1 Static Field Inhomogeneity

This arises from limitations of the magnet design and from differences in magnetic susceptibility between tissues (especially at air-tissue boundaries). The width of a spectral peak is inversely proportional to the effective transverse relaxation time, T_2^* (defined in equation 2.8) [31] of its

corresponding metabolite. Local magnetic field inhomogeneities, ΔB_0 widen and distort the spectral lines.

Maximum homogeneity can be achieved by a technique known as shimming [31]. This involves adjustment of the DC currents in the gradient and shim coils so that the water signal attains a linewidth of about 30 Hz (equivalent to approximately 0.25 ppm).

2.2.7.2 Detection Sensitivity

Metabolites of interest in MRS are often in millimolar concentrations and so unwanted signals could easily corrupt the metabolite signals. Secondly, in a typical acquisition, the MR spectrum arises from more than one metabolite. Inherently, these metabolites differ in their T_2 relaxation times due to differences in their chemical structures. The choice of echo time for an acquisition could therefore reduce the sensitivity of MRS to only those metabolites with longer T_2 relaxation times, and at the same time help reduce the noise signals in the spectrum.

In a typical acquisition, sensitivity can be increased by: i) using larger voxel sizes, ii) using more powerful magnets (typically $B_0 \geq 1.5$ T for human studies) to increase spectral resolution and SNR, iii) using a surface coil for superficial organs or phased-array coil, iv) accumulating many signal averages, NSA to increase SNR (SNR α $\sqrt{}$NSA) and v) collecting more complex data points (the raw data which when Fourier transformed, generates the spectra), so that the spectra in the frequency-domain will be of high resolution; this also enhances the SNR of the MR spectrum [31]. For all acquisitions in this thesis, 4096 complex data points were collected.

2.2.7.3 Solvent Signal

The concentration of water protons is very high compared to that of protons contained in the metabolites of interest. At shorter *TE* acquisitions, the spectrum may also contain significant contributions from fat/lipid signals

coming from outside the skull due to non-ideal selective slice profiles [112], and also depending on the voxel position. The large spectral peaks from the unwanted water/fat signal can obscure and distort the metabolite peaks, making spectral quantification difficult. The water/fat contribution can be reduced by using a series of chemical-shift selective pulses, adjusted to the resonant frequency of water/fat (section 2.2.3.1). This ensures that the water magnetisation is destroyed just before the spectra are acquired. Other strategies include moving the voxel away from the skull, using outer volume saturation bands [112-115] and increasing the *TE* time of the acquisition (though this reduces the SNR of the spectrum [31]). However, none of these methods will reduce macromolecular contributions in the spectrum because macromolecules are a natural component of brain tissue and will always be present within the selected voxel [31].

2.2.7.4 Eddy Currents

Field gradient pulses induce eddy currents in the main magnetic field, which generate additional magnetic fields that add to the static field. There are two types of eddy currents: zero-order eddy current or time-varying B_0 offset and time-varying first or higher order gradient [31]. Zero-order eddy currents cause a frequency-dependent phase shift during signal readout but no decrease in SNR from spin dephasing within the voxel. They can be corrected with a B_0 coil. First-order eddy currents cause the spins within the voxel to dephase, decreasing SNR. Both types of eddy currents together with magnetic field inhomogeneities distort the peak shapes. Spectral distortion from eddy currents can be corrected by a technique known as QUAntification by converting to the LorentzIan TYpe (QUALITY) deconvolution [116]. This involves dividing the spectral time domain signal by the unsuppressed-water time domain signal (section 1.4.3) [45, 46, 116]. Another technique involves doing a point-by-point phase correction of the time domain signal, which also uses the unsuppressed-water signal. This is often known as Eddy Current Correction (ECC) [46, 117]. QUALITY corrects spectral distortion due to zero- and first-order eddy currents and B_0 inhomogeneities, while ECC only corrects spectral distortion due to zero-order eddy currents [31]. The former technique was used in this thesis.

2.2.7.5 Phase Detection

Differences in design between the two channels of an analogue quadrature receiver can introduce artefacts into the spectrum. If the amplifier gains between the channels are not equal, or if their phase difference is not 90^o, there will be ghosting of the peaks mirrored about zero frequency. This is known as a quadrature ghost. A spike results if the DC offsets between the two channels is not zero. Phase cycling can be used to correct these artefacts. It is implemented by switching the transmitter phase between 0^o and 180^o during each repetition of the pulse sequence. The number of times the switching is done is known as number of excitations, denoted by NEX. The signal collected with the transmitter phase at 180^o is subtracted from the signal collected with the transmitter phase at 0^o. This adds the signal and subtracts the DC offsets, cancelling the DC artefact. Phase cycling also compensates for imperfect 180^o flip angles during the acquisitions (especially in MR multi-echo imaging) [31]. Receiver designs with only one amplifier plus analogue-digital convertor do not have unequal DC offsets, unequal gains or non 90^o quadrature detection. For all the acquisitions in this thesis (apart from some acquisitions in chapter 8), NEX was set to 8 phase cycles. A phased-array (and not the quadrature) head coil was used in all acquisitions in this thesis.

2.2.7.6 Motion

Increasing the number of signal averages in order to enhance spectral quality (section 2.2.7.2) prolongs the acquisition time. This could result in subject compliance issues. Subject movement and physiological motion of the examined organ during spatial localisation may affect the individual scans. This may cause motion-related signal loss and line-shape deterioration, resulting in considerable degradation of the averaged spectrum [118]. It is always better to use ‘reasonable’ signal averages that will offer tolerable scan times. It may be difficult to avoid motion artefacts in examination of organs in the trunk but for brain studies, a strap and head support can be used to minimise head movement. Post-processing techniques can also be used to restore the signal loss due to motion [119]. This is achieved by correcting each acquisition with the phase offset and frequency shift of its residual water signal before

averaging. By using NEX = 8 for the MRS acquisition, more spectral lines are averaged before data storage. This reduces the effects of motion that could otherwise lead to phase, frequency and signal shifts; the NEX does this by subtraction of these effects from the spectra using the phase cycling scheme described in section 2.2.7.5.

2.3 Materials and Methods

2.3.1 Overview of Spectral Analysis

Metabolite quantification is performed by a spectral analysis procedure that quantifies the area under the peaks of interest within the spectrum. The estimated area is proportional to the absolute concentrations of the metabolites.

Spectral analysis and/or quantification can be performed in either the time domain [120] or frequency domain [121]. In the time domain, the MRS signal is represented as a function of the recording time, whereas in the frequency domain, the signal is represented as a function of the resonance frequency. By Fourier transformation, the time-domain signal can be converted into its equivalent frequency-domain representation [45]. In theory, the two domains are the same [122]; however, the frequency domain representation of data is always preferable because it enables direct visual interpretation of the spectra [45]. For this reason, all MRS data shown in this thesis are represented in the frequency domain.

Frequency domain spectral analysis can be performed in three ways: integration of peaks; peak fitting with Lorentzian or Gaussian lineshapes; and prior knowledge peak fitting.

By the peak integration method, the user selects a frequency range containing only one peak and performs numeric integration. This procedure usually excludes signal contributions to the upper and lower limits of the peak and so the area will be underestimated, possibly by up to 40 % [45, 123]. Peak integration is suitable for spectra that are well separated and do not suffer

from baseline fluctuations. Unfortunately, this is not the case with *in vivo* spectra; they mostly suffer from significant spectral overlap and baseline fluctuations. The area cannot therefore be attributed to a single resonance; the baseline will also result in unknown contributions.

By the peak fitting method, the user initially selects the peaks of interest and rough estimates of the resonance frequency, line width, and peak intensity are performed manually or by an algorithm. Subsequently, a fit is performed by using a least squares optimisation algorithm, which iteratively fits the selected peaks to a line shape model function, so that the fitted spectrum resembles the experimental spectrum as closely as possible [45, 124]. This method is generally robust for spectral overlap. The fit may however be inaccurate if the actual line shapes substantially deviate from Lorentzian or Gaussian model functions. A Lorentzian-Gaussian mixture or Voigt model function [31, 125] could be used in such cases but this can lead to ambiguous results because the fitting procedure introduces more degrees of freedom [45]. The two commonly fitted spectral lineshapes are shown in Figure 2.24.

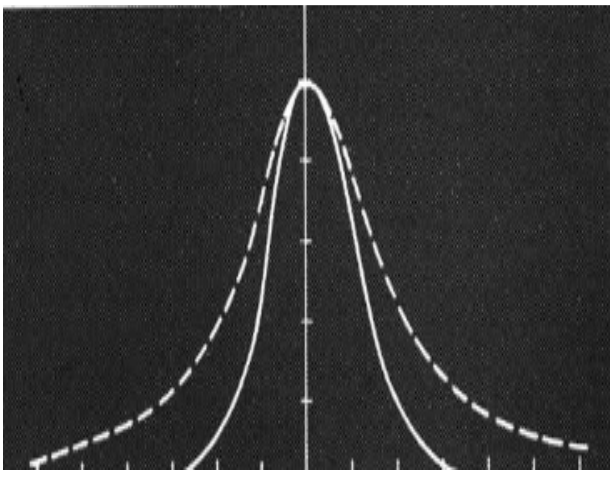

Figure 2.24: The two main spectral lineshapes used in spectral analysis
The Gaussian lineshape is shown in solid line; the Lorentzian lineshape is shown in broken line.

From Figure 2.24, two significant differences between these lineshapes are evident [126]: the Lorentzian is a sharper, narrower function toward the centre; the Gaussian falls off in the wings more rapidly than the Lorentzian. MR spectra are usually sharper, narrower and often overlap at their wings, which is why either of these two lineshapes could be used in spectral fitting.

The Gaussian and Lorentzian lineshapes can be described by equations 2.15 and 2.16, respectively, as follows [126]:

$$f(\upsilon - \upsilon_o) = \frac{\sqrt{\ln 2}}{\sqrt{\pi}\delta} \cdot \exp\left[-(\upsilon - \upsilon_o)^2 \cdot \ln 2/\delta^2\right] \qquad \text{(Eq. 2.15)}$$

$$f(\upsilon - \upsilon_o) = \frac{\sqrt{\delta}}{\sqrt{\pi}} \cdot \frac{1}{\delta^2 + (\upsilon - \upsilon_o)^2} \qquad \text{(Eq. 2.16)}$$

where $f(\upsilon - \upsilon_o)$ is the amplitude of the function, δ is one-half of the width of the function at half-maximum intensity, and $(\upsilon - \upsilon_o)$ is the value of the field measured from the centre frequency.

Prior knowledge fitting incorporates prior knowledge about the metabolites that contribute to the ^{1}H MR spectroscopic signal [45, 127]. Known signal parameters such as chemical shifts (relative frequencies), amplitude ratios, *J*-coupling, splitting patterns, and phases of resonances specific to a given metabolite are used in an algorithm during the fitting routine. An advanced form of prior knowledge fitting also takes into account the type of MR scanner, B_0, pulse sequence, *TE*, *TR*, as well as the pH, ion composition and temperature of the solution in which the individual metabolites are dissolved. This prior knowledge of each metabolite is used to create, by simulation or by phantom measurement, a basis set (template spectra) that matches the *in vivo* conditions. The *in vivo* MR spectra are then analysed as a linear combination of the separately recorded *in vitro* spectra of the individual metabolites. This fitting method introduces less degrees of freedom, takes a shorter time to complete and is mostly accurate [45, 48, 127].

The main challenge of frequency domain spectral analysis is determining the shape of the baseline. When the baseline is underestimated, the peak areas could be overestimated. The baseline can be determined by three common approaches: a user manually selects reference frequency points in the spectrum and fits a straight line, cubic spline or polynomial function through

them [128]; an algorithm automatically selects reference points at predefined frequencies and fits a straight line through them [71]; an algorithm automatically fits a smooth curve to the baseline and fits the metabolite spectra, simultaneously [48].

2.3.1.1 Spectral Fitting in LC Model

LCModel stands for Linear Combination Model. The LCModel software package is a user-independent fitting program that is commercially available [48]. It automatically performs eddy-current correction on the spectrum using the unsuppressed-water signal, phase-corrects the spectrum and fits the spectrum (in the frequency domain) with the linear combination of representative spectra (known as the basis set) of all the individual metabolites.

LCModel estimates the metabolite concentrations by fitting the measured spectrum with a template spectrum of known concentrations. It further uses the transmitter and receiver gains to scale the measured areas to the template areas.

Within the version of LCModel used for this project (version 6.2-4A), the chemicals used to simulate the templates were alanine (Ala), aspartate (Asp), creatine, Cr (CH_2 and CH_3 peaks), γ-aminobutyric acid (GABA), glucose (Glc), glutamine (Gln), glutamate (Glu), glycerophosphorylcholine (GPC), choline (Ch), myo-inositol (Ins), lactate (Lac), N-Acetyl-Aspartate (NAA), N-acetyl-aspartyl-glutamate (NAAG), scyllo-inositol (Scyllo), taurine (Tau) and guanadinoacetate (Gua). The CH_2 and CH_3 peaks of creatine were fit as separate singlets. As long as the molecular structures of the various metabolites are accurately known, a simulated template does not suffer from systematic errors and offers a more robust fit compared to a phantom measured template [45]. This is because T_1 and/or T_2 relaxation times sometimes differ between the *in vivo* and *in vitro* situations (e.g. in pathology), and also different resonances in the same metabolite might have different relaxation times (e.g. the CH_2 of Cr has shorter T_1 and T_2 relaxation times than its CH_3 [129]). In such situations, the use of the *in vitro* created

template may require a separate relaxation measurement in order to enhance the fitting accuracy [45].

Two templates of the highest SNR were provided (by the software vendor) in the molecular simulation library of LCModel: one template was simulated for *TE* = 35 ms, *TR* = 5000 ms, NSA = 128 and the other for *TE* = 144 ms, *TR* = 5000 ms, NSA = 128. The templates were suitable for the data collected in this thesis at *TE* times of 35 ms and 144 ms because they (i.e. the acquired data) were influenced by the same *J*-coupling modulation and unknown scanner effects as the simulated spectra. Thus only a minimal fitting error could be achieved and the concentrations will be accurately measured. In this case, the need to modify the existing templates or to create a new template does not arise.

LCModel calculates the Cramer Rao lower bounds (CRLB), otherwise known as the standard deviation (SD), for the concentration estimate of each metabolite. The CRLB or SD values are measures of the reliability of the concentration measurement, and values of SD less than 20 % are generally considered reliable [130, 131]; SD ≤ 50 % has also been considered reliable elsewhere [132]. Sample LCModel outputs are shown in Figures 2.15 and 2.16.

2.3.1.2 Spectral Fitting in SAGE

SAGE stands for Spectroscopy Analysis by General Electric. The SAGE software package is a semi-automated fitting program provided by the GE Company. It has peak integration, peak fitting and prior knowledge fitting capabilities. In this thesis, only the peak fitting capability of SAGE was utilised.

The spectral quantification procedure involves two stages: preprocessing and analysis. In the preprocessing stage, the time domain signals from the eight channels of the head coil are eddy current corrected and combined [133] as illustrated in sections 1.4.3 and 1.4.4, respectively. The resulting FID is Fourier transformed into an MR spectrum in the frequency domain. The spectrum is then phase- and baseline- corrected. Temperature-dependent spectral offsets are corrected by selecting a reference peak (the NAA peak at 2.01 ppm in this case) and then moving it to its actual frequency position. In the analysis stage,

a table of the peaks to be analysed is created. This table contains the rough estimates of the peak amplitude, line width and frequency, as well as the noise standard deviation of the spectrum. These four variables are used by the peak fitting algorithm in SAGE to determine the area under each selected peak.

To evaluate the peak areas, the spectra are fitted to a Lorentzian line shape using the Levenberg-Marquardt method for nonlinear least squares minimisation [134]. The Lorentzian model function was chosen over the Gaussian because it consistently showed minimal misfits between the model and experimental spectra (measured by the chi-square value). The reason for this could have been that the spectral peaks did not fall off rapidly in their wings where they overlapped. If that was the case, the wings of the Gaussian model fits would always fall within (and would not accurately fit) the experimental spectral peaks in a similar way to the representation of Figure 2.24. The Lorentzian model fit would therefore perform better. The fitting algorithm converges when a minimal chi-square value, $\delta(\alpha)$ is attained after 'n' iterations. In theory, for a given set of 'n' experimental datum pairs of independent and dependent variables, (x_i, y_i), the algorithm adjusts or optimises the parameters, α (i.e. amplitude, frequency and line width) of the model curve $f(x, \alpha)$ so that the sum of the squares of the deviations, $\delta(\alpha)$ becomes minimal; where:

$$\delta(\alpha) = \sum_{i=1}^{n} [y_i - (x_i, \alpha)]^2 \qquad \text{(Eq. 2.17)}$$

In SAGE, the fitting algorithm synthesises a signal, $f(x, \alpha)$ based on the rough estimates of the amplitude, line width and frequency of the Lorentzian peak. It then calculates the squared difference between the synthesised signal and the actual signal, y. The parameter variable, α may be adjusted to reduce the size of the difference, $\delta(\alpha)$. The size of the adjustment varies dynamically depending on the success or failure of the previous adjustment attempt. If the adjustment reduces the difference, the current parameters in the peak table are updated. If, however, the adjustment fails to minimise the difference, the size of adjustment is reduced and a new difference is calculated. This process

continues until: a maximum number of iterations have been performed; the difference has decreased to an acceptable value; or the difference fails to fractionally decrease for a certain number of iterations.

The maximum number of iterations is specified by the user at the start of the fitting routine (maximum number of iterations was set to 100 for all fits in this thesis so that any attained number of iterations could fall well within this chosen limit). The Marquardt fitting method in SAGE uses the SNR estimate from the peak table to determine an error value below which changes to the fitted parameters are statistically insignificant and at which value the chi-square estimate (i.e. the acceptable difference in equation 2.17) is produced and the fit is generated. The final fit results contained in the peak table include the peak area, line width, frequency and amplitude.

2.3.1.3 Quantification of Water-suppressed and Unsuppressed-water Spectra

For any MRS data set to be analysed, the number of spectral lines stored in the raw data is a function of the number of spectral averages, NSA and number of phase cycles, NEX. Both NSA and NEX can be set on the MR scanner prior to the MRS acquisitions. At the beginning of the MRS sequence, the GE MR scanner, by default, acquires a minimum of 16 unsuppressed-water spectral lines. However, the actual number of unsuppressed-water spectral lines stored in the raw data also depends on the NEX value used for the acquisition. Thus, the total number of spectral lines, N_l in a typical MRS acquisition will be given by the sum of the unsuppressed-water lines, N_u and the suppressed-water lines, N_s:

$$N_l = N_u + N_s \qquad \text{(Eq. 2.18)}$$

So that:

$$N_l = 16/NEX + NSA/NEX \qquad \text{(Eq. 2.19)}$$

Suppose that two spectral acquisitions are performed with the same NSA value of 16 but with NEX values of 2 (Figure 2.25a) and 8 (Figure 2.25b). According to equation 2.19, N_u and N_s will be 8 each in the former (Figure 2.25a), but will be 2 each in the latter (Figure 2.25b) acquisitions. N_l is therefore 16 and 4 in Figures 2.25a and 2.25b, respectively. NEX can therefore be said to control the number of spectral lines that are averaged by the scanner before data storage. It is this stored data that is then post-processed and analysed in the SAGE software (section 2.3.1.2) to yield the quantified unsuppressed-water and metabolite (i.e. suppressed-water) spectral peaks. This quantifiable water peak obtainable from the 16/NEX part of equation 2.19 can be used for a number of purposes. In fact, Brief et al [58] have used it as a reference unsuppressed-water signal area against which they quantified their cerebral metabolites. Similarly, this thesis corrected this signal area for all possible error sources and used it in absolute metabolite quantification (chapter 7). Specific reference will be made to this unsuppressed-water signal area where it has been used in this thesis.

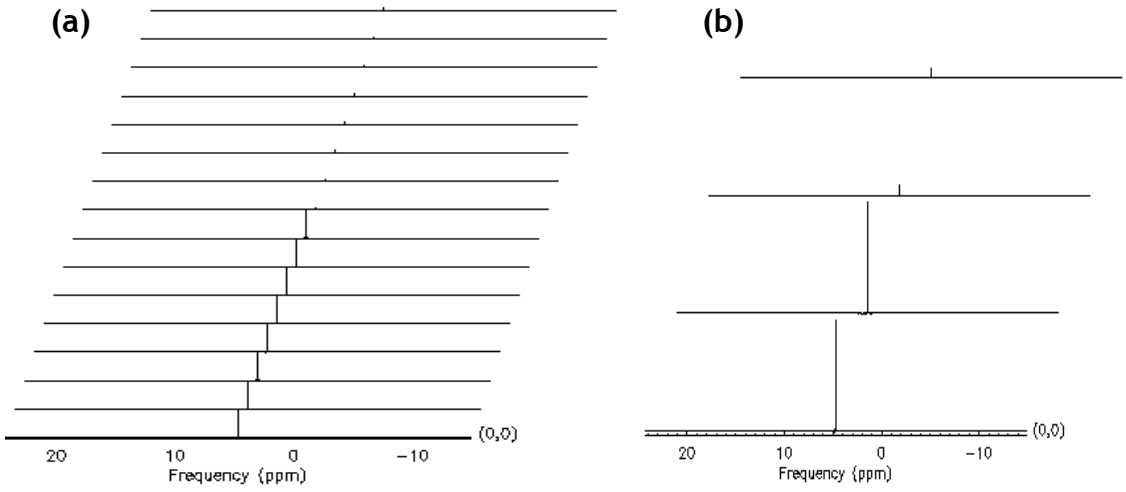

Figure 2.25: Number of stored data frames determined by NEX
NSA = 16 in both acquisitions. In Figure 2.25a, NEX = 2, N_u = 8, N_s = 8; In Figure 2.25b, NEX = 8, N_u = 2, N_s = 2. Note the peak intensity difference between the N_u (taller peaks) and N_s (shorter peaks) lines. The figures are output images from the SAGE software package.

2.3.2 Spectral Fitting Software used in this Thesis

Apart from aspects of the work presented in sections 3.2.2.1 and 3.2.2.2, all spectral analysis in this thesis were performed using the SAGE software package. The spectral peak areas were quantified by peak fitting to Lorentzian lineshapes with the manual baseline determination method using the SAGE software (as described in sections 2.3.1.2-3). In sections 3.2.2.1-2, the LCModel software package was used for spectral analysis (as described in section 2.3.1.1).

LCModel uses prior knowledge peak fitting at the same time as fitting a smooth curve baseline to estimate metabolite concentrations. The fit is performed using a template created for only water-suppressed spectra. Even when the frequency range of the fit is extended to include the water resonance, accurate fitting to the water peak is not possible; and so an error message is returned. The residual water signal is however used by LCModel for phase and eddy current correction [48]. On the other hand, SAGE is able to fit the unsuppressed-water peak.

Specific to the work presented in chapter 3, only the arbitrary estimates of water and metabolite quantities were required to study reproducibility. Therefore, for rapid and consistent spectral analysis, the metabolite and unsuppressed-water spectra for each acquisition were analysed using LCModel and SAGE, respectively. Apart from the use of the LCModel software package for the metabolite quantification work presented in that chapter (in sections 3.2.2.1-2), the software was not used in any other work in this thesis.

2.3.3 The MRI Scanner, Head Coil and MRS Phantom

All experiments reported in this thesis were carried out on a 3 T GE Signa Excite HD (software version 12) MR whole-body scanner equipped with an eight-channel receive-only head coil (Figure 1.1). A GE MRS brain phantom (spherical and ~17 cm in diameter) shown in Figure 2.26 was used for the reproducibility and RF mapping experiments. The contents of the phantom (in millimolar concentration, mM) were NAA (12.5 mM), Cr (10.0 mM), Cho (3.0

mM), m-Ins (7.5 mM), Glu (12.5 mM) and lactate (5.0 mM) at a pH of 7.2. A temperature-sensitive colour strip is included in the body of the phantom for room temperature measurements. The phantom was kept in the scanner room to ensure thermal equilibrium with room temperature. Therefore, the temperature reading indicated on the temperature strip was taken to be the temperature of the phantom.

Figure 2.26: The GE MRS brain phantom
The black temperature strip shows the temperature reading (in orange colour)

2.3.4 Statistics in this Thesis

All statistical tests in this thesis were performed using the Minitab software package (version 16, Minitab Inc.). Statistical tests were chosen depending on whether the data set to be analysed was normally distributed. If a given data set is normally distributed, then it can be subjected to parametric statistical tests; a non-normally distributed data set, on the other hand, can be subjected to non-parametric statistical tests.

To test for normality of data, the Anderson-Darling (A-D) normality test was used. The A-D normality test generates a normal probability plot based on what a normally distributed data set of a given sample size should look like. It then tests the correlation between the predicted normal data with the actual data

(Figure 2.27). The null hypothesis of this correlation test is that there is no difference between the actual data and the generated normal data. The correlation coefficient gives a critical value, p which is usually defined such that this null hypothesis would be rejected if $p < 0.05$; the actual data set however would be considered normally distributed if $p > 0.05$.

An example of the A-D normality test on age distribution of a group of healthy subjects is shown in Figure 2.27. The predicted normal distribution is the blue curve and the actual data is the histogram plot.

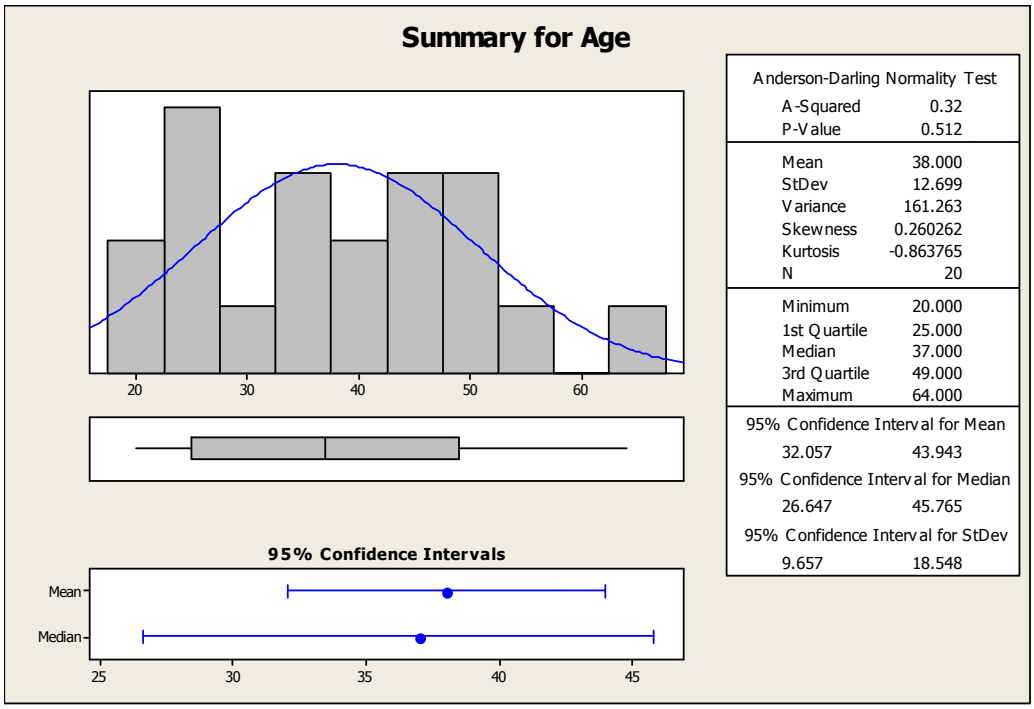

Figure 2.27: The Anderson-Darling normality test for normality of age distribution
This is an output of the A-D normality test using the Minitab software

The mean age of the subjects is 38.0 years (95 % confidence intervals of 32.1 and 43.9). The standard deviation is 12.7 (95 % confidence intervals of 9.7 and 18.5). Using a significance level of 0.05, the A-D normality test (A-squared = 0.32, p-value = 0.512) indicates that the age distribution follows a normal distribution; it is therefore acceptable to assess the data using parametric statistical tests.

The A-D normality test described above was performed on all data in this thesis before choosing a suitable parametric or non-parametric statistical test for

assessing such data set. Generally, data sets were tested for differences and associations. The various parametric and non-parametric statistical tests used for these assessments are summarised in Table 2.1.

Type of analysis	Parametric test	Non-parametric test
Comparison between two quantitative measurements taken from the same subject	Paired t-test	Wilcoxon (signed-rank) test
Comparison between the means of the measurements from two independent groups	Two-sample t-test	Mann-Whitney (two-sample Wilcoxon sum rank) test*
Comparison of the means between three or more independent measurements	One-way analysis of variance (ANOVA)	Kruskal-Wallis test*
Estimation of the degree of association between two quantitative variables	Pearson coefficient of correlation, r	Spearman's rank correlation, ρ

Table 2.1: Parametric and non-parametric statistical tests used in this thesis
*Not used in any test in this thesis but included for the sake of completeness

For all the above tests for differences, a p-value < 0.05 was considered significant, whereas for associations, a correlation coefficient greater than 0.5 was considered strong. The means and standard deviations were mostly calculated over all volunteers. In some cases, the standard error was quoted in place of the standard deviation. The standard error is defined as the standard deviation divided by $\sqrt{n}$, where n is the number of observations (or subjects).

2.3.5 Ethical Approval of Human Studies

The healthy volunteer studies reported in chapters 3, 5, 7, 8, and part of chapter 6 (the MT imaging study) were approved by the West of Scotland Research Ethics Committee 4 (WoSREC4); see Appendix 2.1. All subjects gave prior informed written consent after studying the full research protocol; time was also given for any concerns to be clarified to prospective volunteers.

The healthy volunteers were recruited from within Glasgow through direct (email and phone) contacts by the author. The exact procedures for participation were discussed and informed written consent was taken from each subject before study entry. After taking their consent, each volunteer was screened for any neurological and psychiatric conditions using the General Health Questionnaire (GHQ-12; Appendix 2.2). The MRI safety questionnaire (Appendix 2.3) was then used to screen them for any contraindications they may have going into the MRI scanner environment. All brain scans were reported by a consultant neuroradiologist while a standard clinical protocol was in place to deal with incidental findings.

Two psoriatic arthritis patients were excluded from the TNF-α blockade study in chapter 7. One of them had an ear implant (information gathered during the MRI safety screening) while the other patient was found (after MR imaging and reporting) to have meningioma in the frontal brain region. Nothing was done about the first patient but the latter patient was then contacted for the necessary healthcare action to be taken according to the departmental standard protocol.

Aspects of the human studies of chapters 6 and 7 received ethical approval through other studies. While part of the data in chapter 6 was retrospective, chapter 7 was a prospective study of psoriatic arthritis patients. This psoriatic arthritis study had an MRS component, and was approved by the WoSREC3 (Appendix 2.4). The psoriatic arthritis patients were recruited from the Rheumatology departments of NHS Greater Glasgow & Clyde Hospitals. They also went through the same screening process as described above.

Chapter 3: Reproducibility Measurements of Water and Metabolites

3.1 Introduction and Objectives

MRS is capable of measuring changes in brain chemistry caused by disease. It is therefore necessary to evaluate the inherent uncertainty in concentration estimates from phantoms and healthy brains. Such a study would be useful in informing the extent of errors introduced by other factors apart from disease. The measure of uncertainty, also known as precision, can be obtained from a reproducibility study in healthy subjects or phantoms. Precision is an estimate of how consistent or repeatable a given measurement is, under similar conditions. The knowledge of precision therefore can be used in study design, MRS data interpretation and to assess the stability of the MR scanner over time.

In study design, precision helps in the determination of the minimum sample size required to conduct a study in order to observe a specific change in metabolite concentration. The smallest detectable change in metabolite concentration (between successive scans in one subject or in a group of subjects) can also be determined from reproducibility studies. In MRS data interpretation, it can be used to establish a confidence interval for the difference (in a given metabolite concentration) observed between, say, the patient and healthy control groups. Variation in the performance of the MR scanner (arising from, say, fluctuations in temperature, CHESS water suppression efficiency, etc) can be assessed by estimation of the precision from various measurements carried out over time.

Previous reproducibility studies have been conducted *in vivo* [135-140]. Most of these studies [135, 137, 139, 140] were conducted at long *TE* times where the spectra were reduced to only NAA, Cr and Cho (as they have longer T_2 times compared to the other spectra). A few studies [136, 138] however measured the precision of m-Ins at a short *TE* time. Nonetheless, an *in vivo* reproducibility study (which compares with the clinical situation) is more likely

to provide a wider margin of error than an *in vitro* study. This is because inter-subject variability (i.e. differences in subject characteristics) could increase the standard deviation of the mean of the measured metabolite concentrations, thus making precision poor. Other factors such as subject movement, reproducibility of voxel placement and health condition of a subject between scans are also likely to affect precision. The use of a phantom in a reproducibility study however appears not to be affected by these factors. A notable source of variation in the measurements using a phantom could come from room temperature changes; it is however generally difficult to interpret variations in phantom studies [1]. It may therefore sometimes be beneficial to conduct a reproducibility study both *in vivo* and *in vitro*. To the best of the author's knowledge, no reproducibility study in the literature has investigated reproducibility of measuring the metabolite and water peaks with short *TE* both *in vivo* and *in vitro* at 3 T.

The objectives of the work presented in this chapter were:

1. To compare the signal-to-noise ratio (SNR) of the PRESS and STEAM localisation sequences as implemented on the MR scanner for this project. The measured SNRs would form the basis on which the sequence of choice was selected for the experiments in this thesis;
2. To use short *TE* MRS acquisition to assess the within-session, between-session and between-exam reproducibility of measuring the peak areas of NAA, Cr, Cho, Glu, m-Ins, Lac and water in a phantom (*in vitro*);
3. To assess the impact of temperature on the *in vitro* reproducibility measurements and the stability of the MR scanner over a period of 18 months (the period within which all the data for this thesis were collected);
4. To use short *TE* MRS to assess inter-subject and intra-subject reproducibility of measuring the peak areas of NAA, total NAA (tNAA), total Cr (tCr), total Cho (tCho), Glu, Gln, Glx, m-Ins and water in a healthy human brain (*in vivo*).

3.2 Methods

The methods described in the following subsections are in respect of the above-stated aims. Section 3.2.1 describes the spectral acquisition and analysis aimed to compare the SNR between the PRESS and STEAM pulse sequences. Section 3.2.2 is the reproducibility study presented in two subsections describing the methods for the phantom (section 3.2.2.1) and human (section 3.2.2.2) reproducibility studies. The spectral analysis for the reproducibility studies is presented in section 3.2.3, and the calculation of precision is presented in section 3.2.4.

3.2.1 PRESS versus STEAM

Single voxel spectra were acquired from the GE MRS phantom (Figure 2.26) using the PRESS and STEAM sequences on the same day; each experiment was performed once using the same receiver gain settings. The phantom remained in place while both experiments were performed. The same acquisition parameters were used in both sequences: *TR* = 2000 ms, voxel size = 2 x 2 x 2 = 8 cm^3, 4096 complex points and a bandwidth of 5000 Hz. Acquisitions were done using two echo times: *TE* = 35 and 144 ms. Metabolite and unsuppressed-water spectra were collected with 128 and 16 averages respectively. As the water signal is inherently large and of high SNR, the minimum number of averages (i.e. 16) on the scanner was used (section 2.3.1.3); this also made the acquisitions quicker. The temperature of the phantom during the experiments was 18 ±1 ^oC (~291 K).

Spectral analysis was performed using the SAGE software package as described in sections 2.3.1.2-3. The signal-to-noise ratio (SNR) estimate for each sequence was obtained from their respective spectra in the frequency domain by defining SNR as [141, 142]:

$$\text{SNR} = \frac{\text{Highest metabolite peak amplitude}}{\text{SD of noise amplitude}} \qquad \text{(Eq. 3.1)}$$

The amplitude [142] of the NAA and water peaks were used to calculate the SNR of the water-suppressed and unsuppressed acquisitions, respectively. The standard deviation (SD) of the noise amplitude was automatically estimated by the SAGE software during spectral analysis. This is usually the amplitude of the highest spike in the region of the spectrum that does not include the metabolite peaks.

3.2.2 Reproducibility Studies

3.2.2.1 Phantom Studies

CHESS water-suppressed spectra were acquired from the MRS phantom (Figure 2.26) by placing an 8 cm^3 voxel at its centre (Figure 3.1). The PRESS sequence parameters used were: *TE* = 35 ms, *TR* = 2000 ms and NSA = 16, 4096 complex points and a bandwidth of 5000 Hz. The temperature of the phantom was recorded before each experiment.

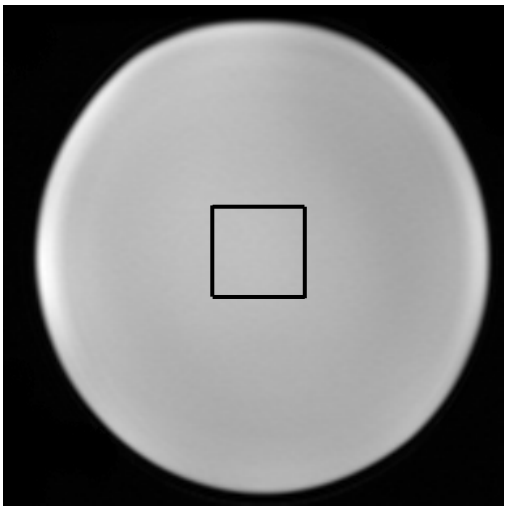

Figure 3.1: Voxel position at the centre of the spherical phantom

Prior to each spectral acquisition, the scanner performs a shimming routine. During shimming, the scanner automatically detects the water centre frequency (course adjustment), sets the transmitter gain, performs a localised shim on the voxel (to optimise B_0 field homogeneity), detects the water centre frequency (fine adjustment), sets the receiver gains and determines the flip angles for the water suppression pulses. This shimming process is also known as

scanner tuning, and it returns the autoprescan results on the scanner console once tuning is completed.

In the within-session study, the voxel was shimmed once and spectra were acquired. With the phantom in the same position, shimming and spectral acquisition (from the same voxel location) were repeated in four successive examinations.

In the between-session study, the position of the phantom and coordinates of the voxel were recorded after the first acquisition. The phantom was removed and replaced (10 minutes later) on the padding in the head coil (Figure 1.1e) using the laser guide and position indicator on the scanner. The laser guide reflected a ray along the temperature strip of the phantom, and this was used to aid consistent positioning of the phantom. The same voxel size was prescribed in the same location as before using the voxel coordinates. Three more successive acquisitions were performed after the first one, with the phantom replaced between successive examinations.

In the between-exam study, the phantom was scanned three times in one session (as in the within-session scans) every month over the course of 18 months. Reproducibility of the phantom position was achieved by positioning the laser guides on its temperature strip and using the position indicator on the scanner. The voxel was consistently positioned at the centre of the phantom. During these scans, the temperature of the phantom was recorded to be used in the serial study of temperature effect on reproducibility.

3.2.2.2 Human Studies

Using a single voxel PRESS sequence with CHESS water suppression, *TE* = 35 ms, *TR* = 2000 ms, 128 signal averages, 4096 complex points and a bandwidth of 5000 Hz, spectra were acquired from an 8 cm^3 voxel positioned in the frontal grey matter region (Figure 3.2) in seven healthy volunteers. Compared to the phantom studies, more averages (at least 128) were required in the human studies to improve SNR; thus minimising noise contributions arising from lipids and macromolecules in the brain, which are absent in the phantom. Specific

anatomical landmarks were clearly identified to serve as guides so that voxel positioning would be reproducible. Three reproducibility studies were conducted *in vivo*: inter-subject, same day; inter-subject, same month; and intra-subject, same year.

Figure 3.2: Voxel position in the frontal grey matter brain region

For the inter-subject, same day study, three healthy volunteers were scanned approximately 1 hour apart. For the inter-subject, same month study, four healthy subjects were scanned approximately 1 week apart within the same month. For the intra-subject, same year study, one healthy volunteer was scanned three times over the course of one year.

3.2.3 Spectral Analyses in Reproducibility Studies

To quantify the unsuppressed-water spectral peak areas in both phantom and human reproducibility studies, spectral fitting was performed using the SAGE software package (sections 2.3.1.2-3). Both phantom and human metabolite spectra were fit using the LCModel software package (section 2.3.1.1). The reasons for using different spectral analysis software packages for the water and metabolite quantification were discussed in section 2.3.2. Briefly, the LCModel basis set does not include the unsuppressed-water resonance and so fitting to the water peak does not return any result. SAGE is however able to quantify this water peak but is semi-automated, unlike LCModel which is

automated. Due to the volume of data to be analysed, speed and consistency were critical. Moreover, only the arbitrary (and not the absolute) concentrations of water and metabolites would be required in the reproducibility studies.

3.2.4 Assessment of Reproducibility

Reproducibility was assessed using the estimate of the coefficient of variation (CoV), defined as:

$$\text{CoV} = \frac{\text{Standard deviation}}{\text{Mean}} \text{ X } 100\ \% \qquad \text{(Eq. 3.2)}$$

CoV is an estimate of the uncertainty in the spectral peak area measurements. A smaller value of CoV means reproducibility is better.

3.3 Results and Discussion

3.3.1 PRESS versus STEAM SNRs Compared

This section presents the results for the first study aim: the comparison of the signal-to-noise ratios (SNRs) of the two commonly used MRS pulse sequences. The rationale for this was to make a choice (based on their SNRs) of pulse sequence to use for the experiments in this thesis.

The SNR values of the PRESS and STEAM MRS localisation sequences are compared in Table 3.1. Both protocols were implemented on the MRS brain phantom as discussed in section 3.2.1.

Localisation sequence	**PRESS**		**STEAM**	
Echo time (ms)	***35***	***144***	***35***	***144***
NAA peak amplitude x 10^5 (a.u.)	9.01	6.83	7.26	5.55
Noise SD (CHESS ON)	252.98	250.82	523.86	298.48
SNR (CHESS ON) x 10^3	**3.56**	**2.72**	**1.39**	**1.86**
Water peak amplitude x 10^5 (a.u.)	1601.10	1057.20	1596.50	1095.50
Noise SD (CHESS OFF)	316.78	257.74	358.49	287.56
SNR (CHESS OFF) x 10^5	**5.05**	**4.10**	**4.45**	**3.81**

Table 3.1: Comparison of the SNR values of the PRESS and STEAM sequences at short (35 ms) and long (144 ms) *TE* times.
CHESS ON is the water-suppressed acquisition; CHESS OFF is the unsuppressed-water acquisition; a.u. means arbitrary units. All the above measurements were done on the MRS brain phantom (Figure 2.26).

For the short *TE* CHESS ON scan (i.e. metabolite spectral acquisition), PRESS showed as much as twice the SNR of STEAM (3.56 vs. 1.39). This is because the spin echo signal produced by PRESS has two times the intensity of the stimulated echo produced by STEAM. For the long *TE* CHESS ON scan, the SNR of PRESS was about 1.5 times greater than that of STEAM (2.72 vs. 1.86). This reduced SNR of PRESS at the longer *TE* could be because at such longer *TE* times, the rise time of the selective pulses in PRESS is prolonged; this results in signal decay (due to T_2 losses) and distortion (due to *J*-coupling), and consequently a drop in SNR [1]. The non-uniform flip angle profile with the 180^o pulses of PRESS causes spectral distortion at the voxel edges [57]. This could also be a factor in the reduced SNR of PRESS particularly at longer *TE* times.

Using *TE*/*TR* = 288/1500 ms and 32 signal averages to acquire CHESS water-suppressed and unsuppressed-water spectra from an 8 cm^3 voxel, Drost et al [31] reported the SNR for PRESS and STEAM. The NAA peak was used to calculate the SNR of their water-suppressed acquisition. They observed that for the water-suppressed and unsuppressed acquisitions, the SNR of PRESS was about 1.78 and 2.31 times better than that of STEAM, respectively. These results are consistent with those reported in this thesis.

Ideally, for a CHESS OFF scan (i.e. unsuppressed, fully relaxed water signal acquisition), *TE* should be set to the minimum value on the scanner and *TR* to about 15 s (which is ~5 times the T_1 of water). However, the respective *TE* and *TR* values of 35 and 2000 ms used in the CHESS OFF acquisitions in this study caused significant T_1 and T_2 losses to the water signal with the PRESS and STEAM sequences. However, PRESS still showed greater SNR than STEAM at both *TE* times. PRESS was therefore found to consistently show higher SNR than STEAM in agreement with theory, and so was the sequence of choice for the MRS measurements in this thesis.

3.3.2 Reproducibility Results

In this section, results for three studies are presented in respect of study aims 2-4: firstly, results for the reproducibility studies measuring water and the metabolites in a phantom are discussed in section 3.3.2.1 (study aim 2); then investigation of the effect of temperature on the phantom reproducibility measurements/stability of the MR scanner is presented in section 3.3.2.2 (study aim 3); lastly, results for the human reproducibility studies are discussed in section 3.3.23 (study aim 4).

3.3.2.1 *In vitro* Measurements

The *in vitro* reproducibility results are summarised in Table 3.2. The mean of the coefficient of variations (CoVs) and standard deviations (SDs) of the CoVs were calculated for all the metabolites (Table 3.3).

The water peak was not acquired with CHESS OFF. However, the scanner always acquires some unsuppressed-water lines for eddy current and phase corrections, as well as combination of the phased-array coil data. With SAGE, it is possible to extract these water lines and process them into the water peak (section 2.3.1.3). This water peak was processed for both *in vivo* and *in vitro* reproducibility studies.

Peak	Within-Session CoV (%) (n=5)	Between-Session CoV (%) (n=5)	Between-Exam CoV (%) (n=18, 3 scans per exam)
m-Ins	3.62	6.35	4.47
Cho	1.48	7.20	4.33
Cr	1.83	6.80	4.49
Glu	3.24	7.22	4.44
NAA	1.90	5.28	3.95
Lac	4.63	6.28	5.74
Water	3.00	3.46	12.73

Table 3.2: Reproducibility of MRS measurements in the GE MRS phantom

The within-session and between-session CoVs for the water peak were similar; between-exam reproducibility, however, was relatively less. This could be due to inconsistencies of the CHESS water suppression module or changes in the transmitter gains (which was observed to vary within ± 4 dB, representing a percentage change within ± 3.45 %).

For all metabolites, both within-session and between-exam CoVs were better than between-session CoV; within-session was the most reproducible. The absence of possible phantom repositioning errors in the within-session experiments could have been a factor in its better reproducibility than those for the between-exam and between-session experiments. The large number of scans performed in the between-exam study could have contributed to its lower CoVs (as standard deviation is reduced) compared to those for the between-session study.

The mean CoVs for all metabolites were closer to the LCModel percentage standard deviations (Table 3.3), a similar observation made by Hancu et al [136]; and has been reported to be the actual case [48]. This is in contrast to the trend observed in the *in vivo* study: the SDs of the mean CoVs were rather closer to the LCModel %SDs. For the *in vivo* study, the means of the CoVs were greater than the LCModel %SDs. The inherent variability in the subject group and the small sample size could have been the sources of the large discrepancy between the two parameters.

Metabolite	Mean CoV	SD of mean CoV	LCModel %SD for between-exam CoV
m-Ins	4.64	1.49	8.0
Cho	4.39	2.86	4.0
Cr	4.32	2.48	3.0
Glu	4.96	2.04	8.0
NAA	3.88	1.77	2.0
Lac	5.55	0.84	9.0

Table 3.3: Mean CoVs and standard deviations of the measured metabolites in all the three studies (n = 64).
The mean CoVs for NAA, Cr and Cho are comparable to their average %standard deviations from LCModel; for all metabolites, the SD of the means were however found to be smaller than the average % SDs from LCModel

Simmons et al [135] performed a reproducibility study on a similar phantom as the one used in this thesis. They acquired spectra using PRESS with *TE/TR* = 136/2000 ms and 256 averages. Using the SAGE software, the NAA, tCr and Cho peaks were fit to Lorentzian line shapes using the Levenberg-Marquardt fit, and normalised to the water peak. CoVs were calculated for three studies: five serial scans with single shim, while the phantom was unmoved (within-session), five serial scans with separate shims, while the phantom was repositioned each time (between-session), and one scan per week over 2 years (between-exam). The within-session CoVs (%) were: NAA = 0.5, tCr = 0.8, Cho = 1.2; between-session CoVs (%) were: NAA = 0.8, tCr = 1.0, Cho = 1.0; and the between-exam CoVs (%) were: NAA = 1.5, tCr = 1.5, Cho = 2.4. Only the CoV for Cho in the within-session study by Simmons et al was comparable to the study here. All other CoVs were at least twice as good as those in this thesis.

A number of factors could have accounted for this difference in the results: Simmons et al acquired 256 averages while only 16 averages were acquired in this thesis. SNR is proportional to √NSA [31], which means that the SNR of their signals were a factor of 4 more than those here. For the within-session scans in this thesis, shimming and water suppression were performed per scan (but Simmons et al performed shimming once in a similar exam). Variations in the efficiency of the scanner doing these two procedures (i.e. shimming and water suppression) could have propagated errors into the estimated CoVs, thus

making them larger. For the between-session scans, a time delay of ~10 minutes was allowed between scans; Simmons et al, however, only retracted the couch of the scanner and replaced the phantom. Thus, there was a greater chance of equipment instabilities manifesting themselves in the CoV estimates of this thesis. Differences in the *TE* times (35 versus 135 ms), B_0 (3T versus 1.5T) and spectral quantification techniques (LCModel versus SAGE) could have also been the sources of the disagreements.

Generally, the CoVs for all metabolites measured *in vitro* were better than the *in vivo* CoVs. The inherent sources of variability (e.g. voxel content, motion, etc) associated with the *in vivo,* that were absent in the *in vitro,* studies could have been the reason for this relationship between the two sets of CoVs. Temperature effects were also thought to have a role in this discrepancy, and so investigation of this *in vivo* became an interest. However, it is impossible to vary the temperature of the human body; only the temperature variations in a phantom could be measured in such studies. The effect of temperature variation on the *in vitro* reproducibility and/or stability of the MR scanner was therefore investigated (section 3.3.2.2).

3.3.2.2 Temperature Effect on *in vitro* Measurements

Temperature affects T_1 more than T_2; T_1 relaxation time increases with temperature. In fact, both T_1 and T_2 (and hence magnetisation) have been reported to vary by about 2-3 % per ^oC [1]. Despite this argument from theory, the concentration estimates in this thesis were generally observed to remain fairly stable with room temperature over the period of the experiments. In fact, only the experiment in month '4' corroborated the temperature-concentration argument.

Figure 3.3 shows a long term serial study assessing the stability of the metabolite concentration measurements. The graph indicates that even though the room temperature varied significantly, that did not introduce large variations in the concentration measurements. The CoVs for water, NAA, Cr, Cho, Glu, m-Ins, and Lac were respectively 12.73 %, 3.95 %, 4.49 %, 4.33 %, 4.44 %, 4.47 % and 5.74 % (Table 3.2). The results thus indicate that

temperature variation did not cause substantial variations in the measured metabolite and water spectral peak areas.

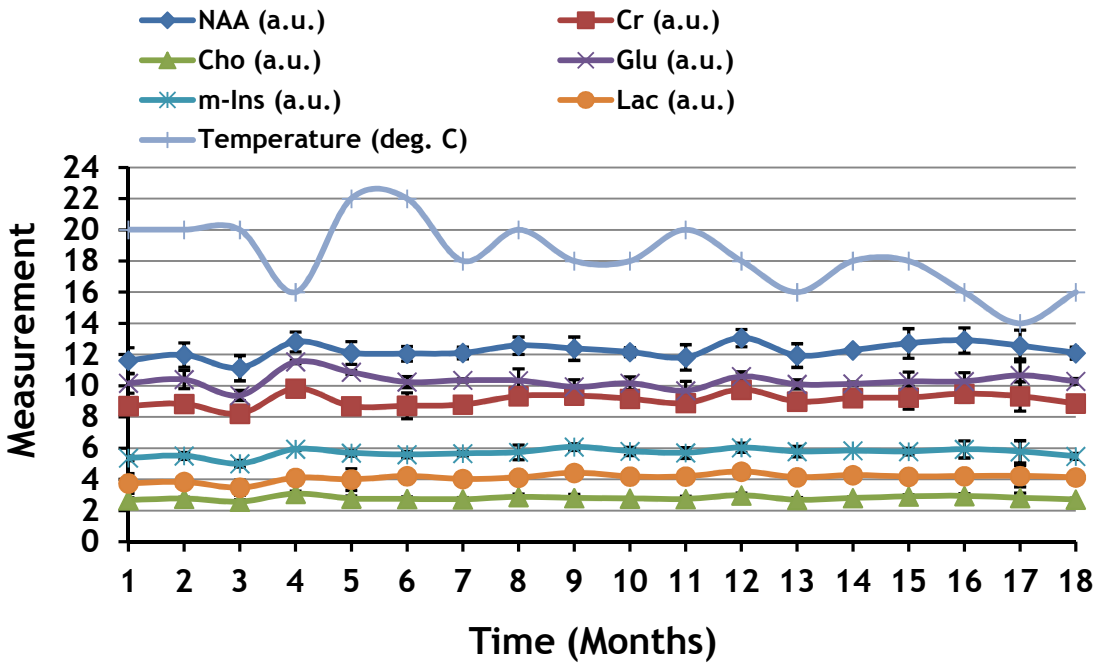

Figure 3.3: Reproducibility of phantom measured metabolite concentrations over a period of 18 months (October 2010 to March 2012).
The topmost line (in light blue) is the variation of the temperature (in ^{o}C) of the phantom over the course of the reproducibility study period. Error bars are ±standard deviations of the LCModel concentrations

3.3.2.3 *In vivo* Measurements

The *in vivo* reproducibility results are summarised in table 3.4, and the spectra acquired from each reproducibility study are shown in Figures 3.4-6. The mean of the coefficient of variations (CoVs) and standard deviations (SDs) of the CoVs were calculated for all the metabolites (Table 3.5).

For m-Ins, tCho and tNAA, the intra-subject, between-exam was the most reproducible, followed by inter-subject, same month and then inter-subject, same day. For Cr, tCr, NAA and water, intra-subject (between-exam) reproducibility was again the best, but this time, followed by inter-subject, same day and then inter-subject, same month reproducibility measurements. However, for Glu, Gln and Glx reproducibility, intra-subject, between-exam

was the worst, followed by inter-subject, same month; inter-subject, same day exam was the most reproducible. Intra-subject reproducibility of the water peak was the best, followed by inter-subject, same day; inter-subject, same month reproducibility was the worst. Using n = 3 for the inter-subject, same month measurements did not change the above comparisons.

Peak	Inter-Subject, same day CoV (%) (n=3)	Inter-Subject, same month CoV (%) (n=4)	Intra-Subject, same year CoV (%) (n=1, scanned 3 times)
m-Ins	25.88	24.15	13.20
tCho	15.12	14.59	3.87
Cr	23.01	40.04	22.86
tCr	11.22	17.95	10.51
Gln	27.72	71.94	N.D.*
Glu	4.58	9.95	26.05
Glx	5.95	11.88	26.23
NAA	11.93	16.70	3.13
tNAA	14.50	11.99	5.98
Water	11.99	13.63	7.63

Table 3.4: Reproducibility of MRS measurements in healthy volunteers.
*Gln was not detected (ND). tCho, tCr and tNAA mean total Cho, Cr and NAA, respectively.

The standard deviations of the mean CoVs for the metabolites in all the studies were found to be comparable to the average LCModel standard deviations for the intra-subject, between-exam, same year study (Table 3.5). This was notable for m-Ins, Cr, tCr, Glu and Glx. It is therefore possible that the LCModel standard deviations could as well be used to assess reproducibility roughly. Estimating CoV in this manner might be useful in the clinical setting to save time having to conduct a rigorous reproducibility study as presented in this chapter.

Metabolite	Mean CoV	SD of mean CoV	LCModel %SD for Intra-subject, same year CoV
m-Ins	21.07	6.88	7.67
tCho	11.19	6.35	3.67
Cr	28.64	9.87	10.00
tCr	13.23	4.11	3.00
Gln	33.22	36.28	ND
Glu	13.53	11.17	9.33
Glx	14.69	10.43	10.00
NAA	10.58	6.88	3.67
tNAA	10.83	4.38	2.33

Table 3.5: Mean CoVs and standard deviations of the measured metabolites in all the three studies (n = 10).
ND = not detected. The standard deviations of the mean CoVs are comparable to the average %standard deviations from LCModel

In most cases, less variability will be expected from scanning the same healthy subject over a period of time. Possible sources of variation could come from motion, variability in the voxel placement, RF non-uniformity, shimming efficiency or change in hardware such as a head coil. However, for a number of subjects, variability in their own characteristics (e.g. age, gender, etc), biological variation, voxel placement, tolerance level in the scanner (e.g. motion), in addition to the above factors could worsen reproducibility. This might explain the better reproducibility in the intra-subject compared to inter-subject studies.

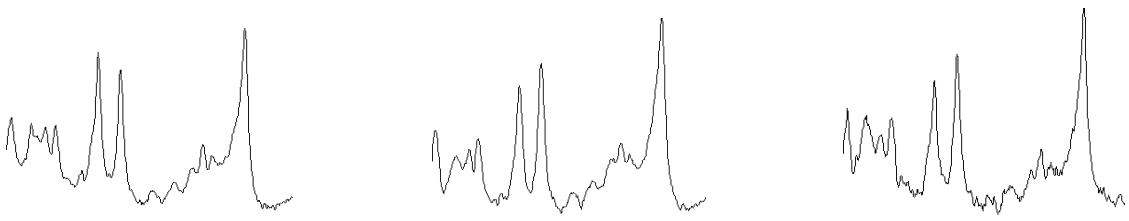

(a) 1st subject **(b) 2nd subject** **(c) 3rd subject**

Figure 3.4: Inter-subject, same day reproducibility spectra

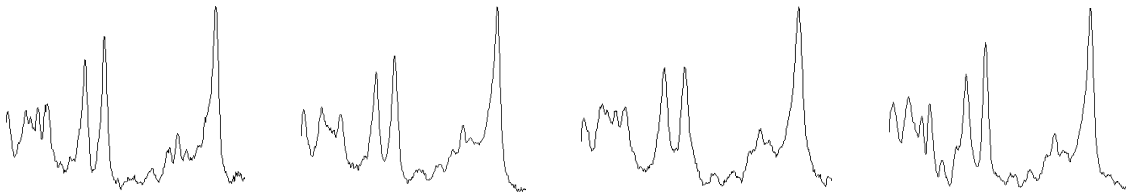

(a) 1st subject **(b) 2nd subject** **(c) 3rd subject** **(d) 4th subject**

Figure 3.5: Inter-subject, same month reproducibility spectra

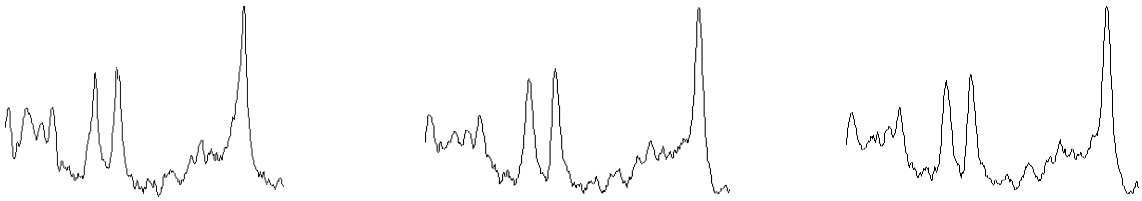

(a) 1st scan **(b) 2nd scan** **(c) 3rd scan**

Figure 3.6: Intra-subject, same year reproducibility spectra

Hancu et al [136] compared the reproducibility of the conventional PRESS sequence with that of their *TE*-averaged PRESS sequence (PRESS-J). They acquired spectra from the posterior cingulate gyrus of two volunteers using *TE*/*TR* = 35/2000 ms and 256 averages for each sequence, except that the *TE* of PRESS-J was varied from 35 to 355 ms in steps of 2.5 ms. Volunteers were scanned three times a day on five different days over 6 months. The calculated CoVs (%), with their LCModel standard deviations in brackets, were: PRESS: NAA = 4.47 (3.97), Cr = 4.74 (3.94), Cho = 5.67 (5.88), Glu = 6.50 (7.76), m-Ins = 7.51 (8.27); PRESS-J: NAA = 2.74 (2.18), Cr = 3.56 (3.55), Cho = 3.25 (4.15), Glu = 7.59 (10.36), and m-Ins = 13.57 (14.06). The standard deviations of all metabolites measured with both sequences were comparable to those reported in this study. The intra-subject CoVs for NAA, Cho and m-Ins of this study were comparable to those of Hancu et al [136]; while the inter-subject CoV between the two studies were also similar.

Simmons et al [135] performed a reproducibility study on 8 subjects using PRESS (*TE*/*TR* = 136/2000 ms), and placing their voxel in the left occipital lobe (comprising a grey-white matter mix). Five successive spectra were acquired within one session; all 8 subjects were again scanned five times over 3 months; and one volunteer was scanned 14 times over 2 years. The spectra were fitted to Lorentzian lineshapes with the Levenberg-Marquadart fitting algorithm, and normalised to the water peak. Calculated CoVs (%) for NAA, Cr and Cho were: within-session for all 8 subjects (NAA = 1.4, Cr = 2.7, Cho = 4.9); between-exam for all 8 subjects (NAA = 2.5, Cr = 3.8, Cho = 6.4); 1 subject scanned 14 times over 2 years (NAA = 3.6, Cr = 5.6, Cho = 6.9). Between-exam reproducibility for all 8 subjects by Simmons et al was better than those reported in this thesis. However, the results in this thesis were comparable to theirs for the between-exam, intra-subject reproducibility.

Marshall et al [140] measured the CoVs for within-session and between-exam of the parietal white matter region of 12 volunteers using PRESS with *TE*/*TR* = 135/1600 ms and 64 averages. Spectra were analysed using a custom software package ("Water Fit", WFIT). The within-session CoVs (%) were; NAA = 4.4, Cr = 17.2, Cho = 8.2, whereas the between-exam CoVs were; NAA = 8.1, Cr = 25.8, Cho = 11.4. The between-exam CoVs reported by Marshall et al were comparable to those reported in this work but no within-session study was conducted *in vivo* in this thesis.

Using the PRESS sequence (*TE*/*TR* = 136/6000 ms), Duc et al [139] collected spectra from the frontal, parietal, occipital, cerebellum and hippocampal regions in "sequential" and "separate" scans of 28 volunteers. The reported percentage CoVs for NAA, Cr and Cho in the frontal region (for comparison with the work in this thesis) were: sequential (NAA = 7.4, Cr = 25.9, Cho = 20.5); separate (NAA = 6.5, Cr = 21.3, Cho = 15.0). Generally, the calculated reproducibility values in this thesis were better than those reported by Duc et al.

Brooks et al [138] used STEAM with *TE*/*TR* = 30/2000 ms to acquire spectra from the occipitoparietal white matter region in 10 healthy subjects. Within one session, six successive acquisitions were done; this was repeated after one

hour, and again in a month's time. Spectral analysis was performed in the java-based Magnetic Resonance User Interface (MRUI) software by fitting Gaussian line shapes to the NAA, Cr, Cho and m-Ins peaks normalised to the water peak. The mean CoVs (%) for each individual in a session (similar to the intra-subject CoVs of Table 3.4) were calculated to be 3.30, 4.32, 5.30 and 8.10 for NAA, Cr, Cho and m-Ins respectively. Even though the sample size for this thesis was small, the reproducibility results were comparable to most of the literature values.

3.4 Summary and Conclusions

In this chapter, the PRESS and STEAM pulse sequences were compared for their respective SNRs. For the same acquisition parameters, and using an MRS brain phantom, PRESS was found to produce spectra whose SNR was typically twice as much as that of spectra from STEAM. The PRESS sequence was therefore preferred over STEAM for subsequent experiments in this thesis.

Using the PRESS sequence, reproducibility studies were conducted both *in vivo* and *in vitro*, measuring the water and metabolite signal areas. These studies also included serial measurements of the most common *in vivo* metabolites in order to assess the stability of the MR scanner and the impact of temperature variations on the measurements.

The phantom studies showed that measurements performed while the phantom remained in place (i.e. within-session) were the most reproducible. For all metabolites, the standard deviations of the mean CoVs of their measurements were found to be better (i.e. lesser) than their corresponding LCModel estimated average % standard deviations. Generally, temperature variations during the phantom experiments did not introduce significant uncertainties in the measured metabolite and water spectral peak areas. To the best of the author's knowledge, no other reproducibility study in the literature has studied the impact of temperature variation on reproducibility measurements at 3 T.

The human studies on the other hand indicated that apart from Glu and Glx, longitudinal measurements of all the other metabolites and water in the same volunteer were the most reproducible. Unlike the phantom studies, for all metabolites, the standard deviation of the mean CoVs of their measurements were comparable to their respective LCModel estimated average % standard deviations.

It has been noted [1] that precision could be worse if measured from repeat scans over a long period of time, compared with short-term repeats. This is because over the prolonged measurement period, additional sources of variations are introduced into the measurements. The *in vitro* precision results (Table 3.2) of this thesis were consistent with this assertion. The *in vivo* results (Table 3.4) were however in contrast to this observation. In the same-day and same-month human studies, different subjects were scanned and so the contribution of subject-specific bias in the measurements cannot be ruled out. The year-long reproducibility human study on the other hand was conducted on the same subject, and so any error arising from the measurements could be considered to be the same in each experiment. This could have been the reason for the better precision in the year-long measurements. In case of the *in vitro* experiments, the same phantom was scanned in all sessions, and is most likely to be the ideal situation being referred to in the above principle; which could be the reason why the *in vitro* results agree with that assertion.

Following the PRESS versus STEAM study, the rest of the studies in this thesis commenced and were then conducted concurrently with the longitudinal reproducibility studies. Since the scanner was found to be consistent in its measurements of the metabolite signals, as suggested by the work in this chapter, the subsequent MRS data may be considered not to be affected significantly by temperature and/or inconsistencies in the performance of the MR scanner.

Chapter 4: RF Field Mapping Using the Unsuppressed-Water Signal

4.1 Overview and Objectives

In section 1.1.3, it was indicated that the non-uniform response of the phased-array head coil could serve a good purpose in quantitative MRS. In this chapter, the sensitivity maps of the eight-channel RF coil (Figure 1.1b) will be deduced using the unsuppressed-water signal. The application of these sensitivity maps for referencing in absolute quantification of cerebral water formed the impetus for this chapter.

The objective of this chapter was therefore to develop standard mathematical models from the RF sensitivity maps of the phased-array head coil. These standard models will be functions of voxel position, and will represent the spectral peak area of unsuppressed-water for any *in vivo* voxel position. Given any *in vivo* acquisition, the voxel coordinates should correspond to at least one of these mathematical functions. Substitution of these coordinates into the appropriate function would give a theoretical signal area at the same voxel position as the *in vivo* signal. This derived signal was suggested in this thesis as a reference in the absolute quantification of cerebral water, which itself has been used as a reference concentration in this thesis.

The referencing method suggested in this chapter is novel and so it is necessary to discuss the commonly used referencing methods (section 4.1.2) in quantitative MRS (section 4.1.1) and the impact of phased-array coils on the accuracy of quantitative MRS (section 4.1.3). These background sections will then serve to clarify the differences between the methodology presented here and the existing methods.

4.1.1 Absolute versus Relative Quantitative MRS

Metabolite levels are generally expressed as ratios or in absolute millimolar concentration units. Each one of these two quantification schemes has its practical advantages and disadvantages.

The use of ratios commonly involves referencing each spectral peak area to that of Cr. The advantage of this technique is that it involves shorter acquisition times since there is no requirement for a separate acquisition of the reference signal. In acquisitions where the voxel includes some CSF (e.g. around the hippocampus), the use of ratios circumvents the need to perform partial volume correction (section 5.1.3)[1]. For such cases, both the reference and metabolite signals are affected by the same partial volume effect, which cancels out in the ratio. Reproducibility with ratios is therefore normally reported to be good [1]. However, metabolite ratios are vulnerable to pathological processes in which Cr changes, and also systematic variation of tissue Cr content with age [1]. The concentration of a reference has to be fairly constant, but grey matter (GM) changes with ageing have been associated with increased GM Cr in the elderly [1]. There has also been a reported significant increase in white matter Cr with age in young to middle-aged adults [143].

Regional, tissue-specific and age-related [143, 144] variation in Cr concentration underscores the need for absolute metabolite concentrations. Moreover, changes in metabolite ratios observed between two examinations of the same individual or between two groups are ambiguous and have to be interpreted with caution. This is because the change may either be due to the numerator or the denominator. Therefore, ratios cannot withstand detailed comparison across different brain regions [1].

Expressing metabolite concentrations in absolute units, on the other hand, requires a more rigorous technique [1] with careful consideration to the type of reference concentration, which is usually constant or fairly stable. In general, the accuracy and precision of absolute concentrations depend on the type of concentration standard chosen (section 4.1.2). Internal referencing is not

affected by effects due to coil loading and local B_1 variation as with external referencing.

The next consideration is the choice of *TE* and *TR* for the acquisition, which largely depends on the aim of the study. The challenge however is that the metabolites differ in T_1 and T_2 relaxation times. Therefore, the *TE* and *TR* values chosen will cause signal losses due to either T_1 or T_2 relaxation effects or both (section 2.1.2.1-2). Nonetheless, relaxation effects can be minimised by selecting a short *TE* and a long *TR* [132].

When the B_1 non-uniformity or coil loading and relaxation effects are corrected, the other sources of error (including partial volume effects) do not affect accuracy of absolute quantification by more than 5-10 %; and reproducibility stays well within 10 % [145]. Once all the necessary corrections are made, absolute metabolite concentrations provide direct means of interrogating tissue metabolite levels, and are not ambiguous. This is because the concentration of the reference does not change; therefore any observed change in concentration is purely due to change in the measured metabolite. For this reason, absolute concentrations improve the utility of MRS in the characterisation of pathological and developmental changes in metabolite levels. With absolute concentration estimates, MRS results from different sites can be compared in multicentre clinical trials, as long as the protocols are similar [30].

4.1.2 Internal versus External Referencing

The reference signal for absolute quantification may be acquired from a substance within the brain (internal) or outside of the brain (external). The concentration of the internal substance is usually assumed empirically [30, 62] or estimated at the same time as the metabolite concentrations [58]. Brain tissue water and Cr are widely used as concentration standards [62, 71, 146, 147]. The concentration of the external reference on the other hand is always accurately known [30, 145]. Various chemicals have been used to prepare

solutions of known concentrations for external referencing; examples of these include Cr [145], cyclohexane and water [148].

External referencing can be performed in two ways [1]: “same-place” and “same-time” external standards. A same-place external standard is scanned in place of the brain on a separate occasion, whereas a same-time external standard is placed next to the head in the RF coil, and is scanned at the same time as the brain; but with different voxel positions [1, 30].

For an acquisition involving the same-time external standard, the brain and reference signals are affected by difference in flip angles of the RF pulse, and so a correction for B_1 field non-uniformity is required [149]. The same-place external referencing technique may not require B_1 non-uniformity correction on the assumption that the spatial sensitivity of the coil remains the same over the head. However, systematic errors in the quantification could arise from local B_0 and B_1 field inhomogeneities, loading effects, eddy currents and standing waves, all of which may depend on the properties of the human head and size, geometry, position and electrical properties of the filling substance in the phantom [30, 62, 144, 148]. The chemical composition of an external standard can be carefully controlled and its concentration is accurately known [62]. However, external referencing could complicate, prolong and introduce more errors into the quantification process [1].

For internal referencing, a water-suppressed acquisition is performed first, and then from the same voxel, the signal from unsuppressed tissue water is acquired, which serves as the concentration reference [45]. Tissue water content could as well be derived from proton density weighted images [150, 151]. This approach gives absolute concentration in units of molality (i.e. moles/kg of tissue water), which can be converted into molar concentration (i.e. moles/litre of tissue water) by using the density of brain tissue (section 6.2.4.1) [71]. However, determination of brain density and brain water content can be challenging [45, 58], and so a value is usually applied from the literature [62].

The use of literature values require some caution since brain tissue water content is known to be affected by a number of pathologic conditions. For instance, it has been reported that hydrocephalus [152], brain tumours [152] and multiple sclerosis [153, 154] can cause brain water content to be as high as 120 %, 50 % and 12 %, respectively, compared to the water content in healthy subjects. It might therefore be useful to measure the brain tissue water signal directly in such situations. Nonetheless, an internal standard is insensitive to the local variations in B_0 and B_1 fields suffered by an external standard, and so there is no requirement for non-uniformity correction [1, 62].

Tissue water content as a concentration reference is uniformly distributed, in the absence of lesions and hydrocephalus, cerebral water content varies over a relatively small range (10-20 %) in most other pathologies [62]. The acquisition time for internal referencing is shorter (since acquisition is done in the same voxel using the same sequence), and only a few averages of the water signal need to be collected as it has a high SNR [1]; the technique is also less complicated (since it requires fewer corrections to be performed) and may have less compliance issues (since there is no object next to the subject's head in the RF coil) compared to external referencing.

4.1.3 Spatial Sensitivity of the RF Coil

Receive-only surface coils and phased-array coils help increase the SNR of the MRS signal but significant standing wave effects due to the geometry of the human head (even at 1.5 T) cause inhomogeneous signal-receive characteristics of the RF coils [1, 144]. Signal losses due to T_1 relaxation processes will also vary according to the flip angle at each location within the coil [1]. If uncorrected, the RF non-uniform response, which usually assumes a convex profile across the coil [30], could give rise to signal intensity variation of up to 29 % in large water-filled phantoms [30], and up to 50 % in the human head [145]. These variations have been observed as signal intensity decreases from the centre of the coil to the edges. Thus voxel position in the brain could therefore determine the amount of signal acquired relative to noise [144, 155]:

metabolite concentrations will be overestimated and underestimated for voxel positions towards the centre and edge, respectively, of the coil.

However, RF field non-uniformity cannot directly be measured by a uniform phantom [1, 144], because the coils are not used for transmission [144]. One way of correcting the received signal for RF field inhomogeneities is by recording the localised water signal using both the receive coil and the body coil. The recorded signal intensity may then be used to scale the low SNR metabolite signals to obey the receive characteristics of the transmit/receive body coil [47, 156]. However, with phased-array coils, the water and metabolite signals will have to be combined using consistent signal weights (section 1.4.4). This is because the low SNR of the metabolites is most likely influenced by noise, and the weights will account in part for the noise [144]. Since the normalisation of the signal is required for each voxel position, it will mean that this correction technique will have to be repeated for every single MRS acquisition. RF field mapping is thus the only rigorous means of correcting for the non-uniformity [1]. Even though this is time-consuming and may not be feasible in a clinical setting, it provides correction factors for all possible voxel positions within the field-of-view of the RF coil. RF mapping was performed in this thesis on a phantom, not to correct for the non-uniform response of the coil, but to deduce a reference signal for the absolute quantification of cerebral water content.

4.2 Methods

The head coil can be considered to have a 3-dimensional geometry described by three (anatomical) axes: right-left (RL), anterior-posterior (AP) and superior-inferior (SI). Therefore, the design allows for NMR signal reception from a 3-dimensional object such as the human head or the GE MRS phantom (Figure 2.26). To obtain the RF sensitivity maps, spectra were recorded from varying voxel positions, firstly along these three principal axes (sections 4.2.1-3), and then within a 2-dimensional space (defined by the RL-AP axes) along the SI axis (section 4.2.4). For each acquisition, the unsuppressed-water spectral lines were processed (section 4.2.5) and plotted to give the sensitivity maps (section 4.2.6).

The process of switching OFF the CHESS water-suppression module on the MR scanner is not straightforward. Since many voxel positions were to be acquired in this study, it would have meant that the same process of turning OFF CHESS water-suppression be repeated prior to each acquisition. The water signal has a very good SNR and so only a few averages (at least one) of unsuppressed-water lines should be sufficient for the RF mapping study. Meanwhile, it is still possible to obtain at least two unsuppressed-water lines from a CHESS water-suppressed acquisition (section 2.3.1.3). Therefore, acquisition of the CHESS water-suppressed spectra in this case made it possible to perform the experiments quicker, and then to obtain two unsuppressed-water lines (using NEX = 8) from the data set for this study.

4.2.1 Sensitivity mapping along the RL axis

An axial T_2-weighted FSE/propeller (*TR*/*TE* = 4050/110 ms) MRI of the phantom was acquired with 31 slices (3 mm thick per slice), and FOV of 20.0 x 20.0 cm^2.

The MRS protocol used was the PRESS localisation sequence with *TE*/*TR* = 35/2000 ms, 64 signal averages, NEX = 8 and VOI = 10.0 x 10.0 x 10.0 mm^3. All spectra were acquired with the CHESS water suppression module turned ON.

The voxel was positioned at the origin along the RL axis of the MR image and spectra were acquired from this location. This was the isocentre of the receiver coil. Maintaining fixed coordinates for the AP and SI axes, the voxel was moved every 5.0 mm up to the right (R) edge of the image where the maximum possible coverage was -70.0 mm. The voxel was again moved by 5.0 mm up to the left (L) edge of the image, a displacement of 70.0 mm from the isocentre. Twenty-eight voxel positions were covered; three acquisitions were made in each position, giving a total of eighty-four acquisitions.

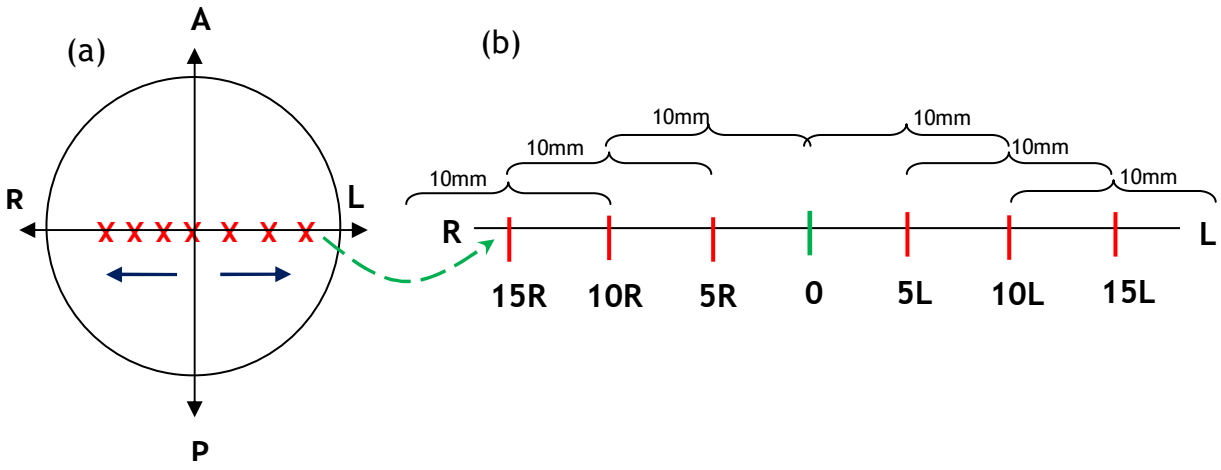

Figure 4.1: A schematic of the voxel locations for the MRS acquisitions along the RL axis
A few voxel positions along the RL plane of the phantom image are shown in (a) and a magnified representation of the RL axis is shown in (b).
In figure 4.1(b), the isocentre is position 0; displacements to the right of the isocentre are indicated by the measure of the distance with an 'R'; displacements to the left are marked with an 'L'. The 'R' values are negatives, whereas the 'L' values are positives. All displacements were displayed with the aid of a position indicating cursor on the scanner console. The voxel was positioned such that its centre at one location was 5.0 mm away from its previous centre position. Since the length of the voxel was 10 mm, there was always an overlap of its length by 5.0 mm between neighbouring positions. Thus, spectra were collected effectively at each location along the RL axis.

4.2.2 Sensitivity mapping along the AP axis

For measurements along the AP axis, a sagittal T_1-weighted FLAIR (*TR*/*TI*/*TE* = 2500/920/9 ms) MRI of the phantom was acquired with 21 slices (3 mm thick per slice), and FOV of 20.0 x 20.0 cm^2. The same MRS protocol described in section 4.2.1 was used for the spectral acquisitions but this time, after the acquisition at the isocentre along the AP axis, the voxel was moved to the anterior end of the image up to -70.0 mm; acquisitions were then made with voxel positions up to the posterior end of the image at 75.0 mm from the isocentre. Voxel displacements were in steps of 5.0 mm (as in Figure 4.1) and so with the voxel length of 10.0 mm, spectra were collected at every location along the AP axis. The coordinates along the RL and SI axes were kept constant throughout the measurements. Twenty-nine voxel positions were covered; three acquisitions were made in each position, giving a total of eighty-seven acquisitions.

4.2.3 Sensitivity mapping along the SI axis

For measurements along the SI axis, a coronal T_2-weighted FLAIR (*TE*/*TR* = 158/9000 ms) MRI of the phantom was acquired with 21 slices (3 mm thick per slice), and FOV of 20.0 x 20.0 cm^2. The same MRS protocol described in section 4.2.1 was used in these measurements but in this case, the coordinates in the RL and AP axes were kept constant throughout the acquisitions.

Spectra were collected at the isocentre along the SI axis; the voxel was subsequently moved in steps of 5.0 mm up the SI axis to a maximum displacement of 80.0 mm from the isocentre. In steps of 5.0 mm, spectra were collected from voxel positions down the SI axis to a maximum displacement of -65.0 mm from the isocentre. As the length of the voxel was 10 mm, spectra were collected from all points along the SI axis. With three acquisitions in all twenty-nine voxel positions, a total of eighty-seven acquisitions were made.

4.2.4 Sensitivity mapping in the RL-AP plane along the SI axis

For these measurements, an axial FSE/propeller (*TE*/*TR* = 110/4050 ms) MRI of the phantom was acquired with 34 slices (5 mm thick per slice), a matrix size of 160 x 160 pixels, and FOV of 20.0 x 20.0 cm^2. The MRS protocol used in section 4.2.1 was maintained but this time, a voxel size of 20.0 x 20.0 x 20.0 mm^3 was used.

Three positions were chosen above and below the isocentre along the SI axis. These selected points were each 20 mm apart; the length of the voxel used was also 20 mm. The centre of the voxel was placed on each of these selected points. Thus, one edge of the voxel at a particular position always coincided with the other edge in the next position. This made it possible to collect spectra at every point in a given row. The six selected points along the SI axis were accessed by scrolling in-plane through the slices of the axial image, using the position indicating cursor on the scanner console.

For a given axial slice (i.e. a selected point on the SI axis; Figure 4.2), spectral acquisitions were conducted in such a way that the voxel was moved along the RL axis until all points were covered. Acquisitions were subsequently made with this row of voxel positions along the AP axis of the same slice. When all points were covered on a particular slice, the next SI point was assessed by scrolling to the appropriate slice (in-plane or into the screen) on which acquisitions were made again until all voxel positions were covered. Due to the spherical geometry of the phantom, the number of voxel positions covered decreased towards the edges. For the six SI points, the numbers of voxel positions covered from the superior to inferior ends of the phantom were 19, 27, 32, 31, 26 and 17. The measurements were not repeated at the voxel positions in this case due to the large number of voxel positions. Thus a total of 152 acquisitions were made.

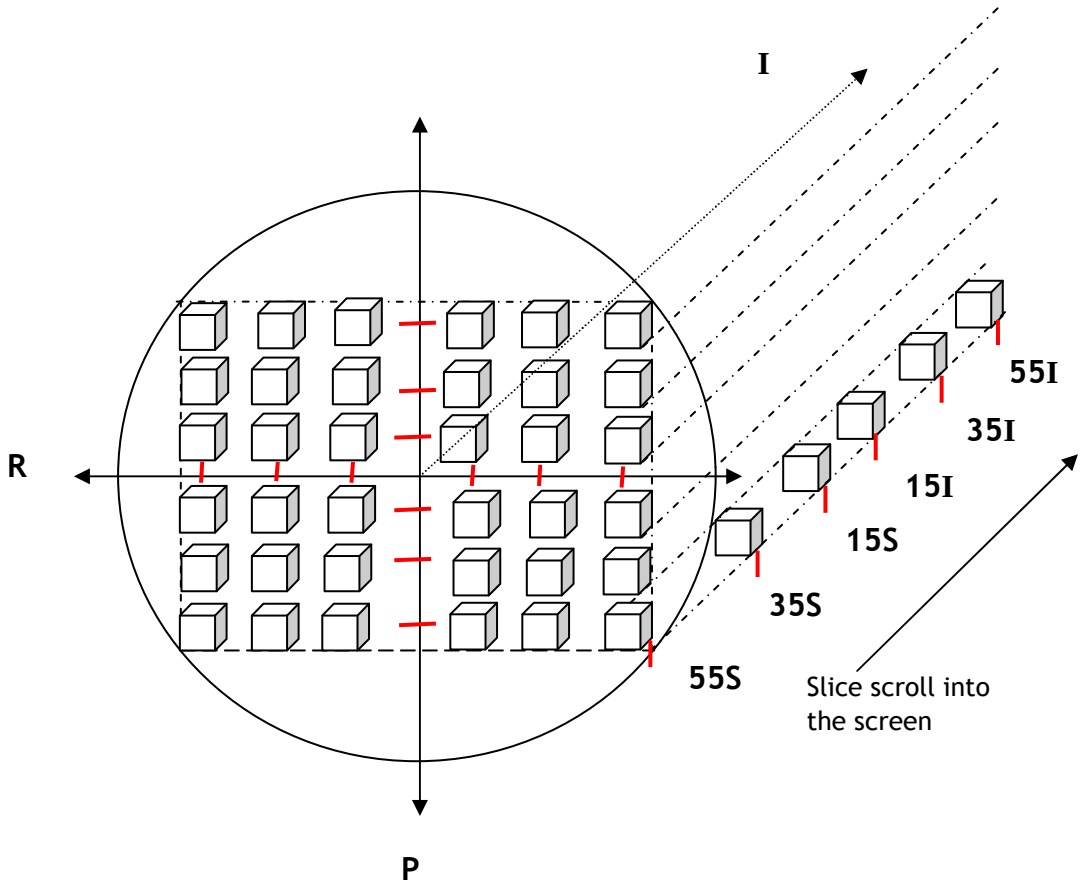

Figure 4.2: A schematic of the voxel positioning in the RL-AP plane
The six SI positions are as shown. In this diagram, acquisitions are being made in slice 55S, the topmost part of the phantom image. When all positions are covered as shown by the matrix of voxel positions, the next slice, 35S is assessed and another matrix of positions are conducted. The other voxel positions in the subsequent slices in-plane are represented by the single voxels at their respective positions. The voxels were not spaced as shown here. In fact, their positions were such that the edge of each voxel coincided with the edge of the next one in the actual acquisitions, as shown in Figure 4.3

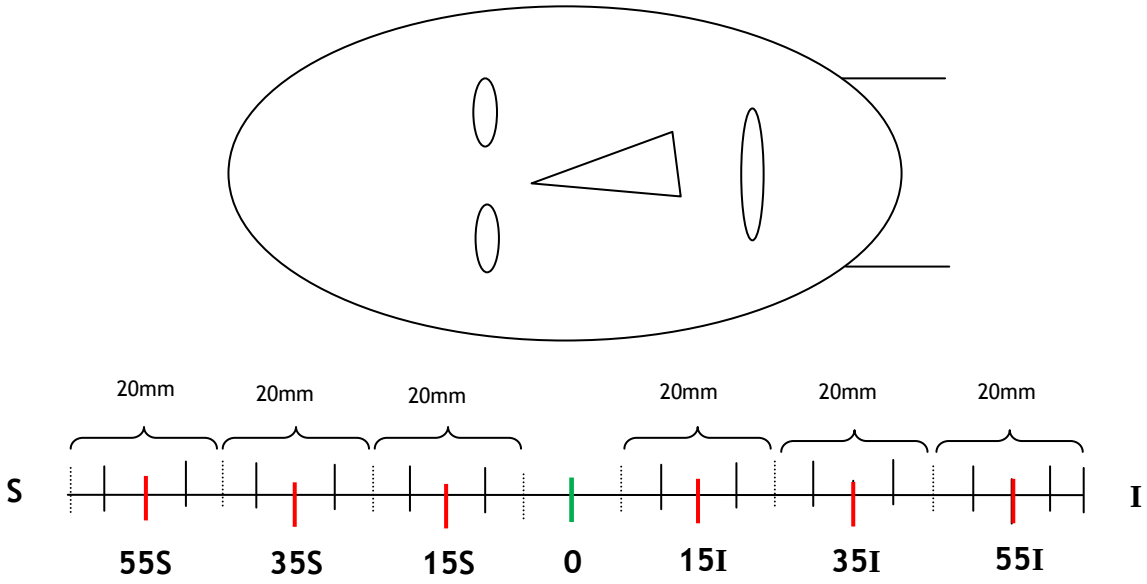

Figure 4.3: SI positions through which the RL-AP plane acquisitions were made. Position O was covered during the acquisitions along the RL axis (section 4.2.1)

4.2.5 Data Analysis

As mentioned in section 4.2, water spectra extracted from the 16/NEX part of equation 2.19 was processed as described in section 2.3.1.2. Spectra from each one of the three acquisitions per voxel position were quantified in the same way to yield the unsuppressed-water peak area, A_u. Each A_u value was corrected for transmit gain, TG (a measure of coil loading), VOI size and relaxation effects to yield a corrected value, A_{phan} as follows:

$$A_{phan} = \frac{A_u \times K_{TG}}{VOI \times [1-\exp(-TR/T_1)] \times \exp(-TE/T_2)} \qquad \text{(Eq. 4.1)}$$

where VOI is the voxel size used for the acquisition, K_{TG} is the correction factor for transmit gain given by $10^{(TG/200)}$ [149], *TR* and *TE* are respectively the repetition and echo times (for these acquisitions, *TE* = 35 ms, *TR* = 2000 ms), T_1 and T_2 are respectively the longitudinal and transverse relaxation times of water at room temperature (where T_1 = 3.3 s and T_2 = 2.5 s [1]). The

transmitter gain value, TG in decibel units is provided on the scanner console during the acquisition, and is subsequently stored in the MRS header file.

A_{phan} in equation 4.1 is the corrected water signal area acquired from the phantom. It was the mean of the three measurements of A_{phan} at each voxel position that was used for the RF field maps along the principal axes (section 4.2.6). The mean for A_{phan} was however not calculated in the case of the data obtained in section 4.2.4 as the measurements were not repeated.

4.2.6 Derivation of Sensitivity Maps

To deduce the sensitivity maps along each one of the principal RL, AP and SI axes, a polynomial fit was performed on a plot of the mean water peak area, A_{phan} against the voxel positions in the respective axes. The equation of the best polynomial fit was then chosen as the model describing the sensitivity map of the receiver coil along that axis.

To deduce the sensitivity map in the RL-AP plane along the SI axis, for each SI position (or slice), a 3-dimensional space was defined in MATLAB (version 7.8.0.347, R2009a) and a surface plot of the water peak area, A_{phan} against the voxel positions in the RL-AP plane was obtained. Polynomial fits along the RL and AP axes were performed, and the equation of the best polynomial fit was chosen as the model describing the sensitivity map of the coil within that slice.

4.3 Results and Discussion

4.3.1 RF Field Maps along the Principal Axes of the RF Coil

Figure 4.4 shows the sensitivity maps of the receiver coil along the RL, AP and SI axes using the unsuppressed-water signal. Water signal intensities recorded at voxel position –55 mm from the isocentre along each one of the RL and SI axes were far underestimated compared to the rest of the data; the reason for this observation was unclear. Their inclusion in the plots gave poor polynomial

fits to the data (Appendix 4.1). They were therefore regarded as outliers and subsequently removed from the plot to give better fits as shown in Figure 4.4. However, in both planes, this exclusion does not create any gap that was not covered by the voxel. This is because neighbouring voxel positions were already overlapping by 5 mm and so taking out one point between any two points will make the voxel edges at the remaining two points to coincide.

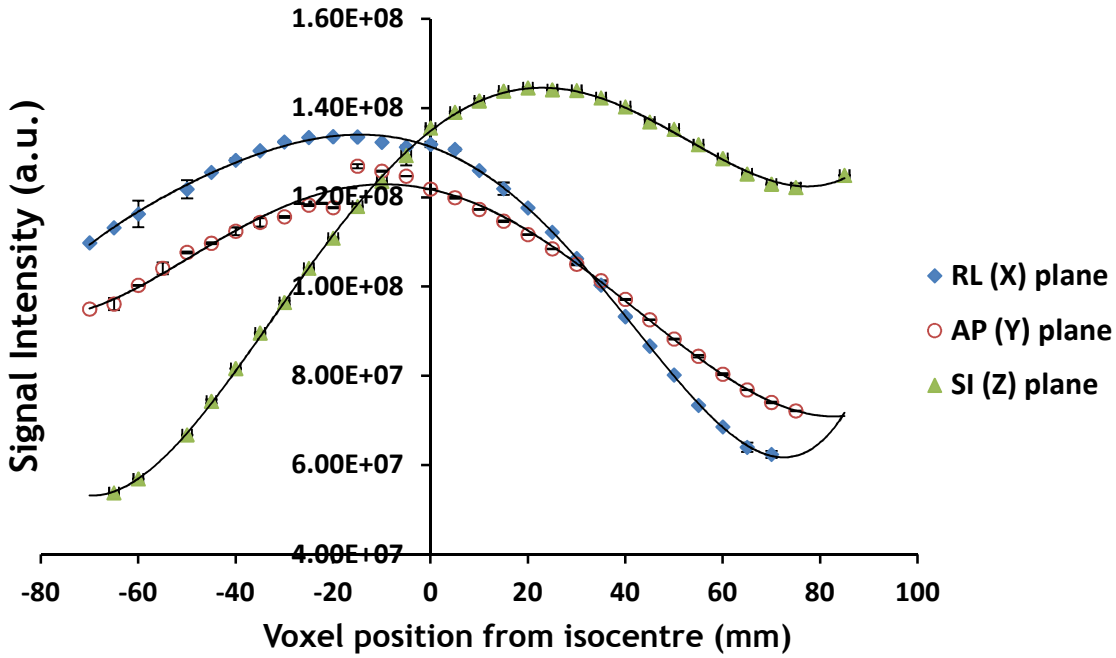

Figure 4.4: RF field maps in the RL, AP and SI planes
Error bars are ±standard deviations of the mean of three measurements at each voxel position

No such variations of over 180 % in signal intensity from the isocentre of the phased-array head coil (Figure 4.4) have been reported in the MRS literature. The sensitivity maps along the RL, AP and SI axes were best fit with polynomial functions of the following forms:

$$RL_{-70:70}(y_0, z_0) = Ax^5 + Bx^4 + Cx^3 + Dx^2 + Ex + F \quad \text{(Eq. 4.2)}$$

$$AP_{-70:75}(x_0, z_0) = Ay^5 + By^4 + Cy^3 + Dy^2 + Ey + F \quad \text{(Eq. 4.3)}$$

$$SI_{-65:85}(x_0, y_0) = Az^4 + Bz^3 + Cz^2 + Dz + E \quad \text{(Eq. 4.4)}$$

where $SI_{-65:85}(x_0, y_0)$ means signal intensities at voxel positions between -65 mm (or 65I) and 85 mm (or 85S) from the coil centre along the SI axis, while the voxel coordinates in the RL and AP were kept constant at 0 mm, represented respectively by x_0 and y_0, etc. The variables x, y and z in each equation are the voxel positions in the RL, AP and SI planes, respectively. The constants A, B, C,…, F are the coefficients of the polynomial fits given in Table 4.1. The RL and AP data were both best fit to fifth-degree, whereas the SI data was best fit to fourth-degree polynomials.

Axis	Coefficient of polynomial fit					
	A	B	C	D	E	F
RL	0.01	1.11	-43.45	-14749	-388472	1.00e8
AP	-1.90e-3	0.95	27.06	-12225	-235667	1.00e8
SI	1.72	-70.74	-17919	850716	1.00e8	0

Table 4.1: Values of the coefficients of the polynomial fits to the RF sensitivity maps along the principal axes of the receiver coil

4.3.2 Inter-slice RF Field Maps along the SI Axis of the RF Coil

The spatial variation of the sensitivity of the receiver coil is represented by the field maps shown in Figures 4.5-10. The 3D plots are presented in order: the topmost slice at the superior end (i.e. 55S) is shown first (Figure 4.5), followed by the intermediate slices down to the bottommost slice at the inferior end (i.e. 55I) shown in Figure 4.10. This order matches with *in vivo* anatomical slices taken from the top of the head down to the neck; thus covering the entire volume of the receiver coil.

Due to the spherical shape of the phantom, fewer voxel positions were possible at the extreme ends (i.e. 55S and 55I). For this reason, the data collected in those slices were fewer compared to the data from the intermediate slices. Therefore, slices 55S and 55I were each best fit to fourth-degree whereas slices 35S, 15S, 15I and 35I were best fit to fifth-degree polynomial functions. The

generic polynomial equation describing the RF maps of all the slices is of the form as given by equation 4.5. The coefficients of the polynomial fits are represented by A, B, C,…, U, the values of which are listed in Table 4.2.

The lengths of the sides of the voxel used for these acquisitions were 20 x 20 x 20 mm^3. This means that if the centre of the voxel is placed at 55S, it will extend 10 mm above and 10 mm below this point. Therefore, in order to deduce the RF sensitivity maps using these standard equations, it is appropriate to describe the signal sensitivity profile in terms of this possible range of voxel positions. Hence, the sensitivity map for slice 55S will be denoted by $SI_{45:65}(x, y)$. In this notation, 45:65 is the length of the voxel extending 10 mm below and 10 mm above 55S; this range means that the polynomial function, $SI_{45:65}(x, y)$ is appropriate for any *in vivo* voxel whose SI coordinate lies anywhere between 45 and 65 mm; and (x, y) is the corresponding voxel coordinates in the (RL, AP) plane at any SI position (i.e. within any slice). All the polynomial equations have therefore been expressed in the same notation as $SI_{45:65}(x, y)$.

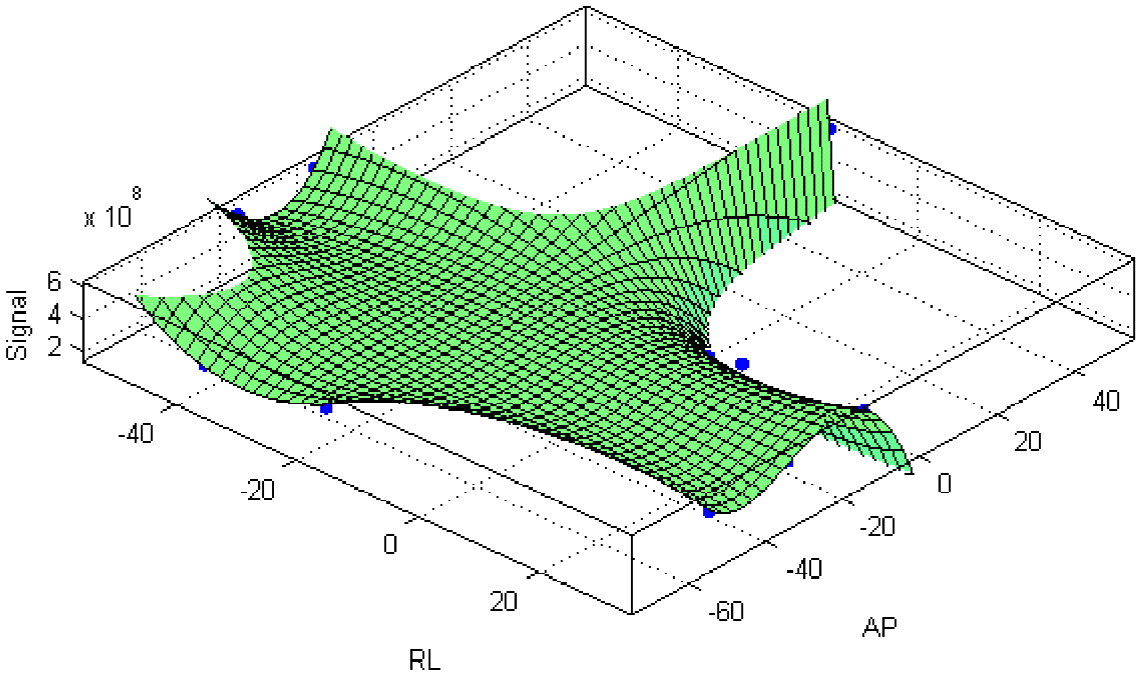

Figure 4.5: RF Field map of slice 55S

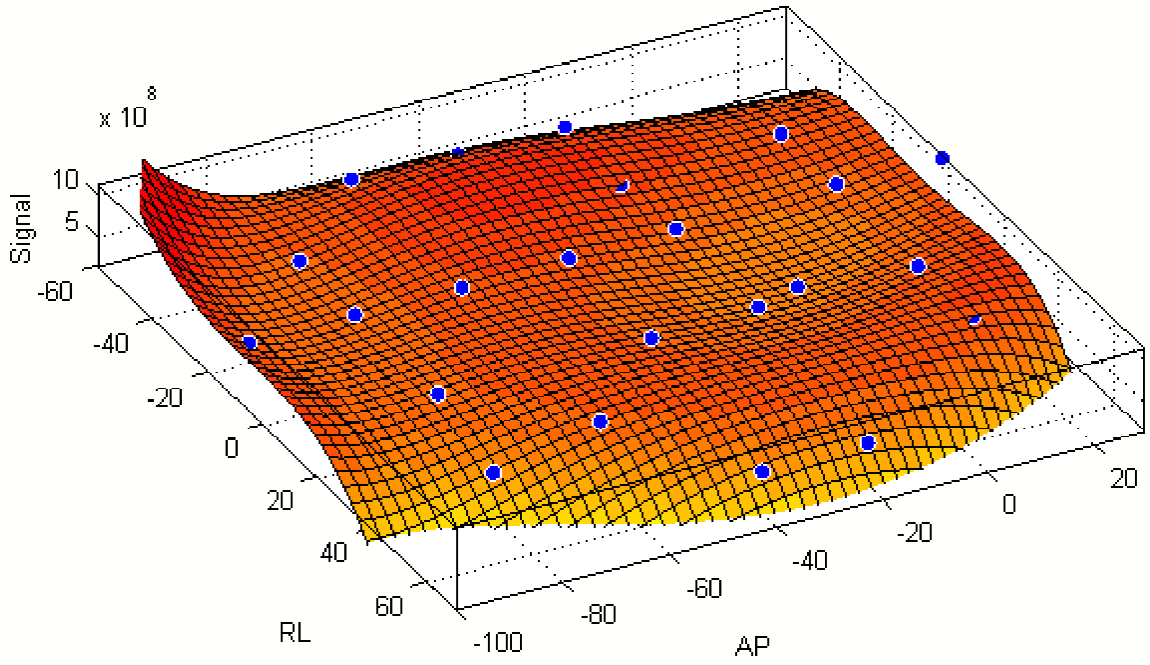

Figure 4.6: RF Field map of slice 35S

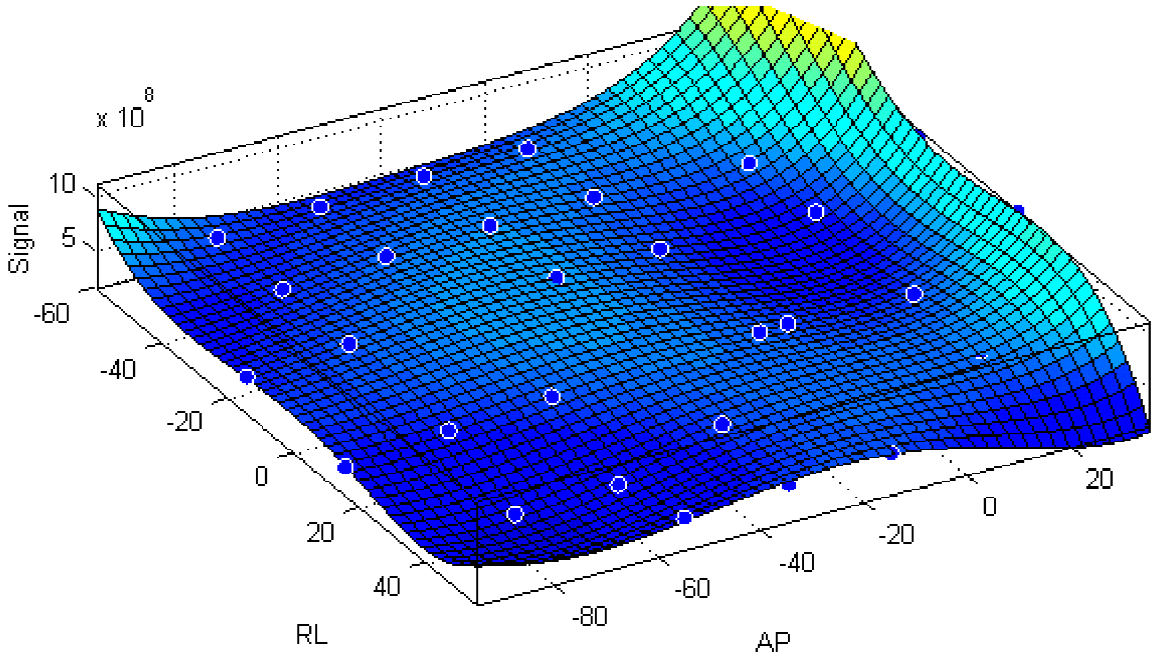

Figure 4.7: RF Field map of slice 15S

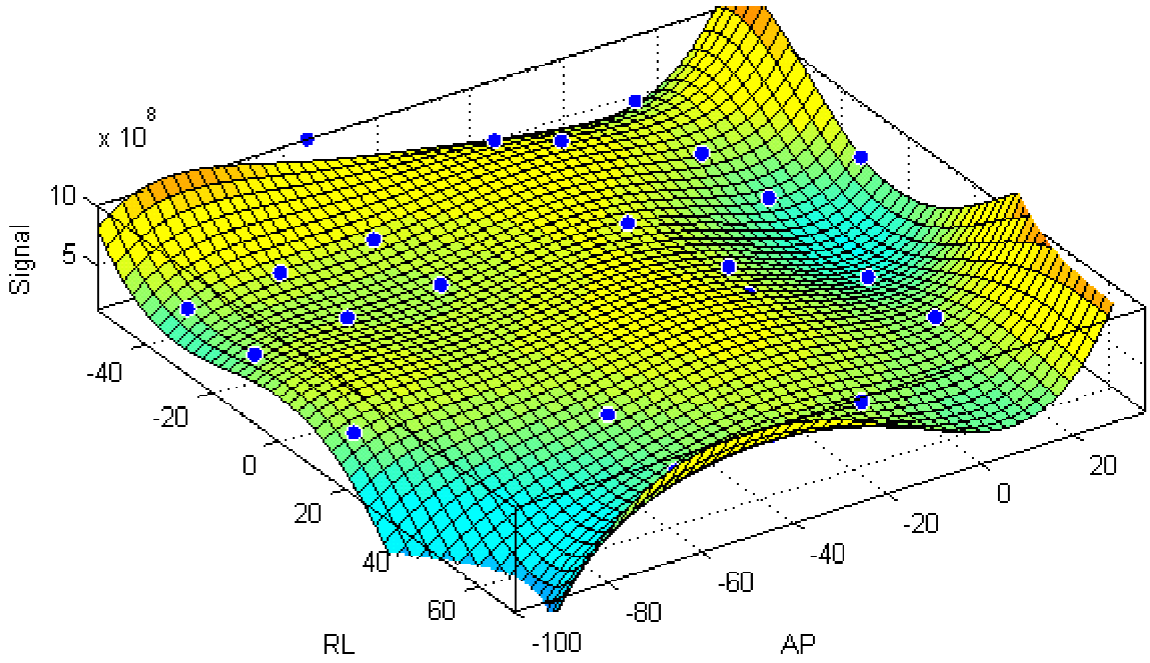

Figure 4.8: RF Field map of slice 15I

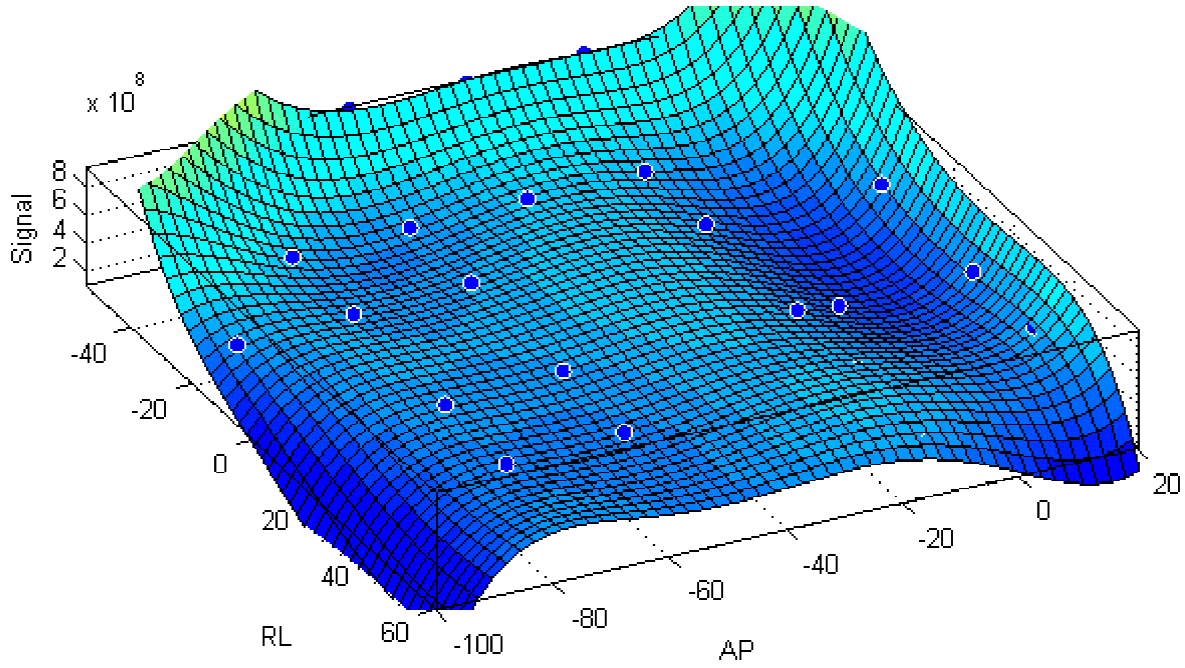

Figure 4.9: RF Field map of slice 35I

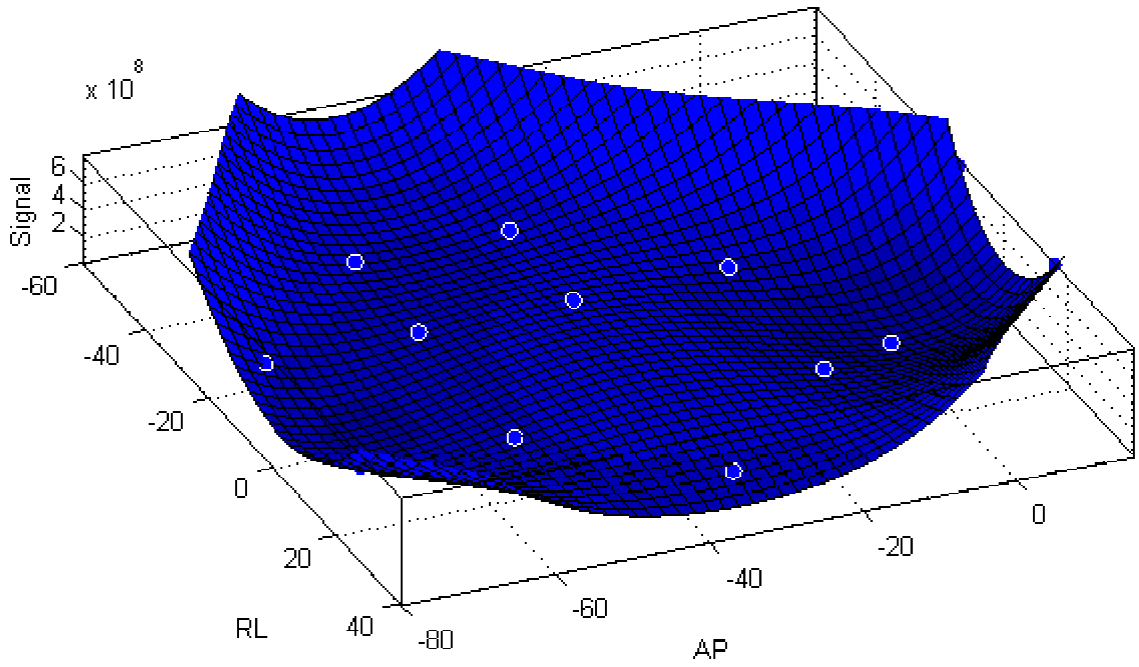

Figure 4.10: RF Field map of slice 55I

Slice	Coefficient of polynomial fit																			
	A	B	C	D	E	F	G	H	I	J	K	L	M	N	O	P	Q	R	S	T	U
55S	1.70e8	-2.56e7	-3.58e7	2.85e5	-2.26e6	-1.03e6	5475	1.61e4	-6.38e4	-8980	6.29	154.90	204	-581.30	3.53	0	0	0	0	0	0
35S	3.85e8	2.00e6	2.74e6	3.82e5	1.90e5	2.81e5	-1862	-1769	-333	154.10	-141	-95.34	-180.40	-92.04	-85.59	0.10	-1.14	-1.83	-1.11	-0.71	-0.65
15S	4.38e8	4.44e6	-4.88e6	1.42e5	1.27e5	2.29e5	-3552	5595	-2579	8341	-35.04	-111.30	-31.44	-45.52	81.44	0.40	-1.36	-0.91	-0.51	-0.12	0.25
15I	4.29e8	1.07e6	-1.39e7	1.71e5	2637	-1.04e5	-3161	8353	2611	8594	-60.11	6.90	139.60	49.45	170.10	0.94	-1.63	-0.44	1.24	0.23	0.87
35I	2.03e8	1.55e6	-8.06e6	1.38e5	-5660	8.05e5	-85.29	7320	-9696	3.65e4	0.66	-101.70	10.02	-254.10	503.80	-0.87	-1.17	-1.35	-0.54	-1.73	2.29
55I	9.53e7	1.41e6	-6.90e5	8.11e5	2.69e4	9.55e5	-6520	4.66e4	2025	2.64e4	37.21	-109.90	576	30.68	185.20	0	0	0	0	0	0

Table 4.2: Values of the coefficients of the polynomial fits to the inter-slice spatial RF sensitivity maps of the receiver coil

The general polynomial equation describing the RF map of any given slice is given by:

$$SI_{a:b}(x, y) = A + Bx + Cy + Dx^2 + Exy + Fy^2 + Gx^3 + Hx^2y + Ixy^2 + Jy^3 + Kx^4 + Lx^3y + Mx^2y^2 + Nxy^3 + Oy^4 + Px^5 + Qx^4y + Rx^3y^2 + Sx^2y^3 + Txy^4 + Uy^5 \quad \text{(Eqn 4.5)}$$

where $SI_{a:b}(x, y)$ is the calculated unsuppressed-water peak area, **a:b** is the range of possible voxel positions within an *in vivo* slice, x and y are respectively the RL and AP coordinates of the *in vivo* voxel, A, B, …, U are the coefficients of the polynomial equation (Table 4.2). Each slice was 20 mm thick, and so the corresponding **a:b** values for slices 55S, 35S, 15S, 15I, 35I and 55I are 45:65, 25:45, 5:25, -5:-25, -25:-45, and -45:-65, respectively. The appropriate equation is chosen by checking to see which **a:b** range its SI coordinate falls within.

4.4 Use of RF Field Maps in Cerebral Water Quantification

Polynomial equations describing a wide range of voxel positions within the eight-channel head coil have now been deduced (equations 4.2-5). Using equation 4.5 in particular, which is a function of voxel position in 3D, the coordinates of any *in vivo* spectral acquisition can be substituted in place of the variables x, y, and z which respectively represent the RL, AP and SI coordinates. For the human head, this substitution utilises the SI coordinate as a guide to select the appropriate slice coefficients (Table 4.2) that define the *in vivo* voxel position. The coefficients (representing the *in vivo* RL and AP coordinates) are then substituted into equation 4.5. When the substitution is done, the value of $SI_{a:b}(x, y)$ obtained becomes a theoretically deduced spectral peak area for the unsuppressed-water. Since this area is generated from the polynomial fits, it shall be represented by A_{fit} in equation 6.1, where it will be used as a reference signal in the absolute quantification of cerebral water content.

4.5 Summary and Conclusions

In this chapter, the spatial non-uniform response of a typical receiver coil has been investigated using the unsuppressed-water signal as a reference. For the first time, generic signal sensitivity maps have been deduced for a wide range of voxel positions in 3-dimensional space within the phased-array head coil. Polynomial fits to the sensitivity maps were performed to derive standard mathematical equations that represented the signal response of the RF coil in 3-dimensional space. Using these equations, which were functions of voxel position, a novel method was suggested to calculate a signal value from any of the fits that best described a given *in vivo* voxel position. It was concluded that this theoretically derived signal area could be used as a reference signal in the absolute quantification of cerebral water. Thus, this work also showed the NMR response of water with varying voxel positions within the head coil, *in vitro*.

Such a study has also been conducted *in vivo* in chapter 6, but with limited voxel positions as it is impractical to investigate a wide range of voxel positions in any single volunteer.

Chapter 5: Corrections for Relaxation and Partial Volume Effects

5.1 Overview and Objectives

In section 1.1.3, it was mentioned that in MRS, voxel with straight edges are used to acquire spectra from brain regions that are usually small and curved. The usual practice therefore is to use relatively large voxel sizes which would, in most cases, inevitably encompass some fraction of cerebrospinal fluid (CSF). A method of removing the CSF fraction from the MRS voxel is thus described and implemented in this chapter.

Secondly, even when the voxel grey/white matter fraction has been obtained after CSF correction, the MRS signal still suffers from some losses due to relaxation effects. This usually arises due to the *TE* and *TR* times used for the spectral acquisition. Absolute quantification of cerebral water content would therefore require a correction factor accounting for relaxation effects in brain tissue. The absolute quantification of metabolite concentrations on the other hand would require correction factors for the relaxation effects in both brain tissue and the metabolites. These correction factors are normally obtained from equations involving the use of the T_1 and T_2 relaxation times of brain tissue water and the metabolites measured from the same brain regions from which the water and metabolite signals have been acquired. Thus, in order to correct for relaxation effects in the MRS signals in this thesis, the T_1 and T_2 relaxation times of brain tissue water and the metabolites were measured in the specific brain regions in which the MRS voxels were placed in the various studies (chapters 6 and 7).

Cerebral water content was quantified in chapter 6 in five brain regions: frontal white matter (WM), parietal WM, occipitoparietal white/grey matter and the hippocampus. In chapter 7, water content and metabolite

concentrations were quantified in the prefrontal grey matter and hippocampal brain regions. The T_1 and T_2 relaxation times of brain tissue were therefore measured for all these brain regions in this chapter; cerebral metabolite T_1 and T_2 relaxation times were also measured in the prefrontal grey matter and hippocampal brain regions. These measured relaxation times were then used in the calculation of the correction factors for the correction of relaxation effects in MRS measured water and metabolite signals from these regions.

Before presenting the experiments for the above correction factors, it is necessary to provide some background to these relaxation and partial volume effects. These are discussed in subsections 5.1.1-2.

5.1.1 NMR Relaxation Effects

Signal attenuation occurs due to relaxation processes (section 2.1.2). For a given metabolite, relaxation effects can be kept to the minimum if *TE* ≈ 0 ms and *TR* ≈ 5 x the T_1 of the signal of interest. Ideally, a short *TE* and a long *TR* (theoretically *TE* = 0, *TR* = ∞) should be used for minimal signal losses due to relaxation effects [31]. However, since gradients must be applied to define the voxel, *TE* can never be zero, and because the sequence has to be repeated many times, a *TR* of infinity is not practical. Instead, the MR spectrum from a typical acquisition consists of various metabolite signals collected together, and so the *TE* and *TR* are chosen depending on the main metabolites of interest, which still differ substantially in T_1 and T_2 relaxation times. The measured MRS signal is therefore always affected by saturation (T_1) and relaxation (T_2) effects. For instance, in normal tissue, a *TR* of 2000 ms will cause only a 50 % recovery (between repetitions) of the longitudinal magnetisation of the metabolites; a *TR* of 7000 ms will enable recovery of up to 99 % of the longitudinal magnetisation [1] but will increase acquisition time significantly. At 1.5 T, a *TE* of 30 ms will cause 7-14 % signal losses due to T_2 relaxation effects in metabolites with long T_2 relaxation times (i.e. NAA, Cr and Cho with T_2 range of 200-400 ms); metabolites with short T_2 relaxation times will suffer more than 14 % signal losses.

Absolute quantification of metabolites without correction for T_1 and/or T_2 relaxation effects may therefore significantly underestimate and/or overestimate some metabolites. For instance, in this thesis, metabolite and water spectra have been acquired with *TE*/*TR* = 144/1500 ms (chapter 6), *TE*/*TR* = 35/2000 ms and *TE*/*TR* = 144/2000 ms (chapter 7). These spectra would therefore have suffered at least 50 % and 14 % signal losses due to T_1 and T_2 relaxation effects, respectively. Absolute quantification of either cerebral water and/or metabolites will therefore require some corrections for these T_1 and T_2 relaxation effects in their respective spectra. These relaxation effects can be corrected by performing separate measurements of the T_1 and T_2 relaxation times of brain tissue and the metabolites of interest in the specific brain regions that correspond to the MRS voxel positions.

5.1.2 Partial Recovery of Longitudinal Magnetisation of Water

In the measurement of cerebral water content, particularly, in this thesis, the fully recovered water signal was not acquired; the CHESS water-suppression module was not also turned OFF. However, spectral acquisition with CHESS turned ON was not a major issue regarding its effect on the amount of unsuppressed-water signal collected. This is because the scanner still acquired some quantifiable unsuppressed-water lines prior to the PRESS localisation sequence (section 2.3.1.3). In fact, the only issue that could affect the amount of unsuppressed-water signal collected was the *TE*/*TR* for the acquisitions.

In order to acquire the maximum water signal, it is not possible to use the expected *TE* = 0 ms and *TR* = 5 xT_1 of water (section 5.1.1) for the acquisitions. If the T_1 of water is approximately 3000 ms, then that will mean that the ideal *TR* should be 15000 ms. Since these theoretical conditions cannot be met for reasons mentioned in section 5.1.1, *TE* values of 35 and 144 ms, and *TR* values of 1500 ms and 2000 ms were used in this thesis to acquire the water signal that was quantified to yield cerebral water content.

It should be emphasised that the water signal area was quantified from a water-suppressed acquisition (i.e. originally metabolite data). For this reason, using the shortest possible *TE* on the scanner should not cause significant T_2 relaxation effects in both the water and metabolite peaks. However, using the longest *TR* possible in consideration for the collection of a greater amount of the water signal would lead to significant decay of the metabolite signals. In order to have a fair balance in the amounts of water and metabolite signals, therefore, the above *TE*/*TR* values were used. However, that still required correction of the metabolite signals for T_1 and T_2 relaxation effects. The water signal on the other hand would have suffered more losses due to T_1 than it would have due to T_2 relaxation effects. With *TR* = 1500 ms and 2000 ms, only about 39.3 % and 48.7 %, respectively, of the longitudinal magnetisation, M_z of water would have recovered. Meanwhile, it is the amount of M_z tipped into the xy-plane that determines the amount of NMR signal recorded. This therefore means that only a fraction of the water signal would have been used to derive the unsuppressed-water peak area for the quantification of cerebral water content. Therefore, whereas the T_1 correction involved an extra consideration for this partial recovery, T_2 correction of the water peak area was done in the same way as was done for the metabolite spectra.

This additional consideration in correcting the water signal for T_1 relaxation effects involved the calculation of a partial recovery constant, k_{pr}. This constant is defined as a ratio of the unsuppressed-water signal area obtained from the optimum *TE*/*TR* to the suppressed-water signal area obtained from a standard *TE*/*TR*. In theory, the optimum *TE*/*TR* for acquiring the water signal should be 0/15000 ms, respectively. However, the minimum *TE* on the MR scanner used for acquisitions in this thesis was 23 ms. Thus, k_{pr} was defined as:

$$k_{pr} = \frac{A_{TE23\_TR15000}}{A_{TE\ acq\_TR\ acq}} \qquad \text{(Eq. 5.1)}$$

where $A_{TE23\_TR15000}$ is the water peak area obtained from a CHESS OFF acquisition with the optimum *TE*/*TR* of 23/15000 ms, and $A_{TE\ acq\_TR\ acq}$ is the

water peak area obtained from a standard CHESS ON acquisition (i.e. those of this thesis for water quantification).

The constant, k_{pr} represents the lost water signal fraction and so when multiplied by the quantified water signal area (acquired using the above *TR* values), a corrected signal area is obtained. This corrected peak area can be considered to be approximately equal to the total water signal acquired with *TR* = 5 x T_1 of water. The k_{pr} constant also accounts for T_1 relaxation effects, and so there is no need to correct the water signal for T_1 relaxation effects as long as the k_{pr} correction factor is used. However, since *TE* was not equal to 0 ms, the k_{pr}-corrected signal area will then be corrected for the minimal T_2 relaxation effects left.

5.1.3 Partial Volume Effect

The voxel may contain CSF, and it may contain both grey and white matter. CSF contains no metabolites (except lactate and glucose); thus any metabolite peaks that are observed in the spectrum must be located in the brain parenchyma (i.e. either grey or white matter) [1, 144]. It is the mean concentration in the parenchyma that is required and not the mean in the whole voxel. If the voxel CSF fraction is not corrected for, the metabolite spectrum will be contaminated by signal originating from CSF; and the final metabolite concentrations will be underestimated [144]. For instance, for the same voxel size, metabolite signal intensities from a voxel containing 50 % tissue and 50 % CSF would be half of that acquired from a voxel containing 100 % tissue [78].

Three approaches of correcting for partial volume effects are reported in the literature: correction with grey matter fraction, bi-exponential fitting using multiecho dataset, and segmentation of a structural MR image.

In the grey matter fraction technique [157-159], signals are acquired using a series of voxels with known, differing grey matter fractions. In a plot of signal

intensity against grey matter fraction, the y-axis intercepts at grey matter fractions of 0 and 1 give the amounts of signal arising from white and grey matter respectively. The disadvantage of this technique is that it prolongs the acquisition time, and also the estimation of the fraction of grey matter in the voxel is likely to be subjective. Reproducibility of the measurements may therefore not be good.

The bi-exponential fitting technique distinguishes between signal from CSF and that from tissue water [144, 160]. In its implementation, a multiecho spectral acquisition is performed and a bi-exponential fit of the T_2-decay can reveal long-T_2 and short-T_2 components. The long-T_2 decay is attributable to CSF and thus gives a measure of the amount of CSF in the voxel; the short-T_2 component is attributable to water trapped between myelin sheaths in brain tissue [58, 160]. However, the T_2-decay in healthy brain is reported to exhibit three distinct pools of water: CSF with $T_2 > 1000$ ms, intra/extra-cellular water with 80 ms $< T_2 <$ 200 ms, and myelin water with 10 ms $< T_2 <$ 50 ms [59]. The number of water pools could even be increased in pathology [161, 162]. To correctly measure the T_2-decay of water, considerations to these 'pool effects' will have to be taken into account; a full water T_2-decay will also have to be acquired and fit accurately. The fitting routine usually employs a non-negative least squares fitting method [59, 154, 163], the accuracy of which depends on the number of plotted points. At least twelve time points yield reasonable goodness of fits [54]; this therefore means more acquisitions. Consequently, the measurement time may be clinically unacceptable [58], and could be affected by motion artefacts.

For the imaging-based CSF correction technique, a high resolution structural 3D MR image (usually T_1-weighted) is used to determine the proportions of CSF, grey and white matter in the voxel. The T_1-weighting gives CSF a low pixel intensity value relative to brain tissue. An image segmentation routine is then performed on the 3D image to segment it into CSF, grey and white matter fractions, and also return the corresponding mean probabilities over all pixels for each segment within the voxel. The average probability for CSF serves as

the estimate for the CSF fraction in the voxel [144]. This technique practically adds about 8-10 minutes to the main MRS acquisition, but the time could be reduced down to 3-5 minutes by using an SPGR sequence, which does not use the inversion pulse (IR). Resolution obtained with this non-IR sequence is however about 35 % lower compared to that obtained with the IR sequence.

In any case, the acquisition time with the imaging-based partial volume correction is not as long as the times for the other two techniques. Moreover, subject displacements between the MRS and 3D MRI acquisitions can be corrected for by co-registration of the 3D MRI to the 2D MRI used for planning the MRS voxel [164]. The technique has fewer potential error sources and is therefore more reproducible and reliable. It was therefore the method of choice for correction of partial volume effects in this thesis (in chapters 6 and 7).

5.1.4 Objectives

Since the MRS data would always be affected by the above sources of error, the work presented in this chapter was aimed to:

1. Measure the T_1 and T_2 relaxation times of brain tissue in the frontal, parietal, occipital and hippocampal regions (the reason for these regions was discussed in section 5.1);
2. Measure the T_1 and T_2 relaxation times of the cerebral metabolites and water in the frontal and hippocampal brain regions (section 5.1 explains the reason for these regions);
3. Develop a method for correcting the partially recovered *in vivo* unsuppressed-water signal for fractional signal losses;
4. Develop and demonstrate a method for correcting the MRS voxel for partial volume effects.

From these experiments, correction factors could then be obtained to correct the acquired MR spectra for the respective errors.

5.2 Methods

In the order of the study objectives (section 5.1.4), this section describes the methods for measuring the relaxation times of brain tissue (section 5.2.1) and the MR spectra (section 5.2.2); the procedures for obtaining k_{pr} and correcting for partial volume effects are also presented in sections 5.2.3 and 5.2.4, respectively.

5.2.1 Measurement of NMR Relaxation Times in the Brain

Five subsections are presented in this section: section 5.2.1.1 describes the characteristics of the study volunteers, section 5.2.1.2 describes the MRI protocol for the acquisition of structural MR images, sections 5.2.1.3 and 5.2.1.4 present the imaging methods for recording the various signals to be used in the estimation of T_1 and T_2 of brain tissue, and section 5.2.1.5 explains the selection of the various brain regions of interest, and estimation of the T_1 and T_2 relaxation times for these brain regions.

5.2.1.1 Subjects

Four subjects (2 males, 2 females) were studied for T_1 measurements; another group of four subjects (3 males, 1 female) was studied for T_2 measurements. The mean ages of subjects in the T_1 and T_2 studies were 32.0 and 32.5 years, with ranges from 23 to 51 and 29 to 38 years, respectively.

5.2.1.2 MR Imaging

All images were acquired using the spin echo (SE) pulse sequence (section 2.1.3.2). Axial slices covering the whole brain were planned along the hippocampal angle. Each slice was 3 mm thick without slice gaps; and a matrix of 256 x 128 pixels was used to give a reasonable compromise between image

resolution and total experimental time. A field of view (FOV) of 25.6 x 25.6 cm^2 was selected to cover the entire axial image, including the hippocampi. For each subject, a high resolution T_1-weighted 3D image of the whole brain was also acquired using an axial slab along the hippocampus. This high resolution axial 3D image gave a better grey/white matter tissue contrast than the SE axial images. These high-resolution 3D MR images served as references during ROI selection in the SE images by co-registration of each SE image to the 3D image. Thus the SE images were all corrected for rotational errors, and were now in the same orientation after co-registration to the corresponding 3D image. The advantage of using axial slices for this study is that in all acquisitions, they provide access to consecutive slices that contain sufficient grey and white matter for the placement of regions of interest (ROIs). Measurements of the T_1 and T_2 relaxation times were performed in separate examination sessions.

5.2.1.3 Imaging for the Estimation of T_1 Relaxation Times

T_1 measurements were carried out using a saturation recovery method with a variable *TR* spin-echo imaging sequence. A constant echo time (*TE*) of 11.0 ms was maintained, while axial images were acquired at eight successive *TR* times of 200, 350, 550, 750, 1000, 1500, 2000 and 4000 ms.

5.2.1.4 Imaging for the Estimation of T_2 Relaxation Times

For the T_2 measurements, a multi spin-echo pulse sequence was used. A constant *TR* value of 3000 ms was maintained and twelve T_2-weighted images were acquired using the following *TE* values: 16, 25, 30, 32, 48, 50, 60, 64, 75, 90, 100 and 120 ms. The multi spin-echo pulse sequence on the GE MR scanner used for the measurements produces images at four echo times for each user-selected *TE* value. The *TE* values of these generated images are multiples of the user-selected *TE* value set. For these T_2 measurements, three *TE* values were selected: 16, 25 and 30 ms. Thus *TE* = 16 ms produced images at *TE* times

of 16, 32, 48 and 64 ms. The *TE* values of 25 and 30 ms also produced four images each, resulting in twelve image sets at the above *TE* times.

5.2.1.5 ROI Selection and Estimation of Relaxation Times

In the T_1 and T_2 images acquired in sections 5.2.1.3 and 5.2.1.4 respectively, four anatomical sites were chosen in each hemisphere, plus one frontal region of the brain. This resulted in a total of nine ROIs per subject, as shown in Figures 5.1a and 5.1b. Care was taken in selecting the ROIs, which did not include the ventricles or extra-axial CSF. The shapes of the ROIs were either circular, rectangular or freehand-drawn (in the Image-J software, version 1.46r) depending on what best fit the target area. In selecting the ROIs in a given image, reference was made to its corresponding high resolution 3D axial image in the same slice in order to verify that each ROI selection contained the required brain tissue.

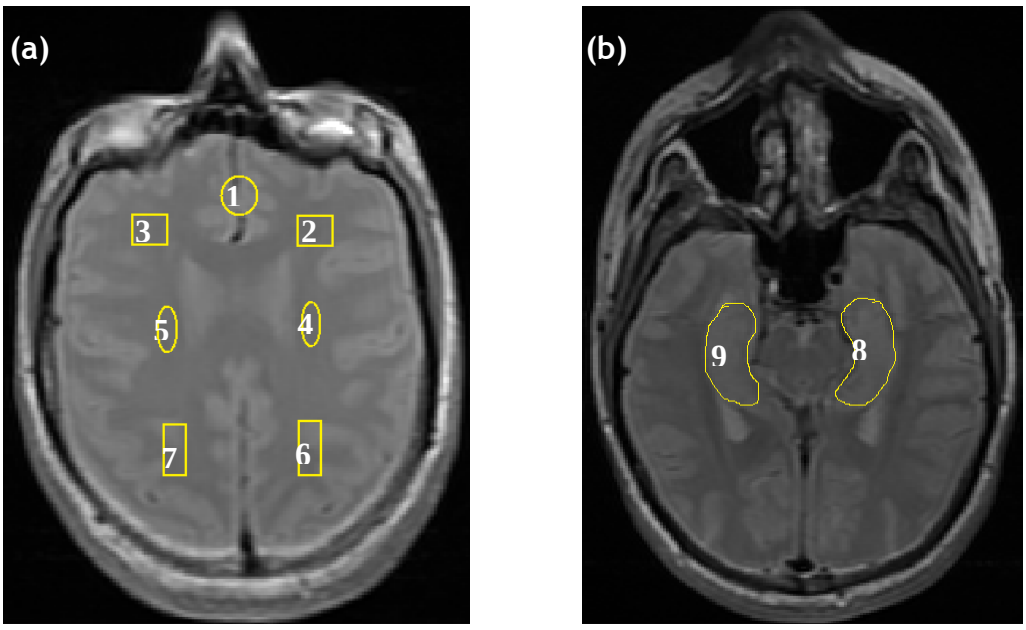

Figure 5.1: T_2-weighted MRI scan of an axial slice through the prefrontal brain region (a) and the bilateral hippocampi (b) in a healthy volunteer.
The 3 mm thick slices shown in figures (a) and (b) are typical of those chosen for analysis in all subjects. The ROIs are indicated by a circle, squares, ovals, rectangles and freehand-drawn selections, all in yellow. Numbers correspond to brain structures listed in Table 5.1 and voxel positions in chapters 6 and 7

Estimates of the brain tissue T_1 relaxation times were obtained from a nonlinear least square monoexponential fit of the signal intensities measured (from ROIs 1 to 9 in Figures 5.1a-b) at their respective *TR* values. The fitting method solved equation 2.10 for T_1.

Estimates of the brain tissue T_2 relaxation times were obtained from a nonlinear least square monoexponential fit of the mean pixel intensity values (measured from ROIs 1 to 9 in Figures 5.1a-b) at their corresponding *TE* times. The fitting method solved equation 2.11 for T_2.

Curve fitting for the estimation of both T_1 and T_2 relaxation times were performed using the curve fitting toolbox in MATLAB (version 7.8.0.347, R2009a).

5.2.2 Measurement of the NMR Relaxation Times of Cerebral Metabolites and Water

5.2.2.1 Subjects

A total of eighteen subjects (10 males, 8 females) were studied for T_1 and T_2 relaxation times of the metabolites and water. Volunteers were randomly assigned to four relaxation measurement experiments denoted by labels 5A-D as follows:

(5A) T_1 of the ventromedial prefrontal cortex (ROI number 1 in Figure 5.1a), involving three (1 M/2 F) volunteers aged 27-55 years (mean age = 34.3 years);
(5B) T_2 of the ventromedial prefrontal cortex, involving seven (3 M/ 4 F) volunteers aged 27-60 years (mean age = 33.4 years);
(5C) T_1 of the bilateral hippocampi (ROI numbers 8 and 9 in Figure 5.1b), involving three (2 M/1 F) volunteers aged 25-33 years (mean age = 22.3 years); and

(5D) T_2 of the bilateral hippocampi, involving five (4 M/1 F) volunteers aged 27-53 years (mean age = 34.6 years).

The sample sizes in the various experiments varied because volunteers were randomly assigned to the groups as they were being recruited. Three volunteers were studied initially in the following order of experiments: 5B, 5D, 5A, and 5C. Time was not sufficient for another batch of volunteers to be recruited and assigned to all the experiments (except for 5B and 5D) following the above order.

5.2.2.2 MR Imaging

To plan the MRS voxels, two structural scans of the brain were conducted on each subject: sagittal T_1-weighted FLAIR (*TE*/*TR*/*TI* = 9/2685/920 ms) and axial T_2-weighted FSE/propeller (*TE*/*TR* = 110/5000 ms) MRI. For the sagittal scan, 21 slices (each of thickness 4 mm) were planned along the long axes of the hippocampi. For the axial scan, 22 oblique slices (each of thickness 5 mm) parallel to, and covering, the hippocampi were planned. In both structural scans, a field of view of 24.0 x 24.0 cm^2 was chosen, with an in-plane image matrix of 512 x 512 pixels to give good image resolution. The T_2-weighted FSE/propeller also meant that images were acquired with good grey/white matter contrast.

5.2.2.3 MRS Protocol

The following MRS protocol was used for both spectral acquisitions described in sections 5.2.2.4 and 5.2.2.5. The protocol involved the acquisition of 128 averages of CHESS water-suppressed spectra from the ventromedial prefrontal grey matter (region 1 in Figure 5.1a) and the bilateral hippocampi (regions 8 and 9 in Figure 5.1b). The average voxel size on region 1 was 2.0 x 3.0 x 2.0 cm^3 while that on regions 8 and 9 was 3.5 x 1.2 x 1.0 cm^3 in the AP x LR x SI directions, respectively. For the acquisitions in regions 8 and 9, the same voxel was moved from region 8 to region 9 after recording spectra from the former.

In all acquisitions, NEX = 8 was maintained in order to make data averaging faster; so two (or 16/NEX) unsuppressed-water lines were stored.

Since these unsuppressed-water lines are acquired from the same voxel as the metabolite lines, they (i.e. both the water and metabolite signals) should be affected by the same factors such as effects of eddy currents, motion and relaxation [46-48]. Therefore, when processing the metabolite spectra from the relaxation experiments, the unsuppressed-water lines within each data set could be quantified as well. Using the same analysis procedure, it should be possible to estimate the T_1 and T_2 relaxation times for cerebral water and metabolites from the same data set.

5.2.2.4 Estimation of Metabolite and Water T_1 Relaxation Times

T_1 measurements were carried out using the saturation recovery method with a variable *TR* PRESS localisation sequence. A constant *TE* value of 23.0 ms was maintained, while single voxel spectra were acquired at six *TR* times: 1070, 1200, 1500, 2500, 3000 and 3500 ms.

For each *TR* acquisition, the two unsuppressed-water lines and metabolite spectra were quantified separately in the SAGE software package as described in sections 2.3.1.2-3. This yielded the metabolite and water spectral peak areas.

Estimates of the metabolite and water T_1 relaxation times were obtained from a nonlinear least square monoexponential fit of the measured peak areas at their respective *TR* values using equation 2.10. The solution to the fitting routine yielded the T_1 of either water or the given metabolite.

5.2.2.5 Estimation of Metabolite and Water T_2 Relaxation Times

For T_2 measurements, the PRESS localisation pulse sequence was used with a fixed *TR* value of 2000 ms. Spectra were acquired with a variable *TE* spin-echo method: 35, 85, 128, 164, 262, 326, 400 and 600 ms.

The metabolite and water signals were quantified in the same way as described in sections 2.3.1.2-3. Metabolite and water T_2 relaxation times were estimated from a nonlinear least square monoexponential fit of the measured peak area at each *TE* value. The fitting routine solved equation 2.11 for T_2 of either water or the given metabolite.

The curve fitting routines for the estimation of both T_1 and T_2 relaxation times of the MR spectra were performed using the curve fitting toolbox in MATLAB (version 7.8.0.347, R2009a).

5.2.3 Compensation for the Lost Fraction of Water Signal

In one healthy male volunteer, aged 29 years, 16 averages of CHESS water-suppressed spectra were recorded from an 8 cm^3 voxel positioned in the prefrontal grey matter brain region. The following *TE*/*TR* pairs were used in turn: 35/2000 ms, 144/2000 ms, and 144/1500 ms. NEX = 8 was used in all acquisitions.

Maintaining the same voxel position and NEX value, the CHESS water-suppression module was turned OFF and 16 averages of the fully recovered water signal was acquired using *TE*/*TR* = 23/15000 ms.

Only the two unsuppressed-water lines were quantified in both the CHESS ON and OFF acquisitions to yield the two signal areas $A_{TE\ acq\_TR\ acq}$ and $A_{TE23\_TR15000}$, respectively (as described in sections 2.3.1.2-3). The ratio of these signal areas

produced the correction factor, k_{pr} (equation 5.1) which will be used to compensate for the lost fraction of the water signal acquired from the standard CHESS ON spectral acquisitions (section 5.1.2) of chapters 6 and 7.

5.2.4 Estimation of MRS Voxel CSF Content

In this thesis correction of MRS voxels for CSF content (otherwise known as partial volume correction) involved the use of high resolution T_1-weighted 3D MR brain images of the study subjects. These images were acquired within the same exam session as the MRS acquisitions, being performed either before or after the MRS.

In this section the partial volume correction (PVC) procedure will be described and implemented. The illustration will be presented using analysis of example data from one healthy volunteer. The same correction procedure was applied for the rest of the volunteer data presented in chapters 6 and 7. The PVC method developed in this thesis can be described in six steps as follows:

1. Calculation of Starting Values from VOI coordinates

The MRS voxel is a region of interest defined in three-dimensional space. Thus, a three-coordinate space can be used to represent the three sides, LR x AP x SI of the voxel, where these sides correspond to the x, y and z axes, respectively (Figure 5.2). A voxel is normally specified in three (xyz) dimensions by three quantities: “starting values”, “centre coordinates” and “dimensions”. The starting values represent the coordinates of each corner of the voxel and the dimensions are the lengths of each side of the voxel; the centre coordinates define the centre of the voxel. These three quantities are related such that when any two of them is known, the third can be calculated.

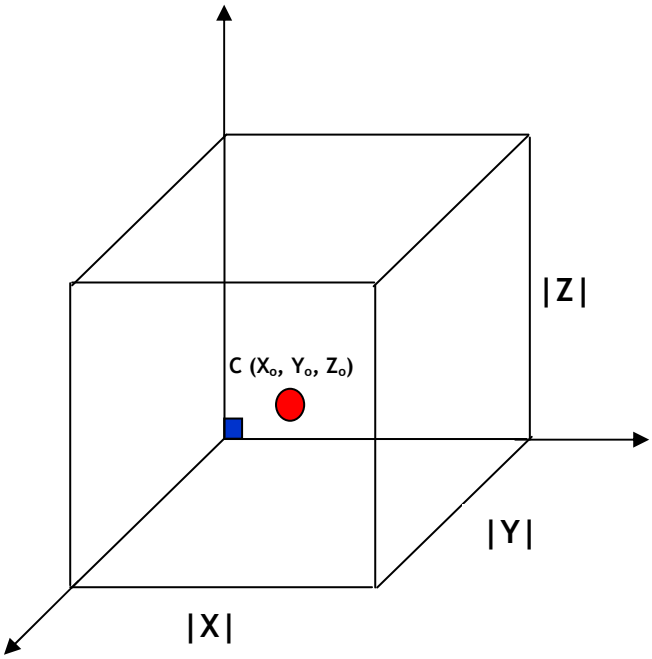

Figure 5.2: A three-dimensional representation of the MRS voxel
The small blue square represents the starting point for the RL side (along the x-axis) of the voxel; the small red circle is the centre, C of the voxel with coordinates X_o, Y_o, Z_o; the dimensions of the three sides, RL, AP and SI of the voxel are respectively represented by |X|, |Y| and |Z|.

The dimensions of the voxel and their corresponding centre coordinates are usually stored in the SAGE header file after every spectral acquisition. Therefore, the starting values for each side of the voxel can be calculated using the following equations for each side of the voxel:

$$X_{start} = X_o - (|X|/2); \quad Y_{start} = Y_o - (|Y|/2); \quad Z_{start} = Z_o - (|Z|/2) \qquad \text{(Eq. 5.2)}$$

These calculated starting values are usually predefined by SAGE in scanner anatomical space (SAS). By this convention, a voxel side lies along, say, the R or L axis but not along the RL axis. Therefore, the voxel dimensions will normally be presented in SAGE, for example, as 20R x 20A x 20I and not as 20RL x 20AP x 20SI. It should be noted, however, that certain sign conventions apply to the relationships stated in equation 5.2: X_{start} and Y_o should be negated when the SAS labels are L and P, respectively. In this case, the negation of Y_o should be done before calculating Y_{start}. This is necessary due to the change in image orientation (and hence the voxel) when loading the MR

image/voxel in the FSL (FMRIB's Software Library, www.fmrib.ox.ac.uk/fsl) program. The Z-axis serves as the mirror line for the reorientation and so its values are not negated.

2. Generation of Coordinate Space Starting Values

In order to localise the MRS voxel in its corresponding 3D MR image, the FSL program requires the starting values in the coordinate space (CS). The CS starting values are generated automatically by FSL when the calculated SAS starting values are entered. Note should however be taken of the above sign conventions when entering the SAS starting values.

3. Segmentation of the 3D MRI

The brain tissue is extracted from the skull (Figures 5.3a-b) using the brain extraction tool (BET) in FSL (Figure 5.3c). The brain is then segmented into three tissue classes using the FMRIB's Automated Segmentation Tool (FAST) of FSL (Figures 5.3d-f) [165]. The segmentation routine also corrects the image for spatial intensity variations, also known as bias field or RF inhomogeneities. For a three-tissue class segmentation, the FAST algorithm assigns intensity values (between 0 and 1) to all voxels of the image and then classifies these intensities as high, intermediate and low. Tissue classes 0, 1 and 2 have low, intermediate and high intensities, and are thus assigned to CSF (Figure 5.3d), grey matter (Figure 5.3e) and white matter (Figure 5.3f), respectively. The output images of the tissue classes are known as partial volume maps, whose intensity values represent the proportion of each tissue class in the voxels of the 3D MRI [165].

4. Localisation of the voxel in brain segments

The voxel is localised in, and 'cut out' from, the 3D MR image (Figure 5.3j) by running the following command on the image of each tissue class in the command line:

'fslroi <Input tissue class> <Output voxel image> X_{start} |X| Y_{start} |Y| Z_{start} |Z|'

where X_{start}, Y_{start} and Z_{start} are the coordinates of one of the vertices, and |X|, |Y| and |Z| are respectively the dimensions in the RL, AP and SI axes of the voxel as stated in procedure 1. Output voxel images are produced and saved for each one of the CSF (Fgure 5.3g), grey matter (Figure 5.3h) and white matter (Figure 5.3i) fractions.

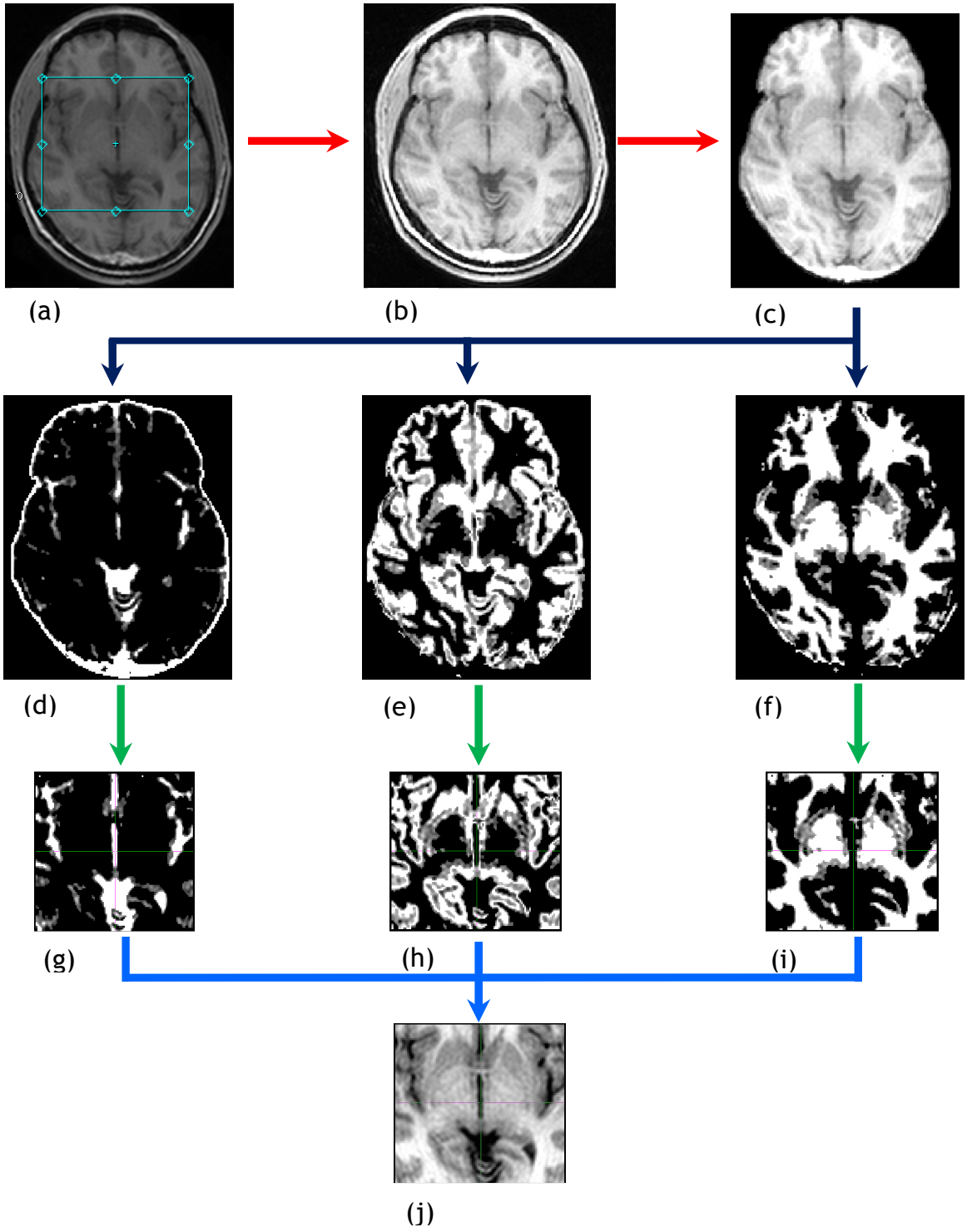

Figure 5.3: A schematic of the voxel localisation procedure in the 3D MR image.
A large voxel (AP x RL x SI = 92.0 x 103.7 x 20.0 mm^3) was planned in one healthy volunteer to validate the accuracy of the localisation technique. Figures (d), (e) and (f) are the partial volume maps of CSF, GM and WM. Figures (g), (h) and (i) are the amounts of CSF, GM and WM within the localised VOI in the corresponding partial volume maps.

5. Estimation of brain tissue and CSF contents of the voxel

The volume of CSF, grey matter and white matter of each voxel image (in voxel units) is calculated as the product of the mean pixel intensity value of the voxel image and the volume of that tissue class in the voxel image. Estimation of the voxel content in this way is known as partial volume estimation, executed in the command line by the following lines of code on each one of the CSF, grey matter and white matter voxel images [165]:

```
vol=`$FSLDIR/bin/fslstats voxel image -V | awk '{print $1}'`
mean=`$FSLDIR/bin/fslstats voxel image -M`
tissuevol=`echo "$mean * $vol" | bc -l`
echo $tissuevol
```

This returns the tissue volume in voxel units, stored in the variable 'tissuevol'. To get the volume in mm^3, {print $1} is replaced with {print $2} in the first line.

6. Estimation of voxel fraction of GM/WM tissue

If υ_{CSF}, υ_{GM} and υ_{MW} are the FSL estimated voxel volumes of CSF, grey and white matter, respectively, then the tissue content of the voxel will be ($\upsilon_{GM} + \upsilon_{WM}$) and the fractions of grey (f_{GM}) and white (f_{WM}) matter will be $\upsilon_{GM}/(\upsilon_{GM} + \upsilon_{WM})$ and 1 - f_{GM}, respectively. This calculation excludes υ_{CSF} leaving behind only solid brain tissue (i.e. grey and white matter fractions).

5.3 Results and Discussion

Results for four groups of experiments are presented in this section in relation to the four aims of this chapter: relaxation times of brain tissue (section 5.3.1), metabolites and water (section 5.3.2), the partial recovery (section 5.3.3) and volume (section 5.3.4) correction factors. At the end of the discussion of each results subsection, the applications of those measurements in correcting the MRS data in this thesis are restated. However, correction for

relaxation effects (using the relaxation time results) is mentioned only in subsection 5.3.2 so that the same discussion is not repeated twice in that section and in section 5.3.1, as the correction procedure involving their use is the same.

5.3.1 Brain Tissue NMR Relaxation Times

Table 5.1 summarises the relaxation times measured in each of the ROIs defined in Figures 5.1a and 5.1b. The tabulated results are averages of measurements in the ROIs on the left and right cerebral hemispheres. The uncertainties of all measurements are given in terms of the standard error (SE), calculated as a ratio of the standard deviations of the measurements to the square root of the sample size measured. The goodness of the relaxation curves were assessed in terms of their R^2 values generated by the non-linear least square curve fitting program (i.e. MATLAB).

Label	Brain Region	T_1 (ms, ±SE) n = 4	T_2 (ms, ±SE) n = 4
1	Ventromedial prefrontal grey matter	1942 (29)	147 (9)
2	Left frontal white matter	1235 (52)	122 (5)
3	Right frontal white matter	1170 (64)	120 (4)
4	Left parietal white matter	1238 (21)	128 (4)
5	Right parietal white matter	1196 (36)	134 (8)
6	Left occipitoparietal white/grey matter	1441 (40)	127 (1)
7	Right occipitoparietal white/grey matter	1410 (47)	127 (2)
8	Left hippocampus	1439 (96)	134 (15)
9	Right hippocampus	1432 (94)	150 (5)

Table 5.1: Average Regional Relaxation Times in the Brain

Both T_1 and T_2 relaxation times varied significantly among all ROIs by one-way ANOVA ($p < 0.05$). For those measurements in bilateral grey (GM) and white (WM) matter regions, there were no significant ($p > 0.05$) differences in T_1 and T_2 relaxation times between the left and right hemispheres: T_1 estimates in the left hemisphere were generally observed to be greater than those in the right hemisphere, but this difference was not significant ($p > 0.05$).

At 4 T, Kim et al [166] also observed that the average T_1 of GM was greater in the left than in the right hemisphere, even without performing any significance test on their results. Similarly, Wansapura et al [54] also observed at 3 T that out of nine ROIs in each hemisphere, eight ROIs in the left had greater T_1 estimates than the same regions in the right hemisphere. They only found this difference to reach statistical significance in GM insular. Garber et al [167] also reported higher T_1 values in the left than right hemispheres in GM and WM regions at 1.5 T.

Hemispheric T_2 differences were not significant in most regions. However, right parietal WM and hippocampal T_2 values were observed to be greater than the T_2 values for the same regions in the left hemisphere. Even though they did not study the same regions as has been studied in the thesis, Wansapura et al [54] did not find any difference in T_2 between the two hemispheres for all their nine ROIs. They reported that they could not cite any literature reporting hemispheric T_2 differences. They attributed the T_1 differences they observed between the two hemispheres to non-uniformity of the B_1 field caused by the non-uniform characteristics of brain tissue. Tissue-type differences give rise to standing waves in the head which cause variation in the flip angles across the brain with the application of the RF pulse [1, 144]. The extent of the standing waves effect depends on the tissue water proton density of the region of interest. Thus, Wansapura et al [54] did not find differences in T_1 and T_2 between left and right ROIs selected on the image of a uniform $MnCl_2$-doped water phantom.

T_1 values in GM regions were observed to be greater than those in WM regions. Even though a similar observation has been made previously [54], this difference was not significant. This is because due to the dependence of T_1 on B_0 field strength [168, 169], at high fields (≥ 3T), tissue relaxation rates approach that of water, resulting in low GM/WM T_1 contrast [54]. The hippocampi, which are GM structures, showed the highest T_2 values compared to the other structures, while the frontal WM regions had the lowest T_2 values. This observation compares with the finding of Wansapura et al [54]; they found

the highest and lowest T_2 estimates in the occipital GM and frontal WM, respectively. The lower T_2 relaxation rates in WM tissue could be attributable to its high ferric iron content [170], which is reported to reduce T_2 relaxation times [170-173].

Generally, studies of hemispheric and regional differences in quantitative T_1 and T_2 measurements in the brain are not based on a consistent selection of ROIs or subjected to tests of statistical significance [54]. It is therefore difficult to do a more rigorous comparison between the results reported in this thesis and those in the literature. Nonetheless, the results in this thesis are consistent with those reported in the literature for the selected brain regions at high fields.

5.3.2 Cerebral Metabolite and Water Relaxation Times

Tables 5.2 and 5.3 summarise the mean relaxation times of the metabolites and water measured, respectively, in the ventromedial prefrontal GM brain region (region 1 in Figure 5.1a) and bilateral hippocampi (regions 8 and 9 in Figure 5.1b). The uncertainties of all measurements are given in terms of the standard error (SE). In all measurements, if less than five points (i.e. signal intensity versus *TE* or *TR*) for a particular metabolite were available for the least square fit, the data was removed from the analysis. This was necessary because those fits generated negative R^2 values and so were regarded as unreliable.

The two regions studied were both predominantly GM regions. For the prefrontal region, the voxel was placed centrally across the two hemispheres and so the relaxation time estimates were averages from both hemispheres. Water and all the metabolites exhibited similar T_1 and T_2 relaxation times in the three regions studied (Tables 5.2 and 5.3). Both T_1 and T_2 relaxations times for the regions studied were in agreement with published results.

Metabolite	T_1 (ms, ±SE) n = 3	T_2 (ms, ±SE) n = 7
NAA	1199 (363)[a]	212 (28)
Glu	1193 (265)[a]	62 (7)
Gln	1436 (131)	56 (10)
Cr	1266 (167)	148 (23)
Cho	1527 (286)	208 (24)
mI	1368 (262)	125 (21)
Water	1574 (61)	147 (6)

Table 5.2: Relaxation times of the metabolites and water in the ventromedial prefrontal grey matter.
[a]Averages from 2 subjects; NAA and Glu data for one subject were removed from the analysis due to unreliable least square fitting

With a similar measurement technique to the one reported in this thesis, T_2 relaxation times of NAA, Cr and Cho in the cingulate gyrus GM were found to be 254 (15), 161 (10) and 242 (37) ms respectively in six healthy subjects at 3 T [129]; where the values in parenthesis are standard deviations. However, in reporting their T_1 values, averages from the occipital WM, motor cortex and fronto-lateral WM/GM were provided [129]: NAA, Cr, Cho and mI exhibited 1.34 (0.08), 1.11 (0.11), 1.14 (0.07) and 0.98 (0.16) s, respectively; where values in parenthesis are standard deviations. Pure GM (in the occipital region) T_1 values have also been reported elsewhere [174]: NAA, Glu, Cr, Cho and mI had 1.47 (0.12), 1.27 (0.10), 1.46 (0.07), 1.30 (0.06) and 1.23 (0.09) s, respectively; where values in parenthesis are standard errors. However, relaxation times for Gln and water in the ventromedial prefrontal GM have not been reported in the literature to the best of the author's knowledge.

Metabolite	T_1 (ms, ±SE); n = 3		T_2 (ms, ±SE); n = 4*	
	Right	Left	Right	Left
NAA	1283 (472)	1547 (119)[c]	114 (32)	153 (43)
Cr	1131 (337)	1144 (232)	113 (28)	105 (16)
Cho	1414 (206)[b]	1365 (207)	251 (70)	338 (101)
mI	1462 (442)[b]	1772 (797)[c]	-	-
Water	1389 (58)	1475 (68)	273 (98)	178 (83)

Table 5.3: Relaxation times of the metabolites and water in the bilateral hippocampi.
Due to unreliable least square fitting, some data were removed from the analyses: [b]right hippocampal Cho and mI data for one subject; [c]left hippocampal NAA and mI for one subject; and *the whole MRS T_2 data for one subject out of the 5 subjects studied.

With the STEAM sequence at 2 T, the relaxation times of NAA, Cr, Cho and mI were measured and averaged in the bilateral hippocampi of eight healthy subjects [175]. The average hippocampal T_1 relaxation times were: NAA = 1408 (253), Cr = 1554 (317), Cho = 1438 (365), mI = 1726 (512) ms; whereas the T_2 values were: NAA = 283 (62), Cr = 191 (43), Cho = 334 (106), mI = 138 (14) ms, where the values in parenthesis are standard deviations. Thus, these estimates are comparable with those reported in this thesis. Unlike the T_1 of brain tissue, T_1 of the metabolites do not seem to depend on the field strength [174], which could be why the results in this thesis at 3 T are comparable to those of Choi and Frahm at 2 T. The reason for this non-dependence of metabolite T_1 on B_0 could be that the major metabolite peaks in the spectrum arise from non-exchangeable protons, and unlike water protons, they have reduced interactions with less mobile macromolecular protons [174].

No study was found in the literature reporting the relaxation times of water in the hippocampus.

For the MRS acquisitions of chapters 6 and 7, the spectra are affected by relaxation effects according to the *TE* and *TR* values chosen for the acquisitions. Using the PRESS localisation sequence, the spectra are corrected for T_1 and T_2 relaxation effects according to the following equations [31]:

$$A(T_1)_{corrected} = \frac{A_{measured}}{[1 - \exp(-TR/T_1)]} \qquad \text{(Eq. 5.3)}$$

$$A(T_2)_{corrected} = \frac{A_{measured}}{\exp(-TE/T_2)} \qquad \text{(Eq. 5.4)}$$

where $A_{measured}$ is the measured spectral peak area, $A(T_1)_{corrected}$ and $A(T_2)_{corrected}$ are the spectral peak areas after T_1 and T_2 corrections, respectively.

Correction of the data for total relaxation effects to yield $A_{T\_corrected}$ would thus take the form [31]:

$$A_{T\_corrected} = \frac{A_{measured}}{\exp(-TE/T_2) \times [1 - \exp(-TR/T_1)]} \quad \text{(Eq. 5.5)}$$

The MRI measured relaxation times (section 5.3.1) were used to correct tissue-specific relaxation effects, whereas the MRS measured relaxation times were used to correct the metabolite signals for relaxation effects in the brain regions corresponding to the respective voxel positions in chapters 6 and 7. In those equations in chapters 6 and 7, the relaxation correction factors (i.e. the denominators of equations 5.3-5) for T_1, T_2 and total relaxation effects will be represented by R_1, R_2 and R_T, respectively.

5.3.3 Partial Recovery Correction Factors

The CHESS OFF unsuppressed-water peak area, $A_{TE23\_TR15000}$ acquired with the optimum *TE*/*TR* pair was found to be 4.99e8 a.u. The CHESS ON unsuppressed-water peak areas (in a.u.) from the standard acquisitions were as follows:

A_{TE35_TR2000}, = 3.97e8, A_{TE144_TR2000} = 3.81e8 and A_{TE144_1500} = 3.78e8.

Dividing the value of $A_{TE23\_TR15000}$ by each one of the above water signal areas (equation 5.1), the partial recovery correction factors, k_{pr} for each standard acquisition was obtained; thus:

k_{pr} for acquisition *TE*=35/*TR*=2000, *TE*=144/*TR*=2000 and *TE*=144/*TR*=1500 were 1.26, 1.31 and 1.32, respectively. The first two k_{pr} values were multiplied by the unsuppressed-water peak areas acquired with the respective *TE*/*TR* values in chapter 7; whereas the last k_{pr} value was multiplied by the unsuppressed-water peak area acquired at the same *TE*/*TR* pair in chapter 6. Thus, the fractional signal losses from these partially recovered water signals (as *TR* was not equal to 15000 ms in each case) were accounted for by these k_{pr} values.

As *TE* was not also equal to 0 ms in each case, it meant that the water signals still suffered some losses due to T_2 relaxation effects. Therefore, correction for these T_2 relaxation effects was done for each k_{pr}-corrected water peak area. It is important to mention that this k_{pr} correction applied to only the water peak area, and not to the metabolites. This is because the metabolites have shorter T_1 relaxation times than water, and so at the *TR* times of the measurements, their longitudinal magnetisations would have recovered far more than that of water. The partial recovery effect would thus not be applicable in the case of the metabolites. Therefore, T_1 (and not k_{pr}) and T_2 relaxation corrections were done for the metabolite peak areas (chapter 7).

In order to quantify the total water signal area measured by MRS, Brief et al [58] used *TE*/*TR* = 30/2500 ms for their spectral acquisitions. Their unsuppressed-water lines were quantified from the 16/NEX part of equation 2.19 (section 2.3.1.3), as has been done in this thesis. Thus, their water peak area also required correction, k_{pr} for the partial recovery effect. In their case, they obtained k_{pr} using MRI (compared to the use of MRS in this thesis). They used a modified multi-echo imaging pulse sequence to measure 32 echoes from the human brain with *TE* values ranging from 10 ms to 320 ms (in steps of 10 ms). They then fit a mono-exponential curve to their measured MRI water signal intensities and extrapolated this curve to *TE* = 0 ms, where they theoretically obtained the total MRI estimated water signal area, A_{MRI_TE0}. Another MRI of the same subject was acquired at *TE* = 30 ms, which was the same *TE* of their MRS acquisition; the MRI water signal area, A_{MRI_TE30} was obtained from this acquisition. The ratio A_{MRI_TE0}/A_{MRI_TE30} yielded k_{pr}, which was then multiplied by their MRS measured water peak area to correct it for the partial recovery effect.

However, the difference in the use of k_{pr} between the study by Brief et al [58] and this thesis is that while this thesis considers it to correct for T_1 relaxation effects, Brief et al considered it as a correction for T_2 relaxation effects. This is because in the MRI acquisitions by Brief et al, both A_{MRI_TE0} and A_{MRI_TE30} were acquired using the same *TR* (of 3000 ms) and so had the same T_1 relaxation

effects which cancelled out on division. Measurements of the two peak areas however differed in *TE*, where A_{MRI_TE0} was considered to be corrected for T_2 relaxation effects; so dividing it by A_{MRI_TE30}, which was not T_2 corrected, would yield a result, k_{pr} equal to the fraction by which A_{MRI_TE30} would have decayed by T_2 relaxation relative to A_{MRI_TE0}. Thus, k_{pr} in this case should be a T_2 relaxation correction factor for the water peak, while T_1 correction is done for the water and metabolite spectral peaks in the same way.

This thesis, on the other hand, did not perform a multi-echo signal acquisition to determine k_{pr}; only the total water signal area, $A_{TE23\_TR15000}$ was measured using $TR = 5 \times T_1$ of water. The total signal area was therefore considered to be T_1 corrected. This thesis measured $A_{TE23\_TR15000}$ and A_{TEacq_TRacq} using different *TR* values, and so k_{pr} should equate a factor by which A_{TEacq_TRacq} would have lost some signal by T_1 relaxation relative to $A_{TE23\_TR15000}$. Hence, k_{pr} should be a T_1 relaxation correction factor for water in this case. T_2 correction was then done for the water and metabolite spectral areas in the similar manner.

5.3.4 Partial Volume Correction Factor

For the large voxel prescribed in the single volunteer shown in Figure 5.3, the partial volume estimates in voxel units of CSF (Figure 5.3g), GM (Figure 5.3h) and WM (Figure 5.3i) were 16744, 90986 and 127662 mm^3, respectively. These represented 7 %, 39 % and 54 % of CSF, GM and WM, respectively, in the voxel.

Excluding the CSF content of the voxel to correct for partial volume effects, the voxel tissue content then had a total partial volume estimate of 218648 mm^3, representing 93 % (or a fraction of 0.93) of the voxel. This tissue fraction of the voxel was then made up of 42 % (or 0.42) and 58 % (or 0.58) of GM and WM, respectively (section 5.2.4).

The voxel localisation technique presented in this thesis is accurate for non-oblique voxel placements, which was the case with most of the acquisitions reported in this thesis. For oblique voxel placements, the orientation angle will

have to be taken into account. In this case, a rotation matrix involving the voxel starting values and rotation angle would have to be used. However, unlike the Siemens scanner used elsewhere [176], the GE scanner used for the experiments in this thesis does not generate information on the orientation angle of the voxel in the MRS header files; and there is no straightforward way of obtaining such information.

The need for oblique voxel placement arises when MRS acquisitions are required in brain structures such as the hippocampus which lies obliquely within the brain (Figure 5.4a). Since the hippocampus was one of the regions of interest in this thesis, in all the MRI acquisitions for voxel placement, the slices were planned along the hippocampal axis. By doing this, the hippocampi in both hemispheres were now reasonably horizontal (Figure 5.4b) so that there was no need to tilt the MRS voxel to cover most of the length of the hippocampus.

The slice planning for the structural MRI, voxel placement and partial volume correction techniques described in this section were applied to the MRS data presented in chapters 6 and 7. Correcting the measured MRS signal area, $A_{measured}$ for partial volume effects usually takes the form [1]:

$$A_{corrected} = A_{measured} / (f_{GM} + f_{WM}) \qquad \text{(Eq. 5.6)}$$

where f_{GM} and f_{GM} are the fractions of grey and white matter tissues in the voxel (i.e. excluding CSF) and $A_{corrected}$ is the corrected spectral peak area after excluding CSF from the voxel. Thus, even though CSF actually contributes some amount of signal to $A_{measured}$, the partial volume correction technique assumes otherwise.

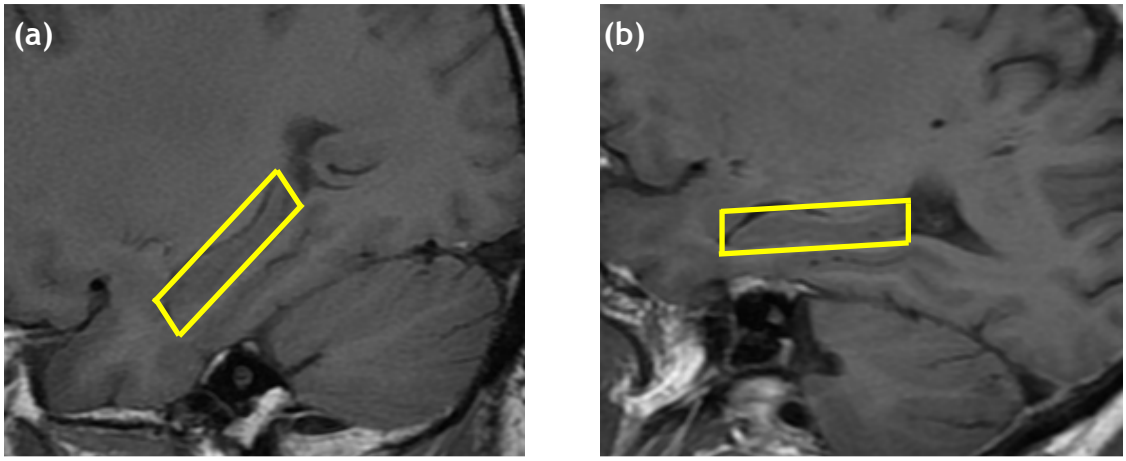

Figure 5.4: Sagittal MRI scans showing voxel placements on the hippocampus in (a) its normal oblique orientation and (b) a horizontal orientation

5.4 Summary and Conclusions

The work in this chapter was primarily aimed at measuring and developing techniques to deal with the main factors that introduce large errors in spectral quantification (sections 5.1.1-3) by the internal referencing method. The cerebral water signal has been chosen as the internal reference in this thesis. Thus the two main factors that could impact on the accuracy of quantitative MRS using this reference were dealt with. These factors were: signal relaxation and partial volume effects.

Relaxation times in the brain and of metabolites and water were therefore measured. The T_1 and T_2 values obtained compared with values in the literature. For most regions of the brain, T_1 was observed to be slightly higher in the left hemisphere but T_2 did not vary widely regionally. Unlike brain tissue T_1, metabolite T_1 estimates tend not to depend on B_0 field, and so metabolite T_1 values were comparable at different field strengths. Measurement of the relaxation times of water in the hippocampus using MRS has been done for the first time in this chapter.

The reference unsuppressed-water signal in this thesis is affected more by T_1 than by T_2 relaxation effects. This is because at the *TR* of the acquisitions, only a fraction of the water signal has recovered its longitudinal magnetisation. A

method of estimating the unrecovered or lost signal fraction was suggested. This signal compensation method was also suggested to include correction for T_1 relaxation effects.

A method for partial volume correction using MR image segmentation of the MRS voxel was also presented. Though the voxel localisation technique described is not suitable for cases where oblique voxels are used, a method of dealing with this was suggested. It was recommended that for brain structures like the hippocampus that are in oblique orientation, the MRI of the brain should be acquired with slices tilted to the region of interest so that the voxel can be prescribed on that region in a non-oblique orientation.

The results presented in this chapter will be used to estimate the correction factors for relaxation and partial volume effects in the spectral quantification of chapters 6 and 7.

Chapter 6: Quantification and Assessment of Regional Brain Water Content

6.1 Introduction and Objectives

The advantages of using brain tissue water content as an endogenous reference concentration in quantitative MRS were discussed in section 4.1.2. However, the direct measurement of brain tissue water content with MRS remains a challenge. To date, all non-invasive MRS measurements of this endogenous tissue water concentration involve the use of another external reference concentration [58, 59, 61]. This defeats the full benefit of internal referencing to tissue water content and potentially introduces more errors into the estimate, depending on the type of external reference used and where it is positioned in the receiver coil [1]. When metabolite quantification is needed in the same study, the examination is prolonged because the metabolite signals will have to be recorded separately [58]. Even when the water concentration estimate is taken from the literature, a separate unsuppressed-water signal acquisition is usually conducted [30, 45, 61, 62]. Using a mathematical model that relates the peak area of this unsuppressed reference signal, the literature or measured value of tissue water content and the metabolite peak area, the concentrations of the metabolites of interest are obtained (this is further explored in chapter 7).

Ideally, the reference water and metabolite signals should be recorded from the same voxel, and simultaneously. The intensity of this acquired water signal should also be enough to give an estimate of tissue water concentration within the region of interest (i.e. where the voxel is placed). If such an estimate of water concentration is used as an endogenous reference specific to the region of interest, then it will be possible to have a reference concentration that will always correspond to each voxel position. Such a quantification scheme will be

implementable within clinical examination times, and will be less susceptible to the errors inherent in the previous quantification methods.

The MRS measured water signal could also be probed by magnetisation transfer (MT) imaging. This is because MT imaging measures signal intensities related to the amount of tissue-bound water; MRS on the other hand is capable of measuring the total water signal from tissue, and if CSF contribution to this signal is excluded, then what is left is the tissue-bound component. The amount of tissue-bound water as measured by MT imaging is indicated by the MT ratio (MTR). The MT effect is greater in regions of high macromolecular content but less bulk water (e.g. in myelin sheaths). In a healthy or developing brain, the relative amounts of MTR in different brain regions mainly point to the relative amounts of white/grey matter or degrees of myelination [1]. It is therefore possible that in the same healthy subject, MRS measured tissue water content could be related to MTR obtained from MT imaging of the same regions of interest. This potential relationship (between MRS and MT imaging) and its practical implication for future studies were investigated and are presented in section 6.3.5.

The dependence of cerebral water content on age [177]and brain region [61] has been reported previously. There are also indications of MTR variation with age [178, 179] and brain region [180, 181]. However, no single study in the literature has, at the same time, investigated both cerebral water content and MTR variations with age, gender, brain region and/or tissue type. Such a study would help rule out these factors as possible sources of variance (or otherwise) in cerebral water content. Findings involving these factors may have implications for studies that utilise published estimates of cerebral water content (from healthy volunteers) for referencing in quantitative MRS. The agreement (or otherwise) of the findings between the MTR and water content studies would also indicate whether or not any one of the two measurements could be used to validate the other.

The studies presented in this chapter were therefore aimed to:

1. Develop an MRS technique to accurately quantify brain tissue water content without the need for extra unsuppressed-water signal acquisition;
2. Assess the variation of quantified tissue water content across the brain including brain tissue water variation by gender and the possible associations of brain water content with voxel tissue content and age;
3. Compare (for the same regions of interest) the brain tissue water contents and MT ratios as measured by MRS and MT imaging, respectively.

6.2 Methods

Data from three different studies were used for the work presented in this chapter. Two studies were retrospective MRS studies whereas one was a prospective MT imaging study conducted during this PhD project. The brain tissue water quantification technique was developed and implemented using the retrospective MRS data; the MT imaging results for the same regions investigated in the MRS studies were then compared to the MRS results. The three studies are specified as follows:

Study 6A: A retrospective single-voxel MRS study measuring metabolite signals from three voxel positions in the left hemisphere of healthy subjects

Study 6B: A retrospective single-voxel MRS study measuring metabolite signals from the left and right hippocampi of healthy subjects

Study 6C: A prospective MT imaging study assessing the MT effects in the voxel positions of studies 6A and 6B in healthy volunteers.

The tissue water quantification technique involved a novel spectral processing method that quantified the unsuppressed-water signal from a CHESS water-suppressed acquisition (sections 2.3.1.2-3). The method was successfully implemented in studies 6A and 6B where both MRS data were CHESS water-suppressed. The details of the methods for this chapter are discussed in subsections 6.2.1-4.

6.2.1 Subjects

Table 6.1 summarises the age-sex distribution of the subjects in the three studies.

Study	Sample Size (Males/Females)	Mean age ± SD (range) in years		
		Total Sample	Males	Females
6A	11/11	38 ± 13 (20-64)	37 ± 10 (20-52)	39 ± 15 (23-64)
6B	37, all males	51 ± 9 (38-66)	51 ± 9 (38-66)	-
6C	4/4	32 ± 9 (23-51)	37 ± 10 (29-51)	26 ± 4 (23-32)

Table 6.1: Age-sex distribution of the healthy volunteers for the three studies.
In a two-sample t-test, the mean ages of males and females were not significantly different in studies 6A ($p = 0.840$) and 6C ($p = 0.101$)

6.2.2 MRI, MRS and Voxel Placement

In both studies 6A and 6B, high resolution T_1-weighted axial 3D MR images of the brain of each subject were acquired to be used for partial volume correction by image segmentation (section 5.2.4). In each study, structural 2D MRI scans of the brain were also performed (Table 6.2) for planning the MRS voxel positions (Figures 6.1 and 6.2).

MRI parameters	Study A	Study B		
Sequence (image orientation)	T_2-w FSE (sagittal)	T_1-w FLAIR (sagittal)	T_2-w FSE/propeller (axial)	T_2-w FSE (coronal)
TR/*TE*/*TI* (ms)	4040/91.8/0	2557/8.9/920	5000/109/0	4060/127/0
FOV (cm^2)	20 x 20	24 x 24	24 x 24	20 x 20
Matrix size	256 x 256	320 x 224	512 x 512	512 x 512
Number of slices	20	18	21	11
Slice thickness/gap	5.0/1.0	5.0/2.0	5.0/1.5	4.0/1.0

Table 6.2: Structural MRI parameters for voxel planning in the two retrospective studies

In both studies, the PRESS localisation sequence was used to acquire CHESS water-suppressed spectra, with *TR*/*TE* = 1500/144 ms, NEX = 8, 4096 complex points and a spectral width of 5000 Hz. Spectral averages of 128 and 256 were acquired in studies 6A and 6B, respectively. In study 6A, spectra were recorded from a voxel of 20 x 20 x 20 mm^3 placed in the frontal, parietal and occipital regions of the left brain hemisphere (Figures 6.1a-f). In study 6B, spectra were recorded from a voxel of 10 x 20 x 15 mm^3 (in the LR x AP x SI directions, respectively) positioned in the right (Figures 6.2a-c) and left hippocampi.

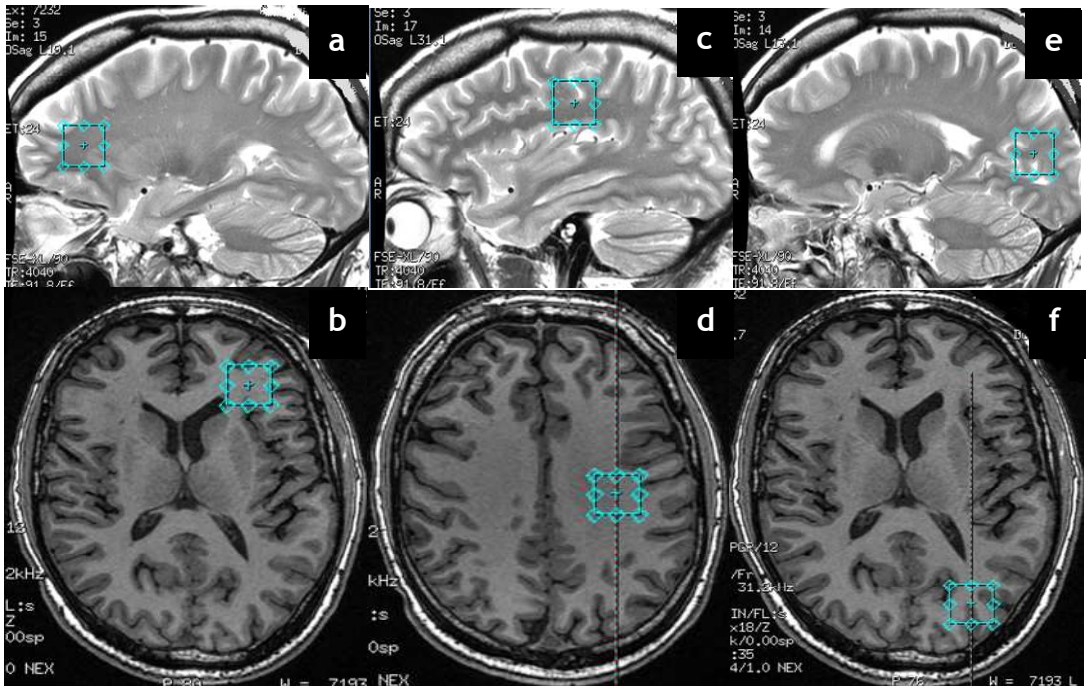

Figure 6.1: Voxel placement in study 6A in the frontal (a and b), parietal (c and d) and occipital (e and f) regions of the left brain hemisphere of the same subject.
The top row (a, c and e) shows the voxel positions in the sagittal view; the bottom row (b, d and f) shows the voxel positions in the axial 3D MRI

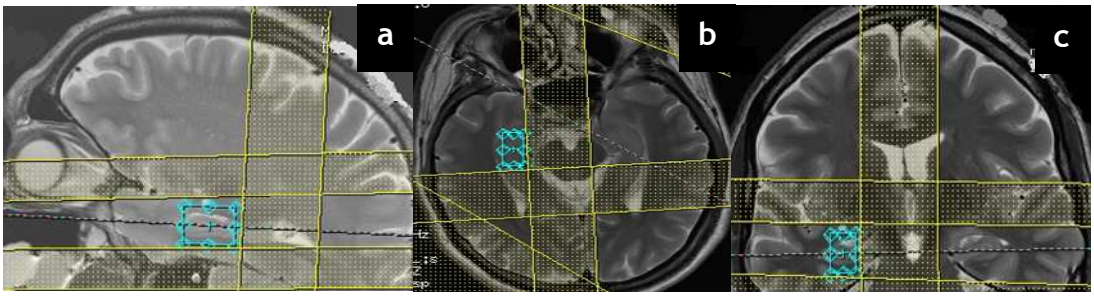

Figure 6.2: Representative sagittal (a), axial (b) and coronal (c) MR images showing the voxel placement in the right hippocampus of the same subject in study 6B.
The yellow lines are saturation bands prescribed by the scanner around the voxel edges; these help prevent signal contamination from adjacent tissue. They are applied in all the MRS acquisitions in this thesis but have only been shown in this example.

6.2.3 MT Imaging

Without turning the MT pulse ON, an axial MRI of the brain was acquired using a gradient echo pulse sequence with the following parameters: *TR*/*TE* = 3000/35 ms, 15 slices (4 mm thick per slice without gaps) planned along the hippocampal angle, FOV = 25 x 25 cm^2 and a matrix size of 256 x 128. Following this acquisition, the MT saturation pulse (frequency offset = 1000 Hz, flip angle = 5^o) was then switched ON and the same MRI parameters were used to acquire an MT image.

6.2.4 Data Analysis

The MRS and MT imaging data were analysed using the SAGE (version 7) and Image-J (version 1.46r) software packages, respectively. The SAGE spectral fitting method was discussed in section 2.3.1.2. For the work in this chapter, only the water resonance at 4.7 ppm was analysed. Therefore, only the use of the SAGE results (i.e. spectral peak areas) for the calculation of tissue water content will be presented in this chapter (section 6.2.4.1). The Image-J software package gives image intensities from selected ROIs, the intensities being associated with the presence and absence of the MT effect in the corresponding images (details in section 6.2.4.2).

6.2.4.1 Calculation of Tissue Water Content

In this thesis, the brain tissue water content, WC refers to the tissue-bound water component (i.e. excluding cerebrospinal fluid, CSF). The complete equation describing the total tissue water contents, WC in grey matter, GM and white matter, WM tissues was given by:

$$WC = \frac{A_{brain}}{A_{fit}} \times \frac{K_{pr}}{k_{temp}} \times \frac{k_{TG\_brain}}{VOI_{brain}} \times \left(\frac{f_{GM}}{R_{2\_GM}} + \frac{f_{WM}}{R_{2\_WM}} \right) \qquad \text{(Eq. 6.1)}$$

A_{brain} is the spectral peak area of the *in vivo* unsuppressed-water signal derived from the spectral analysis of the 16/NEX lines (sections 2.3.1.2-3); A_{fit} is the peak area obtained by substitution of the *in vivo* VOI coordinates of A_{brain} into the appropriate position-dependent polynomial equation from the phantom experiments (section 4.4); k_{temp} is the temperature correction factor that accounts for the larger proton population difference between water in the phantom (which is at lower temperature) and brain tissue water [1]; k_{pr} is the compensation factor for the fractional water signal loss due to partial recovery and T_1 relaxation effects together (section 5.3.3); k_{TG} is the transmitter gain factor (section 4.2.5) accounting for differences in coil loading effects between the phantom and the head; VOI is the voxel size in the respective spectral acquisitions; f_{GM} and f_{WM} are the voxel fractions of grey and white matter tissues respectively, after CSF exclusion (section 5.2.4); R_{2_GM} and R_{2_WM} are the compensation factors for T_2 relaxation effects in grey and white matter tissues, respectively (equation 5.4).

A_{fit} in equation 6.1 is already corrected for T_1, T_2, VOI and transmitter gains according to equation 4.1 (section 4.2.5), and since it is obtained primarily from phantom experiments, using it for referencing here would require corrections for temperature, coil loading and VOI differences between the MRS phantom and the human brain as in equation 6.1.

The temperature correction factor, k_{temp} was calculated from [1]:

$$k_{temp} = (273.2 + T_{phantom})/310.2 \qquad \text{(Eq. 6.2)}$$

$T_{phantom}$ is the temperature of the phantom in degree Celsius; which was 18 ^{o}C during the phantom experiments, giving a k_{temp} value of 0.94.

In section 5.3.3, k_{pr} was found to be 1.32. Thus, the k_{pr}/k_{temp} factor in equation 6.1 becomes 1.32/0.94 = 1.40.

Tissue-specific absolute WC was obtained from equation 6.1 as follows:

$$WC_{tissue} = \frac{A_{brain}}{A_{fit}} \times \frac{K_{TG\_brain}}{VOI_{brain}} \times \frac{f_{tissue}}{R_{2\_tissue}} \times 1.40 \qquad \text{(Eq. 6.3)}$$

where f_{tissue} and R_{2_tissue} are the GM or WM tissue fraction in the voxel and T_2 relaxation correction factor, respectively; the fraction k_{pr}/k_{temp} is replaced by the constant value of 1.40. Thus the WC for GM and WM were calculated separately as WC_{tissue}.

The WC calculated in either one of equations 6.1 and 6.3 is in percentage units. To express WC in units of g/mL, it was multiplied by the density of water at 37 ^{o}C (0.9934 g/mL [58]); this yielded tissue water density, WC_{ρ}. WC was also expressed in concentration units per kilogram of wet tissue weight. This was done by multiplying WC by the concentration of water (55.51 mol/L); WC in mol/L was then divided by the density of water at 37 ^{o}C (0.9934 g/mL), resulting in units of mol/kg wet weight for WC, denoted by WC_{kg}^{-1}. It was necessary to express WC in both units in order to allow for direct comparison with literature values that are expressed in either unit.

The technique for the measurement and quantification of brain tissue water content presented in this section is unique compared to the previous methods in the following ways: from a normal water-suppressed acquisition, the

unsuppressed-water signal area can be derived. To obtain the reference signal area (in equation 6.3), the *in vivo* voxel coordinates are used in the appropriate polynomial equation to calculate the required signal area. There is therefore no need for prolonged or any extra acquisitions in the estimation of brain tissue water content. The technique is thus less time consuming and less stressful for patients.

6.2.4.2 Calculation of MT Ratios

ROIs were drawn in the ventromedial prefrontal GM, and bilateral frontal, parietal, occipital and hippocampal brain regions (regions 2-9 as shown in Figures 5.1a and 5.1b) of the MR images acquired with and without the MT saturation pulse. These ROI selections included all the brain regions in which the water content has been estimated in studies 6A and 6B. To ensure the same ROI was selected in the MT ON and OFF images of the same subject, the ROI Manager tool in the Image-J software package (version 1.46r; National Institutes of Health, USA) was used to store the coordinates of the selected ROI in the image that was loaded first. When the next image was loaded, the stored ROI coordinates were superimposed on it at exactly the same location as in the first image. This method yielded the same results as co-registration of the two images and selecting the ROIs. Therefore, any difference in voxel intensity value between the two images was only as a result of the MT saturation difference and not due to inconsistent ROI selection. The fraction of the magnetisation transfer (MT) effect was estimated from the MT ratio (MTR) expressed as a percentage in the following equation [22]:

$$MTR = (1 - M_s/M_o) \times 100\ \% \qquad \text{(Eq. 6.4)}$$

M_s and M_o are the pixel intensity values of the ROI selections in the MR images with and without MT saturation, respectively. Example images acquired without and with MT saturation are shown in Figures 1.4a and 1.4b, respectively.

6.3 Results and Discussion

The details of the technique developed for the calculation of brain tissue water content, WC has been discussed in section 6.2.4.1 (see objective 1). The results obtained by implementing the technique will be presented and discussed in the following subsections in relation to WC values in the literature, variation across the brain, by gender, age, and voxel tissue content (sections 6.3.1-3) - see objective 2. Results for the regional variation in MTR are also presented (section 6.3.4) and then compared to variation in WC for the same brain regions (section 6.3.5) - see objective 3.

6.3.1 Hemispheric Tissue Water Content

Subsections 6.3.1.1-5 discuss the results for study 6A recording MRS data from the left hemisphere, along the frontal, parietal and occipital brain regions. The results presented in the subsections include comparison between GM and WM water contents, WC for the three brain regions (section 6.3.1.1), assessment of regional mean WC (section 6.3.1.2), comparison of the regional mean and GM/WM water contents between males and females (section 6.3.1.3), assessment of the association between voxel tissue and water contents (section 6.3.1.4), and the investigation of WC variation with age (section 6.3.1.5).

6.3.1.1 GM versus WM Tissue Water Contents

Before presenting the results for tissue water content, it is necessary to assess the relative amounts of grey (GM) and white (WM) matter in the three hemispheric voxel positions. These are summarised in Table 6.3.

Region	Mean GM fraction ± SD (range)	Mean WM fraction ± SD (range)	p-value
Frontal	0.54 ± 0.04 (0.50-0.68)	0.46 ± 0.04 (0.32-0.50)	< 0.01
Parietal	0.53 ± 0.04 (0.37-0.58)	0.47 ± 0.04 (0.42-0.63)	0.010
Occipital	0.48 ± 0.09 (0.37-0.76)	0.52 ± 0.09 (0.24-0.63)	0.346

Table 6.3: Voxel tissue compositions in the left hemisphere of all subjects.
Comparisons were done by paired t-tests for the parietal and occipital regions; the Wilcoxon signed rank test was used for comparisons in the frontal region as the data did not follow a normal distribution

The frontal ($p < 0.01$) and parietal ($p = 0.01$) voxel positions had significantly greater amount of GM than WM; only the occipital voxel did not contain significant amount of either tissue type than the other ($p = 0.35$). A one-way ANOVA indicated a significant variation of voxel GM content among the three regions ($p < 0.01$), with frontal > parietal > occipital. Voxel WM content also varied significantly among the three regions ($p < 0.01$), with frontal < parietal < occipital. The impact of the tissue content of the voxels on water content is discussed in subsection 6.3.1.4.

The mean GM and WM water contents in the three voxel positions are shown in Table 6.4. Estimates for the water content are provided in concentration (WC_{kg}^{-1}) and density (WC_{ρ}) units. Since both quantities have been derived from the same base equation (equation 6.3), it was expected that their variation by tissue type and sex should be the same. However, a correlation analysis was still performed between WC_{kg}^{-1} and WC_{ρ} for all voxel positions in studies 6A and 6B. As was expected, each correlation analysis resulted in a Pearson correlation coefficient of 1, which meant that both quantities were accurately and directly proportional; thus, inferences drawn from statistical tests on either one of the two quantities could be applied to the other. As shown in Table 6.4, the paired t-tests between GM and WM for WC_{kg}^{-1} and WC_{ρ} gave the same p-values for all three brain regions. Therefore from this point, tissue water content will be provided in concentration units, WC_{kg}^{-1}; and conclusions drawn with WC_{kg}^{-1} will also apply directly to tissue water density, WC_{ρ}.

Brain region	Mean WC_{kg}^{-1} ± SE (range) in mol/kg wet weight		p-value	Mean WC_{ρ} ± SE (range) in g/mL		p-value
	GM	WM		GM	WM	
Frontal	46.37 ± 2.58 (26.70-48.25)	42.86 ± 2.46 (25.44-46.77)	0.016	0.82 ± 0.05 (0.57-0.94)	0.75 ± 0.04 (0.53-0.88)	0.016
Parietal	37.23 ± 1.70 (30.59-48.12)	34.14 ± 2.02 (29.82-42.72)	0.031	0.66 ± 0.03 (0.54-0.86)	0.61 ± 0.04 (0.53-0.83)	0.031
Occipital	34.92 ± 2.34 (31.00-49.56)	37.45 ± 2.35 (29.70-48.99)	0.435	0.62 ± 0.04 (0.53-0.88)	0.67 ± 0.04 (0.50-0.87)	0.435

Table 6.4: Mean regional brain tissue water content by tissue type within the left hemisphere.
Comparisons were done by paired t-tests

Generally, the relative amounts of GM/WM water contents appear to follow the same pattern as their amounts in the three voxel positions (more in section 6.3.1.4). GM water content was found to be significantly higher than WM water content of the frontal ($p = 0.02$) and parietal ($p = 0.03$) brain regions. WM water content was higher (but not significantly) than GM water content in the occipital region. Water content of GM is known to be slightly higher than that of WM [49, 58, 59]. This observed relative water contents of the two tissue types, and the relative amounts of GM and WM in the frontal and parietal voxels may explain the significantly higher GM water content than that of WM in the frontal and parietal brain regions.

The occipital voxels contained more or less equal amounts of GM and WM tissues. The mean water contents of GM and WM were therefore not significantly different ($p = 0.44$). GM tissue water content varied significantly among the three voxel positions ($p = 0.007$), with frontal WC > parietal WC > occipital WC. WM tissue water contents of the three voxels also varied significantly ($p = 0.012$), with frontal WC > occipital WC > parietal WC. The significant variation in the water contents of GM and WM in the three voxel positions originated from higher WC values for the frontal GM and WM. The

parietal and occipital regions did not vary significantly in WC of either GM ($p = 0.105$) or WM ($p = 0.241$).

The following discussion compares the results of this thesis with those of previous studies.

With a voxel size of 7.84 mL (compared to 8.0 mL in this study; section 6.2.2) containing an average (standard error) of 86 (1) % (compared to 47 (0.9) % in this study; Table 6.3) white matter in parietal voxels and 73 (3) % (compared to 49 (1.9) % in this study; Table 6.3) of grey matter in occipital voxels, Brief et al [58] measured the water contents in GM and WM tissues to be 0.73 ± 0.01 and 0.77 ± 0.01 g/mL (mean ± standard error). They measured the total water signal by a multi-echo (32 echoes) MR imaging technique and fit a monoexponential curve to the points to obtain A_{brain} at $TE \approx 0$ ms. The water signal was then referenced to a signal acquired from an external water phantom. They reported that due to the voxel tissue mixture used in their measurements, their GM and WM tissue water contents were slightly under and over estimated, respectively, compared to literature estimates. Compared to the study by Brief et al, the average voxel contents of WM and GM in this study were lower and so were their water contents: 0.61 ± 0.04 in parietal WM and 0.62 ± 0.04 g/mL in occipital GM (Table 6.4).

Whittal et al [59] used a similar method to that of Brief et al and measured the water content of pure WM and GM brain regions to be 0.71 ± 0.01 and 0.83 ± 0.03 g/mL, comparable to post mortem water content estimates of 71.6 % and 81.9 % for pure WM and GM, respectively [60]. In concentration units, pure WM and GM water estimates have been reported to be 39.2 and 46.8 mol/kg wet weight [62]. Even though these estimates are well within the range of the WM and GM water contents measured in this study (Table 6.4), the average estimates in this study were found to be lower for the parietal and occipital voxels. Only the means of the water contents for both GM and WM in the frontal voxels were directly comparable to those in the literature: 0.82 ± 0.05 for GM and 0.75 ± 0.04 g/mL for WM in density units, and 46.37 ± 2.58 for GM

and 42.86 ± 2.46 mol/kg wet weight for WM in concentration units. The relative amounts of CSF in the three voxel positions and the voxel tissue mix (i.e. no "pure" GM or WM in the voxels) could have accounted for the discrepancies between the reported mean WC and those measured in the parietal and occipital voxels in this study. In fact, most of the WC values measured in those two voxels were relatively lower (see the ranges in Table 6.4).

Elsewhere [160], the T_2 contribution of myelin water to the total water signal has been subtracted from the decay curve. This yields a signal attributable to only "solid brain" tissue which is then referenced to an identical volume of pure water in an external standard. With this technique, Ernst et al [160] estimated the water content of pure WM and GM to be 0.646 ± 0.015 and 0.780 ± 0.015 g/mL, respectively. They however reported average relative signal losses of 35.4 % and 20.2 % in WM and GM, respectively. An observation by Whittall et al [59] suggests an explanation to these signal losses in that the fast relaxing myelin water component accounts for about 11 % and 3 % of the signal in normal WM and GM, respectively. It is therefore likely that in neglecting the T_2 contribution from myelin water, the fully-relaxed water signal is underestimated, leading to the brain tissue water content being underestimated. This means that in order to accurately measure the total tissue water signal, multi-echo techniques will have to acquire as many echo points as possible, and these should include points close to TE = 0 ms.

The technique of measuring the total tissue water signal presented in this thesis is not relatively complicated and includes contributions from all possible "water pools" in the brain. As long as K_{pr} is accounted for in the model for WC, the total water signal obtained yields estimates for tissue water content comparable to the literature estimates. No voxel contained as much of GM or WM as those amounts in the above studies, and yet all the mean literature estimates for both GM and WM water contents fall within the range of WC values for the two tissue classes in this thesis.

6.3.1.2 Regional Hemispheric Mean Water Contents

For each brain region, the mean of the GM and WM water contents were calculated. This was to allow for further comparison of the results from the technique of this thesis to the results of other studies that reported average brain tissue water contents. As shown in Figure 6.3, the mean ± SD of the water contents in the frontal, parietal and occipital brain regions were 40.06 ± 7.84, 35.69 ± 5.73 and 36.18 ± 7.71 mol/kg wet weights, respectively. The mean water contents in the three regions did not vary significantly ($p = 0.064$), even though the mean water content in the frontal region was slightly higher.

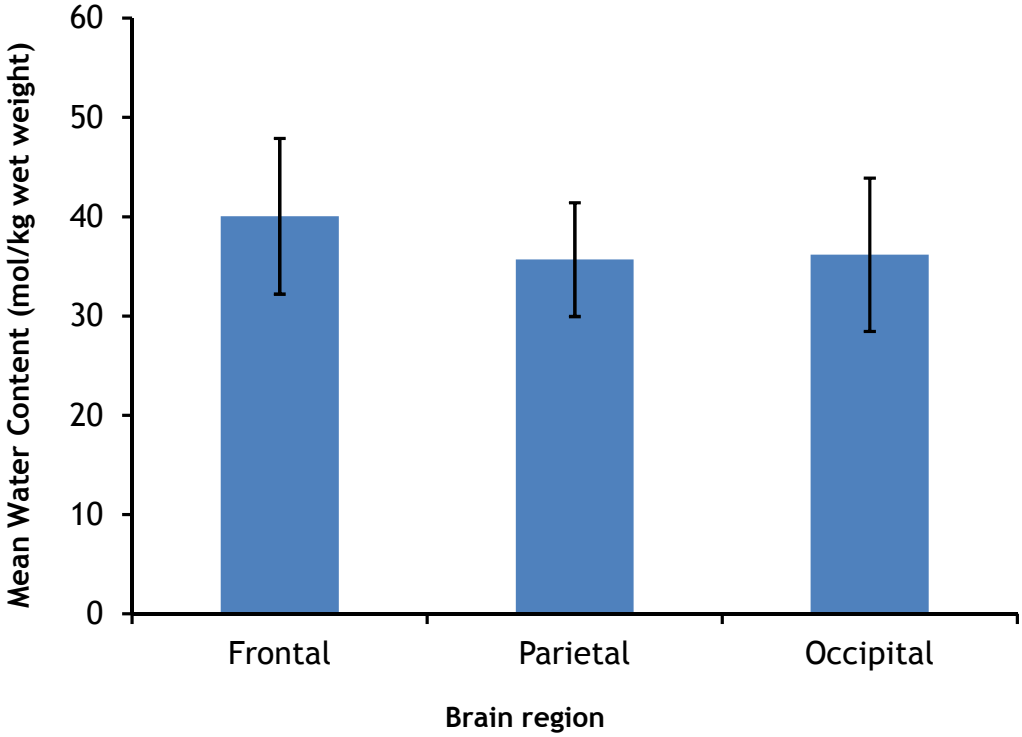

Figure 6.3: Mean water content in the left hemispheric frontal, parietal and occipital voxels
Error bars represent ±standard deviations

These estimates compare with the average brain tissue water content of 36 moles reported elsewhere [31]. In a study of the water contents in four brain regions among four age groups, Christiansen et al [61] measured the unsuppressed-water signal and referenced it to an external water-filled bag.

Among adolescents (aged 10-15 years), adults (aged 22-28 years) and the aged (60-74 years), they estimated water contents in the frontal, temporal, occipital and basal ganglia to be between 35.8 and 39.6 mol/kg wet weight (mean = 36.9 mol/kg wet weight). The water content was not significantly different among the four brain regions. The average water content (of 51.5 mol/kg wet weight) in a group of newborns (aged 0-23 days) was however found to be significantly higher than that in the other three groups ($p < 0.01$). This thesis did not include newborns; however, the ages of the subjects studied fell between the adult and aged groups of Christiansen et al. The estimates of the water contents for the adult population were comparable between the two studies. Similarly, this thesis did not also find significant difference in water content in the three regions of interest.

6.3.1.3 Tissue Water Content by Sex

The voxel tissue contents are compared between males and females in Table 6.5. The mean voxel GM and WM tissue contents were not significantly different between the two sexes in all three brain regions ($p > 0.05$). However, most voxels in the frontal region of the females had more GM tissue compared to those in the males; nonetheless the mean voxel GM tissue content difference between them was not, but close to being, significant ($p = 0.061$).

Brain region	Mean GM fraction ± SD (range)			Mean WM fraction ± SD (range)		
	Males	Females	p-value	Males	Females	p-value
Frontal	0.52 ± 0.01 (0.50-0.55)	0.56 ± 0.05 (0.51-0.68)	0.061	0.48 ± 0.11 (0.45-0.50)	0.44 ± 0.13 (0.32-0.49)	0.783
Parietal	0.52 ± 0.06 (0.37-0.58)	0.51 ± 0.02 (0.47-0.55)	0.397	0.48 ± 0.06 (0.42-0.63)	0.49 ± 0.02 (0.45-0.53)	0.357
Occipital	0.47 ± 0.07 (0.37-0.55)	0.49 ± 0.10 (0.40-0.76)	0.684	0.53 ± 0.07 (0.45-0.63)	0.51 ± 0.10 (0.24-0.06)	0.519

Table 6.5: Voxel tissue compositions in the left hemisphere of subjects by sex.
Comparisons were done by two-sample t-tests

Water contents of GM and WM did not vary significantly between males and females in the frontal, parietal and occipital brain regions (Table 6.6). The

mean water contents ± SD in mol/kg wet weight for males/females in the frontal (43.2 ± 11.5/47.4 ± 11.9; p = 0.412), parietal (33.63 ± 5.15/37.6 ± 10.0; p = 0.271) and occipital (33.8 ± 3.39/38.6 ± 10.1; p = 0.183) regions were also not significantly different. Females however showed slightly higher mean water content than males in all the three brain regions (Figure 6.4).

Brain region	GM Water content ± SD (mol/kg)			WM Water content ± SD (mol/kg)		
	Males	Females	p-value	Males	Females	p-value
Frontal	42.8 ± 11.4	47.0 ± 11.8	0.406	47.1 ± 11.7	45.6 ± 13.0	0.783
Parietal	36.4 ± 5.7	38.0 ± 9.6	0.656	30.8 ± 6.2	37.1 ± 10.8	0.116
Occipital	31.9 ± 5.0	37.9 ± 13.6	0.213	35.7 ± 6.7	39.2 ± 13.5	0.476

Table 6.6: Mean GM and WM water contents compared between males and females

Among the males, GM water content varied significantly (p = 0.016) across the brain such that frontal WC > parietal WC > occipital. WM water content also varied significantly (p = 0.001) such that frontal WC > occipital WC > parietal WC. However, the mean water contents in the three regions were not significantly different (p = 0.199). The variation in water contents of both GM and WM followed the same pattern in females but they did not vary significantly in the three regions (p = 0.136 for GM, p = 0.265 for WM). Mean water content did not also vary significantly in the three regions (p = 0.128) in the female group.

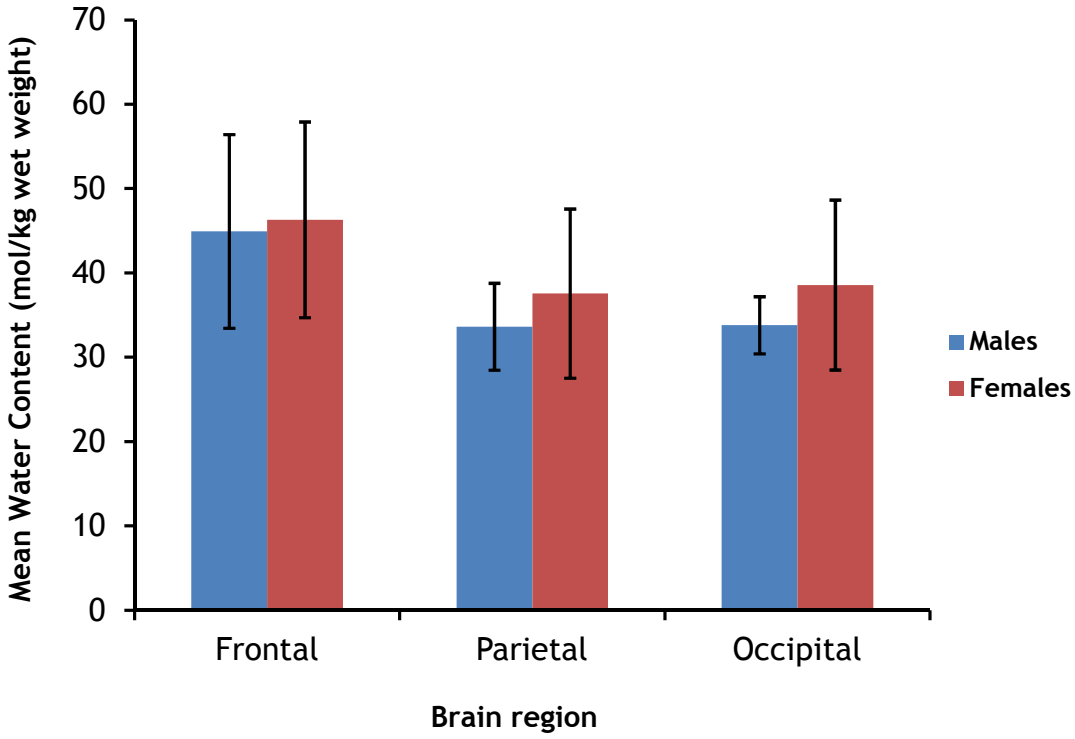

Figure 6.4: Mean water contents in the three voxel positions compared between males and females.
Error bars represent ±standard deviations

To the best of the author's knowledge, no study in the literature has compared brain tissue water contents of the above brain regions as measured by MRS between males and females.

6.3.1.4 Association between Voxel Tissue and Water Contents

The tissue-specific and mean WC values depend on a number of parameters (equation 6.3), each contributing in a different way to the estimate. However, since the thesis focuses on tissue-bound water content, it was necessary to assess the extent to which the amount of voxel tissue contributed to its corresponding water content. It can be deduced from equation 6.3 that voxel tissue and water contents are directly related. It is thus the strength of this relationship that is investigated in this section.

The contributions of the voxel contents of GM (Table 6.7) and WM (Table 6.8) to the estimated water contents in the two tissue classes, and to the mean water content, for the three regions of interest were investigated by Pearson's correlation analysis.

Association; Significance	Frontal voxel		Parietal voxel		Occipital voxel	
	GM WC	Mean WC	GM WC	Mean WC	GM WC	Mean WC
r;	0.678;	0.070;	0.939;	0.206;	0.361;	0.113;
p-value	0.001	0.768	< 0.01	0.399	0.118	0.636

Table 6.7: Pearson's correlation analysis of the association between voxel GM tissue content, GM WC and mean WC.
The mean water content is the average of the GM and WM water contents of the region of interest; r is the Pearson's correlation coefficient; and p-value is the strength of the association

Association; Significance	Frontal voxel		Parietal voxel		Occipital voxel	
	WM WC	Mean WC	WM WC	Mean WC	WM WC	Mean WC
r;	0.566;	0.070;	0.945;	0.798;	0.638;	0.113;
p-value	0.009	0.768	< 0.01	< 0.01	0.002	0.636

Table 6.8: Pearson's correlation analysis of the association between voxel WM tissue content, WM WC and mean WC

In the frontal voxels, both GM and WM contributed significantly to their respective water contents. For the GM water content, the voxel content of GM tissue contribution alone was significant at 45 % (i.e. 0.678^2; p = 0.001); whereas the contribution to WM water content of WM tissue alone was about 32 % (p = 0.009). Both tissue types contributed equally, but not significantly (p = 0.768), to the mean frontal water content.

In the parietal voxels, both tissue types again contributed significantly (p < 0.01) to their respective water contents. However, WM alone still contributed (about 64 %; p < 0.01) significantly to the mean GM/WM water content. The parietal brain region is predominantly WM tissue, and so even though the mean parietal GM was higher than the mean parietal WM (Table 6.3), most voxels were positioned in the deep WM brain region (see the range of voxel WM tissue

contents in Table 6.3). This might explain why WM tissue contributed more, and significantly, to the mean water content in the parietal voxels but GM tissue did not.

The occipital brain region is predominantly GM. However, most occipital voxels were placed deeper in the brain, containing more WM tissue (Table 6.3). Therefore, WM alone contributed significantly to its water content but GM did not; both tissue types then contributed equally, but not significantly, to the mean GM/WM occipital water content.

6.3.1.5 Variation in Brain Tissue Water Content with Age

In all the three brain regions, neither tissue-specific nor mean water content variation was found to be associated with age in both sexes, and in the whole study sample put together. An example regression plot of mean frontal water content versus age is shown in Figure 6.5. The plot shows an average water content of 37.38 mol/kg wet weight whose change over time is indicated by the gradient of the straight line. The gradient, which measures the change in water content with age, is only 0.0704; this is not a significant change ($p = 0.655$). In fact, Christiansen et al [61] did not also find a significant difference in water content in their groups of adolescents, adults and the aged (ages between 10 and 74 years). Brain tissue water content variation has also been reported elsewhere [177] to remain insignificant with age in a group of healthy subjects, aged 20 to 70 years. Similarly, brain tissue water content appears to be fairly stable with age within the studied age group (between 20 and 64 years) of adults in this thesis.

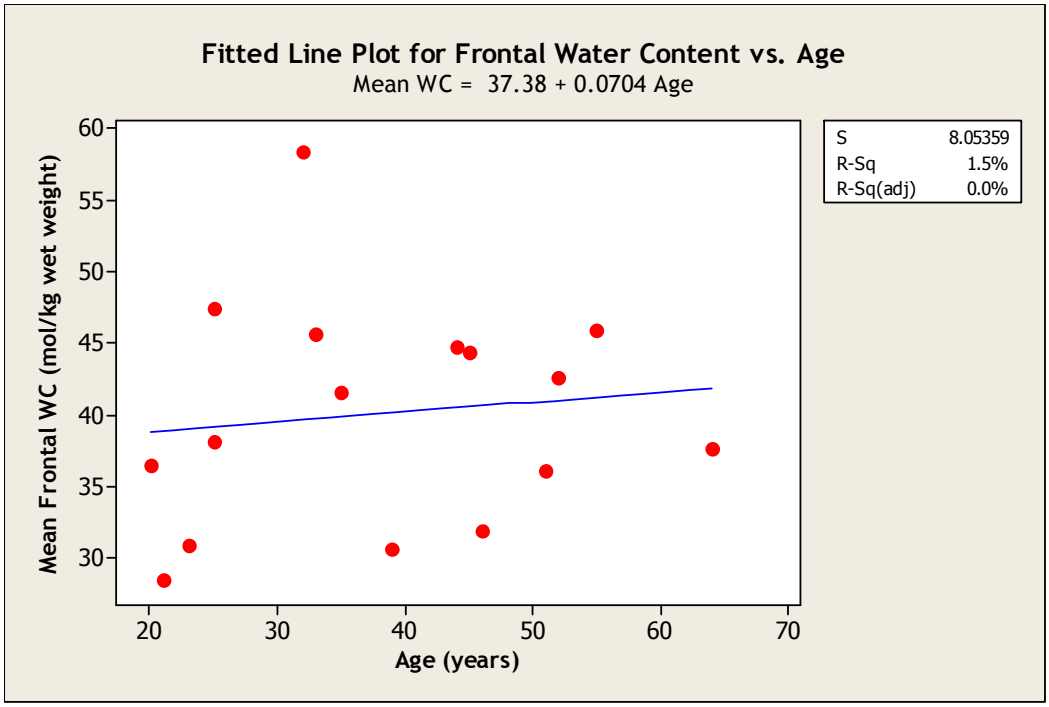

Figure 6.5: Variation in brain tissue water content with age.
No significant change with respect to age was observed: p = 0.655; r = 0.121 (this is only a 1.4 % increase in tissue water content with age)

6.3.2 Hippocampal Tissue Water Content

Subsections 6.3.2.1-2 discuss the results for study 6B recording MRS data from the left and right hippocampi of male subjects. The results for this study are presented in two subsections: the first (section 6.3.2.1) compares the mean water contents between the left and right hippocampi, and the second (section 6.3.2.2) investigates variation in hippocampal water content with age. All the subjects in this study were males, and so it was not possible to do the water content analysis by gender in this case.

6.3.2.1 Left versus Right Hippocampal Water Contents

The mean ± SD percentage of hippocampal tissue fraction covered by the voxel in the left (82 ± 6 %) and right (82 ± 8 %) hemispheres did not differ (p = 0.706). The mean ± SD of the left hippocampal water content (37.34 ± 8.02 mol/kg wet weight) was not significantly different (p = 0.648) from that of the right hippocampus (36.24 ± 13.93 mol/kg wet weight) as shown in Figure 6.6. In both

hippocampi, the voxel tissue contents were found to contribute significantly ($p < 0.05$) to their respective mean water contents.

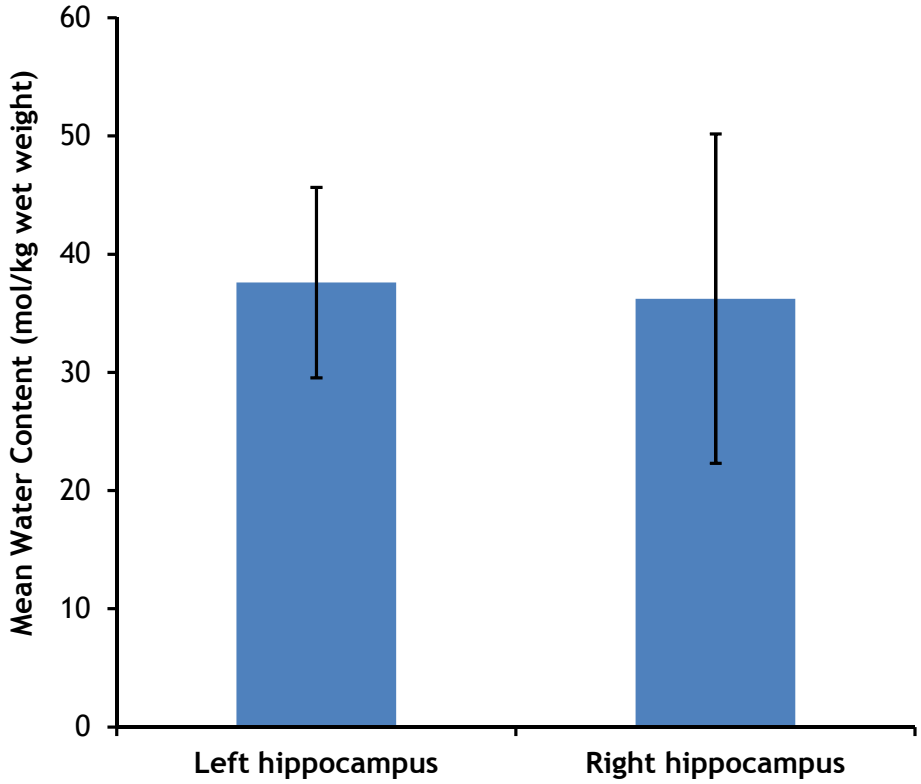

Figure 6.6: Mean water contents in the left and right hippocampi compared.
Error bars represent ±standard deviations

6.3.2.2 Variation in Hippocampal Water Content with Age

Variation in hippocampal water content with age was assessed by correlation tests. The regression plots representing the variation in water contents with age of the left and right hippocampi are shown in Figures 6.7 and 6.8, respectively. In both hippocampi, tissue water content did not vary significantly with age ($p > 0.05$). The small, but not significant, decreases in hippocampal water content over time may be suggesting hippocampal tissue atrophy associated with normal ageing. This could result in a small increase in CSF within the hippocampal regions over time; the increase in CSF fraction of the MRS voxel over time has been reported elsewhere [177].

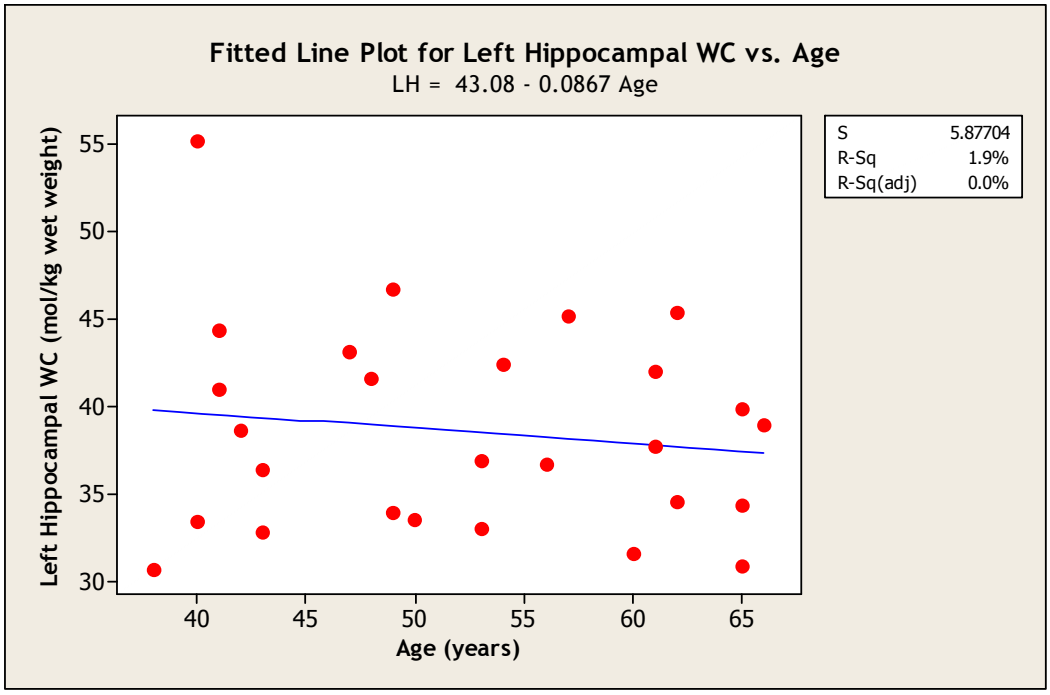

Figure 6.7: Variation in left hippocampal water content with age.
No significant change with respect to age was observed: p = 0.493; r = -0.138 (this is only a 1.9 % decrease in tissue water content with age)

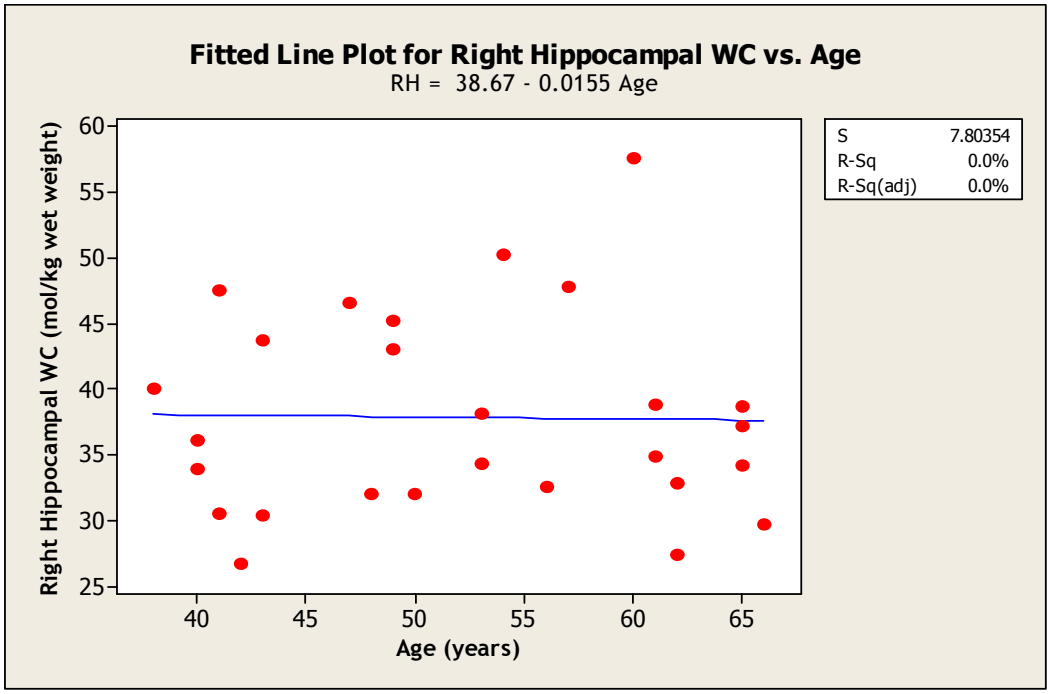

Figure 6.8: Variation in right hippocampal water content with age.
No significant change with respect to age was observed: p = 0.926; r = -0.019 (this is only a 0.04 % decrease in tissue water content with age)

6.3.3 Distribution Profile of Brain Tissue Water Content

An exploratory one-way ANOVA test was performed on the hemispheric and hippocampal water contents in order to assess whether whole brain tissue water content varied across the voxel positions in the two studies (i.e. studies 6A and 6B). This analysis was based on the assumption that the water contents were estimated for each subject in the frontal, parietal, occipital, left and right hippocampal voxels. It became necessary to make this assumption because no single subject in this thesis was scanned in all these voxel positions. The consequence of the assumption, however, could be that some amount of inter-subject variability could influence the result of the statistical test.

Figure 6.9 shows the variation of brain tissue water content in the frontal, parietal, occipital, left and right hippocampi. The exact water content values for all these brain regions are provided in Table 6.10. The ANOVA test indicated that the mean water contents did not vary significantly ($p = 0.599$) among the five voxel positions. The results thus suggest that brain tissue water content might be uniformly distributed across the brain (considering the five regions investigated).

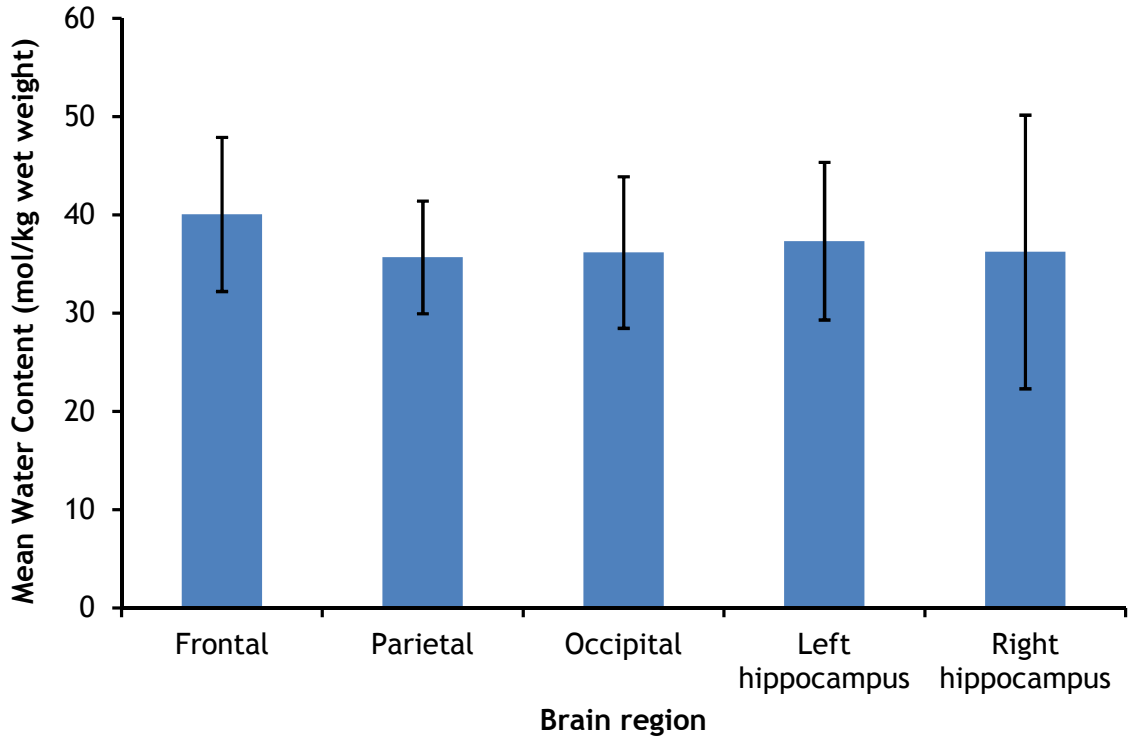

Figure 6.9: Brain tissue water distribution profile.
Error bars represent ±standard deviations

The limitation of this study is that only the left hemisphere was investigated for the frontal, parietal and occipital water contents. However, bilateral MT studies (which also probed tissue water content) indicated that water content does not vary significantly between the two hemispheres (Table 6.9). In fact, the left and right hippocampal study also corroborates this argument (section 6.3.2.1). Another limitation is the lack of data for same-brain measurements of tissue water content in all the five voxel positions. Both gender (section 6.3.1.3) and age (sections 6.3.1.5 and 6.3.2.2) do not appear to influence tissue water content significantly. Therefore, the expected inter-subject variability due to the age and gender difference between the two studies should not substantially affect the results of the ANOVA test combining the datasets. Nonetheless, it is recommended that future studies measuring regional brain tissue water content should do so for all voxel positions within the same brain. Only then can the possibility of the inter-subject variability

(due to separate voxel positions in different subject groups) be avoided completely.

6.3.4 Regional Brain Tissue MT Effects

This section presents the results, in three subsections (sections 6.3.4.1-3), of the MT imaging study (study 6C): section 6.3.4.1 compares the MT ratios between the left and right hemispheres, section 6.3.4.2 compares the MT ratios between males and females, and section 6.3.4.3 investigates the variation of the MT effect with age.

6.3.4.1 Left versus Right Hemispheric MT Ratios

Table 6.9 summarises the comparison of the percentage MT ratios between the left and right hemispheres, specifically within the same brain structures investigated for water content (i.e. frontal, parietal, occipital, left and right hippocampi).

Brain region	Mean percentage MT ratio ± SD (range)		p-value
	Left hemisphere	Right hemisphere	
Frontal	29 ± 8 (20-41)	29 ± 9 (18-41)	0.640
Parietal	29 ± 7 (23-40)	29 ± 6 (22-37)	0.135
Occipital	30 ± 9 (19-41)	29 ± 8 (18-40)	0.904
Hippocampus	21 ± 6 (10-27)	22 ± 6 (11-27)	0.264

Table 6.9: Percentage MT ratios in the left and right hemispheres compared

Apart from the hippocampus, none of the other three regions was investigated bilaterally for water content. The paired t-test indicates laterality of percentage MT ratio in all regions. This may as well be the case for water content in the frontal, parietal and occipital regions but data was not available to confirm this. A one-way ANOVA also did not find significant variation in percentage MT ratio among all the regions ($p = 0.081$). Thus, the uniform distribution of percentage MT ratio in these regions corroborates the validity of

the deduction made about the uniform distribution of tissue water content as observed in section 6.3.3.

6.3.4.2 Percentage MT Ratio by Sex

For all ROIs, MT ratios did not vary significantly among both males ($p = 0.136$) and females ($p = 0.310$). Mean percentage MT ratios were also not significantly different between males and females (M/F ± SD) in the frontal (23.72 ± 6.42 %/33.94 ± 7.36 %; $p = 0.091$), parietal (25.56 ± 5.17 %/32.46 ± 6.33 %; $p = 0.152$) and occipital (26.96 ± 6.49 %/32.03 ± 9.25 %; $p = 0.410$) ROIs. Only the mean hippocampal percentage MT ratios between males (17.03 ± 5.28 %) and females (25.14 ± 2.24 %) was found to be significantly different ($p = 0.047$) as shown in Figure 6.10.

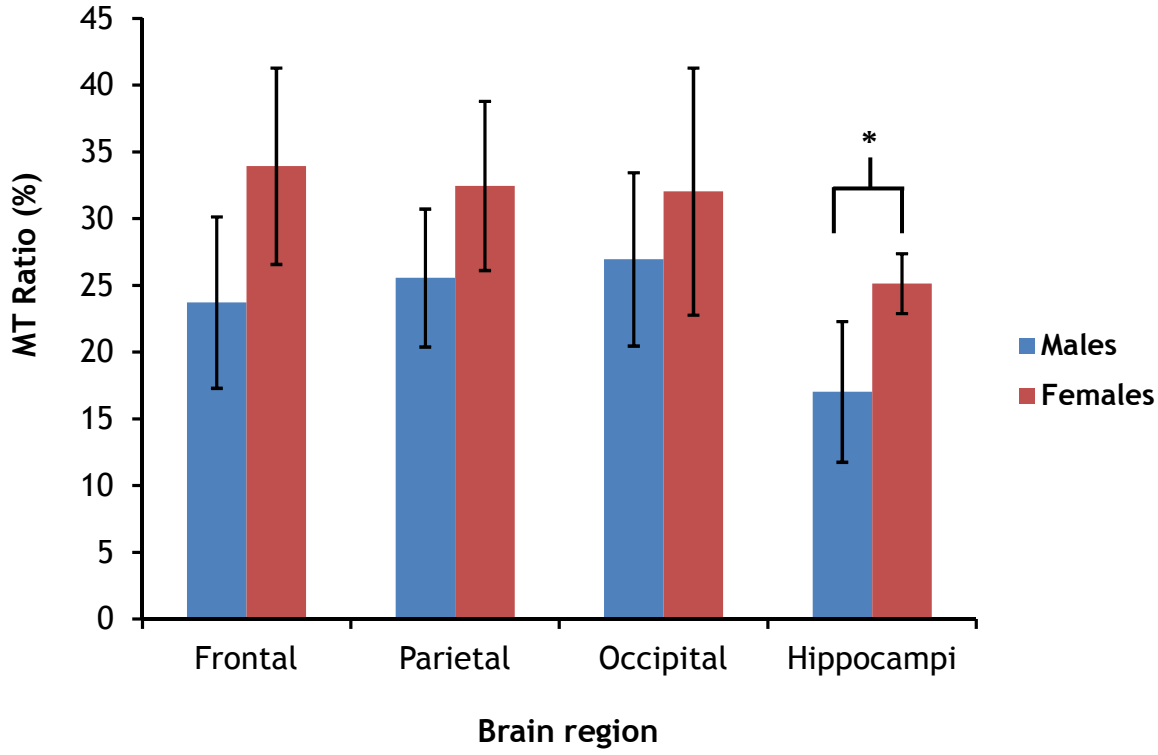

Figure 6.10: Mean MT ratios compared between males and females.
For both groups, the means of the MT ratios for all ROIs in the two hemispheres was averaged; the error bars represent ±standard deviations. *The difference in hippocampal MT ratio between males and females was significantly different ($p = 0.047$).

Hippocampal water content was estimated only in males in this thesis and it is unclear if males and females in a normal population will show a significant difference in mean hippocampal water content (as with the mean hippocampal MT ratio observed here). To the best of the author's knowledge, no study was cited in the literature investigating gender-related hippocampal water content or MT effects.

The difference in the age range between males (29-51 years) and females (23-32 years) was rather too wide, even though the statistical analysis did not show a significant mean age difference between the two groups ($p = 0.101$; Table 6.1). Brain tissue atrophy occurs with normal ageing [1, 182]. Atrophy decreases the amount of water bound in brain tissue which MT imaging measures. MT ratio has therefore been observed to decrease with atrophy [183-185]. Hence, it is likely that the lower mean percentage MT ratio in the male population could be due to age-related atrophy in some of the elderly subjects. It may also be that the hippocampus is more susceptible to age-related brain tissue atrophy than the other brain regions. It may however be misleading to make a conclusion on this significant difference in hippocampal MT ratio with only 4 subjects in each sex group. This therefore warrants further investigation of the MT effects in these ROIs in a larger population of males and females within the same age group. Only then can a conclusion be made on whether the significance observed in this study is accurate or otherwise.

6.3.4.3 Age-MT Ratio Association

Pearson's correlation analysis was performed between age and the mean percentage MT ratios in the frontal, parietal, occipital and hippocampal ROIs.

Age accounted for 12.3 % ($p = 0.395$), 7.3 % ($p = 0.516$), 3.0 % ($p = 0.681$) and only 0.7 % ($p = 0.848$) of the variances in mean percentage MT ratios in the frontal, parietal, occipital and hippocampal ROIs, respectively. The contribution of age (23-51 years) to the measured MT effects within this population was not found to be significant as indicated by the p-values ($p > 0.05$). Age does not therefore appear to explain the significant difference in

the mean percentage hippocampal MT ratios between males and females as was thought initially by the author (see discussion in section 6.3.4.2). This thesis did not however investigate this further due to time limitation.

6.3.5 Comparison between Water Content and MT Ratio Profiles

The mean MT ratio and water content estimates for all the brain regions investigated in this chapter are summarised in Table 6.10.

Brain region	MT ratio ± SD (%)	Water content ± SD (mol/kg)
Frontal	28.83 ± 8.16	40.06 ± 7.84
Parietal	29.01 ± 6.33	35.69 ± 5.73
Occipital	29.50 ± 7.91	36.18 ± 7.71
Left hippocampus	20.61 ± 5.98	37.34 ± 8.02
Right hippocampus	21.55 ± 5.69	36.24 ± 13.93

Table 6.10: Comparison between MT ratio and water content estimates by region of interest

WM is high in myelin sheaths [186] which promote the MT effect [178, 186] and so the MT ratios were observed to decrease with decreasing amount of WM tissue within the selected ROI. Thus in decreasing order of WM tissue content/MT ratios, Table 6.10 shows that: occipital > parietal > frontal > right hippocampus > left hippocampus. The predominantly GM brain regions (i.e. frontal and hippocampal regions) have comparatively less MT effects.

GM water content is reported to be slightly higher than that of WM [49, 58, 59]. Therefore, the predominantly GM brain regions will have more tissue-bound water than the WM regions. Table 6.10 thus indicates decreasing amount of tissue water contents from the GM to WM structures; i.e. frontal WC > left hippocampal WC > right hippocampal WC > occipital WC > parietal WC.

The variations of both MT ratios and water contents were not significant ($p > 0.05$) across the brain regions studied. Estimation of MT ratio does not require

any correction (but its reproducibility is affected by flip angle settings and variation in the B_0 field [1]) as compared to estimation of tissue water content. It is therefore easier and less time consuming to conduct an MT imaging study. The comparison of the two datasets in this section indicates that if both techniques are done on the same subjects, the MT ratio variation could be used to validate the tissue water distribution profile across the same brain regions.

6.4 Summary and Conclusions

The first objective of the work presented in this chapter was to develop an MRS technique for the accurate quantification of brain tissue water content. The technique employs similar corrections (to those in the literature) to the unsuppressed-water signal using a comprehensive mathematical model that yields the water content value. The novelty of the technique lies in the use of the *in vivo* voxel coordinates to deduce a reference signal. In addition to this, the unsuppressed-water signal is also obtained from a water-suppressed acquisition, and a straightforward correction factor is included in the model to account for T_1 and partial recovery losses, simultaneously. Therefore, the developed method is applicable to any water-suppressed acquisition from any voxel position within the eight-channel head coil. The limitation of its use in this thesis was the use of measured T_2 relaxation times in a different sample to correct the water signal for T_2 relaxation effects. Most studies in the literature have corrected for relaxation times in the same way; the study by Brief et al [58] is an example. This is a common practice since it is inherently impractical to perform both relaxation and water content measurements in any single volunteer, simultaneously. In this thesis, the CoVs in the T_1 and T_2 estimates did not exceed 10 % among the subjects; therefore an error of not more than this could have been introduced into the water content estimates.

Following the development of the tissue water quantification technique, the second objective in this chapter was to assess the variation in the quantified tissue water content across the brain. The brain regions (from two separate studies) assessed included the frontal, parietal, occipital, left and right

hippocampi. Aside from the hippocampi, all other regions were studied only in the left brain hemisphere due to lack of data for the right hemisphere. Generally, grey matter (GM) water content was found to be higher (though not significantly) than white matter (WM) water content, in agreement with the findings of previous studies. Water content (WC) was found to vary significantly in both tissue types across the brain, with frontal GM WC > parietal GM WC > occipital GM WC and frontal WM WC > occipital WM WC > parietal WM WC. The left and right hippocampal water contents were not significantly different. The mean water contents did not vary significantly among all the brain regions. Water contents in the frontal, parietal and occipital regions also did not vary significantly between males and females; there was no data for hippocampal water content in females. Water content by tissue type (and mean WC) in all the brain regions did not vary with age in both males and females; but was influenced by the amount of each tissue type in the voxel.

Assessment of the variation in regional brain tissue water content was conducted using the one-way ANOVA test. This was done by putting together the water content results from two studies: frontal, parietal and occipital WC from one study, and left and right hippocampal WC from another. Combining two different datasets from two separate studies investigating different brain regions could introduce some degree of uncertainty arising from inter-subject variability in the ANOVA results. With the developed technique in this thesis, it is possible for future studies to measure water content in all the brain regions in the same subject within tolerable scan times.

The last objective in this chapter was to use MT imaging to assess the variation in the MT effect arising from tissue-bound water. This was to enable the comparison of the variations in brain tissue water content and the MT effect in the same brain regions. In the MT imaging study, it was possible to study all the brain regions that should have ideally been studied in the MRS studies. Thus, bilateral MT effects, expressed as MT ratios (MTR), were measured in the frontal, parietal, occipital, left and right hippocampi. Even though there is evidence of regional/anatomical variation of MT ratios in the normal adult brain [180, 181], and physiological age-related variation in MT ratios [178,

179], this thesis did not find variation in the MTRs among the brain regions, and between the left and right brain hemispheres in those regions. MTR did not also vary significantly with age and among males and females separately. MTR did not also vary in those brain regions between males and females except for mean hippocampal MTR which was significantly higher ($p = 0.047$) in females. This however could not be confirmed for the water content in the hippocampus as no female was studied for hippocampal water content. The female group comprised of a relatively young population compared to the male group. There is evidence for high myelin content in the younger brain [178], and myelin has high amounts of galactocerebrosides which enhance the MT effect, as reflected by high MT ratios. The sample size for the MT study was however small and the influence of random errors (arising from subject-specific bias) on this significant finding cannot be ruled out. Future studies would have to study a larger sample size of males and females of comparable age groups. This will minimise any possible age and sample size related effects on the findings.

Comparison of the MTRs and tissue water contents indicated the same pattern of variation across the brain, and the same associations with age. Both quantities were fairly uniformly distributed across the brain regions investigated, and did not vary with age. However, they were not measured in any one volunteer at the same time and this could be a limitation in the comparison as the regions of interest did not necessarily contain the same relative amounts of GM/WM. At best, the ROIs for the MT imaging study were carefully selected using the structural scans from the MRS studies as a guide. This minimised substantial mismatch between each MT image ROI and its corresponding MRS voxel position.

Finally, the findings of the work presented in this chapter are particularly in support of the suitability of tissue water as a concentration reference for quantifying cerebral metabolites. The results in this chapter suggest that cerebral water content does not appear to vary substantially with age, gender and brain region. However, there could be significant variations in the water contents between grey and white matter tissues. The water content

quantification technique presented will make it more convenient and rapid to quantify the metabolites relative to endogenous tissue water content.

Chapter 7: Brain Tissue Water and Metabolite Concentrations in Psoriasis

7.1 Introduction

Inflammation is a defensive mechanism of the human body against harmful agents. The inflammatory process could however sometimes lead to a harmful condition known as auto-immune disease. Common auto-immune diseases include multiple sclerosis and arthritis. Two forms of arthritis are mostly studied by MRS in the literature: rheumatoid (in the joints, affecting synovial fluid) and psoriatic (mostly on the skin, causing plaques) arthritis. Whereas multiple sclerosis directly affects the brain, arthritis affects peripheral organs of the human body.

It has been reported that cerebral water content could increase by at least 12% [154] with associated changes in the levels of cerebral metabolites [187-189] in multiple sclerosis compared to the normal brain. There is also evidence of the involvement of the human brain even in peripheral inflammation, where the brain is not directly involved. MRS studies of rheumatoid arthritis [190, 191], and at least one study of psoriatic arthritis [191], have also reported changes in the levels of cerebral metabolites (reported in ratio units). No MRS or any brain imaging study has reported changes in the levels of water either in the brain or any part of the body in either forms of arthritis.

In the healthy population, significant changes in the levels of water in body tissue has been reported to be associated with behavioural/mood and performance changes [34, 37]. Similarly, the inflammatory condition is also believed to be associated with behavioural/mood changes in the affected persons [192-194]. MRS brain studies investigating the relationship between mood and cerebral metabolite changes in multiple sclerosis, psoriatic and rheumatoid arthritis have previously been conducted. The most commonly

studied metabolites in these studies of inflammation (i.e. multiple sclerosis, psoriatic and rheumatoid arthritis) were NAA, Cho, Cr, Glu and mI. Mood changes have been found to be associated with changes in mI and Glu, particularly [195]. However, no previous MRS brain study has studied the relationship between mood and cerebral water changes in any one of these inflammatory conditions.

In this chapter, the impact of the peripheral inflammatory condition, psoriatic arthritis on the absolute concentrations of cerebral water and the metabolites (i.e. the notable ones above: NAA, Cr, Cho, mI and Glu) will be investigated, simultaneously. Secondly, the effects of the possible changes in brain metabolism (i.e. changes in water and metabolites) on mood will also be explored. Compared to the previous studies, the above investigations are novel since they involved the simultaneous measurements of the absolute concentrations (rather than ratios) of cerebral water and the metabolites in psoriatic arthritis for the first time. Investigation of the mood-water content relationship in psoriatic arthritis has also not been done previously.

Specific brain regions are believed to be primarily adapted to mood control (e.g. the prefrontal and hippocampal regions). Therefore, the MRS voxel positions were prescribed in the prefrontal grey matter (GM) and bilateral hippocampi. The prefrontal voxel contained predominantly grey matter (mean ± SD = 86 % ± 7), and so the estimated metabolite and water concentrations were considered to be for grey matter (excluding white matter and CSF). The hippocampus is a predominantly grey matter brain structure, and so localising the MRS voxel in the predominantly grey region would make it appropriate to conduct an exploratory analysis of the regional (i.e. in the prefrontal GM and hippocampi) variation in the concentrations of the cerebral metabolites and water. Inclusion of the small amount of white matter tissue in the estimates of the prefrontal concentrations would rather yield an average for the two tissue types, and it would then not be appropriate to conduct the required exploratory analysis. It is important to mention that, the voxel tissue contents of the previous studies of the above inflammatory conditions were

predominantly white matter; thus, the work presented here is unique regarding the brain tissue type studied.

Cerebral water and creatine (Cr) have been used as endogenous references in absolute quantitative MRS. Variation in cerebral water content with age, gender and brain region was investigated in chapter 6 in order to test whether its concentration remains the same with these variables. The work in this chapter thus also tests the variations in the cerebral concentrations of Cr and water with age, gender and brain region in order to compare the two for their stability with these variables. In fact, NAA [196] and Cho [197] are also sometimes used as denominators for expressing metabolite ratios. For this reason, NAA and Cho were also included in the above exploratory analysis.

Before describing the work in this chapter in detail, it would be helpful to provide some background to the cause and progression of inflammation (section 7.1.1.1), and how the brain is implicated in the inflammatory process (section 7.1.1.2). One of the treatment options of the condition is the use of anti-inflammatory medication, which tries to reverse the inflammatory process. Thus, a discussion of the role of anti-inflammatory therapy on brain chemistry and the consequence of this effect on mood is also presented (section 7.1.1.3). Finally, this background section concludes with a brief discussion on what MRS can offer in the studies of inflammation, and the objectives of this chapter (7.1.2).

7.1.1 Brain involvement in Psoriasis

7.1.1.1 Pathogenesis of Inflammatory Disease

The immune system (through vascular tissues) of the body offers complex biological mechanisms to protect it from various disease causing agents known as pathogens, as well as other potential harmful substances such as damaged cells or irritants. This immune response mechanism of the body is known as inflammation. The primary purpose of the inflammatory mechanism is to

remove the injurious agent and initiate a healing process for the tissue. Inflammation is not necessarily an infection but can be caused by an infectious pathogen [198, 199].

In some cases, the immune system of the body inappropriately triggers the inflammatory response in the absence of the harmful agent. This is known as auto-immune response, and it results in the release of white blood cell chemicals that otherwise become harmful to the tissues of the body. The initial inflammatory response increases the movement of plasma and leukocytes from the blood into the injured tissues; this is known as acute inflammation. A cascade of biochemical events may occur and translate the acute response into chronic inflammation which progressively changes the type of cells within the site of the inflammation [200]. Chronic inflammation is characterised by the simultaneous destruction and healing of tissues, which can result in a host of diseases including rheumatoid (RA) and psoriatic (PsA) arthritis [199-201]. The chronic inflammatory, non-contagious autoimmune disease of focus in this thesis is psoriatic arthritis (PsA).

Psoriasis commonly causes red, scaly patches to appear on the skin and joints. The scaly patches, called psoriatic plaques, are areas of inflammation and excessive skin production (which results in the rapid accumulation of skin, silvery-white in appearance, at these sites). Common occurrences of plaques are on the (extensor) skin of the elbows and knees, but can affect any part of the body including the scalp, fingernails and genitals. Psoriatic inflammation (or plaques) of the joint is what is known as psoriatic arthritis. The symptoms vary among different patients, and may also go through various cycles in a patient. The cause of PsA is not clear but it is believed to have a genetic component; and is likely to be aggravated in affected individuals by stress, smoking, excessive alcoholism and withdrawal of systemic corticosteroid [192, 202]. Due to its chronic recurrent nature, PsA is difficult to treat despite the availability of a number of treatment options [191].

7.1.1.2 Involvement of the Central Nervous System in Inflammatory Disease

Apart from immune cells, non-immune cells such as epithelial cells, endothelial cells and fibroblasts also contribute to inflammatory processes [199]. Inflammatory pathways and their target tissues vary widely depending on the nature of stimulants. In the presence of bacterial infection, the immune cells through specific receptors immediately sense pathogens. Activation of pathogen-specific receptors induces the production of inflammatory mediators such as inflammatory cytokines [e.g. tumor necrosis factor (TNF), interleukin-1 (IL-1) and interleukin-6 (IL-6)] and chemokines. These mediators rapidly accelerate the progression of inflammation by modifying the permeability of vascular endothelial tissues; they also direct neutrophils and excess plasma into the site of infection. At the same time, the invading pathogens are targeted and destroyed by the immune cells [192, 199].

In most cases, inflammatory responses extend toward systemic effects through the excessive production of pro-inflammatory cytokines, which mediate the secretion of acute phase proteins by the liver cells [199]. These proteins, in turn, induce brain endothelium and facilitate the production of prostaglandins, which are primarily responsible for the onset of symptoms (e.g. psoriatic arthritis) through their effects on the central nervous system.

7.1.1.3 Effect of Anti-inflammatory Therapy on Brain Chemistry and Mood

In peripheral disease, such as PsA, animal studies [203, 204] have shown that peripheral immune cells access the brain through humoral and/or neural routes, resulting in central neural changes and associated behavioural alterations. TNF-α (a pro-inflammatory cytokine) signalling was implicated as the prerequisite for this peripheral-CNS communication process to occur [199, 203, 204]. This peripheral cytokine (TNF-α) stimulates microglia to produce the harmful protein molecules that access the brain through a number of ways

including crossing the blood brain barrier [192, 193]. There is also an indication [189, 205] that during the inflammatory process, the CNS might attempt to reduce neuroinflammation by conducting some water-soluble proteins out of the brain to the site of inflammation; thus increasing the levels of cerebral water, which could possibly result in edema [205]. Chronic inflammation may arise where this defensive function of the brain has been compromised. Therefore, any form of anti-TNF-α therapy targeted at inhibiting microglial activation or blocking the receptors of microglia could reverse the communication pathway between the CNS and the periphery, and reduce the physiological and behavioural impacts of peripheral inflammation [192-194].

The inflammatory-related physiological changes in the CNS have been reported by brain imaging studies (including fMRI [206], PET [207] and SPECT [208]) to be associated with under-activation of the forebrain structures (notably the dorsolateral prefrontal and anterior cingulate cortices) and over-activation of the limbic structures (notably the hippocampus, amygdala, insula and thalamus). This activation pattern has been shown by various ^{1}H-MRS studies to correlate with changes in brain chemistry in these brain regions [209-213].The consequence of these physiological alterations in these brain regions might explain the associated behavioural changes over time.

7.1.2 The Role of MRS in Studies of Inflammation and Objectives

In section 7.1.1, it can be inferred that inflammation has a molecular basis which involves initial biochemical processes at the cell level. Even though inflammation may affect peripheral organs, the involvement of the brain in the disease process could have implications for normal cerebral metabolism. Thus, subtle biochemical changes may occur in the brain, but may not be visible on a normal MRI of the affected individual. MRS is relatively sensitive [1] at recording the minute inflammation-related biochemical changes before the effects of the disease are manifested on a macroscopic scale on MRI.

The previous section has also indicated that as a chronic inflammatory condition, psoriatic arthritis can be treated by an anti-TNF-α medication that acts to reverse the communication pattern between the mood-regulating brain regions and the peripheral inflammation sites, and possibly impact on mood as a result. In this thesis, therefore, psoriatic arthritis patients received an intravenous injection of anti-inflammatory/anti-TNF-α medication, and MRS of their prefrontal and hippocampal brain regions were studied to observe changes in their neurochemistry (i.e. cerebral water and metabolites), and associated mood changes.

The objectives of this chapter were to:

1. Develop a method to quantify cerebral metabolites using an optimised endogenous water signal from the same MRS acquisition;
2. Quantify changes (from normal and with anti-inflammatory medication) in prefrontal and hippocampal metabolite and water concentrations in psoriatic arthritis (PsA) patients;
3. Investigate possible associations between metabolite concentrations as measured by MRS and mood assessment outcomes in medicated PsA patients;
4. Assess the variation in regional water and metabolite concentrations in the brains of PsA patients and healthy controls.

7.2 Methods

7.2.1 Subjects, Mood Assessment, MRI/MRS and Voxel Placement

7.2.1.1 Recruitment of study volunteers and their characteristics

The patient group in this study were recruited in the context of another study that was not part of this thesis. This patient group comprised of subjects diagnosed with psoriatic arthritis (PsA) and were attending the Rheumatology departments of NHS Greater Glasgow and Clyde Hospitals. Prior to study entry, no patient was receiving the Etanercept medication as a treatment for psoriatic arthritis. On study entry, they received the medication only after their first (or baseline) MRS scans. Etanercept is a TNF-α blockade medication for inflammatory conditions, including PsA. The study and the exact procedure participants went through were described to prospective PsA volunteers and only those who gave prior written consent participated in the study. The control group was recruited for the study in this thesis, specifically. Ethical issues about the study and eligibility screening of the study volunteers were discussed in section 2.3.5.

Each group of the controls and patients comprised of 8 males and 8 females. The controls/patients did not vary significantly in mean age (SD): 38.9 (11.9)/45.9 (9.9) years, $p = 0.068$. There were no significant mean age (SD) differences between males/females in the patient (46.3 (10.3)/45.0 (10.8) years, $p = 0.816$) and control (37.1 (12.9)/36.1 (11.2) years, $p = 0.871$) groups.

7.2.1.2 Medication and Mood Assessment of the Psoriasis Patients

The patients had an MRS scan prior to taking the Etanercept medication (given intravenously), followed by 6-8 weeks of the medication, and another MRS scan post-medication. The Beck's Depression Inventory (BDI), a self-assessment mood questionnaire, was answered by each patient before each one of the MRS scan sessions (i.e. at pre- and post-medications).

The BDI (Appendix 7.1) is a 21-item questionnaire, each item comprising of four questions arranged in worsening order of mood condition that are scored from 0 to 3. For all 21 questions, the volunteer marks the score corresponding to their present mood condition and then sums up all the scores for each one of the 21 questions by counting the marked scores. If the participant scores 3 on all twenty-one questions, then the highest total for the entire test will be 63; and the lowest possible score will be 0 if they scored 0 on each one of the twenty-one questions. When the total depression score is evaluated, the level of depression in the individual can be interpreted according to Table 7.1.

Total BDI score	Level of depression
1-10	These ups and downs are considered normal
11-16	Mild mood disturbance
17-20	Borderline clinical depression
21-30	Moderate depression
31-40	Severe depression
Over 40	Extreme depression

Table 7.1: Interpretation of the Beck's Depression Inventory

A persistent score of 17 or above indicates that the patient requires some medical attention.

7.2.1.3 MRI/MRS Protocol and Voxel Placements

The MRI protocol consisted of T_1-weighted FLAIR sagittal and T_2-weighted FSE propeller axial scans, each with the following acquisition parameters: *TR* = 25000 ms, FOV = 24 x 24 cm^2, 21 oblique slices parallel to the hippocampus, each of slice thickness 4 mm with no slice gaps. A high resolution T_1-weighted IR-FSPGR 3D axial MRI (*TR*/*TE*/*TI* = 6.9/1.6/920 ms, matrix size = 320 x 160 x 4) was also acquired for the purpose of partial volume correction (section 5.2.4).

All MRS acquisitions were performed using the PRESS localisation sequence with CHESS water suppression, NSA = 128, and NEX = 8.

Spectra were acquired from the prefrontal brain region (Figure 7.1) using *TE*/*TR* = 35/2000 ms. The VOI was adjusted for the brain size of each subject, and positioned in the dorso-ventral region of the anterior cingulate cortex, covering sections of both halves of the prefrontal brain, just next to the frontal region of the corpus callosum. The VOI sizes therefore ranged between 8.0 and 14.5 mL, and covered predominantly grey matter tissue. The voxel position in the prefrontal brain region is also known as the anterior cingulate cortex (ACC).

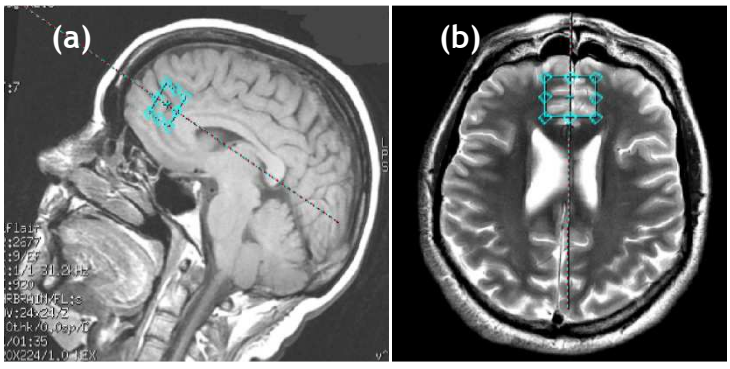

Figure 7.1: Voxel placement in the prefrontal brain (ACC).
The images are shown in the sagittal (a) and axial (b) views

Spectra from the right (Figure 7.2a) and left (Figure 7.2b) hippocampi were acquired using *TE*/*TR* = 144/2000 ms. Rectangular voxels were adjusted for the

brain size of each subject, and planned with the longest dimension along the axis of the hippocampus, starting just posterior to the amygdala. The VOI sizes ranged between 5.3 and 13.2 mL.

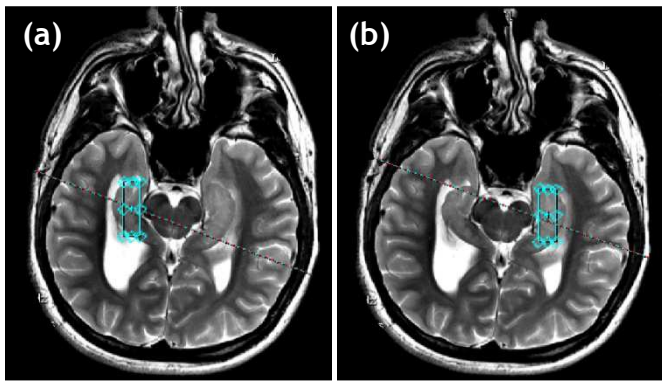

Figure 7.2: Voxel placement in the right (a) and left (b) hippocampi of the same volunteer

Voxels were carefully positioned to avoid artifacts in the spectra arising from the nasal cavity and CSF around the hippocampi. The voxels were varied for the ACC and hippocampal brain regions due to differences in brain sizes of the volunteers. The use of varying voxel sizes in the same MRS study is not new as it has been done previously [214]. However, correction for the varying voxel sizes were performed in the calculation of the concentrations of water and metabolites using the VOI_{brain} (equation 6.1) and f_{tissue} (equation 7.2) correction terms, respectively.

The long *TE* of 144 ms was used for the MRS of the hippocampi in order to eliminate potential signal contributions from CSF and lipids surrounding the hippocampi, a situation which is relatively minimal in the prefrontal region. Therefore, it was possible to measure all the metabolites of interest (i.e. NAA, Cr, Cho, mI and Glu; section 7.1) in the prefrontal region, whereas only NAA, Cr and Cho were those measured from the hippocampal regions. In fact, these were the main metabolites of interest in the hippocampal region; they were required for the regional variation exploratory analysis (section 7.1). Therefore, the *TE* values of 35 ms and 144 ms were appropriate for the studies reported in this chapter.

7.2.2 Data Analysis

7.2.2.1 Calculation and Interpretation of Changes in BDI Scores

For the patient group, the percentage changes in the BDI scores (%Δ BDI) between baseline (BDI_{pre}) and post-medication (BDI_{post}) mood scores were calculated according to:

$$\%\Delta \text{ BDI} = [(BDI_{post} - BDI_{pre})/BDI_{pre}] \times 100\ \% \qquad \text{(Eq. 7.1)}$$

From equation 7.1, a negative value of %Δ BDI corresponds to a reduction in the BDI score post-medication, indicating an improved mood condition; a positive %Δ BDI value on the other hand means a worsened mood condition post-medication.

7.2.2.2 Calculation of Tissue Water and Metabolite Concentrations

MR spectra were analysed as described in sections 2.3.1.2-3: spectral peak areas of water (A_{brain}) and metabolites (A_{Met}) were derived from the 16/NEX and NSA/NEX lines, respectively (equation 2.19). Both prefrontal and hippocampal MRS acquisitions were performed using NEX = 8 and NSA = 128; therefore A_{brain} and A_{Met} resulted from 2 and 16 spectral lines, respectively.

Tissue water content was calculated according to equation 6.3, and expressed in the units of mol/kg wet weight. Brain metabolite concentrations were calculated according to the following equation:

$$[\text{Met}] = \frac{A_{Met}}{A_{brain} \times k_{pr}} \times \frac{R_{2\_brain}}{R_{T\_Met}} \times \frac{2}{N_{Met}} \times \frac{1}{f_{tissue}} \times 55\,510 \text{ mM/L} \qquad \text{(Eq. 7.2)}$$

In equation 7.2, for a given metabolite, [Met] is the metabolite concentration in mM/L, A_{Met} is the spectral peak area of the metabolite, N_{Met} is the number of protons contributing to the spectral peak of the metabolite (NAA: 3, Cr: 3, Cho: 9, mI: 4, Glu: 2 [31]), the constant value of 2 is the number of protons contributing to the water peak area, and R_{T_Met} is the correction factor accounting for both T_1 and T_2 relaxation effects in the metabolite signal from the ACC and hippocampal regions (section 5.3.2). A_{brain} is the spectral peak area of the *in vivo* unsuppressed-water signal from the acquisition of A_{Met}, k_{pr} is the compensation factor for the fractional water signal loss due to partial recovery and T_1 relaxation effects together (section 5.3.3) in A_{brain}, R_{2_brain} is the correction factor for T_2 relaxation effects in A_{brain} (section 5.3.2), f_{tissue} is the voxel tissue fraction (section 5.2.4), and 55 510 mM/L is the concentration of pure water.

Note that the actual total voxel tissue contents should contain both GM and WM, so that $1/f_{tissue}$ would be replaced by $(1/f_{GM} + 1/f_{WM})$, and [Met] would be concentration attributable to the two tissue types, $[Met]_{GM} + [Met]_{WM}$. However, this thesis ignores the small fraction of WM in the voxel (mean ±SD = 7 % ±3), leaving only the metabolite (and water) concentrations in the required GM tissue, $[Met]_{GM}$ (section 7.1). This was done for the prefrontal voxels; for the hippocampal voxels, $1/f_{tissue}$ was the whole hippocampal tissue within the voxel (since the hippocampus is a GM structure). By ignoring the prefrontal WM, this thesis does not assume that the prefrontal voxel contained only GM tissue but only did so for a purpose (see section 7.1). Due to the GM/WM tissue mix in the brain, it is inherently impractical that the voxel can contain exclusively one tissue type. Most MRS studies [22, 58, 190, 215], including the work in this chapter, typically prescribe the voxel in a region where one of the tissue types is predominant, so that concentrations would be reported as though they were from one tissue type.

According to equation 7.2, the concentration of the metabolite, [Met] is expressed in mM/L. However, this was further converted to mM/kg wet weight by dividing the result in equation 7.2 by the density of pure water at 37 ^{o}C

(which is 0.9934 g/mL). This unit conversion was done in order to express both water and metabolite concentrations in similar units, referenced to tissue water density.

7.2.2.3 Estimation of Changes in Water and Metabolite Concentrations in the Patients

In the patient group, percentage changes in water and metabolite concentrations (%Δ C) between baseline (C_{pre}) and post-medication (C_{post}) concentrations were calculated from:

$$\%\Delta C = [(C_{post} - C_{pre})/C_{pre}] \times 100\ \% \qquad \text{(Eq. 7.3)}$$

According to equation 7.3, if there is a concentration increase post-medication, %Δ C will have a positive value; a concentration decrease post-medication will yield a negative %Δ C value.

7.3 Results and Discussion

The results discussed in this section are presented in four subsections: assessment of the mood changes in the psoriasis patients between baseline and follow up (section 7.3.1), comparison of the concentrations of cerebral water and metabolites between PsA patients and controls in the prefrontal (section 7.3.2) and hippocampal (section 7.3.3) brain regions, and assessment of the regional variation in cerebral water and metabolite concentrations in PsA patients and controls (section 7.3.4).

7.3.1 Mood Assessment Outcomes in Psoriatic Patients

The BDI mood assessment (BDI_{pre}) of the 16 psoriatic arthritis patients prior to the Etanercept medication indicated that 7 were normal, 5 had mild mood disturbances, 3 were moderately depressed and only 1 patient was on the

borderline of clinical depression (only those 4 patients in the last two groups could be considered depressed). After medication, percentage changes in BDI scores (%Δ BDI) showed that the mood conditions of 10 patients improved. Of these 10 patients, 6 were initially normal, 2 had mild mood disturbances, 1 each was on borderline depression and moderately depressed. Only one patient (who was initially moderately depressed) was on borderline depression post-medication; the other nine patients were all normal post-medication.

The BDI scores of four patients rather increased post-medication, indicating worsened mood conditions. Of these four, 2 each had mild mood disturbances and moderate depression pre-medication. Following medication, the two patients who were moderately depressed were still moderately depressed, while the other two patients who were mildly depressed were now moderately depressed (representing a worsened mood condition).

One patient had mild mood disturbances initially, and still maintained the same mood condition (with the same BDI score at pre- and post-medication). Another patient who was normal at pre-medication could not be followed up for post-medication BDI assessment – this patient dropped out of the study.

Putting together all those patients who took the BDI assessment at baseline and follow up, there was an average mood improvement (i.e. BDI decrease) of about 9.92 ± 0.34 % (BDI_{pre} = 12.8 ± 1.8; BDI_{post} = 11.5 ± 2.5); values are means ± SE. This average percentage change in BDI was however not significant (p = 0.864).

7.3.1.1 Gender differences in BDI scores

Table 7.2 shows the sex-age distribution of the psoriatic arthritis patients, with their respective BDI scores at baseline (BDI_{pre}), post-medication (BDI_{post}) and percentage changes in BDI scores (%Δ BDI). Only identifiers (e.g. p01, p02, etc) are used to represent the patients' names, consistent with the ethical provisions of the study.

Prior to the anti-inflammatory medication, the mood conditions of the 8 males (M) and 8 females (F) by gender were (BDI scores are given as M/F): normal = 5/2, mild mood disturbances = 2/3, borderline clinical depression = 0/1, and moderate depression = 1/2. At post-medication, one male dropped out leaving a male/female distribution of M/F = 7/8 with the following mood scores (given as M/F): normal = 5/4, mild mood disturbances = 0/1, borderline clinical depression = 0/1, and moderate depression = 1/2 (diagnosis were done according to Table 7.1). Overall, more females showed worse mood conditions than males. This is consistent with observations made previously that depression is more common among women compared to men [190, 216, 217], and so some authors have identified the female gender as a co-morbid diagnosis of depression [218]. However, post-medication, the percentage change (SD) in the BDI scores between males (-16.3 (12) %) and females (-20.8 (21) %) were not significantly different ($p = 0.857$). Both sexes showed improved mood conditions but females responded better to mood improvement than did males (but the mean response, $\%\Delta$ BDI did not reach statistical significance). Indeed, this finding is in agreement with the observation made elsewhere [217] that the antidepressant effect of some antidepressants is faster in women. This implies that the anti-inflammatory medication may as well have this antidepressant effect that is manifested more among the females in this study.

Patient	Sex	Age (years)	BDI_{pre}	BDI_{post}	ΔBDI (%)
p01*	M	38	2	-	-
p02	F	49	17	3	-82.4
p03	M	36	16	22	37.5
p04	F	33	2	1	-50.0
p05	F	34	11	4	-63.6
p06	M	56	5	2	-60.0
p07	M	34	22	23	4.6
p08	F	62	16	16	0
p09	M	49	9	6	-33.3
p10	F	49	7	5	-28.6
p11	M	42	14	10	-28.6
p12	M	53	5	4	-20.0
p13	F	47	25	29	16.0
p14	M	31	7	6	-14.3
p15	F	56	23	18	-21.7
p16	F	32	13	24	84.6

Table 7.2: Patients age-sex distribution and mood scores at baseline and post-medication. Negative values are reductions in BDI, positive values are increases in BDI, ΔBDI is the percentage change in BDI between pre-medication mood scores (BDI_{pre}) and post-medication mood scores (BDI_{post}); *patient dropped out of study

Those patients who were identified to be depressed according to the BDI questionnaire were not further assessed for clinical depression (i.e. major depressive disorder) using either one of the Structured Clinical Interview for DSM-III-R-patient version (SCID-P) [219] or the 17-item Hamilton Rating Scale for Depression (HRSD) [220] criteria. This was because the current study was not aimed at looking at clinical depression specifically but was aimed at assessing mood changes associated with the pathogenesis and treatment of peripheral inflammation (psoriatic arthritis in this case). The BDI assessment was therefore thought to be sufficient for this purpose, and which happens to identify clinical depression as well. Moreover, all 21 BDI items have been reported to be relatively sensitive at picking up depressive symptoms [221].

7.3.1.2 Association between age and BDI Scores

The mood scores were positively, but not strongly, correlated with age at baseline (r = 0.107, p = 0.692) and follow up (r = 0.177, p = 0.529). Age contributed to only about 15.8 % of the variance in the change in BDI scores, and so the correlation (Figure 7.3) between age and %Δ BDI was weak and not significant (ρ = 0.397, p = 0.160).

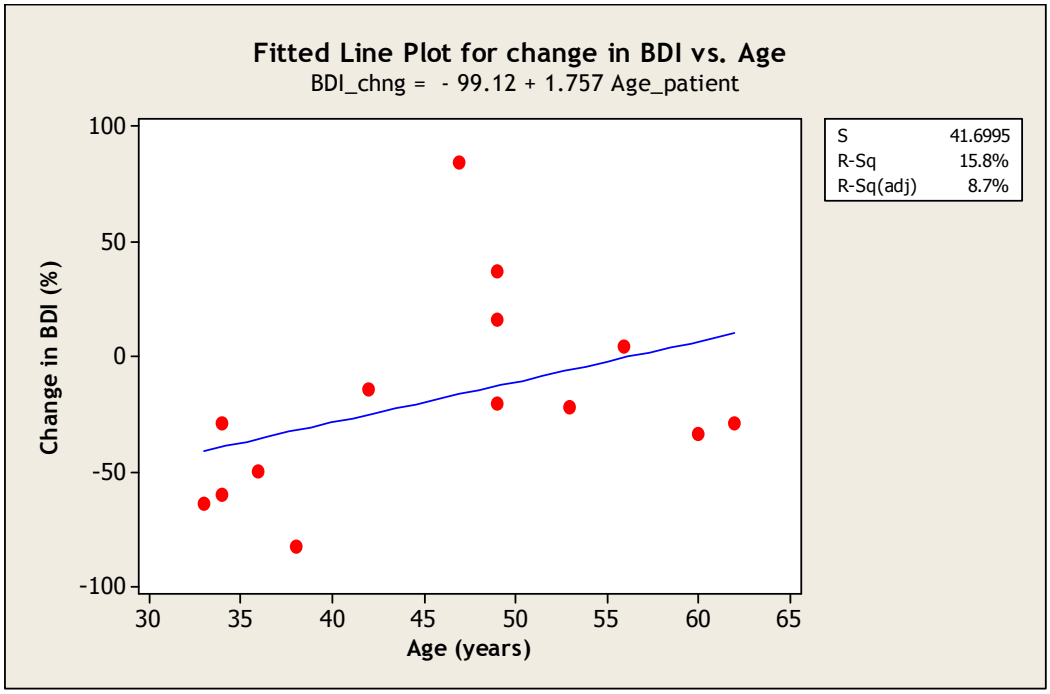

Figure 7.3: Correlation between change in mood scores and age in the patient group

7.3.2 MRS of the Prefrontal Brain

7.3.2.1 Assessment of prefrontal voxel GM/WM tissue contents

The mean (SE) ACC voxel tissue contents were not significantly different between controls and patients at baseline (0.75 (0.07) vs. 0.82 (0.07); p = 0.479), controls and patients post-medication (0.75 (0.06) vs.0.85 (0.07); p =

0.283), and patients at pre- and post-medication (0.80 (0.08) vs. 0.85 (0.07); p = 0.658).

Mean (SE) ACC voxel tissue contents also did not vary significantly between males/females in the control (0.74 (0.10)/0.75 (0.11); p = 0.923) and patient groups at baseline (0.90 (0.08)/0.72 (0.12); p = 0.234) and post-medication (0.89 (0.10)/0.82 (0.10); p = 0.628). There was neither significant difference between males in the control vs. patient groups nor females in the two groups compared, both at baseline and follow up (p > 0.05). Since there were no significant differences in the voxel tissue contents, any group differences or changes between baseline and follow up in the tissue water and metabolite concentrations could not have been due to substantial variations in the voxel tissue contents.

7.3.2.2 Tissue Water Content in Psoriatic versus Healthy Subjects

One patient dropped out and two MRS acquisitions post-medication were of poor quality. Therefore, data for 13 subjects could be analysed at follow up. In order to have equal sample sizes (to that in the post-medication group) at baseline and in the control group, data for 13 subjects (7M/6F) were used in the final analysis. The individual value plots (red dots) comparing the tissue water values of all subjects in the control, pre-medication and post-medication groups are shown in Figure 7.4. The mean tissue water content in each group is shown by the blue dots.

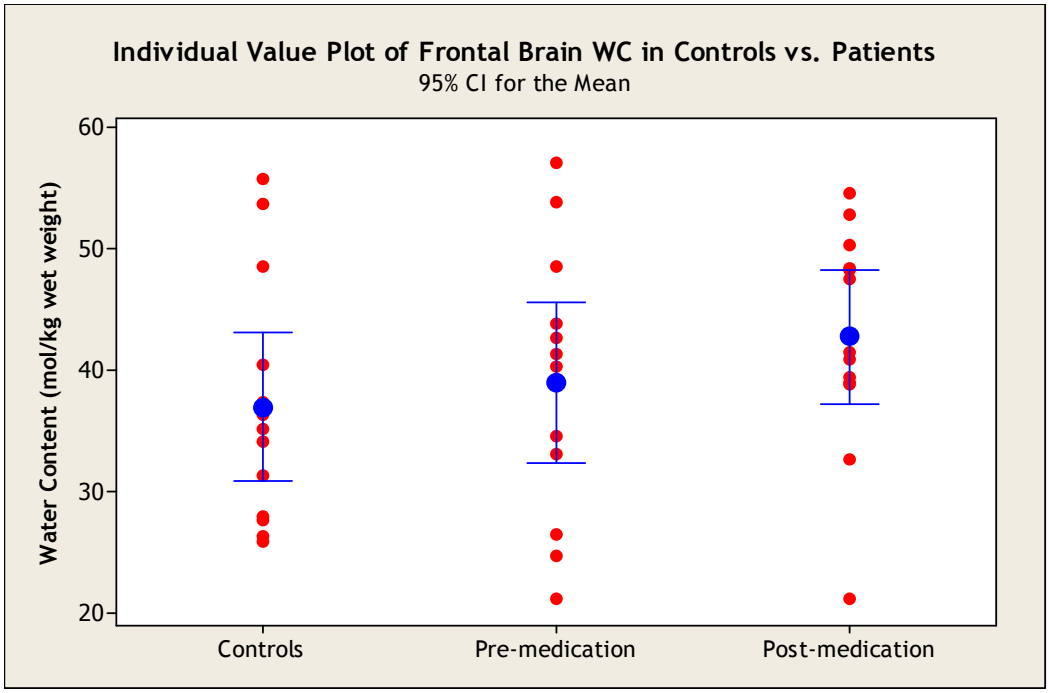

Figure 7.4: Individual value plots comparing the tissue water contents in the prefrontal brains of healthy subjects and psoriatic patients before and after anti-inflammatory medication.
The red dots represent water contents of individual subjects (n = 13 in each group), the blue dots are the mean water contents for each group, and the blue bars are the 95 % confidence intervals of the mean values

The mean tissue water content (SE) in the: controls was 37.0 (2.8), patients at pre-medication was 39.0 (3.0) and post-medication was 42.72 (2.5) mol/kg wet weight. The difference in mean tissue water contents was not significant between controls and patients pre-medication (p = 0.629), between controls and patients post-medication (p = 0.141). Pre- and post-medication mean water contents were not also significantly different (p = 0.352). Indeed, all the 95 % confidence intervals of the mean tissue water values for the three groups shown in Figure 7.4 are overlapping. There is thus no significant difference in the three means.

7.3.2.2.1 Gender differences in prefrontal water content in controls and patients

In the control group, the mean tissue water content (SE) in males (39.0 (3.8) mol/kg wet weight) and females (38.5 (5.4) mol/kg wet weight) were not

different (p = 0.941). Male/female patients did not also show significant differences in mean tissue water contents (SE) in mol/kg wet weight at baseline (45.3 (3.1)/36.8 (6.1); p = 0.245) and follow up (46.0 (4.4)/42.2 (4.7); p = 0.564).

Among male PsA patients alone, baseline (45.3 (3.1) mol/kg wet weight) and follow up (46.0 (4.4) mol/kg wet weight) mean tissue water contents (SE) did not vary significantly (p = 0.961). Females also did not show significant difference (p = 0.430) in mean water content (SE) between baseline (36.8 (6.1) mol/kg wet weight) and follow up (42.2 (4.7) mol/kg wet weight).

Mean water contents (SE) in mol/kg wet weight between controls/patients at baseline were not significantly different in males (39.0 (3.8)/45.3 (3.1); p = 0.222) and females (38.5 (5.4)/36.8 (6.1); p = 0.837). Following medication, the differences in the mean water contents (SE) in mol/kg wet weight between controls/post-medicated patients were still not significant in males (39.0 (3.8)/46.0 (4.4); p = 0.251) and females (38.5 (5.4)/42.2 (4.7); p = 0.618). Thus, the percentage changes in tissue water content were not found to be significant in both male and female patients considered separately ($p > 0.05$ in each case), and also in the two sexes compared (p = 0.315).

7.3.2.2.2 Association between age and prefrontal tissue water content in controls and patients

There was no strong correlation between ACC tissue water content and age in the control (r = 0.119, p = 0.648) and patient groups at baseline (r = 0.025, p = 0.933) and post-medication (r = 0.056, p = 0.850). Similarly, the association between age and change (between pre- and post-medication) in ACC tissue water content was weak (ρ = 0.281, p = 0.659). Age was therefore not expected to be a mediator of any group differences in water content, as well as water content changes following medication. The positive, but weak, correlation of age with water content however indicates that prefrontal brain tissue water content increases slightly with healthy ageing.

7.3.2.2.3 Link between changes in prefrontal tissue water content and mood in psoriasis

Figure 7.5 shows the fitted line plot for percentage changes in mood and tissue water content in the patient group. Along the %Δ BDI axis, most of the plotted points (red dots) fall below the zero mark, indicating that most patients improved in mood post-medication. Most (8/14) points along the %Δ water content on the other hand fall almost along the zero mark, indicating that tissue water content did not change much with medication in most patients. Both parameters however did not change significantly, and the small increase in water content was not necessarily linked to significant improvement in mood.

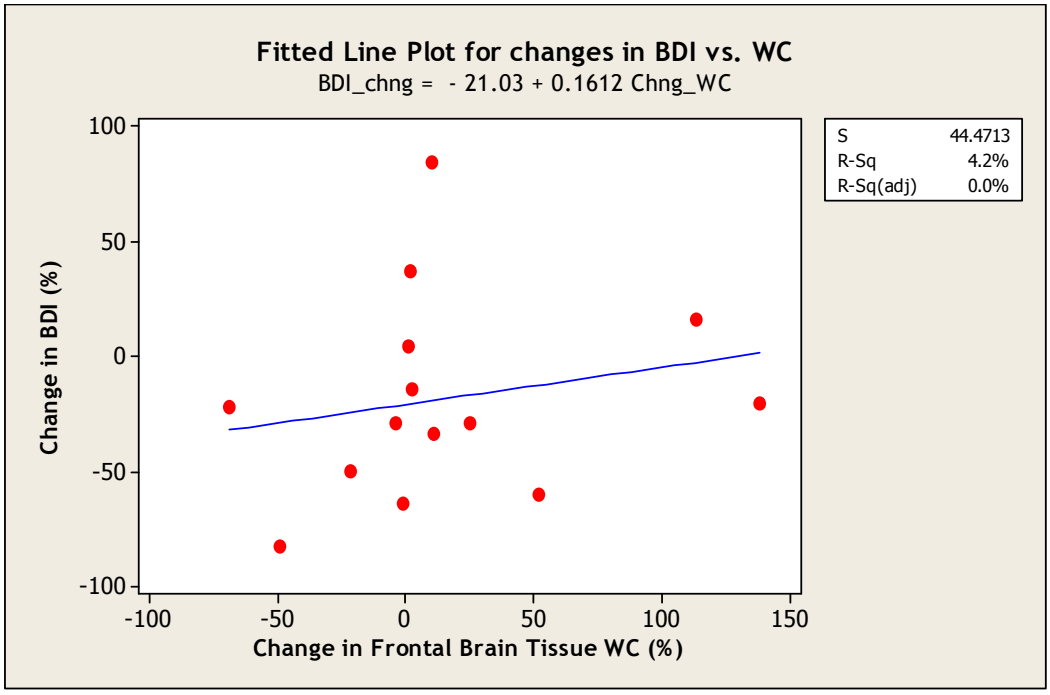

Figure 7.5: Correlation between percentage changes in mood scores and tissue water contents in the PsA patients

The mood scores of patients at baseline ($r = -0.031$, $p = 0.916$) and follow up ($r = -0.326$, $p = 0.287$) were both inversely correlated with the tissue water contents at the respective stages. The inverse correlations meant that a higher

tissue water content is associated with a lower BDI score (i.e. better mood or lesser depression). The percentage changes in BDI scores and tissue water content were positively correlated (ρ = 0.321, p = 0.482). Thus, a greater change in water content was associated with a greater change in mood scores, in the same direction (i.e. either both are increasing or decreasing, simultaneously). From the spearman's correlation coefficient (ρ = 0.321), change in tissue water content contributes about 10.3 % to the change in mood scores. However, all the correlations deduced in these cases were weak (as shown by the r and ρ values) and not significant (p > 0.05 in each case).

7.3.2.3 Metabolite Concentrations in Psoriatic versus Healthy Subjects

The mean concentrations of the five quantified metabolites are compared between controls and patients (at baseline and follow up) in Table 7.3. The mean concentrations are for males and females combined in each group. Separate comparisons of the mean concentrations between males and females in each group are shown in Table 7.4. A sample size of 13 (7M/6F) was used in all those comparisons for the same reason as discussed in the first paragraph of section 7.3.2.2.

Metabolite	Mean concentration (SE) in mM/kg			P-values for group comparisons		
	Controls (C)	Pre-medication (Pr)	Post-medication (Po)	C vs. Pr	C vs. Po	Pr vs. Po
NAA	10.42 (0.49)	9.45 (0.35)	9.51 (0.46)	0.121	0.187	0.882
Cr	7.78 (0.38)	6.34 (0.38)	6.69 (0.25)	0.014	0.027	0.274
Cho	1.83 (0.11)	2.03 (0.10)	1.94 (0.05)	0.170	0.371	0.110
Glu	9.38 (0.32)	8.93 (0.45)	9.05 (0.71)	0.432	0.681	0.800
mI	7.66 (0.55)	6.05 (0.62)	5.87 (0.78)	0.063	0.078	0.322

Table 7.3: Comparison of the quantified metabolite concentrations between controls and patients at baseline and post-medication

Metabolite	Mean Concentration (SE)/mMkg^{-1} in Males/Females; p-value		
	Controls	Pre-medication	Post-medication
NAA	9.65 (0.72)/11.19 (0.59) p = 0.121	9.27 (0.35)/9.66 (0.66) p = 0.619	9.93(0.82)/9.01 (0.27) p = 0.327
Cr	7.64 (0.75)/7.90 (0.35) p = 0.763	6.03 (0.56)/6.66 (0.53) p = 0.433	6.45 (0.29)/6.97 (0.42) p = 0.335
Cho	1.73 (0.14)/1.96 (0.17) p = 0.311	2.17 (0.11)/1.89 (0.15) p = 0.166	2.02 (0.04)/1.85 (0.10) p = 0.156
Glu	8.71 (0.37)/9.65 (0.36) p = 0.330	9.18 (0.55)/8.64 (0.79) p = 0.596	8.32 (0.47)/9.78 (1.3) p = 0.348
mI	7.46 (0.70)/7.94 (0.96) p = 0.693	6.54 (0.95)/5.63 (0.84) p = 0.487	6.33 (1.10)/5.32 (1.20) p = 0.548

Table 7.4: Comparison of the mean metabolite concentrations between males and females in the control and patient groups at baseline and post-medication

In Table 7.3, concentrations of all the metabolites were lower in patients compared to the controls, both at baseline and post-medication; only choline (Cho) was slightly higher in patients than in controls at baseline and post-medication. However, none of these differences reached statistical significance ($p > 0.05$) except for creatine, Cr (see below). The decrease in myo-inositol (mI) concentration in the patients (relative to controls) almost reached significance at baseline ($p = 0.063$) and follow up ($p = 0.078$). Only the concentration of Cr was significantly lower in the patients compared to the controls at baseline ($p = 0.014$) and post-medication ($p = 0.027$). Following medication, the concentrations of all the metabolites increased slightly except those of mI and Cho which were slightly decreased. No metabolite concentration was significantly different between pre- and post medication ($p > 0.05$).

7.3.2.3.1 Gender differences in prefrontal metabolite concentrations in controls and patients

There were no gender differences in all the metabolite concentrations among controls, patients at baseline and post-medication (Table 7.4). This meant that the patterns of metabolite changes in the ACC region resulting from PsA were similar in both males and females. In the control group, all the metabolites

were slightly higher in females than in males; but none of the differences was statistically significant ($p > 0.05$). However, there was no specific trend in metabolite level differences between males and females in the patient group, both at baseline and post-medication.

7.3.2.3.2 Association between age and prefrontal metabolite concentrations in controls and patients

In the control group, age and each one of the NAA ($r = -0.130$, $p = 0.631$), Cr ($r = -0.143$, $p = 0.611$), Glu ($r = -0.354$, $p = 0.259$), and mI ($r = -0.142$, $p = 0.628$) concentrations were inversely correlated. Only the concentration of Cho was positively correlated with age ($r = 0.240$, $p = 0.430$) in the controls. However, none of these correlations was significant ($p > 0.05$ in each case). Nonetheless, the results indicate that in the control group, to some extent, healthy ageing is associated with decreased levels of NAA, Cr, Glu and mI; but increased levels of Cho in the prefrontal brain.

In the PsA patient group, age was inversely correlated with changes in the concentrations of NAA ($r = -0.258$, $p = 0.443$), Cr ($r = -0.297$, $p = 0.348$), and Cho ($r = -0.036$, $p = 0.911$); but was positively correlated with changes in the concentrations of Glu ($r = 0.377$, $p = 0.317$) and mI ($r = 0.465$, $p = 0.207$). None of the correlations was however found to be significant ($p > 0.05$ in each case) but indicated that given the Etanercept medication, older PsA patients are more likely to show smaller changes in the concentrations of NAA, Cr and Cho compared to younger patients; whereas the reverse is true for changes in Glu and mI concentrations.

7.3.2.3.3 Link between changes in prefrontal metabolite concentrations and mood in psoriasis

Percentage changes in the concentrations of NAA ($r = -0.538$, $p = 0.088$) and Cr ($r = -0.436$, $p = 0.156$) were inversely correlated with percentage changes in BDI scores. The percentage changes in the concentrations of Cho ($r = 0.381$, $p =$

0.222), Glu (r = 0.203, p = 0.601) and mI (r = 0.516, p = 0.155) were positively correlated with percentage changes in patient BDI scores.

Even though none of the associations appeared significant, the association with change in NAA concentration was rather strong and almost reached statistical significance. NAA is a neuronal marker and the percentage change observed in this study might not necessarily mean neuronal death but rather neuronal dysfunction. Thus, the correlation analysis may be suggesting that a substantial change in the way neurones function (manifested in %Δ NAA) due to PsA could be linked to very small changes in mood following anti-inflammatory medication. However, further studies on a larger sample size of PsA patients may be required to ascertain this observation.

7.3.3 MRS of the Hippocampus

7.3.3.1 Assessment of the left and right hippocampal voxel tissue contents

For the left hippocampus, the mean voxel tissue fractions (SE) were not significantly different in the following comparisons: patients at pre-medication/post-medication (0.71 (0.01)/0.72 (0.02); p = 0.765), controls/patients at baseline (0.74 (0.02)/0.71 (0.01); p = 0.250), and controls/patients post-medication (0.74 (0.02)/0.72 (0.02); p = 0.497). Left hippocampal voxel tissue fractions (SE) did not also vary significantly between males/females in the pre-medicated (0.71 (0.02)/0.75 (0.02); p = 0.205), post-medicated (0.72 (0.03)/0.73 (0.03); p = 0.869), and control (0.72 (0.02)/0.75 (0.02); p = 0.326) groups. Comparison of the males in the control vs. patient groups at baseline and follow up did not also show significant differences (p > 0.05 in each case) in the left hippocampal voxel tissue fractions; the same was also true among females.

For the right hippocampus, the mean voxel tissue fractions (SE) were not significantly different in the following comparisons: patients at pre-medication/post-medication (0.71 (0.01)/0.73 (0.02); p = 0.515), controls/patients at baseline (0.74 (0.02)/0.71 (0.01); p = 0.264), and controls/patients post-medication (0.74 (0.02)/0.73 (0.02); p = 0.675). Right hippocampal voxel tissue fractions (SE) did not also vary significantly between males/females in the pre-medicated (0.71 (0.02)/0.75 (0.02); p = 0.252), post-medicated (0.72 (0.02)/0.74 (0.02); p = 0.591), and control (0.72 (0.02)/0.75 (0.02); p = 0.409) groups. Comparison of the males in the control vs. patient groups at baseline and follow up did not also show significant differences ($p > 0.05$ in each case) in the right hippocampal voxel tissue fractions; the same was also true among females.

There was no voxel tissue difference between the left and right hippocampi in both groups, and among males and females, separately, in both groups. Thus, there was no possibility of significant contributions to any concentration differences between groups that could arise from differences in hippocampal voxel tissue fractions.

7.3.3.2 Hippocampal Water Content in Psoriatic versus Healthy Subjects

For a sample size of 13 subjects in each group (7M/6F), left and right hippocampal water contents (Figure 7.6) were not significantly different in the control (p = 0.572) and patient groups at baseline (p = 0.102) and post-medication (p = 0.884).

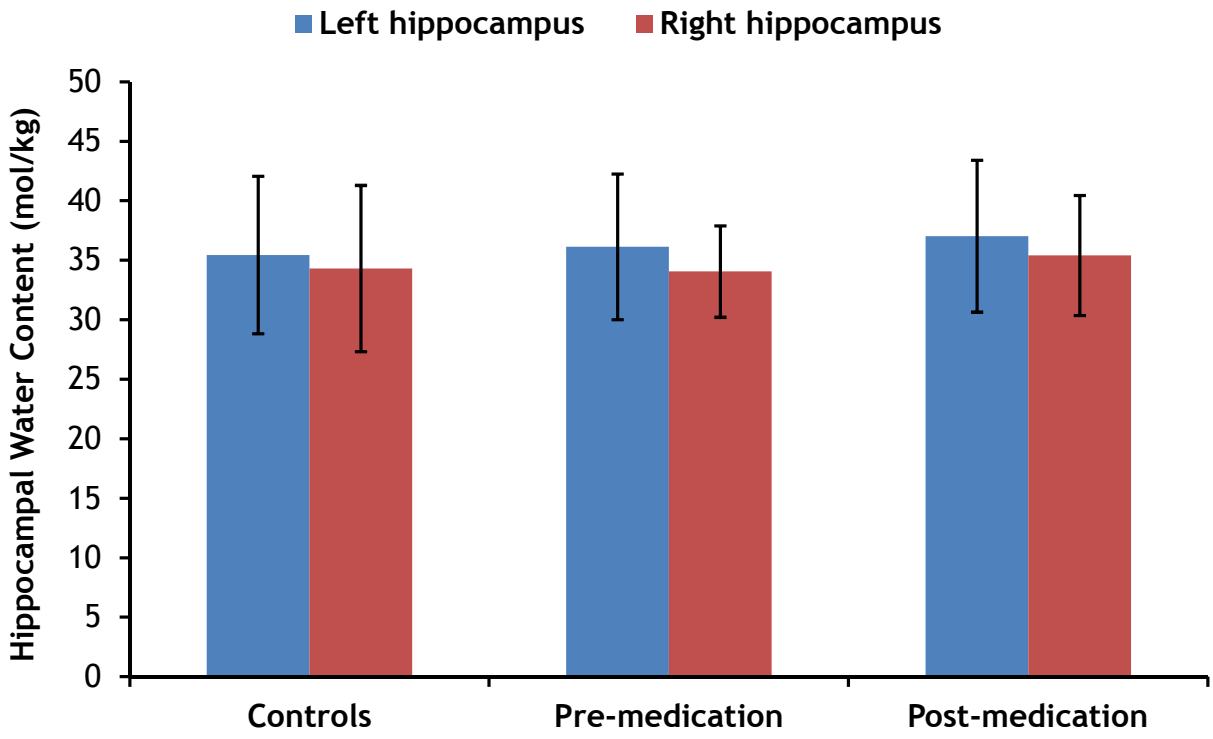

Figure 7.6: Comparison of the mean left and right hippocampal water contents in controls and patients at baseline and follow up.
The error bars represent ±standard deviations of the mean values

For the left hippocampus, mean (SE) water contents in mol/kg wet weight did not vary significantly between: controls/patients at baseline (35.45 (1.80)/36.14 (1.60); p = 0.777), controls/patients post-medication (35.45 (1.80)/37.03 (1.70); p = 0.526), and baseline/post-medication (36.14 (1.63)/37.03 (1.70); p = 0.747). There were also no significant gender differences in left hippocampal water contents in both groups. Water content in males was not significantly different between the two groups; this was true for females too ($p > 0.05$).

For the right hippocampus, mean (SE) water contents in mol/kg wet weight were not significantly different between: controls/patients at baseline (34.31 (2.20)/34.06 (1.20); p = 0.921), controls/patients post-medication (34.31 (2.20)/35.41 (1.60); p = 0.693), and baseline/post-medication (34.06 (1.21)/35.41 (1.60); p = 0.590). There were no significant variation in right

hippocampal water contents between males and females in either group, and among males (and females too) compared between the two groups ($p > 0.05$).

7.3.3.2.1 Association between age and hippocampal water content in controls and patients

Hippocampal water content did not vary with age in either group, and among males or females in each group. Changes in both left ($r = 0.159$, $p = 0.621$) and right ($r = 0.188$, $p = 0.580$) hippocampal water contents were not associated with age in the patient group. Controls did not also show an association between age and hippocampal water contents in both left ($r = 0.131$, $p = 0.654$) and right ($r = 0.169$, $p = 0.547$) hippocampi. The correlation analyses however indicated a tendency of small increments and more changes in hippocampal tissue water content with age in both groups and with medication, respectively.

7.3.3.2.2 Link between changes in hippocampal water content and mood in psoriasis

Percentage changes in the left ($r = 0.370$, $p = 0.193$) and right ($r = 0.508$, $p = 0.134$) hippocampal water contents were positively but not significantly correlated with percentage changes in BDI scores. These correlations were not different between males and females. The correlation for the right hippocampus was rather stronger even with the fewer data points of $n = 13$ (which could have possibly contributed to the non-significance of the correlation analysis). The results thus suggest that compared to the left, changes in the right hippocampal water content might be more associated with mood changes.

7.3.3.3 Hippocampal Metabolite Concentrations in Psoriatic versus Healthy Subjects

At the echo time (*TE*) of the MRS acquisition in the hippocampi, only three metabolites (NAA, Cr and Cho) were reliably detected and quantified. This section thus compares the concentrations of these metabolites in the left (Tables 7.5 and 7.6) and right (Tables 7.7 and 7.8) hippocampi between patients and controls, and between baseline and post-medication in the patient group.

	Mean concentration (SE) in mM/kg			P-values for group comparisons		
Metabolite	Controls (C)	Pre-medication (Pr)	Post-medication (Po)	C vs. Pr	C vs. Po	Pr vs. Po
NAA	7.61 (0.45)	7.98 (0.47)	8.01 (0.56)	0.578	0.588	0.631
Cr	6.54 (0.42)	6.24 (0.43)	6.32 (0.43)	0.622	0.724	0.826
Cho	1.71 (0.10)	1.71 (0.14)	1.41 (0.13)	0.993	0.099	0.086

Table 7.5: Comparison of the left hippocampal metabolite concentrations between controls and patients at baseline and post-medication

	Mean Concentration (SE)/mMkg^{-1} in Males/Females; p-value		
Metabolite	Controls	Pre-medication	Post-medication
NAA	7.72 (0.57)/7.46 (0.78) p = 0.798	7.84 (0.52)/8.07 (0.74) p = 0.807	8.22 (0.97)/7.74 (0.51) p = 0.675
Cr	6.65 (0.52)/6.37 (0.77) p = 0.770	6.09 (0.54)/6.44 (0.76) p = 0.722	6.27 (0.58)/6.41 (0.78) p = 0.893
Cho	1.77 (0.12)/1.62 (0.19) p = 0.499	1.75 (0.23)/1.66 (0.18) p = 0.754	1.45 (0.10)/1.74 (0.16) p = 0.065

Table 7.6: Comparison of the left hippocampal metabolite concentrations between males and females in the control and patient groups at baseline and post-medication

Concentrations of all the three metabolites in the left hippocampus did not vary significantly between patients at baseline and controls, and between post-medication and controls (Table 7.5). Whereas both NAA and Cho were slightly higher, Cr was slightly lower in patients at baseline. At post-medication, while Cr and Cho were slightly lower, NAA was slightly higher in patients. Only Cho reduced considerably with medication but this change did not reach statistical

significance (p = 0.086). Gender-specific analyses (Table 7.6) showed that this considerable reduction in Cho concentration post-medication occurred in males (from 1.75 to 1.45 mM/kg); females on the other hand showed slight increase in Cho (from 1.66 to 1.74 mM/kg) with medication. This might therefore explain the almost significant difference (p = 0.065) in Cho concentration between males and females post-medication (Table 7.6).

However, none of the three metabolite concentrations varied significantly between controls and patients, both at baseline and post-medication in the right hippocampus (Table 7.7). Pre- and post-medication concentrations were not also significantly different for any metabolite. Gender-specific analyses did not also show significant difference in any metabolite concentration between males and females in either group (Table 7.8).

Metabolite	Mean concentration (SE) in mM/kg			P-values for group comparisons		
	Controls (C)	Pre-medication (Pr)	Post-medication (Po)	C vs. Pr	C vs. Po	Pr vs. Po
NAA	8.08 (0.64)	8.23 (0.25)	8.45 (0.45)	0.833	0.640	0.547
Cr	6.59 (0.25)	6.81 (0.19)	6.18 (0.35)	0.502	0.366	0.421
Cho	1.55 (0.13)	1.58 (0.24)	1.48 (0.13)	0.922	0.674	0.610

Table 7.7: Comparison of the right hippocampal metabolite concentrations between controls and patients at baseline and post-medication

Metabolite	Mean Concentration (SE)/mMkg^{-1} in Males/Females; p-value		
	Controls	Pre-medication	Post-medication
NAA	8.06 (0.82)/8.10 (1.20) p = 0.981	8.65 (0.88)/8.09 (0.23) p = 0.649	9.09 (1.20)/8.07 (0.17) p = 0.488
Cr	6.89 (0.33)/6.10 (0.29) p = 0.103	6.60 (0.19)/6.91 (0.28) p = 0.431	5.78 (0.39)/6.43 (0.51) p = 0.356
Cho	1.53 (0.19)/1.59 (0.20) p = 0.854	1.73 (0.49)/1.52 (0.30) p = 0.781	1.53 (0.20)/1.44 (0.18) p = 0.750

Table 7.8: Comparison of the right hippocampal metabolite concentrations between males and females in the control and patient groups at baseline and post-medication

In controls, NAA (p = 0.875), Cr (p = 0.966) and Cho (p = 0.255) concentrations in the left and right hippocampi were not significantly different. At baseline, patients did not also show significant differences in NAA (p = 0.167), Cr (p =

0.298) and Cho (p = 0.466) concentrations in the two hippocampi. Post-medication concentrations of NAA (0.731), Cr (0.714) and Cho (0.642) did not also differ between the two hippocampi. Percentage changes in NAA (p = 0.923), Cr (p = 0.625) and Cho (p = 0.777) concentrations were also not different between the left and right hippocampi. The bilaterality of the concentrations of the metabolites (and their percentage changes) in the two hippocampi was the same in males and females, considered separately, in each group.

7.3.3.3.1 Association between age and hippocampal metabolite concentrations in controls and patients

In the controls, age was positively correlated with the concentrations of NAA (r = 0.326, p = 0.236), Cr (r = 0.629, p = 0.028) and Cho (r = 0.401, p = 0.155) in the left hippocampus; but was inversely correlated with NAA (r = -0.202, p = 0.576) and Cr (r = -0.112, p = 0.717) concentrations in the right hippocampus; only Cho was positively correlated with age (r = 0.011, p = 0.969) in the right hippocampus. However, only the age-Cr concentration direct relationship in the left hippocampus was both strong (r = 0.629) and significant (p = 0.028). This suggests that the concentration of Cr increases gradually with normal ageing, in some brain regions (the left hippocampus in this case). In fact, this finding agrees with previous reports that cerebral Cr increases with age [1, 65].

In the PsA patients, age was found to be inversely related to percentage changes in NAA (left: r = -0.444, p = 0.318; right: r = -0.250, p = 0.633), Cr (left: r = -0.010, p = 0.981; right: r = -0.214, p = 0.729) and Cho (left: r = -0.005, p = 0.993; right: r = -0.021, p = 0.973) concentrations in both left and right hippocampi.

7.3.3.3.2 Link between changes in hippocampal metabolite concentrations and mood in psoriasis

Percentage change in BDI scores was positively correlated with percentage changes in the concentrations of Cr (r = 0.219, p = 0.603) and Cho (r = 0.256, p

= 0.624) in the left (only %Δ NAA concentration was inversely correlated with %Δ BDI (r = -0.812, p = 0.027) in the left hippocampus); but was inversely correlated with percentage changes in the concentrations of NAA (r = -0.115, p = 0.828) and Cr (r = -0.062, p = 0.921) in the right hippocampus (only %Δ Cho was positively correlated with %Δ BDI (r = 0.331, p = 0.586) in the right hippocampus). However, only the %Δ BDI-%Δ NAA concentration inverse association in the left hippocampus was both strong (r = -0.812) and significant (p = 0.027).

7.3.4 Variation in Cerebral Water and Metabolite Concentrations

Four spectra were quantifiable in the ACC and hippocampal voxel positions, at the same time; these were the water, NAA, Cr and Cho spectra. To assess their variation across the three voxel positions, one-way ANOVA tests were performed for each one of the water and metabolite concentrations (in the ACC, left and right hippocampi) in the controls and patients (both at baseline and post-medication). Particularly for the tissue water content in the control group, the results will show whether or not prefrontal and hippocampal water contents vary significantly; thus corroborating or otherwise the accuracy of the deductions made in chapter 6 when the hippocampal and hemispheric water contents were combined in a similar ANOVA test. Data for an equal number of males and females totalling a sample size of 12 (6M/6F) was used in the ANOVA tests in the following subsections.

7.3.4.1 Regional variation in cerebral water contents in controls and patients

Table 7.9 shows the variation of water content among the three regions (i.e. prefrontal GM, left and right hippocampi). The comparisons are done for the control and patient groups using the one-way ANOVA test.

Subjects	Mean water content ± SD (mol/kg wet weight)			p-value
	Prefrontal GM	Left hippocampus	Right hippocampus	
Controls	35.87 ± 9.65	35.90 ± 4.90	34.31 ± 6.99	0.863
PsA-1	36.64 ± 11.07	37.20 ± 6.52	34.06 ± 3.84	0.631
PsA-2	41.92 ± 10.10	35.83 ± 6.08	35.41 ± 5.05	0.107

Table 7.9: Regional water contents in the three voxel positions compared in controls and patients.
PsA-1 and PsA-2 represent the psoriatic arthritis patients at baseline and post-medication, respectively; SD is the standard deviation of the mean. Note that these abbreviations have also been used Tables 7.10-12

The p-values shown in Table 7.9 indicated that water content did not vary significantly among the three brain regions in both controls and patients (at baseline and post-medication).

7.3.4.2 Regional variation in cerebral NAA concentrations in controls and patients

The assessment of regional NAA concentrations (Table 7.10) showed that regional concentration of NAA varied significantly in the patients at baseline ($p = 0.012$); post-medication concentrations however did not vary significantly in the three regions ($p = 0.164$). Controls did not show significant variation in the three regions ($p = 0.089$). Prefrontal GM NAA concentration however was consistently higher in both groups, and almost reached statistical significance in the controls while being significantly higher in the patients at baseline.

Subjects	Mean NAA concentration ± SD (mM/kg wet weight)			p-value
	Prefrontal GM	Left hippocampus	Right hippocampus	
Controls	9.75 ± 1.76	7.93 ± 2.08	8.08 ± 2.04	0.089
PsA-1	10.10 ± 1.49	8.29 ± 1.48	8.23 ± 0.71	0.012
PsA-2	9.58 ± 1.54	8.14 ± 1.74	8.45 ± 1.27	0.164

Table 7.10: Regional NAA concentrations in the three voxel positions compared in controls and patients

7.3.4.3 Regional variation in cerebral Cr concentrations in controls and patients

Regional Cr concentration was not found to vary significantly in both controls and patients (at baseline and post-medication), as shown in Table 7.11.

Subjects	Mean Cr concentration ± SD (mM/kg wet weight)			p-value
	Prefrontal GM	Left hippocampus	Right hippocampus	
Controls	7.38 ± 1.25	6.65 ± 1.58	6.62 ± 0.90	0.337
PsA-1	6.06 ± 1.09	6.57 ± 1.63	6.81 ± 0.48	0.538
PsA-2	6.71 ± 0.82	6.10 ± 1.14	6.35 ± 0.95	0.520

Table 7.11: Regional Cr concentrations in the three voxel positions compared in controls and patients

7.3.4.4 Regional variation in cerebral Cho concentrations in controls and patients

The results in Table 7.12 show that regional Cho concentration did not vary significantly in controls ($p = 0.315$) and patients at baseline ($p = 0.218$); post-medication Cho concentrations however were found to vary significantly ($p = 0.009$). Prefrontal Cho concentration was consistently higher in all cases.

Subjects	Mean Cho concentration ± SD (mM/kg wet weight)			p-value
	Prefrontal GM	Left hippocampus	Right hippocampus	
Controls	1.87 ± 0.29	1.67 ± 0.42	1.59 ± 0.51	0.315
PsA-1	2.00 ± 0.22	1.54 ± 0.43	1.71 ± 0.58	0.218
PsA-2	2.02 ± 0.20	1.55 ± 0.43	1.47 ± 0.36	0.009

Table 7.12: Regional Cho concentrations in the three voxel positions compared in controls and patients

7.4 Comparison with the existing peer reviewed literature

This section discusses the key findings presented in section 7.3 in relation to published results. Three main themes are discussed: results for cerebral water (section 7.4.1) and metabolites (7.4.2), and the assessment of their distributions (section 7.4.3) in the three voxel positions in this chapter. Discussion of the mood assessment outcomes in the patient group in relation to the literature was dealt with in section 7.3.1.

7.4.1 Cerebral Water Content

The tissue water quantification technique developed in this thesis references the unsuppressed-water signal to an estimated *in vitro* signal obtained from the same voxel position (details in chapter 6). The technique offers a unique opportunity of obtaining both the unsuppressed-water and metabolite spectra, simultaneously, within clinical scan times compared to a previous technique [222]. In their method, Dreher and Leibfritz [222] implemented a two-scan method without water suppression involving a short echo time (*TE* = 18 ms) PRESS localisation sequence. Prior to the standard single-voxel PRESS localisation sequence, two scans are implanted: the first is a chemical shift inversion pulse being turned off, and the next is another inversion pulse being turned on, both yielding the time domain (TD) datasets S_A and S_B, respectively. The 180^o inversion pulses, followed by spoiler gradient pulses, invert magnetisation within the spectral range where metabolite signals are expected either upfield or downfield relative to water. The water signal remains unaffected by both inversion pulses and so, together with its associated gradient-induced sidebands, it appears in the same way in both TD signals and the corresponding frequency domain spectra. Thus, the signal difference S_A-S_B yields the metabolite signals (while the water signal and the gradient-induced artifact signals are significantly reduced); and the signal sum S_A+S_B yields the water signal, which may be used for referencing in absolute metabolite quantification.

The method by Dreher and Leibfritz [222] and that in this thesis both do not require extra adjustments in spectral acquisition or sophisticated data post-processing, and scale favourably with increasing B_0 field. However, compared to the method in this thesis, the disadvantage of the two-step method implemented by Dreher and Leibfritz [222] is that it doubles the minimum total measurement time. The study by Dreher and Leibfritz [222] however did not quantify cerebral water content.

Christiansen et al [61] quantified brain tissue water content by acquiring the unsuppressed-water signal and referencing it to a signal acquired from an external water bag. In a group of healthy subjects aged 10-70 years, they estimated cerebral water content in the range of 35.8-39.6 (mean 36.9) mol/kg wet weight for four brain regions: frontal, temporal, occipital and basal ganglia, selecting predominantly GM and WM tissues in separate cases. They did not find significant variation in water content among the four regions, tissue types or with age, similar to the findings in this thesis (the same observation was true even in the psoriasis group, and when compared to controls). By relating signal intensities from selected ROIs in MR images and relating them to fractional brain water content (β_{MR}), Brooks et al [177] did not also find a significant association between age and β_{MR} in the frontal brain. No other study reported gender differences in brain tissue water content.

Compared to controls, cerebral water content in the psoriasis patients was higher in the prefrontal (by 5.41 ± 0.71 %) and left hippocampal (by 1.95 ± 0.11 %) regions, but lower in the right hippocampal (by 0.73 ± 0.45 %) region. After receiving the Etanercept medication, the psoriasis patients showed percentage increases in cerebral water contents by 7.54 ± 2.16 % (males: 4.55 ± 1.30 %; females: 8.67 ± 3.43 %) in the prefrontal, 2.46 ± 0.63 % (males: 1.83 ± 0.17 %; females: 1.97 ± 0.18 %) in the left, and 3.96 ± 0.52 % (males: 1.89 ± 0.22 %; females: 2.04 ± 0.21 %) in the right hippocampal regions. After medication, water content increased more in females than in males for all regions. These increases were observed to be associated (but not significantly) with small

improvement in mood for all three regions but the association in the right hippocampus was the strongest ($r = 0.508$, $p = 0.134$).

The increase in cerebral water content post-medication could imply that psoriasis, even though being peripheral, may be associated with dehydration of brain tissue. Chronic dehydration even as little as 2.2-3.0 % of body mass, as a consequence of psoriasis, could affect brain structure on a macroscopic level (e.g. expansion of the ventricular system [37, 223]). This study however did not incorporate measurement of intracranial volumes with the MRS measurements as has been done by Wilkinson et al [197] or the volumes of the regions studied. Structural brain changes due to dehydration may have various implications depending on the degree of water deficit [224]. However, notable consequences are that water loss slows down visual-motor tracking, psychomotor processing speed and reduces attention/memory performance [34, 37]; and dehydration of up to 10 % could be life threatening [225]. However, not all studies (including this thesis) have found behavioural/mood effects in the reported range of 2-3 % dehydration [37]. On average, the psoriasis patients in this thesis had cerebral water contents well within the normal range. This might explain why most of them did not have low mood according to their BDI scores.

7.4.2 Cerebral Metabolite Concentrations

Metabolite concentrations in this thesis were calculated by referencing their signals to the *in vivo* unsuppressed-water signal obtained within the same acquisition and voxel position. The estimated absolute concentrations for the healthy controls were comparable with those (matched for age) in the literature for the prefrontal [62, 210, 226, 227] and hippocampal [175, 226, 227] regions. All the metabolite concentrations in the investigated voxel regions for both patients and controls were also within the published normal ranges [65]. In the prefrontal region, healthy females were found to have higher concentrations of all the quantified metabolites (NAA: 15.95 %, Cr: 3.40 %, Cho: 13.29 %, Glu: 10.79 %, and mI: 6.43 %) than their male counterparts. In

the left hippocampus, female controls had lower NAA (by 3.38 %), Cr (by 4.21 %) and Cho (by 8.47 %). In the right hippocampus, female controls had higher NAA (by 0.50 %) and Cho (by 2.56 %) but lower Cr (by 11.47 %). None of these metabolite concentration differences was found to be statistically significant between the two sexes. The pattern of gender differences on the other hand was not consistent among patients pre- and post-medication, probably due to the presence of psoriasis.

Sex-dependent cerebral metabolite concentrations however appears to be contradictory. While Wilkinson et al [197] observed significantly higher and lower NAA/Cho and Cho/Cr ratios respectively in females than in males in the parieto-occipital WM, Komoroski et al [228] did not find significant difference in Cho/Cr and mI/Cr ratios in any one of the basal ganglia, frontal, temporal, thalamus and hippocampus. However both studies did not find significant difference between both sexes in NAA/Cr ratio whereas this thesis did not find significant difference in the absolute concentrations of all the metabolites.

In the control group, none of the metabolites was found to vary significantly with age in the prefrontal region. These weak associations however showed tendencies towards increase in only Cho but decrease in all other metabolites; in particular, age-dependent decrease in frontal lobe NAA is reported elsewhere [177]. However, in the left hippocampus, only Cr concentration was found to increase significantly with age ($r = 0.629$, $p = 0.028$). Variations in metabolite concentrations were not associated with age in the right hippocampus. Apart from the significant increase in left hippocampal Cr with age, all other age-metabolite concentration associations in this thesis were comparable to those reported by Saunders et al [229]. There is however an indication that these associations may vary by brain region [230].

In the PsA patients, neither age nor gender had additional effect on response to the treatment. However, metabolite changes were inversely (but not strongly or significantly) correlated with age in both left and right hippocampi; associations in the prefrontal region were not consistent. Changes in NAA and mI were strongly (but not significantly) negatively and positively, respectively,

associated with mood in the prefrontal region. Only change in NAA in the left hippocampus was negatively and significantly correlated with mood ($r = -0.81$, $p = 0.03$). There were no strong or significant associations between metabolite and mood changes in the right hippocampus. The significant association in the left hippocampus appears to agree with previous reports that the left hemisphere of the brain may play a role in the pathogenesis of mood-related conditions [209, 231].

In the prefrontal region, compared to controls, the psoriasis patients had lower mean percentage ± SE NAA (by 9.31 ± 0.29 %), Cr (by 18.51 ± 1.19%), Glu (by 4.8 ± 0.41 %) and mI (by 21.02 ± 1.27 %); only Cho was higher (10.93 ± 1.50 %). Following the anti-inflammatory medication, NAA, Cr and Glu were increased by 0.63 (0.31) %, 5.52 (0.34) % and 1.34 (0.58) %, respectively; Cho and mI were decreased by 4.43 (0.50) % and 2.98 (0.26) %, respectively. In the left hippocampus of the psoriasis patients, compared to controls, NAA and Cho were higher (by 4.86 ± 0.04 % and 8.19 ± 0.40 %, respectively) while Cr was lower (by 4.59 ± 0.02 %). With medication, NAA and Cr levels were increased by 0.38 ± 0.19 % and 1.28 ± 0.10 %, while Cho was decreased by 17.54 ± 0.77 %. In the right hippocampus, patients showed a relatively higher NAA (by 1.86 ± 0.61 %), Cr (by 3.34 ± 0.32 %) and Cho (by 1.90 ± 0.46 %) levels. Post-medication, Cr and Cho levels were reduced (by 9.25 ± 0.84 % and 6.76 ± 0.46, respectively) while NAA was increased (by 2.67 ± 0.8 %). Neither the percentage differences from normal nor changes post-medication was statistically significant in all three regions.

The consistently lower levels of Cr and Glu in this study were directly opposite of the three-fold increases of Cr/glycine and Glu/serine ratios in psoriatic plaque extracts collected from the skin of PsA patients [232]. Ratios can be difficult to interpret regarding which metabolite changed precisely, particularly when it is unclear how a particular disease affects the individual metabolites. In this case, putting the two results together, it appears that the decrease in cerebral Cr and Glu are associated with the increase of the two

metabolites in peripheral tissue, thus suggesting involvement of the brain in peripheral inflammation such as psoriasis.

In a previous study [191] of 5 rheumatoid (RA) and 2 psoriatic (PsA) arthritis patients on various TNF-α blocking medications including Etanercept (3 patients were on this), medication was given after the first scan and repeated 3 days later (24 hours after the time of maximal plasma concentration of Etanercept in those patients who took it). MRI examinations focusing on the left centrum semiovale included MT imaging, diffusion weighted imaging (DWI) and MRS. Neuropsychological tests included global cognitive and executive functioning, memory, and attention. The study did not find difference in the neuropsychological assessment outcome or visual abnormalities on the MR images before and after medication. Apparent Diffusion Coefficient for WM and GM and metabolite ratios of NAA/Cho, NAA/Cr and Cho/Cr did not change significantly with medication. However, significant decreases of the MTR histogram peak heights (MTR-Pht) of WM and GM post-medication were observed. The study thus concluded that the observed decrease of MTR-Pht post-medication suggested loss of parenchyma integrity; nonetheless, those changes were not attributable to inflammation or demyelination according to the DWI and MRS results. The decrease of the MTR-Pht was not observed to result in decreased cognitive function.

In a separate study of 35 RA patients alone also focusing on the centrum semiovale region [190], the patients were on various medications excluding Etanercept. The study reported significantly higher and lower Cho/Cr and NAA/Cho ratios, respectively in active RA patients (who also had elevated erythrocyte sedimentation rates (ESR)) compared to their counterparts who had inactive RA and normal ESR. The NAA/Cho and Cho/Cr ratios were significantly correlated with ESR but medication use had no additional effect on those associations.

It thus appears that even though both RA and PsA are peripheral inflammatory diseases, they may have different ways in which they impact neurochemistry:

while RA seems to show significant metabolite changes [190], PsA does not appear to show significant metabolite changes (based on the findings of this thesis and those of Bijl et al [191]). However, unlike multiple sclerosis [233-235], which involves demyelination of the CNS, both RA and PsA do not appear to be associated with significant mood/neuropsychological symptoms.

However, given that only four PsA patients in this study were depressed, a separate statistical analysis of the spectral changes for these subjects (not shown) indicated that the spectral changes (though not significant) were observed to be comparable with some significant findings in previous studies of depression [209, 211, 236, 237]. Results from the remainder of the data set did not differ significantly from those of the depressed PsA patients. Combining the two types of PsA patients (i.e. depressed and non-depressed) still did not yield significant results in the spectral changes, even though the average changes in some of the metabolite concentrations were comparable with those for depression in the literature. For instance, this thesis found elevated Cho concentrations in all three voxel positions; significantly higher cerebral Cho concentrations in depression have been reported elsewhere [236]. The lower prefrontal mI and Cr concentrations found in this thesis can be compared to a decreased mI/Cr ratio in depression reported previously [211]. Finally, the reduced prefrontal Glu in this study compares with previously [237] observed lower concentrations of Glx and GABA in the same brain region. It is therefore possible that, depending on the sub-type, depressed PsA patients could show similar neurometabolite changes (to specific sub-types of clinically depressed patients) with associated neuropsychological/mood symptoms. The non-depressed state in PsA, on the other hand, may be suggestive that some patients could adapt to cope with the body image and self-esteem issues associated with the skin disorder [238, 239]. Interestingly, this study found an inversely significant association between change in left hippocampal NAA concentration and mood in the PsA patients after the anti-TNF-α therapy, in agreement with reports that the left brain hemisphere may play a role in mood regulation [209].

7.4.3 Regional Distribution of Cerebral water and Metabolites

The regional assessment results (though for only three brain regions) shown in Tables 7.9-12 suggest that water, NAA, Cr and Cho are all uniformly distributed between the prefrontal and hippocampal brain regions (predominantly GM regions) in healthy subjects. However, prefrontal NAA was slightly higher than the hippocampal concentrations; there were no differences in the water and metabolite concentrations between the two hippocampi in both groups. In the psoriasis patients, prefrontal NAA was significantly higher before medication, but normalised post-medication. Prefrontal (compared to hippocampal) Cho increased significantly post-medication. Only water and Cr remained uniformly distributed in the three voxel positions in both controls and patients at baseline and post-medication. From these three predominantly GM regions, cerebral water and metabolites (i.e. NAA, Cr and Cho) therefore appear to be uniformly distributed (at least for this tissue type) as has been reported previously [61, 229].

Water, NAA, Cr and Cho have been used widely to express metabolite ratios in studies of several disease conditions such as brain tumors [240, 241], AIDS [29, 242] and tuberous sclerosis complex [243]. Assessment of regional variation in these will have implications for the choice of reference standard in future studies. It is however important to mention that the findings from this assessment cannot be true in all disease conditions since the metabolite profile varies widely among different diseases. At least, it will be informative in absolute quantitative MRS studies of peripheral inflammation and similar conditions that do not directly affect the brain.

7.5 Summary and Conclusions

The work presented in this chapter was aimed primarily at developing a novel technique to absolutely quantify cerebral metabolites by using an optimised

unsuppressed-water signal acquired simultaneously with the metabolite signals. This was achieved by processing, separately, the unsuppressed-water lines from a normal water-suppressed acquisition to yield the water and metabolite peaks for absolute quantification involving all the necessary corrections. While the cerebral tissue water quantification technique was developed in chapter 6, the metabolite quantification technique was developed in this chapter.

The two techniques were then applied in the prefrontal and hippocampal brain regions in a group of psoriatic arthritis patients and healthy controls with the aims of: quantifying observed changes in the cerebral metabolite and water concentrations associated with psoriasis; assessing the association between the MRS results and mood outcomes in the psoriasis patients; and examining the regional variations in the metabolite and water concentrations in normal brain and in psoriasis. Thus, for the first time, absolute quantification of cerebral water content in peripheral inflammation, assessment of cerebral water content changes with anti-inflammatory medication, and its effect on mood have been carried out in this thesis.

The psoriasis patients did not show significant metabolite and water concentration differences from the healthy controls. The patients did not also show visible abnormalities on their MR images as assessed by a consultant neuroradiologist. Variations in all concentrations either in controls or with medication were neither age nor gender dependent. The psoriasis-related metabolite concentration changes were not associated with mood changes for all brain regions studied, in agreement with previous studies. Most of the other findings reported in this chapter were comparable with those in the literature. However, the only significant and new findings in this chapter were the significant association between: higher Cr levels and old age in the left hippocampus; and lower BDI scores and higher changes in NAA levels, also in the left hippocampus.

Despite the success in the implementation of the techniques, the work presented in this chapter was not without some limitations.

Glu is strongly coupled to Gln and GABA. If not well resolved, then it is possible that any attempt to measure any of those metabolites (e.g. measurement of prefrontal Glu in this study) will result in contributions from the other two metabolites as well. These are best decoupled by post-processing techniques involving spectral editing. Spectral editing was not done in this thesis but at the *TE* and *TR* of the acquisitions, which were performed at 3 T, at least Glu and Gln were well resolved. The contribution from GABA alone was therefore not expected to be significant.

The normal controls were not assessed on the BDI questionnaire and so the absence of normal mood scores did not allow for a clear distinction to be made between the PsA patients and the controls on the mood scale. Such information could also have been useful in identifying the threshold BDI score at which PsA could be associated with a significant mood change. Nonetheless, since most of the PsA patients did not experience significant mood disturbances, the presence of their BDI scores alone was sufficient for the analysis in this chapter. Future studies should improve on the quality of the data by including the mood scores of controls as well.

Detailed patient clinical information was lacking; these included time since the psoriasis symptoms appeared, severity of the condition, blood pressure/heart rate, demographics, present medication, smoking/alcoholism frequencies (if any), blood markers of inflammation such as erythrocyte sedimentation rate (ESR) and/or blood cytokine levels. The presence of these clinical variables could have improved the outcomes of the analyses such that even if the MRS results did not significantly correlate with any one of the available data (e.g. BDI scores, age and gender), there could have been some interesting findings with any one of these missing variables. Moreover, any one of these missing variables could be a possible confound in the final outcome, which should have otherwise been corrected for in the statistical analyses. To increase the specificity of the MRS results and make them more meaningful, future studies should therefore include these missing variables.

Chapter 8: Functional MRS of Brain Tissue Water and Metabolites

8.1 Introduction and Objectives

In section 1.3.4, the blood oxygen level dependent (BOLD) contrast mechanism was discussed. The BOLD signal is generated when an external stimulus causes neural activity to increase above baseline physiological state. The new physiological state is associated with changes in cerebral blood flow, cerebral blood volume and the cerebral metabolic rate of oxygen consumption [244]. Consequently, there is an increased flow of oxygenated blood to the region of activity, resulting in susceptibility gradients spreading around and away from this activation site [245]. With MRI, this susceptibility gradient, associated with changes in T_2^*, can be detected in vessels (intravascular compartment) and tissue near the vessels (extravascular compartment). In general, the extravascular BOLD effect is desirable for mapping locations of functional activation [246], where the effect appears as increased intensity in the pixels that coincide with the site of the neural activity. This is known as BOLD contrast and the technique is called functional MRI. In the same way, MRS is also sensitive to this neural activity. Usually, the BOLD effect in MRS is observed as increases in the spectral peak intensities (or height) accompanied by decreases in spectral linewidth [246, 247]. This application of MRS is called functional MRS (fMRS).

In this chapter, the BOLD effects on the water and metabolite resonances were studied by sustained stimulation of the primary visual cortex (V1) of the normal human brain. The primary objective was to assess the relative degrees of change in the peak areas of water and the metabolites while they responded to the stimulus. The water peak has been chosen as the concentration standard in this thesis. Therefore, this assessment of relative peak area changes was aimed to evaluate the relative consistency (i.e. not changing significantly) or

otherwise of the water peak area during the BOLD response. Furthermore, the study would provide an understanding of the dynamics of the MRS signal during neuroactivation, and hence the implication of this dynamics for cerebral water as a reference standard.

For a given duration of stimulation, the time interval between successive lines of recorded spectra (defined by the NEX value) determines how many lines will be averaged for that acquisition; this is known as the temporal resolution of the data in the frequency domain. The only two NEX values available on the MR scanner (section 8.1.2.3) were used in two separate acquisitions on three healthy volunteers. Thus, the secondary objective of this chapter was to compare the BOLD changes observed (in the water and metabolite resonances) using these NEX values for any significant difference. The findings of this study would explain whether or not NEX could be another source of discrepancy in the results of fMRS studies.

8.1.1 The Theory of fMRS

A localised spin-echo ^{1}H MR Spectroscopy sequence can be used to detect the BOLD effect in fMRS [248]. Compared to fMRI, the fMRS technique has a much higher SNR because its signal is acquired from a relatively large voxel [246]. It is therefore sensitive to subtle BOLD changes in the human brain during sensory stimulation [248, 249]. The NMR signal sources of the gradient-echo based fMRI and spin-echo based fMRS techniques differ remarkably. In order to make these differences clear, it will be useful to initially, and briefly, discuss the relations between the FID and spectrum (Fourier transform of the FID). The associations between the spectrum parameters and the BOLD origins can then be deduced from these FID-spectrum relations.

A spin-echo FID can be defined by three parameters [246]. The first parameter is the FID amplitude (A_{FID}) of the first sampling point at the centre of the echo. A_{FID} is mainly determined by the transverse relaxation time, T_2 and the initial magnetisation, M_o as follows [246]:

$$A_{FID} = M_o \times \exp(-TE/T_2) \quad \text{(Eq. 8.1)}$$

and assuming there is no contribution from spin exchange,

$$1/T_2 = 1/T_{2,int} + 1/T_{2,D} \quad \text{(Eq. 8.2)}$$

where TE is the echo time, $T_{2,int}$ is the intrinsic T_2, and $T_{2,D}$ is the component of T_2 accounting for the contribution of diffusion. M_o is proportional to the proton density (ρ) and the NMR signal intensity.

The second parameter of the spin-echo FID is the FID decay rate ($1/T_2^*$), defined as [246]:

$$1/T_2^* = 1/T_2 + 1/T_{2,SS} \quad \text{(Eq. 8.3)}$$

where $T_{2,SS}$ is the transverse relaxation time related to local static susceptibility. However, these effects of field inhomogeneities cancel out in the spin-echo experiment; but they occur in gradient-echo fMRI experiments.

The third parameter of the spin-echo FID is the FID integral (I_{FID}), which can be determined by both A_{FID} and T_2^*. In the frequency domain, I_{FID}, A_{FID} and T_2^* are quantitatively correlated to three other NMR parameters: peak height (H), linewidth at half peak height ($\Delta\upsilon_{1/2}$), and spectral peak area (A_S). These correlations can be deduced from the following relations [246]:

$$A_S \propto A_{FID} \quad \text{(Eq. 8.4)}$$

$$\Delta\upsilon_{1/2} = 1/\pi T_2^* \quad \text{(Eq. 8.5)}$$

$$H \propto I_{FID} \quad \text{(Eq. 8.6)}$$

Thus, from a typical MR spectrum that is acquired with the spin-echo pulse sequence, information about the following relationships can be deduced: A_S correlates with changes in T_2 and M_o, $\Delta\upsilon_{1/2}$ correlates with changes in T_2 and $T_{2,SS}$, and H correlates with all changes in T_2, $T_{2,SS}$, and M_o. With this information, the BOLD contributions from various origins can be studied by fMRS: neuronal activation increases oxygenated blood supply to neurones; thus, Mo increases and manifests as increase in spectral peak height, H and area, As. T_2* also increases and causes a decrease in $\Delta\upsilon_{1/2}$ [250].

The gradient-echo based fMRI technique on the other hand mainly provides information related to the changes in T_2 and M_o. This difference in detection sensitivity between fMRI and fMRS mainly arises from the fact that the susceptibility gradient caused by neural activation produces only a much smaller linewidth change (~10 Hz) in fMRS than the frequency width of a single pixel (about several kHz) in fMRI [246].

The contribution of $T_{2,SS}$ to the BOLD signal detected by the gradient-echo based fMRI technique is negligible. Thus, the main difference between the fMRI and fMRS techniques is that the contributions of both T_2 and $T_{2,SS}$ to the BOLD effect can be detected simultaneously by fMRS.

To observe the BOLD effects on the water resonance, the CHESS water suppression module was switched OFF during the fMRS studies. The BOLD effect on the metabolite spectra was recorded by switching ON the CHESS water-suppression module. Cerebral water is present in the intracellular and extracellular spaces, CSF and blood. For this reason, the BOLD effects on both intra- and extravascular compartments will contribute to the water signal change during the sensory stimulation. On the other hand, the BOLD effects on the cerebral metabolites only manifest the susceptibility changes in the extravascular tissue compartment [246].

8.1.2 Recording the BOLD Effect in MRS

8.1.2.1 The Main Acquisition Parameters

The accuracy of the functional MRS measurements largely depends on how successful the stimulation period is synchronised with the data acquisition time on the MR scanner. This will then make it possible to capture the maximum BOLD effect available in the MRS data. In order to achieve this, it is necessary to understand the data acquisition schemes implemented on the scanner regarding sequence timing. This section therefore discusses the acquisition timing parameters of the spectroscopy pulse sequence implemented on the scanner, and how this was synchronised to the stimulation period in the fMRS experiments.

For a standard MRS acquisition on the GE MR scanner, the total spectral acquisition time, T_{acq} is a function of the repetition time, *TR*, and number of signal averages, NSA. However, before acquisition of the actual MRS data, some dummy scans (N_{dummy}) are collected during which time the scanner starts running but no data is stored. This allows some time for the scanner to be tuned and the voxel to be shimmed (section 3.2.2.1) prior to data collection. The unsuppressed, reference water lines (N_{ref}) and the suppressed, metabolite data (NSA) are then collected at the *TR* set for the acquisition. The total MRS acquisition time, T_{acq}, is thus given by:

$$T_{acq} = TR \times (N_{dummy} + N_{ref} + NSA) \qquad \text{(Eq. 8.7)}$$

In all acquisitions on the scanner, $N_{dummy} = 8$ and $N_{ref} = 16$, so $(N_{dummy} + N_{ref}) = 24$. All the fMRS experiments presented in this chapter were performed using $TR = 3$ sec; thus, equation 8.7 can be simplified as:

$$T_{acq} = 3 \times (24 + NSA) \qquad \text{(Eq. 8.8)}$$

In order to record the BOLD effect in the MRS data, the stimulus was applied for only the duration within which the actual MRS data was being collected,

which is the 3 x NSA part of equation 8.8. Therefore, the duration of visual stimulation (T_{sti}) was given by:

$$T_{sti} = T_{acq} - 72 \text{ sec} \quad \text{(Eq. 8.9)}$$

Equation 8.9 indicates that visual stimulation should be commenced 72 seconds after the MRS sequence starts running. However, with consideration for a 9 sec deadtime (see section 8.1.2.2), stimulation rather began 63 sec from when the MRS sequence started running.

8.1.2.2 The fMRS Paradigm and Duration of Stimulation

In order to detect signal changes, it was necessary to perform MRS acquisitions both with and without the visual stimulus; i.e. alternating the stimulus periods with equal rest periods. Therefore, two paradigms were designed for the fMRS experiments: one with a rest period followed by a stimulation period of equal duration in separate scans; and another with interleaved three rest and three stimulation periods of equal durations within a single scan. Throughout this chapter, the former paradigm will be called the "Off-On" paradigm, whereas the latter will be called the "block" paradigm.

In the "Off-On" paradigm, NSA = 64 was used, giving T_{acq} = 264 sec and T_{sti} = 192 sec or 3 min, 12 sec; the rest period was also 192 sec. In the "block" paradigm, each block had NSA = 32 (and of duration 32 x *TR* or 96 sec) and so the total NSA for the six blocks was 192 (i.e. 6 x 32), giving T_{acq} = 648 sec and T_{sti} = 576 sec or 9 min, 36 sec; this included the three rest periods interleaved with three stimulus periods. The total length of time for one rest and one stimulus period is known as the cycle duration [251]. Thus, the cycle durations for the "Off-On" and "block" paradigms were 384 sec and 576 sec, respectively.

In addition to the estimated T_{sti} periods, a period of 9 sec deadtime was added between the stimulus being turned on or off and when the scanner began

acquisition of the 3 x NSA part of equation 8.8 (i.e. the actual MRS data; see section 8.1.2.3). The reason for the deadtime was to serve two purposes [251]: firstly, it reduced the possibility of a movement artefact which will arise due to the subject flinching when the lighting level changed suddenly between stimulus and resting conditions. Secondly, within the deadtime period, the changing blood flow stabilises as it alternates between the stimulus and rest periods. This transient response time is about 6.5-8 sec risetime, with falltime duration within 7-9 sec [251, 252]. With the additional 9 sec deadtime, the T_{sti} period in the "Off-On" paradigm was 201 sec and so the cycle duration was 402 sec. However, in the "block" paradigm, T_{sti} was the same as the cycle duration, which was now 585 sec (when the deadtime was added).

8.1.2.3 Accessing the Recorded BOLD Effect in MRS Data

Since the N_{dummy} lines are not stored in an acquisition, only the reference water lines (N_{ref}) and the suppressed spectral lines or actual MRS data (N_{data}) are left. The total number of spectral lines (N_l) in the spectral domain is determined by the number of phase cycles (NEX) as in equation 2.19 (section 2.3.1.3), where 16/NEX and NSA/NEX are the number of spectral lines or data frames stored in N_{ref} and N_{data}, respectively.

The duration of stimulation, T_{sti} was set to match with the time required to acquire N_{data} (section 8.1.2.1), and so the BOLD effect was recorded in those spectral lines. Note that stimulation had not begun during the period in which the N_{ref} lines were collected. Thus, equation 2.19 can now be written in terms of the number of "BOLD effect spectral lines" (N_{BOLD}) as follows:

$$N_{BOLD} = NSA/NEX \qquad \text{(Eq. 8.10)}$$

With NSA = 64 in the "Off-On" paradigm, N_{BOLD} will be 64/NEX; the "block" paradigm with NSA = 192 will have an N_{BOLD} value of 192/NEX. Only two NEX values are available on the scanner used for this project: 2 and 8. Therefore,

setting NEX = 8 will produce 8 (Figure 8.1a) and 24 spectral lines (4 per block) in the "Off-On" and "block" paradigms, respectively. On the other hand, if NEX = 2, 32 (Figure 8.1b) and 96 spectral lines (16 per block) will be stored for the "Off-On" and "block" paradigms, respectively. These stored data frames were those ones processed to estimate the BOLD effects (see section 8.2.4.2) in the fMRS data presented in this thesis.

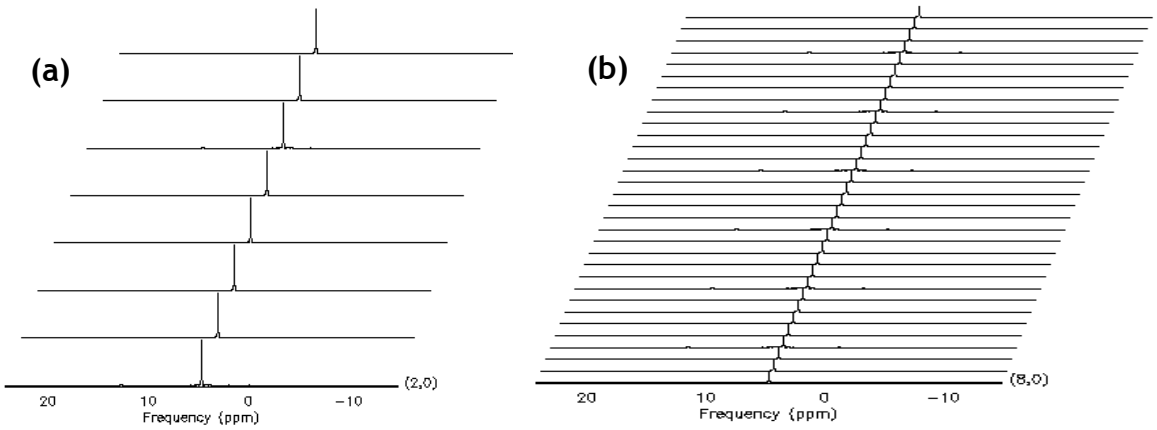

Figure 8.1: Representative data frames from a typical fMRS experiment during the rest period in the "Off-On" (a) and "block" (b) paradigms.
The raw data had already been Fourier transformed and shows the SAGE output of the water peak at 4.7 ppm in both examples

8.2 Methods

8.2.1 Subjects

A total of 6 healthy volunteers (2 females/4 males, aged 29-36 years, mean ± SD = 31.5 ± 2.6 years) participated in all the studies reported in this chapter. Five of these volunteers were scanned on the NEX = 2 protocol; 3 of these 5 volunteers plus one more volunteer (making a sample size of 4) were scanned on the NEX = 8 protocol. Thus, 3 (2males/1 female) volunteers were scanned on both the NEX = 2 and NEX = 8 protocols.

8.2.2 The Visual Stimulus and its Presentation

A previous positron emission tomography (PET) study [253] has shown that a rate of pattern presentation of about 7.8 reversals per second (or 7.8 Hz) induces the maximum blood flow response in the visual cortex. Based on this observation and other fMRS studies [246, 254-256], an in-house 8 Hz black/white pattern-reversal checkerboard was designed by the author (Figure 8.2b) and used for the visual stimulation. During the rest period, a black background was displayed (Figure 8.2a). In both displays, a small fixation cross was centrally placed in order to keep the subject awake and attentive during the scans. There was no background illumination within the scanner room throughout the experiments.

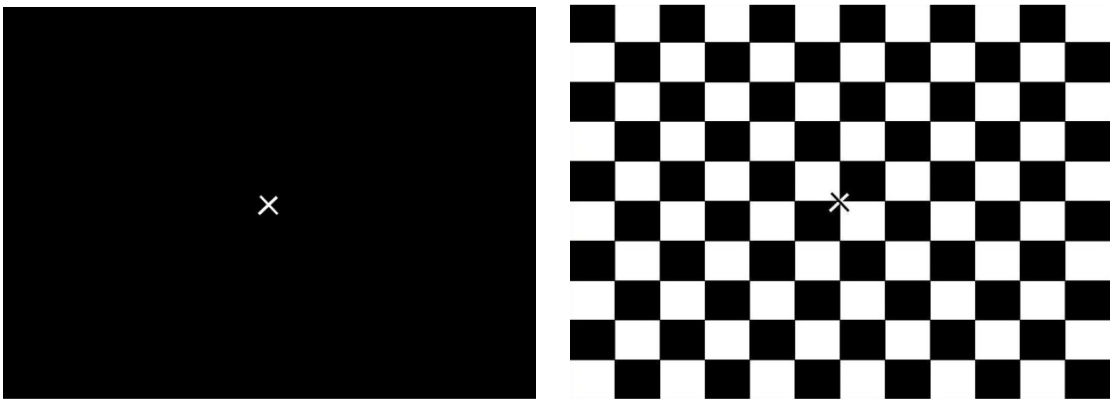

Figure 8.2: The black background with a white centrally placed fixation cross displayed during the rest period (a) and the 8 Hz pattern-reversal checkerboard used for visual stimulation (b).
The checkerboard comprised of a 12 x 10 matrix of black/white squares, each of size 50 x 10 (length x breadth) 'Excel' units

The rest and stimulus displays were each presented using a Windows Media Player (Microsoft Corporation, USA, 2006) installed on a DELL laptop computer. Each display was projected from a screen panel that has image transmission cables passing through an observation window into the magnet room, where the projected image is displayed on bifocal lenses. The lens ensemble (Nordic Neurolabs, NNL; http://www.nordicneurolab.com) was attached to the head coil and positioned vertically above, but close to, the eyes of the subject. For

each subject, the foci of the lenses were adjusted until they could see a single projected and sharp image through both lenses, simultaneously.

8.2.3 Functional MRI and MRS Studies

Following a structural MRI scan, an fMRI examination was performed for each subject prior to the fMRS experiments. The purpose of this preceding fMRI scan was to determine the location and size of the activated V1 area. Using this information, the localised voxel for acquiring the fMRS data was prescribed (Figures 8.3a-b).

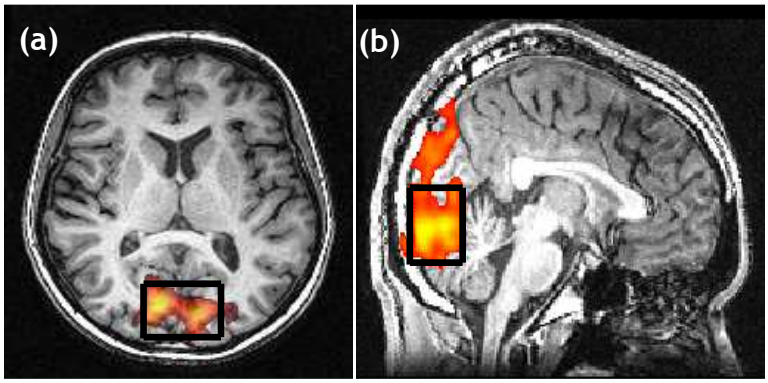

Figure 8.3: Axial (a) and sagittal (b) views of the localised fMRS voxel within the activation map generated in the V1 brain region during the fMRI examination.
The functional activation maps were created by thresholding: z-values ranged from 3 to 12, with a cluster significance value, p = 0.05

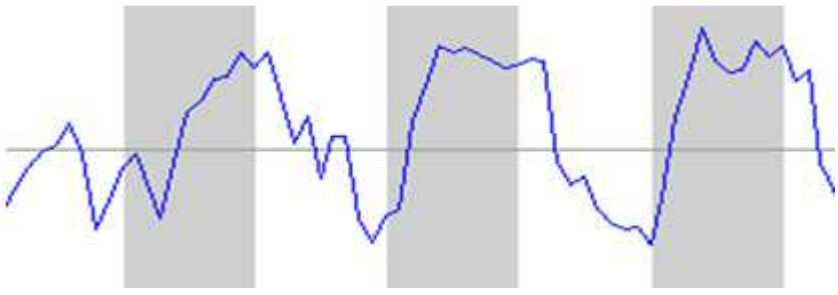

Figure 8.4: Time course analysis plot for the fMRI examination shown in figures 8.3a-b.
This is the on-screen output of the analysis performed by the MR scanner software: the grey bars indicate the stimulus periods; the white bars indicate the rest periods.

8.2.3.1 The fMRI Protocol

Following a 3-plane localiser scan, 40 axial slices were planned parallel to both the anterior commissure-posterior commissure (AC-PC) line and the primary visual cortex, and covering the whole brain. MRI of the head was then acquired using the single-shot gradient echo-planar imaging (GRE-EPI) sequence (64 x 64 image matrix size, 24 x 24 cm^2 FOV, 4.5 mm slice thickness, *TE* = 30 ms, and *TR* = 3000 ms).

Three rest periods and three stimulus periods (each of duration 30 sec, resulting in a 3-minute cycle duration) were designed in an interleaved manner; this paradigm was different from the fMRS block paradigm described in section 8.1.2.2. The fMRI acquisition began with four dummy scans (see section 8.1.2.1); then ten image volumes were acquired in each of the six consecutive periods, resulting in a total of 60 image volumes.

For each subject, the functional activation maps were generated and overlaid on the occipital brain region (Figures 8.3a-b) in real time by the proprietary scanner software (Brainwave RT); the corresponding on-screen time course analysis output (Figure 8.4) was also provided in real time. This information then served as guide during localisation of the fMRS voxel.

8.2.3.2 The fMRS Protocol

A single-voxel (20 S/I x 20 A/P x 30 R/L mm^3) PRESS localisation sequence was used in the fMRS experiments. Outer-volume and CHESS water suppression techniques were incorporated in the PRESS sequence. The PRESS acquisition parameters were: *TE* = 23 ms, *TR* = 3000 ms, spectral width = 5000 Hz; 64 and 192 scan averages (NSA) were used for the “Off-On” and “block” paradigms, respectively; for one set of “Off-On”/”block” experiments, NEX was set to 2, and then to 8 for another set. The “Off-On” paradigm was of the form OFF-ON, whereas the “block” paradigm was OFF-ON-OFF-ON-OFF-ON; where OFF and ON

mean the rest and stimulus periods, respectively. Figure 8.4 is representative of the switching periods between ON and OFF.

The metabolite spectra were recorded first with the CHESS water suppression module turned on. The acquisition protocol was then repeated but with CHESS water suppression turned off to acquire the water spectra. Thus, the water and metabolite spectra were acquired using the same spectral acquisition parameters.

8.2.4 Data Analysis

8.2.4.1 Generation of Activation Maps for fMRI Acquisitions

For each subject, thresholded activation mapping was carried out to visualise the pattern of activation in the V1 brain region; the corresponding time course plot for each experiment was also produced. A representative activation map is shown in Figures 8.3a-b. This example image (just like all the other activation images for each subject) was post-processed and overlaid on a high resolution 3D T_1-weighted brain scan of the same subject (acquired after the fMRI scan). The activation images (colour maps) were generated using FEAT (FMRI Expert Analysis Tool [257]) Version 5.98, part of FSL (FMRIB's Software Library, www.fmrib.ox.ac.uk/fsl). The pre-statistics processing steps involved: motion correction using MCFLIRT [258]; non-brain removal using BET [259]; spatial smoothing using a Gaussian kernel of FWHM 5 mm; mean-based intensity normalisation of all volumes by the same multiplicative factor; highpass temporal filtering (Gaussian-weighted least-squares straight line fitting, with sigma = 37.5 sec). For the post-statistical analysis, Z (Gaussianised T/F) statistic images were thresholded using clusters determined by $Z > 3.0$ and a (corrected) cluster significance threshold of $P = 0.05$ [260]. Co-registration of the GRE-EPI image to the high resolution 3D MR image was carried out using FLIRT [258, 261]. The corresponding time-series statistical analysis was carried out using FILM (FMRIB's Improved Linear Model) with local autocorrelation

correction [262]. The output of this analysis was similar to the time course plot shown in Figure 8.4; an example FSL output is not therefore shown in this thesis.

8.2.4.2 Spectral Analysis and Estimation of the BOLD Effect

Spectra were analysed as described in sections 2.3.1.2-3. However, specific to this chapter, spectral quantification was performed in two ways: firstly, each line in the spectral domain (Figures 8.1a-b) was quantified by invoking a "local" quantification algorithm that utilises the Levenberg-Marquardt method (section 2.3.1.2). The "local" Levenberg-Marquardt method ensures that the same processing and quantification steps are applied to each spectral line. Secondly, all the spectral lines were averaged by invoking a "global" Levenberg-Marquardt method. Both quantification schemes yielded the peak height (H), linewidth at half peak height ($\Delta\upsilon_{1/2}$), and spectral peak area (A_S). The "locally" quantified spectral parameters (i.e. H, $\Delta\upsilon_{1/2}$ and A_s) were used to plot the respective time courses of their changes over the cycle duration. The "globally" quantified spectral parameters on the other hand were used to quantify their respective BOLD effects (i.e. percentage changes in H, $\Delta\upsilon_{1/2}$ and A_s).

The BOLD effect is associated with increase in H following stimulation (Figure 8.5), with a corresponding decrease in $\Delta\upsilon_{1/2}$ and increase in A_s (section 8.1.1). In fMRI, the BOLD effect is associated with increase in pixel intensities. In fMRS, the BOLD effect is most discernible on the spectral peak height (H), and so the term "BOLD change or response" is often used to mean "change in spectral peak height" [246, 247]. Hence, the BOLD change in the tissue water and metabolite resonances was quantified as a percentage change in H as follows:

$$\text{Percentage BOLD change} = [(H_{stimulation} - H_{rest})/H_{rest}] \times 100\ \% \qquad \text{(Eq. 8.11)}$$

where $H_{stimulation}$ and H_{rest} are the spectral peak heights (or intensities) associated with the stimulus and rest periods. The corresponding percentage changes in $\Delta\upsilon_{1/2}$ and A_s were calculated in the same way as in equation 8.11. However, the calculated percentage changes in the peak linewidth (% $\Delta\upsilon_{1/2}$) were negative values but have been reported as positive values in the summary tables (see Tables 8.1-8.6).

In this thesis, the term "BOLD effect" will refer to % ΔH, % $\Delta\upsilon_{1/2}$ and % ΔA_S together, whereas the term "BOLD change" or "BOLD response" will refer to % ΔH alone.

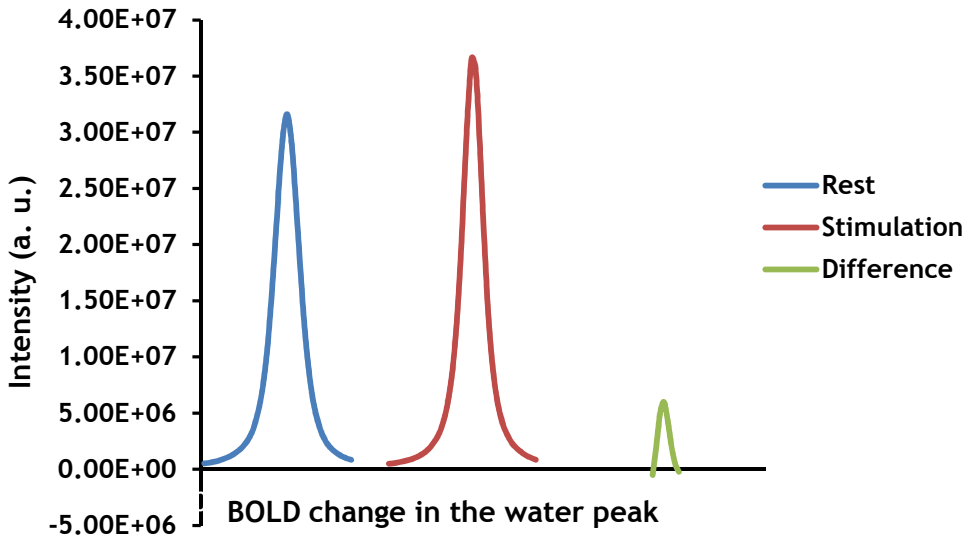

Figure 8.5: Estimation of the BOLD effect on the water resonance peak.
The intensity increase is associated with decrease in linewidth and increase in the area under the peak. The small difference is expressed as a percentage of the intensity at rest. The BOLD effects on the metabolite peaks were estimated in the same manner. This example is the fMRS on subject D_8; see Table 8.3 for the percentage changes in the peak parameters.

Both the rest and stimulation spectral peaks of Figure 8.5 were produced by averaging their individual spectral lines, such as the representation shown in Figure 8.1a. Signal changes due to neuroactivation are usually small [251] and within the noise level [255]. Therefore, spectral averaging over the rest/stimulus cycles in this sense will allow for a clearer discrimination of the

signal changes from background noise [251]. This means that the higher the number of rest/stimulus cycles, the clearer the signal difference will be, since the background noise will be averaged.

8.3 Results and Discussion

This section is divided into three main subsections: the first subsection (section 8.3.1) presents the results of the fMRS study using NEX = 2; this comprises the BOLD effect on the tissue water (section 8.3.1.1) and metabolite (section 8.3.1.2) resonances. The second subsection (section 8.3.2) presents the results of the fMRS study using NEX = 8; this also comprises results for tissue water (section 8.3.2.1) and the metabolites (section 8.3.2.2). The third/last subsection (section 8.3.3) compares the calculated BOLD changes between NEX = 2 and NEX = 8 for three healthy volunteers scanned on both NEX values; this comprises results for the "Off-On" (section 8.3.3.1) and "block" (section 8.3.3.2) paradigms. Sections 8.3.1 and 8.3.2 also show the results for these two paradigms, but they are summarised in tables together.

The 6 volunteers studied in this chapter were each labelled with a unique identifier: A, B, C, D, E and F. Subscripts '2' and '8' were included in the identifiers to distinguish between those scanned on the NEX = 2 and NEX = 8 protocols, respectively. Subjects C, D and E were scanned on both protocols, and are thus identified as C_2, D_2 and E_2 for NEX = 2 (Table 8.1); and C_8, D_8 and E_8 for NEX = 8 (Table 8.3).

8.3.1 Functional MRS Study with NEX = 2

For both tissue water and the metabolite resonances, 64 spectral peaks were quantified for the entire cycle duration (acquisition time window = 6-384 sec, step 6 sec) in the "Off-On" paradigm. On the other hand, 96 spectral peaks (16 peaks per block) were quantified for the cycle duration of the acquisition (time window = 6-576 sec, step 6 sec) in the "block" paradigm. The time activity plots for water shown in Figures 8.6-811 were therefore obtained by plotting

the values of H, $\upsilon_{1/2}$ and A_S for 64 and 96 spectral peaks versus the respective acquisition time windows for the two paradigms. For the metabolites (section 8.3.1.2), only the time course plots for the stimulus periods in the "Off-On" paradigm have been shown (Figures 8.12-8.14). The percentage changes in H, $\upsilon_{1/2}$ and A_S for water and the metabolites were then calculated from 64 and 96 averages of their respective values for the "Off-On" and "block" paradigms.

8.3.1.1 BOLD Effect on the Water Resonance when NEX = 2

Table 8.1 shows the percentage BOLD changes (ΔH %), and the associated linewidth ($\Delta\upsilon_{1/2}$ %) and area (ΔA_s %) changes in water for each one of the five volunteers; the changes are shown for the two paradigms. For both paradigms, the average percentage change (± standard error, SE) for the five subjects in all three peak parameters were calculated. The significance values of the changes are indicated by the P-value (from paired t-tests).

Subject	ΔH (%)		$\Delta\upsilon_{1/2}$ (%)		ΔA_S (%)	
	Off-On	Block	Off-On	Block	Off-On	Block
A_2	5.05	0.20	4.24	0.25	1.34	0.05
B_2	6.58	1.97	3.42	1.99	1.12	0.08
C_2	8.31	1.58	3.50	2.72	0.96	0.12
D_2	9.53	0.42	5.37	1.62	1.19	0.10
E_2	2.91	0.99	6.90	1.96	1.01	0.01
Mean ± SE	6.48 ± 1.17	1.03 ± 0.34	4.69 ± 0.65	1.71 ± 0.41	1.12 ± 0.07	0.07 ± 0.02
P-value	< 0.01	< 0.01	< 0.01	< 0.01	< 0.01	0.91

Table 8.1: Spectral peak height (ΔH), linewidth ($\Delta\upsilon_{1/2}$) and area (ΔAs) changes in water during visual stimulation when NEX = 2.
Note that the percentage $\Delta\upsilon_{1/2}$ values are all negative

For each subject, the percentage changes in the three quantitative parameters of the water peak were significantly greater in the "Off-On" than in the "block" paradigms (% ΔH: P = 0.01; % $\Delta\upsilon_{1/2}$: P = 0.02; % ΔA_S: P < 0.01). The resulting difference between the two paradigms could have been due to two reasons: firstly, the longer stimulation period in the "block" paradigm may

have resulted in volunteer fatigue and loss of attention [251], the effect being a decrease in response to the stimulus after repeated presentations (this is known as the habituation effect). Secondly, 32 (compared to 64 in the "Off-On" paradigm) averages were collected in each one of the rest and stimulus periods of the "block" paradigm. Theoretically, this will mean that the BOLD change that will be recorded in each cycle period of the "block" paradigm will be half of that which will be recorded in the "Off-On" paradigm. Consequently, two cycle periods should have given approximately the same BOLD effect; however, this did not happen even with three cycle periods. Higher spectral noise amplitudes due to the fewer averages collected in each cycle period, in addition to the habituation effect and possibly motion artefacts, could have accounted for the lower BOLD change in the "block" paradigm.

However, the BOLD changes (ΔH) and their associated decrease in spectral linewidth ($\Delta\upsilon_{1/2}$) were small but significant in both paradigms ($P < 0.01$). The effect on the water peak area (ΔA_S) was significant in the "Off-On" ($P < 0.01$) but not in the "block" paradigm ($P = 0.91$). Generally, the changes in H and $\upsilon_{1/2}$ cause only a small change in A_S. Therefore, if the changes in H and $\upsilon_{1/2}$ become considerably smaller with the "block" paradigm, then the change in A_S will not be significant.

The inter-subject variability (in this case, the CoV) in BOLD response varied widely among the volunteers in both paradigms, and was even poorer in the "block" paradigm. The CoVs ([SD/mean] x 100 %) for the "Off-On" paradigm were: ΔH = 40.45 %, $\Delta\upsilon_{1/2}$ = 31.25 % and ΔA_S = 13.41 %; those for the "block" paradigm were: H = 72.65 %, $\Delta\upsilon_{1/2}$ = 53.18 % and ΔA_S = 60.06 %. The generally significant inter-subject variability could arise from differences in vascular architectures and cerebral blood volume changes induced by neural activity [263, 264]. The increased variability with the "block" paradigm may be due to the afore-mentioned factors, plus differences in the tolerance levels (motion and habituation) of the individual subjects to the prolonged and repeated stimulation.

Only two studies, so far, in the literature [246, 247] have measured the BOLD effect on the water resonance. Whereas Zhu and Chen [246] conducted their study at 4 T and used only the "block" paradigm with an 8 Hz visual stimulus, Shih et al [247] performed their experiments at 3 T using the two paradigms with a 6 Hz visual stimulus. Zhu and Chen [246] collected 20 averages in each of their five consecutive periods (designed as three OFF periods interleaved with two ON periods), resulting in a total of 100 spectra. For six volunteers, they reported a mean (SE) percentage BOLD change of 3.0 (0.4) % and associated linewidth percentage decrease of 2.3 (0.3) %. No change in the water peak area was reported. Shih et al [247] on the other hand, collected 128 averages in each of the rest and stimulus periods of their "Off-On" paradigm; and 32 averages for each of their eight consecutive periods (designed as four ONs and four OFFs), resulting in 256 spectra. For five volunteers, they reported a mean (SE) percentage BOLD change of 3.0 (0.5) % and associated linewidth decrease of 0.6 (0.1) Hz; the peak area increased by 0.8 (0.3) %. The estimated BOLD and linewidth changes were said to be the same for both paradigms but it was not clear which paradigm gave the reported area change, which was comparable to the estimate from the "Off-On" paradigm of this thesis (i.e. 1.12 (0.07) %).

Compared to the above paradigm designs, the "block" paradigm presented in this thesis consisted of 32 averages collected for each of the six consecutive periods (three OFFs interleaved with three ONs), resulting in a total of 192 spectra. The "Off-On" paradigm consisted of 64 averages in each one of the rest and stimulus periods. The experiments were conducted with the same *TR* value and with the PRESS sequence as in the above studies (Shih et al used a variant of PRESS that collected the water and metabolite spectra, simultaneously). The *TE* value on the other hand of this thesis differed from that of Shih et al (23 ms vs. 30 ms), but was the same as that of Zhu and Chen. The discrepancies in some of the results reported in this thesis and those in the literature [246, 247] cannot be explained by the differences in the *TE* values or the order of the rest and stimulus periods in the paradigms [265]. There are, however, possible contributions of field strength [246] and the inherent inter-

subject variability observed in this thesis to the discrepancies. At a higher field strength, the susceptibility gradient that is associated with changes in T_2^* increases; and so does the BOLD effect, which varied at the field strength in this study and those in the literature.

The higher field strength used by Zhu and Chen [246] could have accounted for the slightly higher BOLD change they reported; their linewidth change was however comparable to that reported in this thesis (for the block paradigm). In particular, significant habituation effects could have also contributed to the slightly lower BOLD responses in this thesis due to the prolonged examination period. Compared to the study by Shih et al [247], their 6 Hz visual stimulation could have caused a slightly lower BOLD change, even though they reported a similar BOLD change to Zhu and Chen [246]. With only half the number of averages used by Shih et al [247], the BOLD change observed in this thesis was twice what they recorded with the "Off-On" paradigm; the area changes were however comparable between the two studies. The higher BOLD change in this thesis could be due to the stronger stimulus used. The similarity in the BOLD changes between their (Shih et al) two paradigms was rather surprising, particularly when their "block" paradigm was considerably longer. With only one cycle duration difference in the "block" paradigms (same averages per block in both studies) used in the two studies, the BOLD and area changes reported in this thesis were significantly lower compared to those of Shih et al [247]. The large variation in the BOLD responses even among subjects in the "block" paradigm in this thesis could be the main source of this discrepancy.

Figures 8.6-8.8 and 8.9-8.11 show the fMRS time courses for water in the "Off-On" and "block" paradigms, respectively. Each plotted point is the average from five healthy volunteers, and the error bars represent standard deviations. The coloured rectangular blocks on the time axes indicate the task period of visual stimulation.

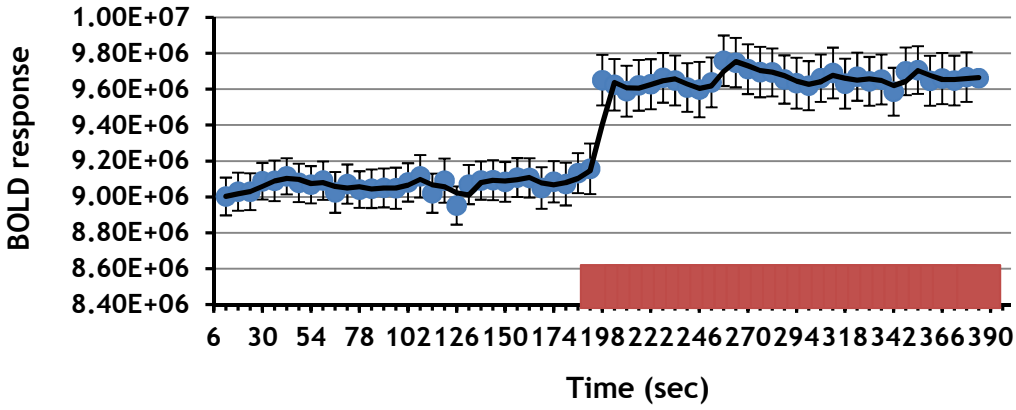

Figure 8.6: Time course ("Off-On") of the fMRS BOLD changes (ΔH %) in tissue water

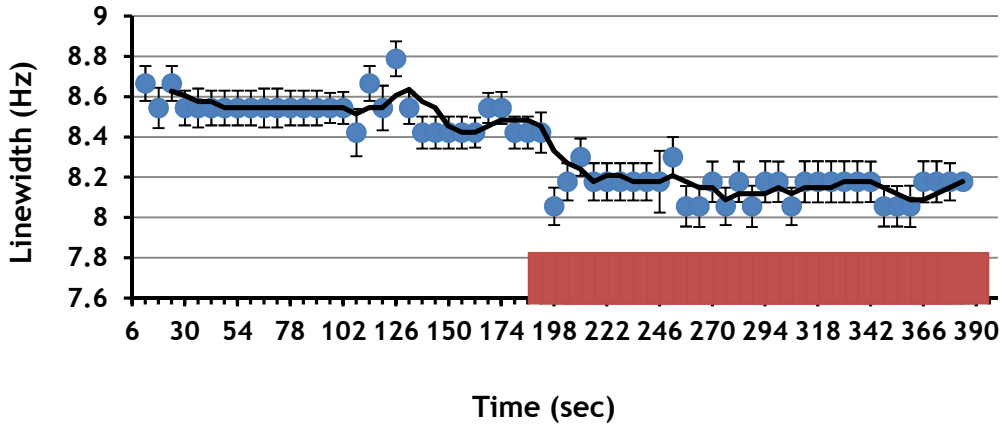

Figure 8.7: Time course ("Off-On") of the fMRS linewidth changes (Δυ %) in tissue water

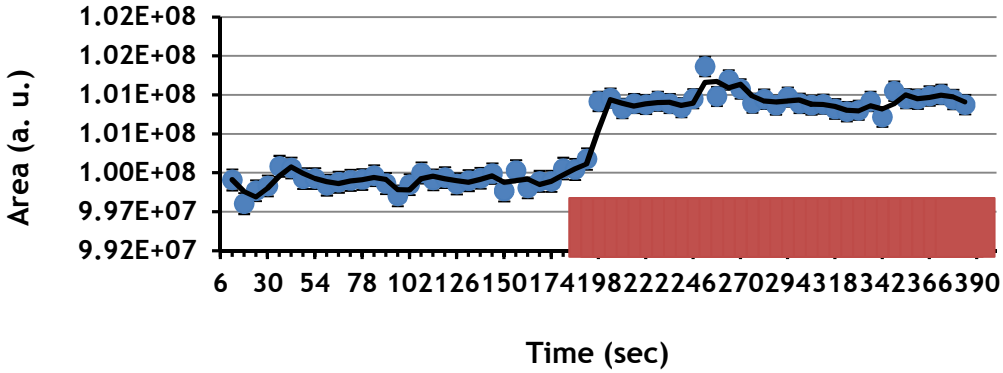

Figure 8.8: Time course ("Off-On") of the fMRS peak area changes (ΔA_S %) in tissue water

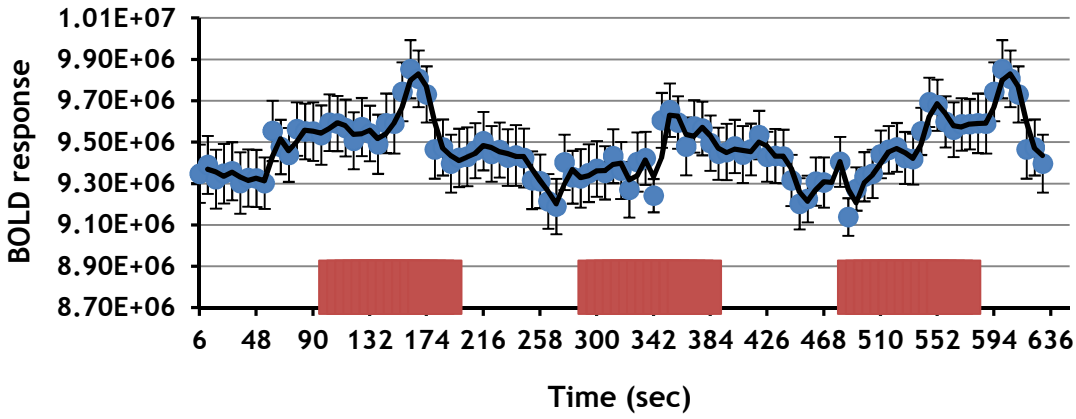

Figure 8.9: Time course ("block") of the fMRS BOLD changes (ΔH %) in tissue water

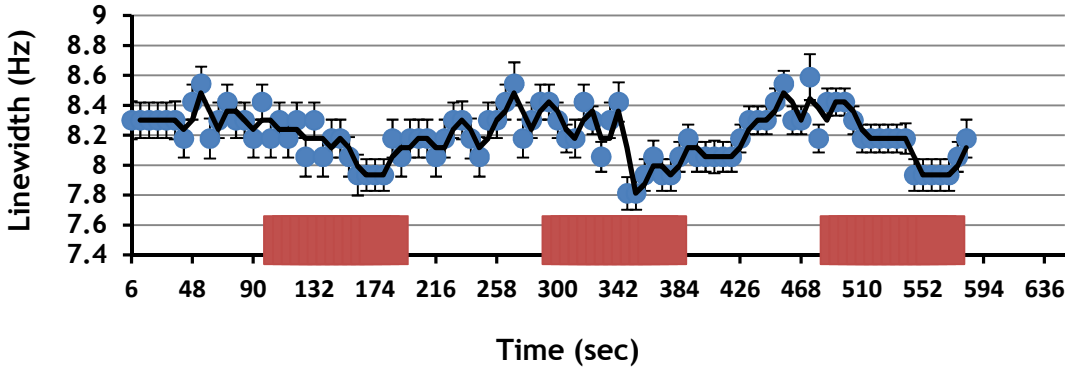

Figure 8.10: Time course ("block") of the fMRS linewidth changes (Δυ %) in tissue water. Note that the linewidth decreases during the stimulus periods and increases during the rest periods

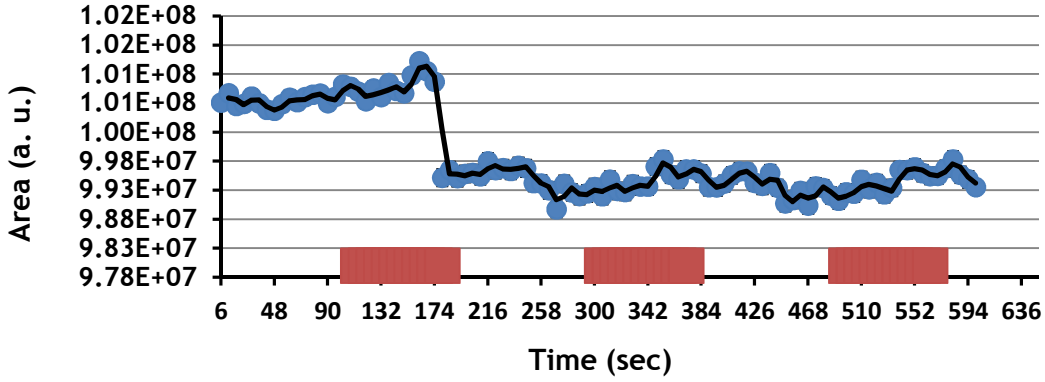

Figure 8.11: Time course ("block") of the fMRS peak area changes (ΔA_S %) in tissue water

8.3.1.2 BOLD Effect on the Metabolite Resonances when NEX = 2

Table 8.2 shows the percentage BOLD changes (ΔH %), and the associated linewidth ($\Delta\upsilon_{1/2}$ %) and area (A_s %) changes in the metabolite resonances. For both paradigms, the average percentage changes (± standard error, SE) are shown. These were calculated from the five subjects in section 8.3.1.1. The significance values of the changes are indicated by the P-value (from paired t-tests).

Peak	% ΔH ± SE (P-value)		% $\Delta\upsilon_{1/2}$ ± SE (P-value)		% ΔA_S ± SE (P-value)	
	Off-On	Block	Off-On	Block	Off-On	Block
NAA	10.20 ± 1.74 (< 0.01)	0.38 ± 0.12 (0.56)	6.12 ± 1.03 (< 0.01)	0.38 ± 0.11 (0.76)	4.09 ± 0.89 (< 0.01)	0.79 ± 0.18 (0.53)
Glu	6.21 ± 1.42 (< 0.01)	1.93 ± 0.27 (0.14)	0.98 ± 0.10 (0.87)	1.23 ± 0.53 (0.81)	9.19 ± 1.78 (0.11)	1.39 ± 0.40 (0.74)
Gln	5.21 ± 2.36 (< 0.01)	0.28 ± 0.13 (0.80)	12.12 ± 2.34 (0.04)	2.05 ± 0.54 (0.66)	15.73 ± 1.44 (< 0.01)	2.59 ± 0.90 (0.47)
Cr	10.27 ± 2.46 (< 0.01)	0.30 ± 0.12 (0.80)	6.55 ± 1.34 (< 0.01)	1.10 ± 0.35 (0.49)	3.45 ± 0.82 (0.03)	1.65 ± 0.42 (0.25)
Cho	11.06 ± 2.69 (< 0.01)	2.31 ± 0.82 (< 0.01)	12.94 ± 1.49 (0.01)	1.76 ± 0.57 (0.46)	17.54 ± 2.02 (< 0.01)	3.61 ± 0.92 (0.11)
mI	5.20 ± 1.16 (< 0.01)	0.11 ± 0.04 (0.92)	0.88 ± 0.17 (0.84)	2.05 ± 0.86 (0.49)	3.63 ± 1.52 (0.38)	1.64 ± 0.47 (0.52)

Table 8.2: Average spectral peak height (ΔH), linewidth ($\Delta\upsilon_{1/2}$) and area (ΔAs) changes in the metabolites during visual stimulation when NEX = 2

The BOLD effect alters the T_2* of both water and metabolite signals [246]. This phenomenon causes a small narrowing (0.2-0.3 Hz) of the spectral linewidth at 4 T of all signals in the spectrum during neural stimulation, which is mostly discernible on the strongest singlets of the methyl group of NAA and total Cr [256] particularly with the single ("Off-On") activation paradigm (see Table 8.2). In fact, all the metabolite peaks in Table 8.2 showed significant BOLD changes (ΔH %) with the "Off-On" paradigm (P < 0.01), which were each also significantly greater than their corresponding changes with the "block" paradigm. Only Cho showed a significant ΔH % with the "block" paradigm but this was lower than its corresponding change with the "Off-On" paradigm. For

the associated ΔA_S %, each metabolite peak changed significantly more with the "Off-On" than with the "block" paradigm. Apart from Glu and mI, $\Delta\upsilon_{1/2}$ % in all metabolite peaks was greater with the "Off-On" than with the "block" paradigm. For Glu and mI, the higher $\Delta\upsilon_{1/2}$ % for the "block" paradigm could have resulted from random line broadening effects during prolonged stimulation as shown by the larger error values. Otherwise, the higher $\Delta\upsilon_{1/2}$ % in the Glu and mI peaks for the "block" compared to that for the "Off-On" paradigm was not expected. Shih et al [247] also did not find any correlation between mI change and stimulation.

For their "block" paradigm, Shih et al [247] reported average changes in the concentrations of Cho, NAA and Cr (in decreasing order) from five volunteers as 6.0, 2.7 and 2.3 %. This study did not calculate the metabolite concentrations but that should not cause any difference in the percentage BOLD changes between the two studies [265]. The BOLD changes (% ΔH) in this study were relatively lower but followed the same decreasing order of changes (Cho: 2.31 %, NAA: 0.38 %, Cr: 0.30 %). The corresponding area changes were however of the form Cho > Cr > NAA.

To record the BOLD effects in their spectra, Zhu and Chen [246] performed the following interleaved acquisition: rest-visual stimulation-rest; eight and sixteen spectra were acquired in the rest and stimulation periods, respectively. They estimated the mean (SE) % ΔH and % $\Delta\upsilon_{1/2}$ for NAA and Cr from six volunteers as: % ΔH; NAA = 2.5 (0.6), Cr = 3.1 (0.7); and % $\Delta\upsilon_{1/2}$; NAA = 1.7 (0.5), Cr = 1.8 (0.5). The estimated % ΔH of this study for both metabolites were comparatively lower but % $\Delta\upsilon_{1/2}$ for Cr was similar in both studies.

Mangia et al [256] reported a 3.0 (1) % increase in Glu concentration (from twelve healthy volunteers) at 7 T during the "Off-On" paradigm. The scanner was equipped with a quadrature transmit/receive half-volume RF coil with increased local sensitivity in the visual cortex. Their rest and stimulus periods lasted for 2.7 and 5.3 minutes, respectively. This study used equal rest and stimulus periods of 3.2 minutes and recorded a BOLD change of 6.2 (1.4) % in

Glu. In their study, Mangia et al observed that Glu exhibited a delayed response to the stimulus and manifested a general tendency of decreasing over time. If this is the case, then their lower percentage concentration change (which is comparable to the BOLD change in this thesis) could have been due to the longer activation period of their paradigm; the percentage change could have been lower with the same activation period at 3 T. Secondly, they minimised the effects of linewidth changes by applying line-broadening filters to their stimulation spectra to match with their rest spectra before the subtraction. This may proportionally decrease the area under the smaller peaks in particular (which includes Glu). Consequently, the percentage change in concentration will be lower since concentration is estimated from the peak area. About 2 % to 11 % stimulation induced increases in lactate, glutathione and Glu during the "Off-On" and "block" paradigms at 7 T have been reported elsewhere [266]. Thus, even though there are some discrepancies in the results, they appear to be within some general range.

In another study at 7 T by Mangia et al [255], they simulated the BOLD effect on spectral line narrowing by applying line-broadening filters that increased spectral linewidth to 0.3-0.4 Hz (the same order of line narrowing due to the BOLD effect at 7 T). For most of the seventeen metabolite spectra they quantified *in vivo* (in two healthy subjects), they reported that the estimated concentrations systematically decreased by almost 1 %. Thus their simulated BOLD changes (in those metabolites of interest in this study) were: NAA = 1.2 %, Glu = 1.1 %, Gln = 0.1 %, Cr = 0.8 %, Cho = 1.4 % and mI = 1.0 %. However, the non-simulated, *in vivo* linewidth changes in this study were at least 1.2 Hz (~ 3 times those simulated by Mangia et al). Therefore, if the stimulated BOLD effects by Mangia et al were adjusted by the respective multiplicative factors (i.e. when the linewidth changes in the two studies are compared) for the metabolites, the results may be directly comparable. It is also likely that the relatively high change in spectral linewidth reported in this study could be due to poor spectral resolution issues at 3 T since the actual T_2^* change due to the BOLD effect is usually small as reported by Mangia et al. However, since the 8 Hz stimulation periods in both paradigms were prolonged, the BOLD effects

became more prominent (evident in the comparisons with previous studies) and discernible in the presence of the poor resolution.

Baslow et al [254] used an 8 Hz stimulus in a 10 minute rest-10 minute stimulation-10 minute rest paradigm at 3 T to study six subjects (aged 31-73 years). Their main metabolite of interest was NAA, which was quantified by the integral of its peak; the BOLD change was therefore defined as the percentage change in peak area. They found a 13.1 % decrease in the NAA peak area during stimulation, which increased gradually to the baseline level during the recovery period (i.e. the last rest period). This negative BOLD effect was attributed to increase in neuronal NAA metabolism, hydrolysis and efflux during stimulation; while its synthesis was decreased. They therefore concluded that NAA possibly acts as a molecular water pump during sustained neuronal activity. However, large variations (standard deviation of up to 12.8 %, and 26.4 % decrease in NAA) in some of their trials were pointed out by Mangia and Tkac [265] as possible factors that could have affected their overall estimates since they (Mangia and Tkac) observed only ~2 % increase in the height of the NAA peak at 7 T in their study [256].

However, a similar negative BOLD effect has also been observed elsewhere [267]. In this study, migraine patients without (MwoA) and with aura (MwA) were compared to control subjects (C) by photic stimulation at 8 Hz. Scans were performed at 1.5 T using a paradigm of the form 3.7 minutes of rest, 25.7 minutes of stimulation and 7.4 minutes of recovery periods. They estimated their BOLD changes in the NAA and Cr peaks as percentage change in their areas. For the three groups (C/MwoA/MwA), the percentage mean BOLD changes (SD) in NAA were 7.42 (1.32)/5.79 (0.25)/14.05 (2.0) and those in Cr were 11.66 (1.87)/11.71 (3.41)/12.50 (0.31). Note that these averages are negatives, indicating decreases in the areas of the two metabolite peaks. Compared to the result of Baslow et al (who studied healthy subjects only), the negative BOLD change in NAA for the controls was much lower (7.4 % vs. 13.1 %); and the positive BOLD effects on the NAA and Cr peak areas were relatively small (if considered as decreases) in this thesis. The signals however were

reported to gradually recover during the rest period, similar to the observation made by Baslow et al. They conceded it was difficult to explain this reversible decrease of the metabolite signals, particularly of NAA. This was because the decrease and recovery did not mean neuronal loss and resynthesis of NAA, respectively. At best, they thought the reason could be due to redistribution of NAA from intra- to extracellular space. It is suggested that [268] this variation in the chemical environment of NAA (and for that matter all the metabolites and water) could result in its NMR visibility, resulting in the rapid signal changes.

The origin of the negative BOLD effect in the visual cortex during visual stimulation has been attributed to a reduction in neural activity, such as attention or higher-order cognitive functions [269]. In an fMRI study at 4.7 T, Harel et al [270] observed a prolonged negative BOLD signal change in the high-order visual cortex region in anaesthetised cats. This region of interest they studied was suggested to experience increased spike activities during the task period. They attributed the negative BOLD change to a decrease in cerebral blood flow (CBF), which they thought was likely induced by a reallocation of blood flow from the less demanding areas to the most CBF demanding regions. They therefore concluded that a negative BOLD change does not necessarily reflect a decrease in spike activity. In the case of fMRS, a reduction in the spike [270] or neural [269] activity during visual stimulation will mean that those lines of data collected during the reduction may have approximately the same peak height, linewidth and area. The average of these stimulation spectral lines may not be too different from the average of the rest spectra; a negative difference could result from the subtraction, which does not necessarily, in this case, represent a BOLD change. The exact origin, nature and approximate absolute value of the negative BOLD change is unclear in fMRS since no other study in the literature (including this thesis), apart from the two discussed, has so far reported such findings.

Summary plots of the time courses for all the metabolites studied in this thesis are shown below: their peak height changes are shown in Figure 8.12, linewidth

changes in Figure 8.13, and area changes in Figure 8.14. Note that the paradigm blocks are not shown in these figures as all the plotted points (or time courses) are related to only the stimulation periods; points for the rest periods are not plotted so that the activation time courses appear clearer.

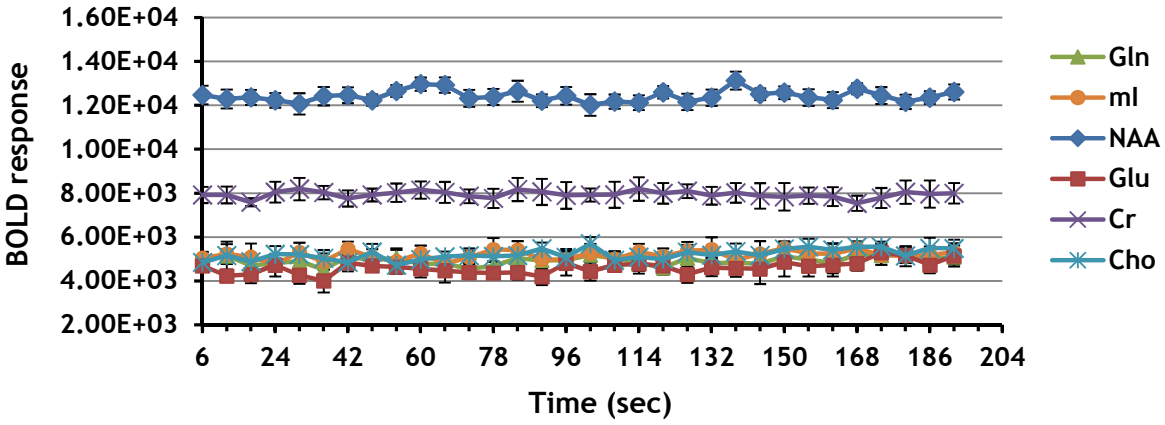

Figure 8.12: Time course of the fMRS BOLD changes (ΔH %) in the metabolites during the stimulation period of the "Off-On" paradigm when NEX = 2

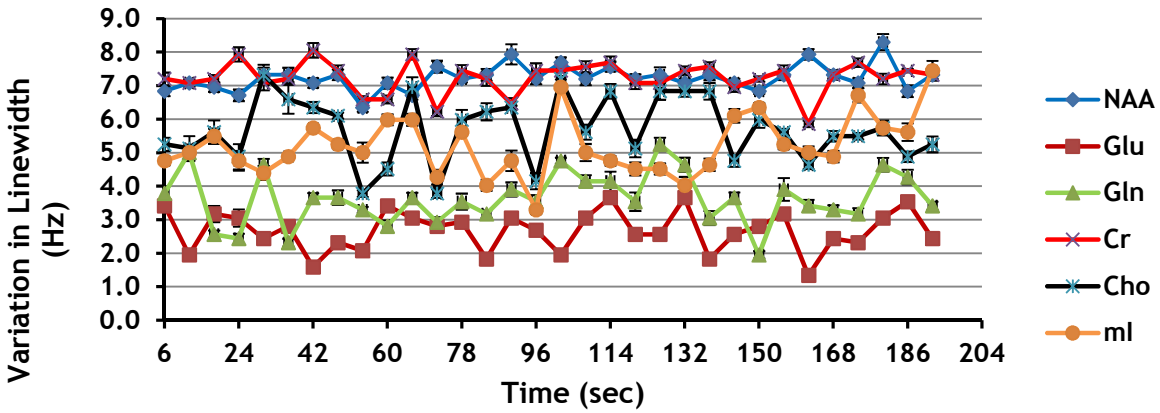

Figure 8.13: Time course of the fMRS linewidth changes ($\Delta\upsilon_{1/2}$ %) in the metabolites during the stimulation period of the "Off-On" paradigm when NEX = 2

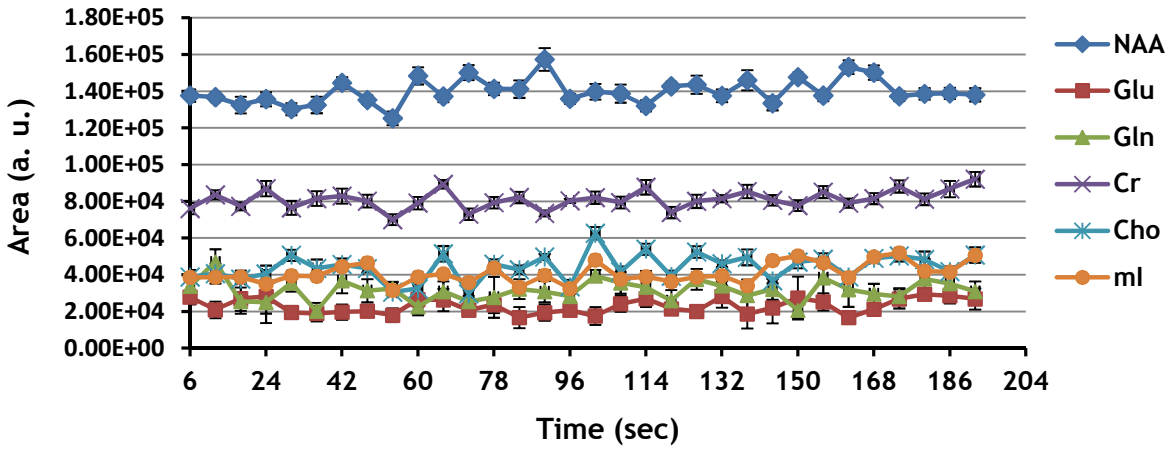

Figure 8.14: Time course of the fMRS area changes (ΔA_S %) in the metabolites during the stimulation period of the "Off-On" paradigm when NEX = 2

8.3.2 Functional MRS Study with NEX = 8

Compared to NEX = 2, when NEX = 8 is used for the fMRS acquisitions, four lines of spectra are collected and averaged to represent a single spectral line (Figure 8.1) with a temporal resolution of 24 sec. This causes the data space to be filled with fewer spectral lines, with the advantage that motion artefacts are reduced [31]. Since a number of lines are averaged per NSA (4 lines/24 seconds in this case), any motion artefact will not be affecting a larger number of individual lines but an average, which is less affected by motion-related noise. Such averaging is usually suitable in the case of normal MRS acquisitions but may impact on how much of the BOLD effect could be recorded in fMRS. It is possible that during spectral averaging, some neural activity may not be captured or that some lines within the rest and stimulus periods could be averaged together. This could then possibly lead to significant losses in the amount of BOLD effect recorded or that if the absolute BOLD change (ΔH) is not affected, then the estimated percentage change (ΔH %) will be underestimated. Thus, the results presented in this section were aimed to investigate the impact of NEX = 8 on the amount of BOLD effect to be recorded during fMRS.

The same acquisition protocol as in section 8.3.1 was used except for the NEX value being switched to 8 for the results presented in this section. The first subsection (section 8.3.2.1) presents the BOLD effects on water and the last subsection (section 8.3.2.2) are the results for the metabolites.

8.3.2.1 BOLD Effect on the Water Resonance when NEX = 8

Table 8.3 shows the BOLD effects on the water resonance peak amplitude (ΔH), linewidth ($\Delta\upsilon_{1/2}$) and area (ΔA_S). The percentage changes are shown for each of three subjects in section 8.3.1, plus one more subject (F_8). The mean percentage changes (± standard error, SE) from all four subjects for the two paradigms are also shown, with the P-values indicating the significance of the change.

Subject	ΔH (%)		$\Delta\upsilon_{1/2}$ (%)		ΔA_S (%)	
	Off-On	Block	Off-On	Block	Off-On	Block
C_8	20.52	0.27	7.20	0.01	0.10	0.01
D_8	14.77	0.05	4.87	0.04	0.31	0.08
E_8	9.93	0.13	1.28	0.02	0.07	0.05
F_8	28.25	0.10	0.45	0.02	0.89	0.31
Mean ± SE	18.37 ± 3.94	0.14 ± 0.05	3.45 ± 1.58	0.02 ± 0.01	0.34 ± 0.19	0.11 ± 0.07
p-value	< 0.01	0.82	< 0.01	1.00	0.24	0.49

Table 8.3: Spectral peak height (ΔH), linewidth ($\Delta\upsilon_{1/2}$) and area (ΔAs) changes in water during visual stimulation when NEX = 8

In a similar pattern to that observed in section 8.3.1.1, the BOLD changes, ΔH with the "Off-On" were significantly greater than those with the "block" paradigm (P = 0.02). However, the corresponding changes in linewidth, $\Delta\upsilon_{1/2}$ (P = 0.12) and peak area, ΔA_S (P = 0.16) were not significantly different between the two paradigms, even though the changes were greater in the "Off-On" paradigm. There was also a significant variability in the BOLD responses among the subjects, indicated by the CoVs for both paradigms ("Off-On": ΔH = 42.92 %, $\Delta\upsilon_{1/2}$ = 91.34 %, ΔA_S = 111.04 %; "block": ΔH = 68.58 %, $\Delta\upsilon_{1/2}$ = 55.92 %, ΔA_S =

119.78 %). Unlike the case for NEX = 2, the CoV of the linewidth changes was better in the "block" than in the "Off-On" paradigm. This is because NEX = 8, with more signal averages as in the "block" paradigm, helps to reduce spectral linewidth broadening due to motion artefacts [31]. Therefore, the reduced contribution of motion to the linewidth changes could have left changes mainly due to stimulation, resulting in a better variability which is then due to the factors mentioned in section 8.3.1.1.

As was expected, the BOLD effects on the three peak parameters were generally lower compared to the BOLD effects with NEX = 2. Incidentally, the mean BOLD change (ΔH) in the "Off-On" paradigm was significantly higher. Even though this appears to be the observed trend between the two NEX values, it is best to make these comparisons for the same subjects scanned with the two NEX values (this was done in section 8.3.3) due to the inherent variability factor introduced into these estimated mean changes by subject F_8.

Indeed, compared to the results of Shih et al [247] and Zhu and Chen [246], the BOLD changes recorded with NEX = 8 were all significantly lower. Only ΔH % for the "Off-On" paradigm with NEX = 8 in this thesis was significantly higher than those of the above studies. The NEX value does not particularly affect the amount of neural activity; it only affects the way (and how much of) the resulting BOLD effect is recorded by the scanner. Therefore, this exceptionally high BOLD change was unexpected; and so it was unclear what might have caused such a change. Acquisitions in the rest and stimulus periods of the "Off-On" paradigm were performed separately and not in a continuous way (as in the case of the six consecutive acquisitions of the "block" paradigm). After the rest scan, the scanner was re-shimmed and the stimulus period acquisition was done. This could have offered two advantages: firstly, the subject had some rest between the "Off" and "On" acquisitions, and so could tolerate the next acquisition with less movement. Secondly, there is no possibility that the scanner will average the "Off" and "On" lines together. This then gives two spectral line sets containing the pure "Off" and "On" effects, where the averaged spectral lines with the "On" effect have less contribution from

motion (so peak height and linewidth changes will be mainly due to the BOLD effect). Therefore, a higher difference in peak heights between the two data sets could result. However, since this is the first study that has investigated this NEX = 8 effect, future studies may be required to further investigate the findings presented.

The time courses of the fMRS BOLD effects on the water resonance are shown in Figure 8.15 for the "Off-On" and Figures 8.16-18 for the "block" paradigms. The plotted points are averages from the four subjects in Table 8.3; the error bars represent standard deviations. The coloured rectangular blocks on the time axes indicate the task period of visual stimulation.

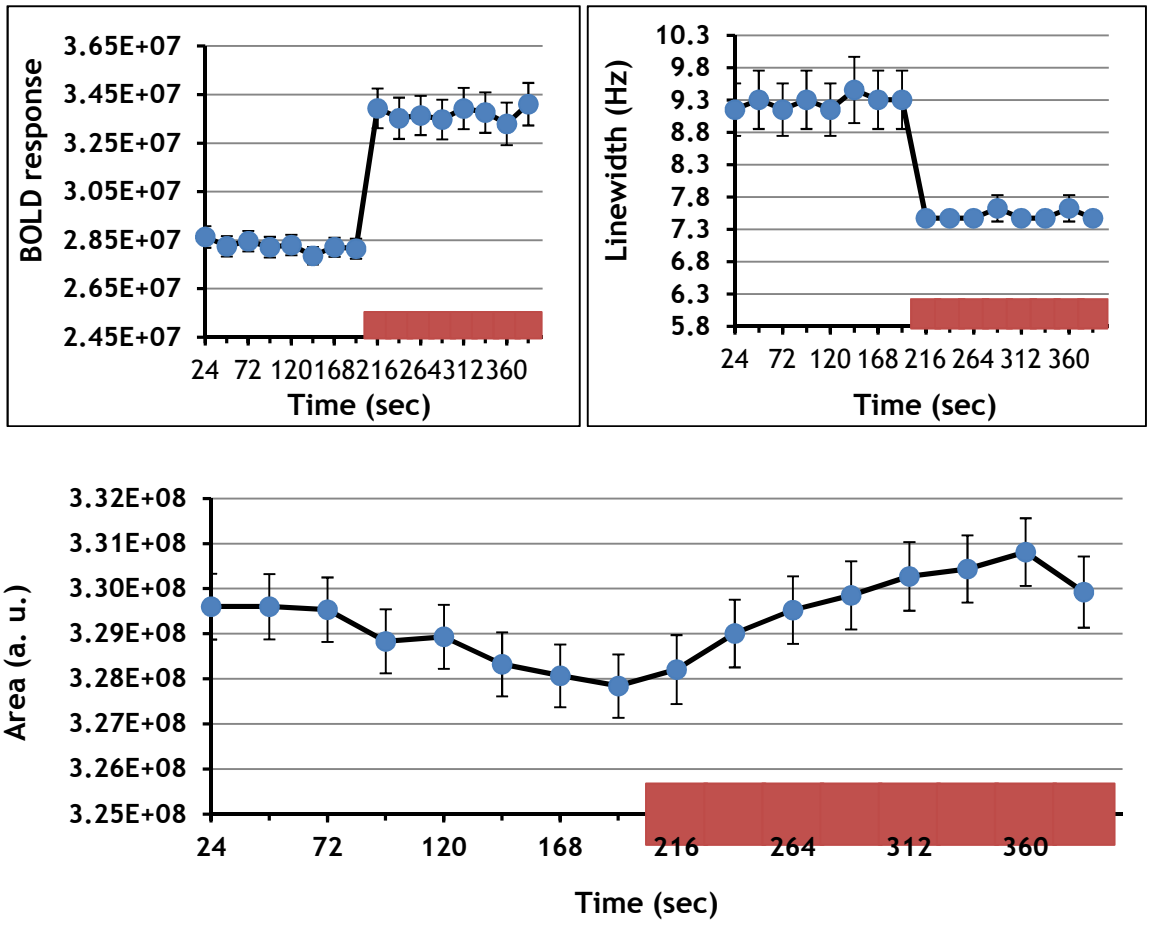

Figure 8.15: Time courses of the fMRS BOLD, ΔH (top left), linewidth, $\Delta\upsilon_{1/2}$ (top right) and area, ΔA_S (bottom) changes in water during the visual stimulation when NEX = 8

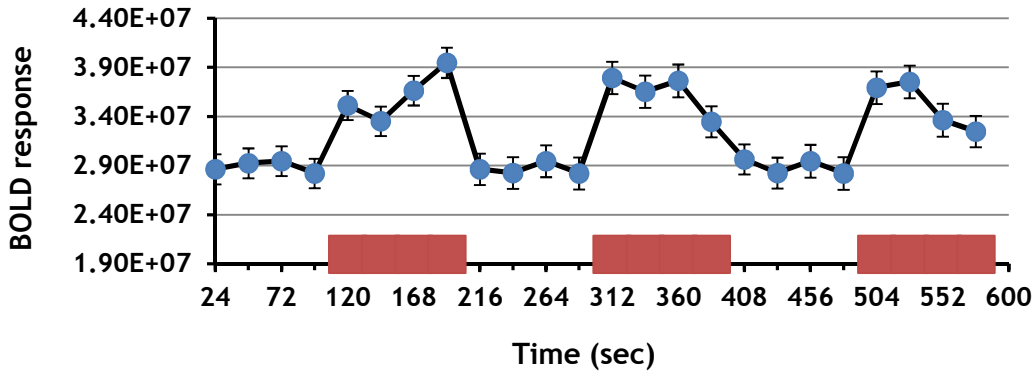

Figure 8.16: Time course of the fMRS BOLD changes (ΔH %) in water during the stimulation period when NEX = 8

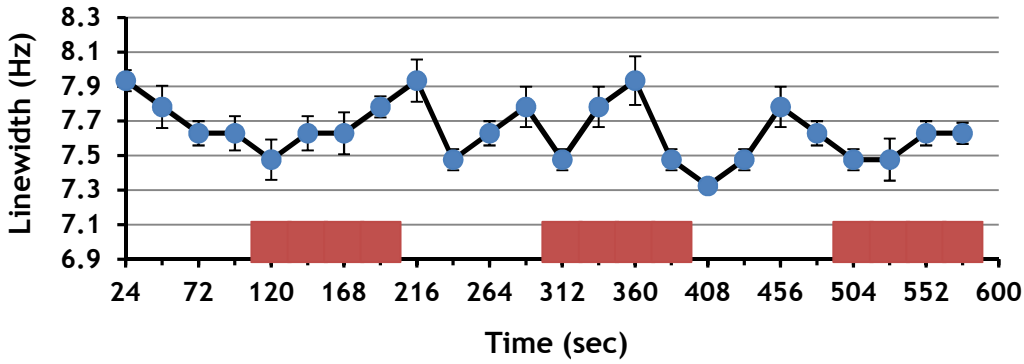

Figure 8.17: Time course of the fMRS linewidth changes ($\Delta\upsilon_{1/2}$ %) in water during the stimulation period when NEX = 8

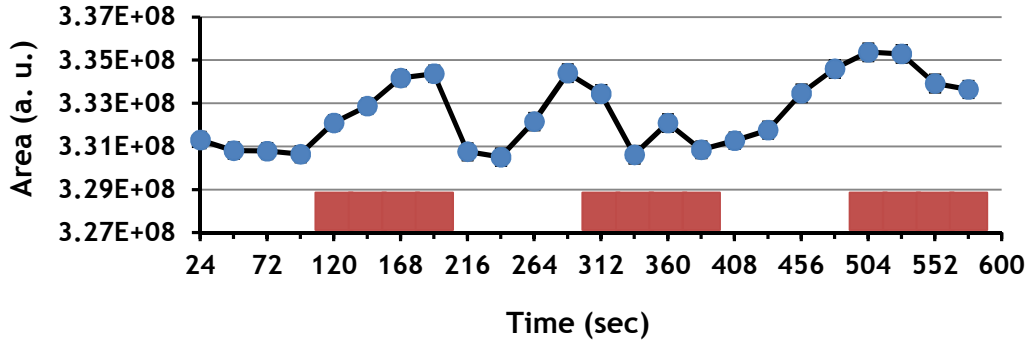

Figure 8.18: Time course of the fMRS area changes (ΔA_S %) in water during the stimulation period when NEX = 8

8.3.2.2 BOLD Effect on the Metabolite Resonances when NEX = 8

Table 8.4 summarises the mean BOLD effects on each of the cerebral metabolite peaks from the four volunteers in Table 8.3. The significance of each average change is denoted by a P-value in parenthesis and under the average value.

Peak	% $\Delta H \pm$ SE (P-value)		% $\Delta\upsilon_{1/2} \pm$ SE (P-value)		% $\Delta A_S \pm$ SE (P-value)	
	Off-On	Block	Off-On	Block	Off-On	Block
NAA	0.49 ± 0.18 (0.72)	1.09 ± 0.41 (0.14)	5.59 ± 1.94 (0.07)	1.09 ± 0.35 (0.45)	11.17 ± 1.94 (0.01)	0.85 ± 0.47 (0.68)
Glu	0.24 ± 0.14 (0.90)	0.05 ± 0.02 (0.98)	4.52 ± 0.78 (0.69)	5.26 ± 1.28 (0.61)	0.57 ± 0.24 (0.95)	4.76 ± 0.57 (0.56)
Gln	1.61 ± 0.46 (0.29)	0.16 ± 0.07 (0.91)	2.06 ± 0.79 (0.72)	7.19 ± 1.24 (0.22)	14.59 ± 1.88 (0.05)	2.42 ± 0.68 (0.11)
Cr	0.78 ± 0.24 (0.53)	0.18 ± 0.09 (0.90)	0.85 ± 0.28 (0.79)	3.05 ± 0.97 (0.04)	7.35 ± 0.94 (0.02)	0.86 ± 0.35 (0.71)
Cho	2.24 ± 0.47 (0.01)	1.41 ± 0.65 (0.25)	2.10 ± 0.95 (0.73)	2.62 ± 0.93 (0.12)	7.59 ± 0.84 (0.11)	2.09 ± 0.63 (0.54)
mI	1.75 ± 0.38 (0.35)	1.23 ± 0.46 (0.35)	1.82 ± 0.47 (0.69)	1.03 ± 0.65 (0.74)	0.86 ± 0.39 (0.85)	2.92 ± 0.74 (0.32)

Table 8.4: Average spectral peak height (ΔH), linewidth ($\Delta\upsilon_{1/2}$) and area (ΔAs) changes in the metabolites during visual stimulation when NEX = 8

The results in Table 8.4 show that only the BOLD change in Cho during the "Off-On" paradigm was significant (P = 0.01); all other metabolites did not respond significantly (P > 0.05) to the BOLD effect. No metabolite showed a significant BOLD response with the "block" paradigm. The linewidth narrowing effect was not significant in all metabolites with the "Off-On" paradigm; and only Cr showed significant linewidth narrowing with the "block" paradigm (P = 0.04). Change in spectral peak area was significant in only NAA (P = 0.01) and Cr (P = 0.02) with the "Off-On" paradigm; Gln (P = 0.05) was on the minimum P-value to showing significance in peak area change. No spectral peak area change was significant with the "block" paradigm.

Compared to the fMRS results with NEX = 2 in Table 8.2, % ΔH in all metabolites were significantly lower with the "Off-On" paradigm; and only changes in NAA and mI were slightly higher with the "block" paradigm. The % $\Delta\upsilon_{1/2}$ in all metabolites were lower with NEX = 8, except for Glu and mI, in the "Off-On" paradigm. However, in the "block" paradigm, % $\Delta\upsilon_{1/2}$ in all peaks were greater with NEX = 8; except for mI. For % ΔA_S, apart from NAA and Cr, all other metabolites showed less changes with NEX = 8 in the "Off-On" paradigm. Finally, only NAA, Glu and mI showed greater % ΔA_S in the "block" paradigm (with NEX = 8).

The NEX = 8 BOLD effects shown in Table 8.4 were found to compare favourably with the BOLD simulation results at 7 T by Mangia et al [255]. The percentage changes in their concentrations compared with the "Off-On" results for Cr (0.8 % vs. 0.78 %); and with the "block" results for NAA (1.2 % vs. 1.09 %), Gln (0.1 % vs. 0.16 %), Cho (1.4 % vs. 1.41 %) and mI (1.0 % vs. 1.23 %); only the BOLD change in Glu was found to be comparatively lower in this study (1.1 % vs. 0.24 %). However, with the "block" paradigm, its peak area change due to the BOLD effect compared with the percentage concentration change in Glu elsewhere, also at 7 T [256] (3.0 ± 1.0 vs. 4.76 ± 0.57).

Specifically for NAA, with the "block" paradigm, % ΔH and % $\Delta\upsilon_{1/2}$ were found to be comparable to the "block" paradigm results of Zhu and Chen at 4 T [246]: 2.5 ± 0.6 vs. 1.09 ± 0.41 for % ΔH, and 1.7 ± 0.5 vs. 1.09 ± 0.35 for % $\Delta\upsilon_{1/2}$.

These findings suggest that even though NEX = 8 appears to 'worsen' the temporal resolution of the data, it tends to average the spectral lines in such a way that the estimated BOLD effects at 3 T now have less uncertainties, which otherwise would have made % ΔH, % $\Delta\upsilon_{1/2}$ and % ΔA_S considerably different from the expected results at higher fields. These similarities of the estimated BOLD effects when NEX = 8 (which gives a temporal resolution of 24 sec) at 3 T with those estimated at higher fields (4 T and 7 T), where better temporal resolutions have been used, imply that using a lower temporal resolution may offer some benefits at lower fields when studying the BOLD effects with fMRS.

However, such a resolution often gives fewer points to plot the time courses of the spectra for the cycle durations. The time courses for the BOLD changes, linewidth and peak area changes for each metabolite are shown in the summary plots of Figures 8.19, 8.20 and 8.21, respectively. The paradigm blocks are not shown in these figures as all the plotted points relate to only the stimulation periods; points for the rest periods are not plotted so that the activation pattern can be more visible in the graphs.

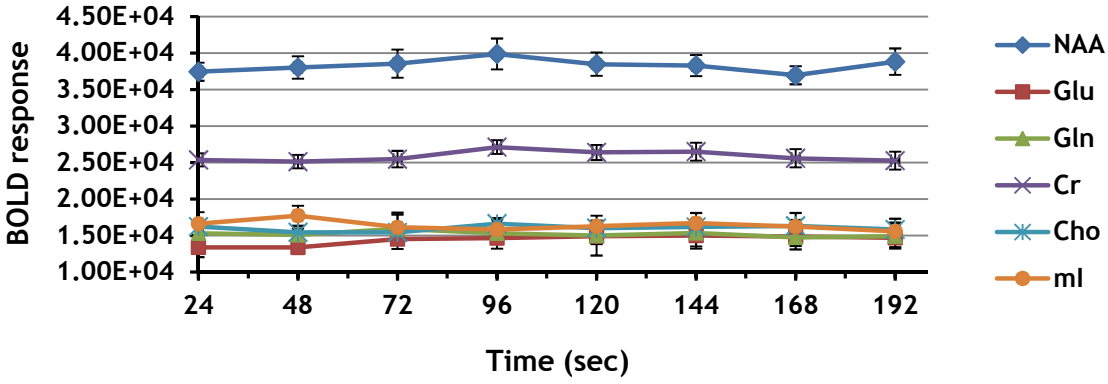

Figure 8.19: Time course of the fMRS BOLD changes (ΔH %) in the metabolites during the stimulation period of the "Off-On" paradigm when NEX = 8

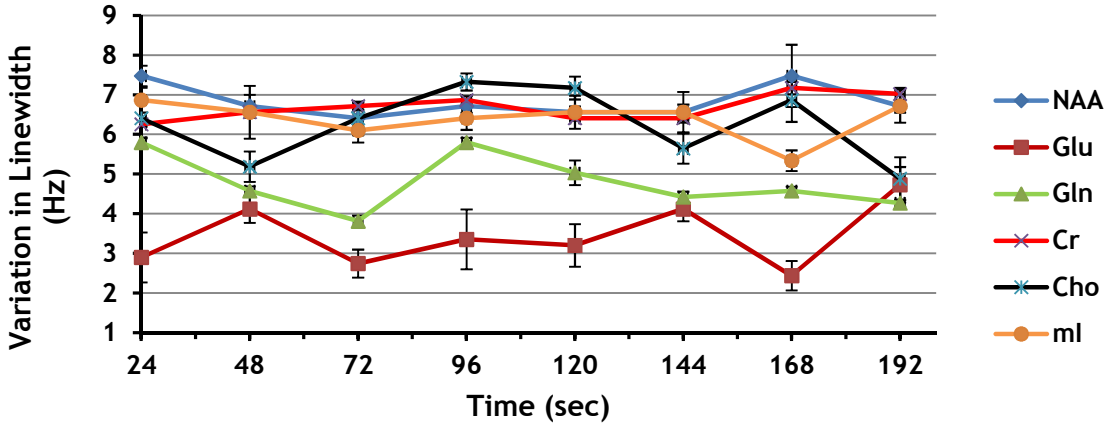

Figure 8.20: Time course of the fMRS linewidth changes ($\Delta\upsilon_{1/2}$ %) in the metabolites during the stimulation period of the "Off-On" paradigm when NEX = 8

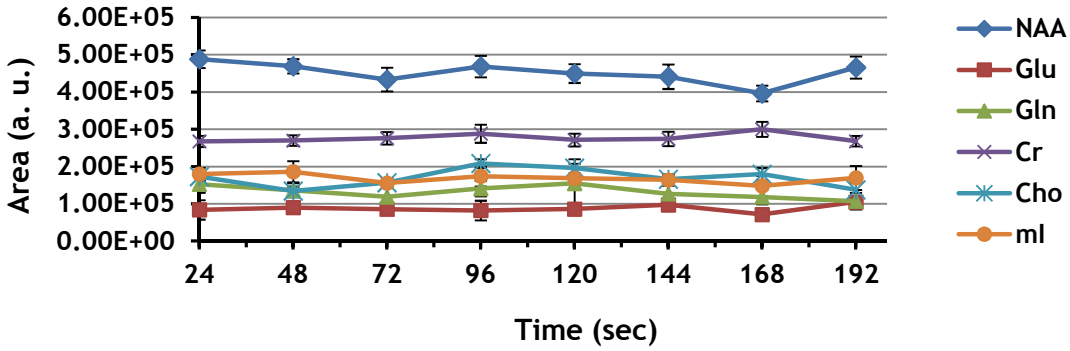

Figure 8.21: Time course of the fMRS area changes (ΔA_S %) in the metabolites during the stimulation period of the "Off-On" paradigm when NEX = 8

8.3.3 NEX = 2 versus NEX = 8 BOLD Effects on the Spectra

The reproducibility of measuring the *in vivo* metabolite and water signals by the MR scanner used for this project was assessed in chapter 3. It was shown that over a course of a year, the CoVs of measuring water, NAA, and Cho were less than 10 %; those for Glu, tCr and mI were about 26 %, 10 % and 13 %, respectively; and Gln was not reliably detected (see Table 3.4). In this section, results are presented for the BOLD effects on water and the metabolites measured in three volunteers with NEX = 2, and again, over the course of about 3-4 months, with NEX = 8. From the CoVs measured previously, the difference in the BOLD effects observed between the two NEX values should also be interpreted in light of the contributions from the respective uncertainties in the spectra arising from the time interval between the experiments. Even though these uncertainties (from the reproducibility results) may appear not to contribute significantly to the changes in the prominent spectral peaks of water, NAA and Cho, they could contribute to significant changes in Gln, Cr and mI.

It was not appropriate to estimate the intra-subject CoV for each peak in the current study because the measurements were not done with the same protocol (i.e. NEX was not the same). Hence, the reproducibility study of

chapter 3 provided the level of uncertainty that should be considered when interpreting the results in this section (see the paragraph above).

8.3.3.1 NEX = 2 vs. NEX = 8 BOLD Effects in the "Off-On" Paradigm

Table 8.5 compares the effects of the two NEX values on the mean % ΔH, % $\Delta\upsilon_{1/2}$ and % ΔA_S in the water and metabolite peaks from three healthy subjects during the "Off-On" paradigm. The P-value next to each comparison is the significance of the difference between the two percentage values.

	% ΔH ± SE			% $\Delta\upsilon_{1/2}$ ± SE			% ΔA_S ± SE		
Peak	NEX =2	NEX = 8	p-value	NEX = 2	NEX =8	p-value	NEX = 2	NEX = 8	p-value
H_2O	6.92 ± 2.03	15.07 ± 3.06	0.06	5.26 ± 0.98	4.45 ± 1.72	0.79	1.05 ± 0.07	0.16 ± 0.08	< 0.01
NAA	7.94 ± 1.23	0.46 ± 0.25	0.03	5.35 ± 1.13	4.34 ± 2.10	0.70	4.19 ± 1.53	12.63 ± 1.81	0.03
Glu	4.55 ± 1.78	0.29 ± 0.18	0.15	0.92 ± 0.16	4.29 ± 1.06	0.11	10.60 ± 1.58	0.70 ± 0.28	0.02
Gln	3.05 ± 1.22	1.26 ± 0.41	0.24	10.13 ± 3.05	1.75 ± 1.02	0.06	14.14 ± 1.92	12.85 ± 0.98	0.30
Cr	8.99 ± 2.41	0.73 ± 0.33	0.09	6.45 ± 1.33	0.85 ± 0.39	0.04	2.93 ± 1.38	7.75 ± 1.20	0.20
Cho	9.32 ± 2.99	2.14 ± 0.65	0.17	11.74 ± 1.67	2.55 ± 1.19	0.02	14.82 ± 1.04	7.50 ± 1.18	0.06
mI	4.62 ± 1.39	1.41 ± 0.26	0.18	0.84 ± 0.30	1.97 ± 0.62	0.30	4.09 ± 2.34	1.08 ± 0.45	0.26

Table 8.5: Average spectral peak height (ΔH), linewidth ($\Delta\upsilon_{1/2}$) and area (ΔAs) changes in water and the metabolites during visual stimulation: comparison between NEX = 2 and NEX = 8 estimated changes in the "Off-On" paradigm

The results indicate that with this paradigm, NEX = 8 reduced the BOLD signal (% ΔH) recorded from all the metabolites except that from water. The BOLD effects on linewidth were also decreased in all resonances except those on Glu and mI. Apart from NAA and Cr, all other resonance peaks also showed lesser changes in their peak areas when NEX = 8 compared to when NEX = 2. However, only NAA showed a significant reduction (P = 0.03) in % ΔH with NEX = 8, only

Cr ($P = 0.04$) and Cho ($P = 0.02$) in % $\Delta\upsilon_{1/2}$, and water ($P < 0.01$), NAA ($P = 0.03$) and Glu ($P = 0.02$) in % ΔA_S.

Even though the reduction in the BOLD effects with NEX = 8 appeared quite large, the paired t-test analysis did not show a significant outcome (i.e. $P < 0.05$) in most cases. This could have been due to a power issue as the sample size ($n = 3$) was small. A small sample size may reduce the sensitivity of the statistical test to picking significant differences. A confidence interval (CI) of 90 % could have been used, so that the minimum P-value for significance becomes 0.10; hence making the statistical test more sensitive. However, this lowers the chances of eliminating significant outcomes arising from large random errors in the measurements. Moreover, changing the significance level at this stage is inconsistent with the P-value of 0.05 set for all significant results in this thesis. In a separate exploratory analysis (not shown) assuming the data was non-parametric, even though it was shown to be parametric, and so using the Wilcoxon (signed-rank) test, the same significance outcomes were obtained. In any case, the limitation of the paired t-test used here is that it assumes that the measurements were carried out at equal time intervals in all subjects and experimental sessions [254], which is practically not the case with the experiments discussed in this thesis.

8.3.3.2 NEX = 2 vs. NEX = 8 BOLD Effects in the "Block" Paradigm

Table 8.6 compares the effects of the two NEX values on the mean % ΔH, % $\Delta\upsilon_{1/2}$ and % ΔA_S in the water and metabolite peaks from three healthy subjects (in Table 8.5) during the "block" paradigm. The P-value next to each comparison is the significance of the difference between the two percentage values.

Peak	%ΔH ± SE		p-value	%Δυ$_{1/2}$ ± SE		p-value	%ΔA ± SE		p-value
	NEX = 2	NEX = 8		NEX = 2	NEX = 8		NEX = 2	NEX = 8	
H_2O	0.99 ± 0.34	0.15 ± 0.06	0.09	2.10 ± 0.33	0.02 ± 0.01	0.03	0.08 ± 0.03	0.05 ± 0.02	0.55
NAA	0.43 ± 0.15	1.38 ± 0.42	0.24	0.42 ± 0.19	0.76 ± 0.18	0.40	0.73 ± 0.31	0.81 ± 0.67	0.93
Glu	2.23 ± 0.33	0.05 ± 0.03	0.02	0.84 ± 0.50	4.91 ± 1.74	0.20	1.76 ± 0.55	4.94 ± 0.76	0.13
Gln	0.43 ± 0.17	0.18 ± 0.10	0.37	2.36 ± 0.88	6.60 ± 1.55	0.03	3.52 ± 1.26	2.30 ± 0.95	0.53
Cr	0.36 ± 0.19	0.21 ± 0.11	0.19	0.69 ± 0.09	2.97 ± 1.37	0.24	2.02 ± 0.63	1.01 ± 0.45	0.11
Cho	3.29 ± 1.00	1.36 ± 0.91	0.37	1.82 ± 0.92	1.77 ± 0.51	0.96	3.91 ± 1.62	1.66 ± 0.67	0.16
mI	0.14 ± 0.07	1.20 ± 0.66	0.21	2.51 ± 1.43	1.36 ± 0.78	0.59	2.01 ± 0.73	3.15 ± 0.99	0.56

Table 8.6: Average spectral peak height (ΔH), linewidth (Δυ$_{1/2}$) and area (ΔAs) changes in water and the metabolites during visual stimulation: comparison between NEX = 2 and NEX = 8 estimated changes in the "block" paradigm

Table 8.6 shows that with the "block" paradigm, NEX = 8 reduced the BOLD changes (% ΔH) in all spectral peaks except those in NAA and mI. The BOLD effects on linewidth were also decreased in most resonances except those on NAA, Glu, Gln and Cr. Apart from NAA, Glu and mI, all other resonance peaks also showed lesser changes in their peak areas when NEX = 8 compared to when NEX = 2. However, only Glu showed a significant reduction (P = 0.02) in % ΔH with NEX = 8, only water (P = 0.03) and Gln (P = 0.03) in % Δυ$_{1/2}$, and no spectral peak showed a significant change in % ΔA_S. For both NEX values however, the BOLD effects with the "On-Off" paradigm were generally greater than those with the "block" paradigm.

NEX = 8 is the default value on most clinical MR scanners and so the user does not have to change it before an acquisition, which is an advantage. Therefore, if NEX = 8 appears not to significantly cause a change in the water peak area in fMRS while providing BOLD changes comparable to literature estimates, then two deductions could be drawn: water has proven to be consistent in its peak area while responding significantly to the BOLD effect; and that for fMRS at 3T,

NEX = 8 may be the suitable choice of temporal resolution as it provides better results (compared to NEX = 2).

8.4 Summary and Conclusions

In this chapter, the BOLD effects on the spectral peaks of water and the metabolites have been investigated with the single-voxel MRS technique called fMRS. The BOLD effect caused increases in spectral peak height with associated narrowing of linewidth, and small increases in peak area. The magnitude of these changes were influenced by local susceptibility changes during elevated neural activity, the changes arising from variations in deoxyhaemoglobin content in blood that create a susceptibility gradient (as well as changes in water diffusion gradient) across the intravascular and extravascular tissue compartments. This phenomenon affects the NMR visibility of both water and the metabolites, and so their rapid changes as observed by fMRS.

Absolute concentrations were not calculated for water and metabolites in this chapter because reliable quantification of the concentrations during functional experiments is demanding. Moreover, estimation of the BOLD effects in percentage units using the peak intensity, linewidth and area do not require any rigorous quantification, which could even introduce more errors in the estimated percentage BOLD changes.

Two objectives were investigated in the chapter: firstly, the consistency of the water peak area during neural stimulation and secondly, the relative effects on the amount of BOLD effects observed in water and the metabolites when the temporal resolution of the data is varied.

The temporal resolution of the spectral lines in fMRS is defined by the NEX value. Only two NEX values were available on the MR scanner used for this project: ‘2’ and ‘8’. Two fMRS experimental paradigms were designed to investigate the above objectives: ‘single’ and ‘repeated’ activation paradigms.

The water peak area was found to be relatively stable with both paradigms, regardless of temporal resolution. Only the peak area change with NEX = 2 in the single paradigm was significant. This significant change during the sustained, single activation paradigm (which was not the case with the metabolites) was possibly due to significant BOLD signal contribution from water within the intra- and extravascular compartments, simultaneously when stimulation persisted; the metabolites are mainly confined to the brain parenchyma and so their BOLD signals are said to originate from only the extravascular cellular compartment. Indeed, the water peak area changes between NEX = 2 and NEX = 8 were found to be significantly different with the single, but not the repeated, activation paradigm.

The investigation of the effect of the temporal resolution, NEX on the quantified BOLD changes at 3 T has been done for the first time in this thesis. For the effects of temporal resolution, the results showed that the single activation paradigm generally gave higher BOLD effects than the repeated activation paradigm (this possibly also contributed to the significant change in the water peak area). For both paradigms, the BOLD effects with NEX = 2 were generally higher than those with NEX = 8. The NEX = 8 BOLD changes however showed better comparison with literature values than the changes with NEX = 2. The estimates of BOLD changes were in good agreement with results at higher fields, specifically at 4 and 7 T, where detection sensitivity is even higher. The study thus shows that temporal resolution of at least 24 seconds (when NEX = 8) at 3 T offers benefits of reduction of motion-related artefacts in the data, quicker signal averaging and better estimation accuracy of the BOLD changes in cerebral water and the metabolites in fMRS experiments. However, the sensitivity to detecting accurate BOLD changes in these experiments can be increased by using field strengths above 3 T.

Chapter 9: Final Conclusions

9.1 Novel Contributions and Main Findings of this Thesis

This thesis embodies a series of studies that have been put together to form a comprehensive and cohesive description of the NMR response of cerebral water under different experimental conditions. The main investigations were: relaxation properties of regional cerebral water content in a healthy brain (chapter 5); effect of varying voxel positions on cerebral water content in a healthy brain (chapter 6); cerebral water content in medicated and unmedicated peripheral inflammation (chapter 7); and cerebral water BOLD signal characteristics in a healthy brain (chapter 8). The investigations in chapters 6 and 7 primarily involved the quantification of cerebral water content, which would not have been possible without partial saturation, T_1 and T_2 corrections (chapter 5), which, in turn, were aided in establishing their reliability by the reproducibility study in chapter 3. It was suggested that the BOLD changes of the functional MRS study in chapter 8 should also be interpreted in relation to the reliability of the measurements, which were established by the reproducibility study (chapter 3). Thus, cohesion was established among all the chapters presented in this thesis. This thesis did not, however, exclude the measurement of cerebral metabolites; chapters 3, 5, 7 and 8 included the metabolites in the respective investigations as well.

In the process of quantifying cerebral water content and investigating its NMR response characteristics, new techniques were developed and novel results were discovered.

Sensitivity maps of the eight-channel RF coil for all possible voxel positions *in vivo* have been established for the first time in this thesis. The maps were obtained by plotting the unsuppressed-water signal areas against their

respective voxel positions in phantom experiments. Polynomial fits to these plots in 3-dimensional space yielded standard polynomial equations. To quantify *in vivo* cerebral water content, the SI-coordinate value of the respective *in vivo* voxel position was used to choose the appropriate polynomial function from the fits. Substitution of the AP and LR coordinates of that voxel position into this polynomial function yielded a signal area that was from the same voxel position as the *in vivo* water signal. The *in vivo* measured water signal was then referenced to the deduced (same-voxel-position) signal using a standard mathematical model that accounted for all necessary corrections; the result was an absolute measure of cerebral water content. This one-time-only external reference calibration method has been developed and applied for the first time in this thesis. This new technique for quantifying tissue water content does not require extra or prolonged signal acquisitions for purposes of referencing; the quantification procedure does not also require correction for spatial variation in coil sensitivity since both the *in vivo* water and deduced reference signals are measured from the same voxel position. In addition to these, the unsuppressed-water signal can be acquired at the same time as the metabolite signals.

Further to the use of the unsuppressed-water signal for quantification of cerebral water content, the same signal area was optimised (by the necessary correction factors) and used as an endogenous reference in the estimation of cerebral metabolite concentrations. Both the water and metabolite quantification techniques yielded estimates that were comparable with published values for the same brain regions and tissue types. Thus, both techniques were validated and could be used in future MRS studies.

In agreement with previous studies [61, 177], cerebral water content was found in this thesis to be uniformly distributed across various brain regions, and was not observed to vary with age or gender. The results also corroborated previous findings [58-60, 62]that water content of grey matter tissue is higher compared to that of white matter tissue.

For the first time, this thesis also compared regional water content and MT ratio variation across the brain. For the same brain regions, the pattern of cerebral water distribution as measured by MRS was found to be comparable to the regional MT ratio estimates derived from MT imaging. MT imaging was thus suggested in this thesis as a possible way of validating regional variation in cerebral water content as measured by MRS. In any case, such comparative deductions have not been done previously, and so the comparison in itself adds to the novel contributions of this thesis.

The voxel contents for the estimation of the cerebral water values in previous MRS studies [58, 59] were either almost grey or white matter tissues. However, the voxel contents of grey and white matter tissues in this thesis did not vary significantly in most cases; yet the tissue water estimates were comparable to those of the previous studies. This was possible due to the inclusion of partial volume correction in the quantification method that ensured the right amount of voxel tissue fraction was used in the estimate. Thus, the water value was scaled to the amount of tissue fraction from which it was quantified. The use of this voxel grey matter/white matter tissue mix in the accurate estimation of tissue-specific cerebral water content is also original.

To date, the few peripheral inflammation (and even fewer psoriatic arthritis particularly) studies [190, 191] have only measured NAA, Cho and Cr, and expressed them in relative units. Using the techniques developed in this thesis, absolute quantification of cerebral water and metabolite concentrations were done for the first time in a group of volunteers diagnosed with, and treated for, psoriatic arthritis. In addition to the three generally measured metabolites (expressed as ratios), this thesis further measured Glu and mI (expressed in absolute units) in the prefrontal brain. Voxel positions in the psoriatic arthritis (PsA) study were the prefrontal, left and right hippocampal regions.

Female PsA patients were found to improve in mood more than their male counterparts; but this did not necessarily mean improvement in their PsA condition as a disability assessment was not done in this study. Even though

cerebral water content in the PsA patients were well within the normal range, they were generally found to have higher tissue water content compared to healthy controls, matched for age and gender. The results of this thesis suggest that in psoriatic arthritis, higher cerebral water content may be associated with improvement in mood. This does not therefore support the suggestion that in peripheral inflammation, brain water content is likely to increase when the normal brain function of recruiting water-soluble proteins to the affected site is compromised (section 7.1.1). In fact, the insignificant changes in the cerebral metabolite concentrations in the PsA patients also indicated that the condition of PsA does not appear to affect cerebral metabolism significantly. Further to this, the patients did not differ significantly from normal in their mood scores. The mood scores did not also vary with cerebral water and metabolite changes following anti-inflammatory therapy.

A significant and new finding from the PsA study was that higher absolute concentrations of left hippocampal NAA may be associated with lower BDI scores (i.e. better mood). This thesis therefore further supports previous studies that have implicated the left brain hemisphere (and structures therein) to play a role in the regulation of mood/behaviour.

In terms of regional variation within the three voxel positions studied in both patients and controls (at baseline and post-medication), only Cr and water were found to be fairly constant. However, in terms of which was stable in PsA, cerebral water was relatively constant. Both were however neither age nor gender dependent in all voxel positions studied.

The stability of cerebral water peak area during sustained neural activation was investigated using two temporal resolution values in the same volunteers, for the first time, in this thesis. Generally, the cerebral water peak area was found to remain fairly constant even though it responded to the activation (the response was manifested as increases in its peak height). Only the peak area change with the temporal resolution of NEX = 2 in a single fMRS paradigm was found to be significant; this was however not the case with the metabolites.

Secondly, there was a significant difference in the BOLD response of cerebral water between NEX = 2 and NEX = 8 in the single, but not repeated, paradigm. It was noted that the origin of the water signal from both intra- and extravascular compartments of the brain might have aided in the significant response to sustained (i.e. single) visual stimulation; the metabolite signals originate from only the extravascular compartment as they are confined in brain parenchyma.

Novel findings from the fMRS studies were that: a single activation paradigm generally gives higher BOLD changes in both water and metabolite peaks; regardless of the fMRS paradigm used, NEX = 2 results in higher BOLD changes compared to NEX = 8; only the BOLD changes recorded with NEX = 8 compare directly with literature values [246, 247, 255, 256]. The reason for this might be that NEX = 8 is the default temporal resolution on most MR scanners (at least on the GE scanner used in this thesis) and so researchers are more likely not to change the NEX value prior to the fMRS experiments. This thesis therefore has revealed that differences in the NEX values used in various studies could be a potential source of discrepancies in their results, in addition to other sources of discrepancies discussed in chapter 8. The results have further shown that BOLD changes could either be significant or not, depending on the paradigm design and temporal resolution (i.e. NEX value) of the MRS data.

Through its novel *in vivo* relaxation time, water content, absolute metabolite and BOLD response measurements, this thesis has improved upon the accuracy and precision of previous MRS studies. In respect of its general objective, this thesis has also corroborated the suitability of cerebral water as a reference concentration in absolute quantitative MRS. Where necessary, the possible sources of the discrepancies between the results presented here and those previously published have been explained. These novel techniques can now be added to the body of knowledge in MRS, and are now ready to serve as tools for future MRS brain studies, both diseased and non-diseased.

9.2 Methodological Limitations and Recommendations

The limitation of the external reference calibration method developed in this thesis was the time taken to acquire all the unsuppressed-water data across the entire FOV of the eight-channel head coil. Future studies may develop and implement quicker MRS pulse sequences to record all the required unsuppressed-water data. On the other hand, a proton-density MRI of a brain phantom may be acquired and used for the same purpose of obtaining the reference signal. The MRI-based method of deducing the reference signal would be possible if there is a way of localising the *in vivo* voxel in the image of the phantom as has been done in this thesis (chapter 4).

The standard equations representing the sensitivity maps of the head coil presented in this thesis may be validated and used for purposes of referencing in future studies. The validation process would require future studies to perform similar measurements on a similar or different scanner type using the eight-channel head coil or a different coil design (e.g. the quadrature head coil). Similar polynomial equations could then be deduced using the unsuppressed-water data. Cerebral water content could then be quantified using the derived reference signals from the different coil designs or experiments. If the results are comparable, it would mean that future studies may not have to perform the RF sensitivity mapping measurements again; and could thus directly use the *in vivo* voxel coordinates substitution method of deriving the reference unsuppressed-water signal.

In the absolute quantification of cerebral water and metabolite concentrations, their respective signals were corrected for T_1 and T_2 relaxation effects using relaxation time estimates from a different set of experiments performed on a separate group of healthy volunteers. Even though this is normally the case in MRS studies [58], errors arising from ROI selections that do not exactly contain the same tissue type as that in the MRS voxel could lead to inaccuracies in the final concentration estimates. Secondly, the health conditions of the two groups of volunteers may vary significantly which may affect the results. With

the techniques developed in this thesis, it is possible to include the *TE* and *TR* of choice for the metabolite acquisition in the T_1 and T_2 measurements; this will allow for the relaxation times and concentrations to be estimated from the same voxel position within the same volunteer, within the same examination session.

For the work on cerebral water quantification and assessment of regional variations (chapter 6), the left and right hippocampal data were only for males. It was necessary to investigate whether hippocampal water content varied by gender; moreover, combining that data set with the hemispheric data set could have introduced some degree of error in the explorative analysis for regional variation in water content. Nevertheless, the hippocampal work in chapter 7 showed that gender was not an issue; neither did regional water content vary significantly as long as the tissue types are the same. However, only data for the left hemisphere was available for the regional water variation in chapter 6. As a recommendation, future studies should take advantage of the shorter acquisition times of the techniques developed in this thesis, and perform the measurements in all the possible voxel positions when assessing regional variation in cerebral water content. This applies to the assessment of regional variation in the metabolite concentrations as well. Regional metabolite concentrations were assessed in only three brain regions (i.e. prefrontal, left and right hippocampi) in this thesis; which is not sufficient for a rigorous test to be done on regional variation in the metabolite concentrations.

Even though the focus of this thesis was not to measure those peaks in the Glx complex, acquisition parameters were carefully selected to ensure that at least the spectral peaks of Glu and Gln were well resolved. The success of the choice of acquisition parameters in this regard was further aided by the higher SNR of the 3 T (compared to 1.5 T) clinical magnet which was equipped with an eight-channel head coil used for all experiments in this thesis. Nonetheless, it was possible that GABA still contributed to the successfully resolved Glu and Gln peaks since no further spectral editing was done to completely resolve those

three components of the Glx complex. Advanced MRS localisation sequences are now available, tailored for the acquisition of the individual components of the Glx complex [271]; spectral editing and even higher field strengths (up to 7 T) are also promising ways of acquiring Glu, Gln and Glx separately [255, 256, 266, 272-274].

In the PsA study, the availability of some important data about the volunteers could have clarified some of the MRS findings. Such data as the BDI scores of the healthy volunteers, comparative MRS data of healthy volunteers at follow up, patient data on disability scores, length of illness and blood cytokine levels (to mention but a few) were crucial to a better understanding of the outcomes of the experiments. Subjects' intake of fluids/water or dehydration status was not accounted for in the estimates of cerebral water content. These pieces of information and some of those discussed in chapter 7 should be included in future studies of cerebral water content in both psoriatic (or any other disease when necessary) and healthy subjects.

9.3 Suggestions for Future Medical Applications

The MRS measurement of absolute metabolite and water concentrations in the human brain *in vivo* can be applied in the study of any disease that has a relationship with the brain. However, one limitation of applying the water content method (described in this thesis) to investigating disease is that the technique assumes that the water content is the same in the intra- and extracellular spaces. In the case of edema or tumor, extracellular water content increases while the intracellular component may remain unaffected. In such a situation, the water signal (and for that matter the water content) attributable to intracellular tissue would be overestimated, and the metabolite concentrations would be underestimated using the water referencing method.

The techniques developed in this thesis can be used in a number of medical applications but the following were the projects of interest to the author and research supervisors during the period of the work presented in this thesis.

9.3.1 Water Measurements in Brain Inflammation and Tumors

In chapter 7, water content and absolute metabolite concentrations were estimated in the brains of patients diagnosed with psoriatic arthritis, PsA (a peripheral inflammatory condition). The technique was sensitive to record subtle changes in cerebral metabolism following anti-inflammatory medication. The technique could therefore even be more sensitive if the condition affects the brain directly, such as tumors and multiple sclerosis, MS (a brain inflammatory condition). T_1 and T_2 corrections for the PsA study were done using T_1 and T_2 estimates from healthy subjects, assuming that the condition did not change the tissue and metabolite T_1 and T_2 relaxation times significantly. However, in the case of direct brain involvement, such as in MS, this assumption may not hold true. Relaxation time corrections are therefore likely to be the challenge in this case. Nonetheless, as proposed in sections 9.1 and 9.2, the quantification technique in this thesis is rapid, and could be combined with relaxation time measurements in the same subject, thus avoiding the need to use T_1 and T_2 values from another study.

9.3.2 Brain Temperature Measurements in fMRS Studies

In section 1.4.2, the application of MRS in brain temperature measurements using the water and NAA peaks was discussed. No human study of fMRS has monitored/measured brain temperature changes resulting from neural stimulation during the experiments. With the spectral processing technique presented in this thesis, it is possible to calculate brain temperature and BOLD changes, simultaneously during neural activation. This could provide an insight into the effect of temperature on the amount of BOLD signal, and also the minimum amount of stimulation that will cause significant temperature rise which may be harmful to a patient. This application can be implemented without the need for any correction to the data since only the displacement between the NAA and water peaks are used to estimate temperature, whereas

the BOLD changes are calculated from the peak height, area and linewidth obtained from the fitting routine described in section 2.3.1.2.

9.3.3 MT Spectroscopy of Cerebral Water Content

Magnetisation Transfer Spectroscopy (MTS) pulse sequences are now available and have been used in previous human studies [275-278]. The MTS method provides the MT ratios of the metabolites in tissue. Only one of these studies used the MTS technique in the quantification of the MT effect on cerebral water content in normal subjects [276]. It would be interesting however to use a normal water-suppressed MTS sequence to acquire both MT on and MT off spectra. Processing these spectra and fitting them in the same way as done in this thesis, it is possible to obtain the unsuppressed-water and metabolite spectral peaks and subsequently calculate their respective MT ratios. This will be advantageous over performing MT imaging and MRS separately on the same subject because the MTS of water and metabolites together will allow for the same voxel position to be used, and will maximise time and equipment. Such a technique could also be used in the assessment of regional water content where MT imaging was used, and has been suggested, to validate the MRS results (chapter 6). Subsequently, such an MTS method could be applied in studies of many disease conditions that impact on brain metabolism, such as in peripheral and CNS inflammation. The calculation of the MT ratios in this case will require only the spectral peak areas which do not need further corrections after spectral fitting.

9.3.4 Cerebral Water Content in Brain Tumor Classification

In fact, this particular project had begun during the preparation of this thesis. The Neurology and Histology Departments of the Southern General Hospital are currently collaborating to undertake the study. Retrospective MRS, radiology and biopsy reports between the years of 2000 and 2010 of 121 tumor patients

have been collected. The MRS data for all patients will be processed using the techniques of this thesis to obtain the unsuppressed-water and metabolite peak areas. While ensuring that the biopsy and radiology reports are blinded to the MRS physicist, the metabolite peak areas will be used in a spectral classifier program, INTERPRET [279], to classify the brain tumors. The metabolite peaks are usually expressed as ratios, relative to either the Cho or Cr peaks [280, 281] (in fact, some other studies [282, 283] have used the water peak for referencing but not in the INTERPRET program). However, in another set of analysis, the default reference peaks will be replaced by the water peak in order to observe any effect this might have on the classification outcomes.

Both classification schemes (i.e. with and without the water peak) will be evaluated for classification accuracy (using ROC curves) by comparison to the biopsy reports (which contain the actual tumor classes). Thus, the water peak will be used in this case, for the first time, to establish a threshold at which brain tumors may vary by classes.

In conclusion, this thesis documents a group of interrelated experiments that have measured and quantified changes (under selected experimental conditions) in the human brain tissue water signal using the single-voxel ^{1}H-MRS technique. These experiments involved the development of novel methods for the quantification of cerebral water and metabolite concentrations, simultaneously. Generally, the findings of this thesis are in support of the use of the endogenous water signal for referencing in absolute quantitative ^{1}H-MRS of the human brain. The developed quantification methods on the other hand do not have subject tolerance issues (as spectral acquisition times are not prolonged), provide accurate results and could therefore be applied in future MRS brain studies involving both patients and healthy subjects.

Appendices

Appendix 2.1: Ethical Approval for Healthy Human Studies

WoSRES
West of Scotland Research Ethics Service

NHS
Greater Glasgow and Clyde

West of Scotland REC 4
Ground Floor, Tennent Building
Western Infirmary
38 Church Street
Glasgow
G11 6NT
www.nhsggc.org.uk

Mr Abdul Nashirudeen Mumuni
PhD Research Student
University of Glasgow
MRI Unit, Institute of Neurological Sciences
1345 Govan Road
Southern General Hospital
Glasgow
G51 4TF

Date 29 September 2011
Direct line 0141-211-1722
Fax 0141-211-1847
e-mail evelyn.jackson@ggc.scot.nhs.uk

Dear Mr Mumuni

Study title:	**Development and Optimisation of MRS Data Acquisition in Studies of Treatment-Resistant Clinical Depression: Reference single voxel Magnetic Resonance (MR) Spectroscopy Brain Scans on Healthy Humans**
REC reference:	**11/WS/0019**

Thank you for your letter of 5 September 2011, responding to the Committee's request for further information on the above research and submitting revised documentation.

The further information was considered in correspondence by a sub-committee of the REC. A list of the sub-committee members is attached.

Confirmation of ethical opinion

On behalf of the Committee, I am pleased to confirm a favourable ethical opinion for the above research on the basis described in the application form, protocol and supporting documentation, as revised, subject to the conditions specified below.

Ethical review of research sites

NHS sites

The favourable opinion applies to all NHS sites taking part in the study, subject to management permission being obtained from the NHS/HSC R&D office prior to the start of the study (see "Conditions of the favourable opinion" below).

Conditions of the favourable opinion

The favourable opinion is subject to the following conditions being met prior to the start of the study.

Management permission or approval must be obtained from each host organisation prior to the start of the study at the site concerned.

Management permission ("R&D approval") should be sought from all NHS organisations involved in the study in accordance with NHS research governance arrangements.

Guidance on applying for NHS permission for research is available in the Integrated Research Application System or at http://www.rdforum.nhs.uk.

Where a NHS organisation's role in the study is limited to identifying and referring potential participants to research sites ("participant identification centre"), guidance should be sought from the R&D office on the information it requires to give permission for this activity.

For non-NHS sites, site management permission should be obtained in accordance with the procedures of the relevant host organisation.

Sponsors are not required to notify the Committee of approvals from host organisations

It is the responsibility of the sponsor to ensure that all the conditions are complied with before the start of the study or its initiation at a particular site (as applicable).

Approved documents

The final list of documents reviewed and approved by the Committee is as follows:

Document	Version	Date
Covering Letter	-	05 September 2011
Investigator CV	-	01 July 2011
Other: Professor B R Condon's CV	-	09 June 2011
Other: Dr J Cavanagh's CV	-	09 June 2011
Participant Consent Form	3.2	05 September 2011
Participant Information Sheet	3.2	05 September 2011
Protocol	1.1	05 September 2011
Questionnaire: The General Health Questionnaire	-	-
REC application	-	-
Response to Request for Further Information	-	-

Statement of compliance

The Committee is constituted in accordance with the Governance Arrangements for Research Ethics Committees (July 2001) and complies fully with the Standard Operating Procedures for Research Ethics Committees in the UK.

After ethical review

Reporting requirements

The attached document *"After ethical review – guidance for researchers"* gives detailed guidance on reporting requirements for studies with a favourable opinion, including:

- Notifying substantial amendments
- Adding new sites and investigators
- Notification of serious breaches of the protocol
- Progress and safety reports
- Notifying the end of the study

The NRES website also provides guidance on these topics, which is updated in the light of changes in reporting requirements or procedures.

Feedback

You are invited to give your view of the service that you have received from the National Research Ethics Service and the application procedure. If you wish to make your views known please use the feedback form available on the website.

Further information is available at National Research Ethics Service website > After Review

11/WS/0019	**Please quote this number on all correspondence**

With the Committee's best wishes for the success of this project.

Yours sincerely

Evelyn Jackson

Dr Brian Neilly
Chair

Enclosures: List of names and professions of members who were present at the meeting
"After ethical review – guidance for researchers"

Copy to: Dr Debra Stuart, R&D Office, Tennent Building, Western Infirmary
Dr Erica Packard, R&D Office, Tennent Building, Western Infirmary

West of Scotland REC 4

Attendance at Sub-Committee of the REC meeting on 30 September 2011

Committee Members:

Name	*Profession*	*Present*	*Notes*
Dr Brian Neilly	Consultant Physician	Yes	
Mr Andrew Maclennan	Lay Member	Yes	

NHS
Greater Glasgow and Clyde

Coordinator: EP/BR
Telephone Number: 0141-211-6208
E-Mail: Erica.Packard@ggc.scot.nhs.uk
Website: www.nhsggc.org.uk/r&d

R&D Management Office
Western Infirmary
Tennent Institute
1st Floor 38 Church Street
Glasgow, G11 6NT

3 October 2011

Professor B Condon
Head of Imaging Physics for GG&C Health Board
MRI Unit, Institute of Neurological Sciences
1345 Govan Road
Southern General Hospital
Glasgow
G51 4TF

NHS GG&C Board Approval

Dear Professor Condon

Study Title:	Development and Optimisation of MRS Data Acquisition in Studies of Treatment-Resistant Clinical Depression: Reference single voxel Magnetic Resonance (MR) Spectroscopy Brain Scans on Healthy Humans
Principal Investigator:	**Professor Barrie Condon**
GG&C HB site	**Southern General Hospital**
Sponsor	**NHS Greater Glasgow & Clyde**
R&D reference:	**GN11NE240**
REC reference:	**11/WS/0019**
Protocol no: (including version and date)	**Version 1.1 dated 5 September 2011**

I am pleased to confirm that Greater Glasgow & Clyde Health Board is now able to grant **Approval** for the above study.

Conditions of Approval

1. **For Clinical Trials** as defined by the Medicines for Human Use Clinical Trial Regulations, 2004
   a. During the life span of the study GGHB requires the following information relating to this site
      i. Notification of any potential serious breaches.
      ii. Notification of any regulatory inspections.

It is your responsibility to ensure that all staff involved in the study at this site have the appropriate GCP training according to the GGHB GCP policy (www.nhsggc.org.uk/content/default.asp?page=s1411), evidence of such training to be filed in the site file.

NHS
Greater Glasgow and Clyde

2. **For all studies** the following information is required during their lifespan.
   a. Recruitment Numbers on a quarterly basis
   b. Any change of staff named on the original SSI form
   c. Any amendments – Substantial or Non Substantial
   d. Notification of Trial/study end including final recruitment figures
   e. Final Report & Copies of Publications/Abstracts

Please add this approval to your study file as this letter may be subject to audit and monitoring.

Your personal information will be held on a secure national web-based NHS database.

I wish you every success with this research study

Yours sincerely,

Dr Erica Packard
Research Co-ordinator

Cc: Mr Abdul Nashirudeen Mumuni, MRI Unit, Institute of Neurological Sciences, SGH

Appendix 2.2: The General Health Questionnaire-12

The General Health Questionnaire

GHQ-12

Please read this carefully.

We should like to know if you have had any medical complaints and how your health has been in general, over the last few weeks. Please answer ALL the questions simply by underlining the answer which you think most nearly applies to you. Remember that we want to know about present and recent complaints, not those that you had in the past.

It is important that you try to answer ALL the questions.

Thank you very much for your co-operation.

Client's name …….. Date ……..

HAVE YOU RECENTLY:

1 – been able to concentrate on whatever you're doing?	Better than usual	Same as usual	Less than usual	Much less than usual
2- lost much sleep over worry?	Not at all	No more than usual	Rather more than usual	More more useful
3- felt that you are playing a useful part in things?	More so than usual	Same as usual	Less useful than usual	Much less useful
4- felt capable of making decisions about things?	More so than usual	Same as usual	Less so than usual	Much less capable
5- felt constantly under strain?	Not at all	No more than usual	Rather more than usual	Much more than usual
6 – felt you couldn't overcome your difficulties?	Not at all	No more than usual	Rather more than usual	Much more than usual
7 - been able to enjoy your normal day-to-day activities?	More so than usual	Same as usual	Less so than usual	Much less than usual
8- been able to face up to your problems?	More so than usual	Same as usual	Less able than usual	Much less ablel
9- been feeling unhappy and depressed?	Not at all	No more than usual	Rather more than usual	Much more than usual
10- been losing confidence in yourself?	Not at all	No more than usual	Rather more than usual	Much more than usual
11- been thinking of yourself as a worthless person?	Not at all	No more than usual	Rather more than usual	Much more than usual
12- been feeling reasonable happy, all things considered?	More so than usual	About same as usual	Less so than usual	Much less than usual

Published by The NFER-NELSON Publishing Company Ltd, Darville House, 2 Oxford Road East, Windsor, Berkshire SL4 1DE

Appendix 2.3: The MRI Safety Checklist

MRI INVESTIGATION DETAILS AND SAFETY CHECKLIST May 2008

Patient Name:		Consultant:	
Address		X-Ray Number:	
		Ward:	
Post Code:	Sex:	Date:	
Date of Birth:	Weight (kg):	Hospital Number:	

Area of Interest:

SAFETY QUESTIONS

Does the patient have, or have they EVER had:?

	Yes	No
A cardiac pacemaker or defibrillator or internal pacing wires		
An operation on their heart		
A brain aneurysm clipped or treated		
A plate in their skull		
Any operations on their head		
A vascular clamp, coil or stent		
An artificial heart valve		
A bladder implant		
An insulin or infusion pump		
An ear implant		
A pain relief implant		
Any electronic implants (e.g. Neurostimulator)		
Any other implants or prostheses		
Metal enter their bodies from an industrial accident or through military service		
An eye injury or attended an eye department or had eye surgery		
Worked on milling or drilling machines or in the shipyards where metal may have entered their eyes		
Any artificial joints or limbs or screws or pins or plates for broken bones		
Suffered from fits or blackouts		
Had any surgical operations or endoscopy in the last six weeks		
Had a spinal fracture		

Please tick...

	Yes	No
Had any surgical operations		
Wearing coloured contact lenses		
Have tattoos or permanent eye-lining		
Is the patient pregnant		
Are they up to 14 weeks pregnant		
Have a contraceptive diaphragm		
Have breast implants		
Have they removed?:		
All removable dentures		
Everything from their pockets		
All hairclips and earrings		
Their watch, credit and cash point cards		
Any braces and corsets		
All hearing aids		
All skin patches		
All make-up		
All body piercing material		
Bra if for spine, torso or shoulder scan		
If they may be given contrast and are of child bearing age:		
Are they breast feeding		

I confirm that the answers to the above safety questions are correct

Signature of patient/parent/guardian/volunteer: Date:

If the patient is unable to sign please state why here:

If any of the answers to the Safety Questions have been **YES** consult the INS MRI Safety Information Book

Note the details of the implants/operations here and indicate whether the book says they are **SAFE** or **UNSAFE**:

If the implant/operation is not included in the book or you are unsure then you **MUST** refer this to the Supervising Radiologist. If they subsequently agree to the scan they should sign here:

Authorising Signature

The Radiologist should sign here if no clear history of implants or operations can be obtained (e.g. the patient is comatose or confused) to confirm they are safe to image:

Authorising Signature

If the scan is to proceed because of urgent clinical need despite contraindications (i.e. UNSAFE) the Consultant Radiologist must sign here:

Authorising Signature

Signature Of:

Checklist Radiographer Scanning Radiographer

Appendix 2.4: Ethical Approval for the Psoriatic Arthritis Study

WoSRES
West of Scotland Research Ethics Service

NHS
Greater Glasgow and Clyde

West of Scotland REC 3
Ground Floor – The Tennent Institute
Western Infirmary
38 Church Street
Glasgow G11 6NT
www.nhsggc.org.uk

Dr Rajeev Krishnadas
Clinical Lecturer in Psychological Medicine
University of Glasgow
Sackler Institute
Southern General Hospital
Glasgow G51 4TF

Date 18 Feb. 10
Your Ref
Our Ref
Direct line 0141 211 2123
Fax 0141 211 1847
E-mail Liz.Jamieson@ggc.scot.nhs.uk

Dear Dr Krishnadas

Study title: **An imaging study of effect of TNF alpha blockade on brain SERT and DAT availability and fMRI in patients with Psoriatic and Rheumatoid arthritis**
REC reference: **09/S0701/77**
Amendment number: **AM01**
Amendment date: **09 February 2010**

The above amendment was reviewed at the meeting of the Sub Committee held on 18 February 2010.

Ethical opinion

The members of the Committee taking part in the review gave a favourable ethical opinion of the amendment on the basis described in the notice of amendment form and supporting documentation.

Approved documents

The documents reviewed and approved at the meeting were:

Document	Version	Date
Summary of Changes		
Protocol with Tracked Changes	Version 2	09 February 2010
Protocol	Version 2	09 February 2010
Notice of Substantial Amendment (non-CTIMPs)	AM01	09 February 2010
Covering Letter		09 February 2010

Membership of the Committee

The members of the Committee who took part in the review are listed on the attached sheet.

R&D approval

All investigators and research collaborators in the NHS should notify the R&D office for the relevant NHS care organisation of this amendment and check whether it affects R&D approval of the research.

Statement of compliance

The Committee is constituted in accordance with the Governance Arrangements for Research Ethics Committees (July 2001) and complies fully with the Standard Operating Procedures for Research Ethics Committees in the UK.

09/S0701/77:	**Please quote this number on all correspondence**

Yours sincerely

Mrs Liz Jamieson
Committee Co-ordinator

E-mail: Liz.Jamieson@ggc.scot.nhs.uk

Enclosures: List of names and professions of members who took part in the review

Copy to: R&D office for NHS care organisation at lead site

West of Scotland REC 3

Attendance at Sub-Committee of the REC meeting on 18 February 2010

Name	*Profession*	*Capacity*
Mrs Liz Jamieson	Committee Co-ordinator	None
Mr Eoin MacGillivray	Lay Member	Lay
Dr Robert McNeill	General Practitioner	Expert

#]

Appendix 4.1: Polynomial fitting of the unsuppressed-water signal intensities acquired along the principal axes of the RF coil

Inclusion of water signal intensities recorded at voxel position -55 mm from the isocentre along the RL and SI axes resulted in poor polynomial fits. These points were far underestimated compared to the rest of the plotted points.

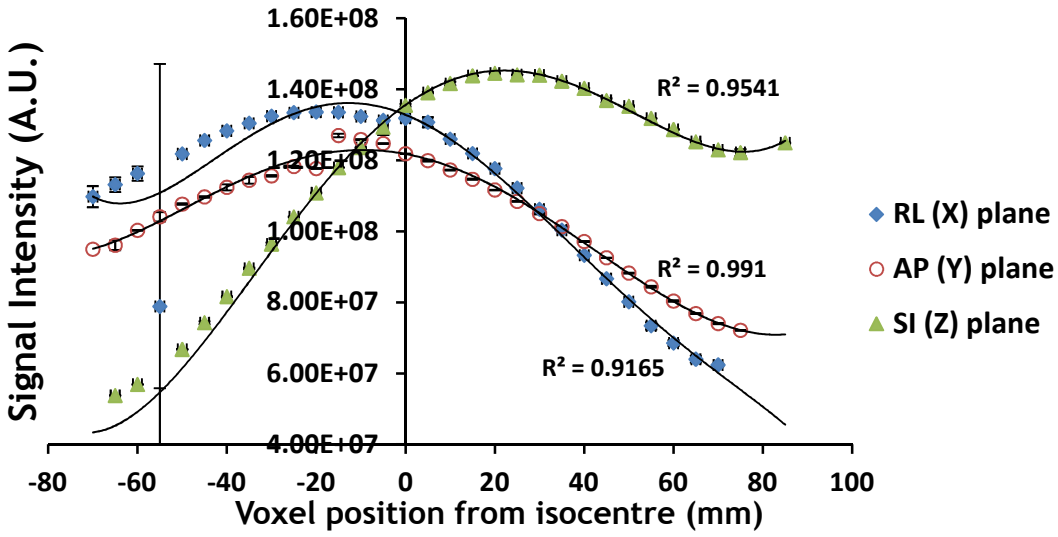

Removal of those plotted points at -55 mm from the isocentre resulted in better polynomial fits.

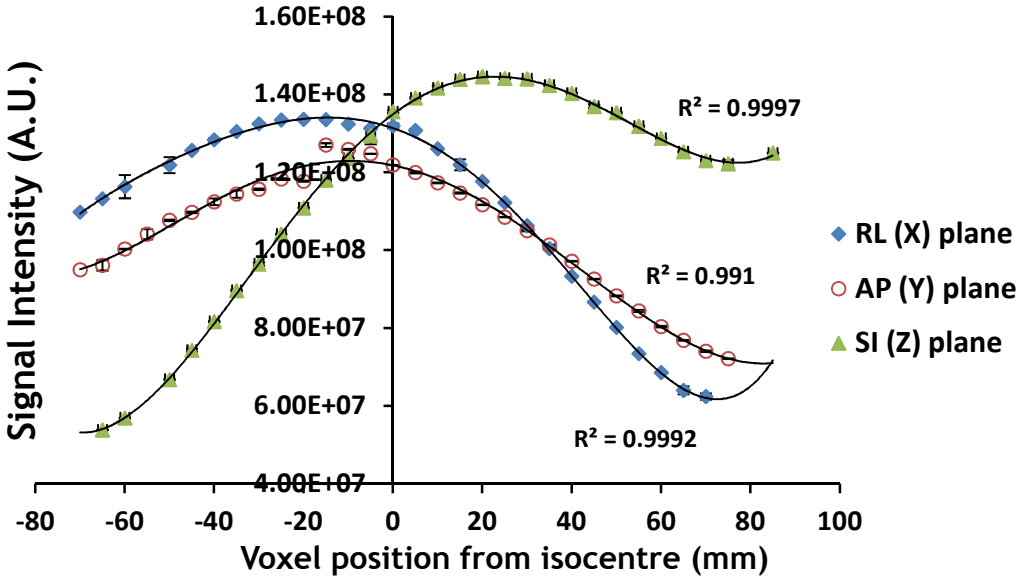

Appendix 7.1: The 21-item Beck's Depression Inventory (BDI) used for Mood Assessment

Beck's Depression Inventory

This depression inventory can be self-scored. The scoring scale is at the end of the questionnaire.

1.
- 0 I do not feel sad.
- 1 I feel sad
- 2 I am sad all the time and I can't snap out of it.
- 3 I am so sad and unhappy that I can't stand it.

2.
- 0 I am not particularly discouraged about the future.
- 1 I feel discouraged about the future.
- 2 I feel I have nothing to look forward to.
- 3 I feel the future is hopeless and that things cannot improve.

3.
- 0 I do not feel like a failure.
- 1 I feel I have failed more than the average person.
- 2 As I look back on my life, all I can see is a lot of failures.
- 3 I feel I am a complete failure as a person.

4.
- 0 I get as much satisfaction out of things as I used to.
- 1 I don't enjoy things the way I used to.
- 2 I don't get real satisfaction out of anything anymore.
- 3 I am dissatisfied or bored with everything.

5.
- 0 I don't feel particularly guilty
- 1 I feel guilty a good part of the time.
- 2 I feel quite guilty most of the time.
- 3 I feel guilty all of the time.

6.
- 0 I don't feel I am being punished.
- 1 I feel I may be punished.
- 2 I expect to be punished.
- 3 I feel I am being punished.

7.
- 0 I don't feel disappointed in myself.
- 1 I am disappointed in myself.
- 2 I am disgusted with myself.
- 3 I hate myself.

8.
- 0 I don't feel I am any worse than anybody else.
- 1 I am critical of myself for my weaknesses or mistakes.
- 2 I blame myself all the time for my faults.
- 3 I blame myself for everything bad that happens.

9.
- 0 I don't have any thoughts of killing myself.
- 1 I have thoughts of killing myself, but I would not carry them out.
- 2 I would like to kill myself.
- 3 I would kill myself if I had the chance.

10.
- 0 I don't cry any more than usual.
- 1 I cry more now than I used to.
- 2 I cry all the time now.
- 3 I used to be able to cry, but now I can't cry even though I want to.

11.

0 I am no more irritated by things than I ever was.
1 I am slightly more irritated now than usual.
2 I am quite annoyed or irritated a good deal of the time.
3 I feel irritated all the time.

12.

0 I have not lost interest in other people.
1 I am less interested in other people than I used to be.
2 I have lost most of my interest in other people.
3 I have lost all of my interest in other people.

13.

0 I make decisions about as well as I ever could.
1 I put off making decisions more than I used to.
2 I have greater difficulty in making decisions more than I used to.
3 I can't make decisions at all anymore.

14.

0 I don't feel that I look any worse than I used to.
1 I am worried that I am looking old or unattractive.
2 I feel there are permanent changes in my appearance that make me look unattractive
3 I believe that I look ugly.

15.

0 I can work about as well as before.
1 It takes an extra effort to get started at doing something.
2 I have to push myself very hard to do anything.
3 I can't do any work at all.

16.

0 I can sleep as well as usual.
1 I don't sleep as well as I used to.
2 I wake up 1-2 hours earlier than usual and find it hard to get back to sleep.
3 I wake up several hours earlier than I used to and cannot get back to sleep.

17.

0 I don't get more tired than usual.
1 I get tired more easily than I used to.
2 I get tired from doing almost anything.
3 I am too tired to do anything.

18.

0 My appetite is no worse than usual.
1 My appetite is not as good as it used to be.
2 My appetite is much worse now.
3 I have no appetite at all anymore.

19.

0 I haven't lost much weight, if any, lately.
1 I have lost more than five pounds.
2 I have lost more than ten pounds.
3 I have lost more than fifteen pounds.

20.

0 I am no more worried about my health than usual.
1 I am worried about physical problems like aches, pains, upset stomach, or constipation.
2 I am very worried about physical problems and it's hard to think of much else.
3 I am so worried about my physical problems that I cannot think of anything else.

21.

0 I have not noticed any recent change in my interest in sex.
1 I am less interested in sex than I used to be.
2 I have almost no interest in sex.
3 I have lost interest in sex completely.

INTERPRETING THE BECK DEPRESSION INVENTORY

Now that you have completed the questionnaire, add up the score for each of the twenty-one questions by counting the number to the right of each question you marked. The highest possible total for the whole test would be sixty-three. This would mean you circled number three on all twenty-one questions. Since the lowest possible score for each question is zero, the lowest possible score for the test would be zero. This would mean you circles zero on each question. You can evaluate your depression according to the Table below.

Total Score	Levels of Depression
1-10	These ups and downs are considered normal
11-16	Mild mood disturbance
17-20	Borderline clinical depression
21-30	Moderate depression
31-40	Severe depression
over 40	Extreme depression

A PERSISTENT SCORE OF 17 OR ABOVE INDICATES THAT YOU MAY NEED MEDICAL TREATMENT. IF YOU HAVE ANY CARDIAC CONCERNS, PLEASE CONTACT CARDIOVASCULAR INTERVENTIONS, P.A. at 407-894-4880

List of References

1. Tofts, P., *Quantitative MRI of the brain : measuring changes caused by disease,* 2003; Chichester: Wiley. xvi, 633 p.

2. Rabi, I.I., et al., *A New Method of Measuring Nuclear Magnetic Moment*. Physical Review, 1938. **53**(4): p. 318-318.

3. Bloch, F., *Nuclear Induction*. Physical Review, 1946. **70**(7-8): p. 460-474.

4. Purcell, E.M., H.C. Torrey, and R.V. Pound, *Resonance Absorption by Nuclear Magnetic Moments in a Solid*. Physical Review, 1946. **69**(1-2): p. 37-38.

5. Carr, H.Y., *Field gradients in early MRI*. Physics Today, 2004. **57**(7): p. 83-83.

6. Ernst, R.R. and W.A. Anderson, *Application of Fourier Transform Spectroscopy to Magnetic Resonance*. Review of Scientific Instruments, 1966. **37**(1): p. 93-102.

7. Lauterbur, P.C., *Image Formation by Induced Local Interactions: Examples Employing Nuclear Magnetic Resonance*. Nature, 1973. **242**(5394): p. 190-191.

8. Lauterbur, P.C., *Magnetic-Resonance Zeugmatography*. Pure and Applied Chemistry, 1974. **40**(1-2): p. 149-157.

9. Mansfield, P. and A.A. Maudsley, *Medical imaging by NMR*. British Journal of Radiology, 1977. **50**(591): p. 188-194.

10. Damadian, R., *APPARATUS AND METHOD FOR DETECTING CANCER IN TISSUE*, 1974: United States.

11. Wakefield, J., *The "Indomitable" MRI - Raymond Damadian's imaging machine set off a revolution, but not without controversy*. Smithsonian, 2000. **31**(3): p. 22.

12. Mansfield, P., et al., *Human Whole-Body Line-Scan Imaging by NMR*. British Journal of Radiology, 1978. **51**(611): p. 921-922.

13. Moon, R.B. and J.H. Richards, *Determination of Intracellular pH by 31P Magnetic Resonance*. Journal of Biological Chemistry, 1973. **248**(20): p. 7276-7278.

14. Hoult, D.I., et al., *Observation of tissue metabolites using 31P nuclear magnetic resonance*. Nature, 1974. **252**(5481): p. 285-287.

15. Bottomley, P.A., et al., *In vivo solvent-suppressed localized hydrogen nuclear magnetic resonance spectroscopy: a window to metabolism?* Proc Natl Acad Sci U S A, 1985. **82**(7): p. 2148-52.

16. Foster, M.A., *Magnetic resonance in medicine and biology*. 1st ed1984, Oxford, OX, England ; New York: Pergamon Press. xi, 244 p.

17. James, T.L., *Nuclear magnetic resonance in biochemistry : principles and applications*1975, New York: Academic Press. xii, 413 p.

18. Duarte, J.M.N., et al., *The neurochemical profile quantified by in vivo 1H NMR spectroscopy*. NeuroImage, 2012. **61**(2): p. 342-362.

19. Frahm, J., K.-D. Merboldt, and W. Hänicke, *Localized proton spectroscopy using stimulated echoes*. Journal of Magnetic Resonance (1969), 1987. **72**(3): p. 502-508.

20. Narayana, P.A., et al., *Regional in vivo proton magnetic resonance spectroscopy of brain*. Journal of Magnetic Resonance (1969), 1989. **83**(1): p. 44-52.

21. Muñoz Maniega, S., et al., *Choline and Creatine Are Not Reliable Denominators for Calculating Metabolite Ratios in Acute Ischemic Stroke*. Stroke, 2008. **39**(9): p. 2467-2469.

22. Kimura, H., et al., *Proton MR spectroscopy and magnetization transfer ratio in multiple sclerosis: correlative findings of active versus irreversible plaque disease*. AJNR Am J Neuroradiol, 1996. **17**(8): p. 1539-47.

23. Majos, C., et al., *Brain tumor classification by proton MR spectroscopy: comparison of diagnostic accuracy at short and long TE*. AJNR Am J Neuroradiol, 2004. **25**(10): p. 1696-704.

24. Loos, C., E. Achten, and P. Santens, *Proton magnetic resonance spectroscopy in Alzheimer's disease, a review*. Acta Neurol Belg, 2010. **110**(4): p. 291-8.

25. Kantarci, K., *1H magnetic resonance spectroscopy in dementia*. Br J Radiol, 2007(2): p. S146-52.

26. Tanaka, Y., et al., *Quantitative magnetic resonance spectroscopy of schizophrenia: relationship between decreased N-acetylaspartate and frontal lobe dysfunction*. Psychiatry Clin Neurosci, 2006. **60**(3): p. 365-72.

27. Bhagwagar, Z., et al., *Reduction in occipital cortex gamma-aminobutyric acid concentrations in medication-free recovered unipolar depressed and bipolar subjects*. Biol Psychiatry, 2007. **61**(6): p. 806-12.

28. Nery, F.G., et al., *Normal metabolite levels in the left dorsolateral prefrontal cortex of unmedicated major depressive disorder patients: a single voxel (1)H spectroscopy study*. Psychiatry Res, 2009. **174**(3): p. 177-83.

29. Chinn, R.J., et al., *Toxoplasmosis and primary central nervous system lymphoma in HIV infection: diagnosis with MR spectroscopy*. Radiology, 1995. **197**(3): p. 649-54.

30. Keevil, S.F., et al., *Absolute metabolite quantification by in vivo NMR spectroscopy: II. A multicentre trial of protocols for in vivo localised proton studies of human brain*. Magn Reson Imaging, 1998. **16**(9): p. 1093-106.

31. Drost, D.J., W.R. Riddle, and G.D. Clarke, *Proton magnetic resonance spectroscopy in the brain: report of AAPM MR task group #9*. Medical Physics, 2002. **29**(9): p. 2177-2197.

32. Weishaupt, D., V.D. Köchli, and B. Marincek, *How does MRI work? : an introduction to the physics and function of magnetic resonance imaging*. 2nd ed 2006, Berlin; New York: Springer. x, 169 p.

33. Kleiner, S.M., *Water: An essential but overlooked nutrient*. Journal of the American Dietetic Association, 1999. **99**(2): p. 200-206.

34. Suhr, J.A., et al., *The relation of hydration status to cognitive performance in healthy older adults.* Int J Psychophysiol, 2004. **53**(2): p. 121-5.

35. Armstrong, L.E. and Y. Epstein, *Fluid-electrolyte balance during labor and exercise: concepts and misconceptions.* Int J Sport Nutr, 1999. **9**(1): p. 1-12.

36. Murray, R., *Rehydration strategies--balancing substrate, fluid, and electrolyte provision.* Int J Sports Med, 1998. **19 Suppl 2**: p. S133-5.

37. Lieberman, H.R., *Hydration and cognition: A critical review and recommendations for future research.* Journal of the American College of Nutrition, 2007. **26**(5): p. 555s-561s.

38. Turner, A.J., *Biochemistry and the central nervous system (fifth edition): By H. McIlwain and H S Bachelard. pp 660. Churchill Livingstone, Edinburgh. 1985. #40 ISBN 0-443-01961-4.* Biochemical Education, 1986. **14**(1): p. 46.

39. Lang, F., et al., *Functional significance of cell volume regulatory mechanisms.* Physiological Reviews, 1998. **78**(1): p. 247-306.

40. Bridger, W.A. and J.F. Henderson, *Cell ATP*. Transport in the life sciences,1983, New York: Wiley. x, 170 p.

41. Danbolt, N.C., *Glutamate uptake*. Prog Neurobiol, 2001. **65**(1): p. 1-105.

42. Trip, S.A. and D.H. Miller, *Imaging in multiple sclerosis.* J Neurol Neurosurg Psychiatry, 2005. **76 Suppl 3**: p. iii11-iii18.

43. Cady, E.B., et al., *The estimation of local brain temperature by in vivo 1H magnetic resonance spectroscopy.* Magn Reson Med, 1995. **33**(6): p. 862-7.

44. Murakami, T., et al., *Brain temperature measured by using proton MR spectroscopy predicts cerebral hyperperfusion after carotid endarterectomy.* Radiology, 2010. **256**(3): p. 924-31.

45. Jansen, J.F., et al., *1H MR spectroscopy of the brain: absolute quantification of metabolites.* Radiology, 2006. **240**(2): p. 318-32.

46. Klose, U., *In vivo proton spectroscopy in presence of eddy currents.* Magn Reson Med, 1990. **14**(1): p. 26-30.

47. Natt, O., et al., *Use of phased array coils for a determination of absolute metabolite concentrations.* Magn Reson Med, 2005. **53**(1): p. 3-8.

48. Provencher, S.W., *Estimation of metabolite concentrations from localized in vivo proton NMR spectra.* Magn Reson Med, 1993. **30**(6): p. 672-9.

49. Gasparovic, C., et al., *Quantitative spectroscopic imaging with in situ measurements of tissue water T1, T2, and density.* Magn Reson Med, 2009. **62**(3): p. 583-90.

50. Condon, B.R., et al., *A quantitative index of ventricular and extraventricular intracranial CSF volumes using MR imaging.* Journal of computer assisted tomography, 1986. **10**(5): p. 784-92.

51. Kroeker, R.M. and R.M. Henkelman, *Analysis of Biological Nmr Relaxation Data with Continuous Distributions of Relaxation-Times.* Journal of Magnetic Resonance, 1986. **69**(2): p. 218-235.

52. Poon, C.S. and R.M. Henkelman, *Practical T2 Quantitation for Clinical-Applications.* Journal of Magnetic Resonance Imaging, 1992. **2**(5): p. 541-553.

53. Crawley, A.P. and R.M. Henkelman, *Errors in T2 estimation using multislice multiple-echo imaging.* Magn Reson Med, 1987. **4**(1): p. 34-47.

54. Wansapura, J.P., et al., *NMR relaxation times in the human brain at 3.0 tesla.* Journal of Magnetic Resonance Imaging, 1999. **9**(4): p. 531-8.

55. Bottomley, P.A., T.B. Foster, and R.D. Darrow, *Depth-Resolved Surface-Coil Spectroscopy (Dress) for Invivo H-1, P-31, and C-13 Nmr*. Journal of Magnetic Resonance, 1984. **59**(2): p. 338-342.

56. Ernst, T. and L. Chang, *Elimination of artifacts in short echo time H MR spectroscopy of the frontal lobe*. Magn Reson Med, 1996. **36**(3): p. 462-8.

57. SCHICK, et al., *Lactate quantification by means of press spectroscopy: influence of refocusing pulses and timing scheme*. Vol. 13. 1995, Kidlington, ROYAUME-UNI: Elsevier.

58. Brief, E.E., et al., *Absolute metabolite concentrations calibrated using the total water signal in brain H-1 MRS*. NMR in Biomedicine, 2009. **22**(3): p. 349-354.

59. Whittall, K.P., et al., *In vivo measurement of T2 distributions and water contents in normal human brain*. Magn Reson Med, 1997. **37**(1): p. 34-43.

60. Norton, W.T., S.E. Poduslo, and K. Suzuki, *Subacute sclerosing leukoencephalitis. II. Chemical studies including abnormal myelin and an abnormal ganglioside pattern*. J Neuropathol Exp Neurol, 1966. **25**(4): p. 582-97.

61. Christiansen, P., et al., *MR-visible water content in human brain: a proton MRS study*. Magn Reson Imaging, 1994. **12**(8): p. 1237-44.

62. Barker, P.B., et al., *Quantitation of proton NMR spectra of the human brain using tissue water as an internal concentration reference*. NMR in Biomedicine, 1993. **6**(1): p. 89-94.

63. Soher, B.J., et al., *Quantitation of automated single-voxel proton MRS using cerebral water as an internal reference*. Magn Reson Med, 1996. **36**(3): p. 335-9.

64. Christiansen, P., et al., *In vivo quantification of brain metabolites by 1H-MRS using water as an internal standard*. Magn Reson Imaging, 1993. **11**(1): p. 107-18.

65. Govindaraju, V., K. Young, and A.A. Maudsley, *Proton NMR chemical shifts and coupling constants for brain metabolites.* NMR in Biomedicine, 2000. **13**(3): p. 129-53.

66. Pouwels, P.J. and J. Frahm, *Regional metabolite concentrations in human brain as determined by quantitative localized proton MRS.* Magn Reson Med, 1998. **39**(1): p. 53-60.

67. Berridge, M.J. and R.F. Irvine, *Inositol phosphates and cell signalling.* Nature, 1989. **341**(6239): p. 197-205.

68. Ross, B.D., *Biochemical considerations in 1H spectroscopy. Glutamate and glutamine; myo-inositol and related metabolites.* NMR in Biomedicine, 1991. **4**(2): p. 59-63.

69. Brand, A., C. Richter-Landsberg, and D. Leibfritz, *Multinuclear NMR studies on the energy metabolism of glial and neuronal cells.* Dev Neurosci, 1993. **15**(3-5): p. 289-98.

70. Michaelis, T., et al., *Absolute concentrations of metabolites in the adult human brain in vivo: quantification of localized proton MR spectra.* Radiology, 1993. **187**(1): p. 219-27.

71. Kreis, R., T. Ernst, and B.D. Ross, *Absolute Quantitation of Water and Metabolites in the Human Brain. II. Metabolite Concentrations.* Journal of Magnetic Resonance, Series B, 1993. **102**(1): p. 9-19.

72. Klunk, W.E., et al., *Quantitative 1H and 31P MRS of PCA extracts of postmortem Alzheimer's disease brain.* Neurobiology of Aging, 1996. **17**(3): p. 349-357.

73. Van Zijl, P.C.M. and P.B. Barker, *Magnetic Resonance Spectroscopy and Spectroscopic Imaging for the Study of Brain Metabolisma.* Annals of the New York Academy of Sciences, 1997. **820**(1): p. 75-96.

74. Peet, A.C., et al., *Short echo time 1 H magnetic resonance spectroscopy of childhood brain tumours.* Childs Nerv Syst, 2007. **23**(2): p. 163-9.

75. Albers, M.J., et al., *Proton-decoupled 31P MRS in untreated pediatric brain tumors.* Magn Reson Med, 2005. **53**(1): p. 22-9.

76. Calvar, J.A., et al., *Characterization of brain tumors by MRS, DWI and Ki-67 labeling index.* J Neurooncol, 2005. **72**(3): p. 273-80.

77. Hall, W.A., et al., *Improving diagnostic yield in brain biopsy: Coupling spectroscopic targeting with real-time needle placement.* Journal of Magnetic Resonance Imaging, 2001. **13**(1): p. 12-15.

78. Panigrahy, A., et al., *Quantitative short echo time 1H-MR spectroscopy of untreated pediatric brain tumors: preoperative diagnosis and characterization.* AJNR Am J Neuroradiol, 2006. **27**(3): p. 560-72.

79. Rudkin, T.M. and D.L. Arnold, *Proton magnetic resonance spectroscopy for the diagnosis and management of cerebral disorders.* Arch Neurol, 1999. **56**(8): p. 919-26.

80. Kaldis, P., et al., *'Hot Spots' of Creatine Kinase Localization in Brain: Cerebellum, Hippocampus and Choroid Plexus.* Developmental Neuroscience, 1996. **18**(5-6): p. 542-554.

81. Ilyin, S.E., et al., *Creatine kinase-B mRNA levels in brain regions from male and female rats.* Brain Res Mol Brain Res, 1996. **41**(1-2): p. 50-6.

82. Wang, Y. and S.J. Li, *Differentiation of metabolic concentrations between gray matter and white matter of human brain by in vivo 1H magnetic resonance spectroscopy.* Magn Reson Med, 1998. **39**(1): p. 28-33.

83. Saunders, D.E., et al., *Aging of the adult human brain: In vivo quantitation of metabolite content with proton magnetic resonance spectroscopy.* Journal of Magnetic Resonance Imaging, 1999. **9**(5): p. 711-716.

84. Tong, Z., et al., *In vivo quantification of the metabolites in normal brain and brain tumors by proton MR spectroscopy using water as an internal standard*. Magn Reson Imaging, 2004. **22**(7): p. 1017-24.

85. Chang, L., et al., *Proton spectroscopy in myotonic dystrophy: correlations with CTG repeats*. Arch Neurol, 1998. **55**(3): p. 305-11.

86. Rothman, D.L., et al., *Homonuclear 1H double-resonance difference spectroscopy of the rat brain in vivo*. Proc Natl Acad Sci U S A, 1984. **81**(20): p. 6330-4.

87. Pan, J.W., et al., *Spectroscopic imaging of human brain glutamate by water-suppressed J-refocused coherence transfer at 4.1 T*. Magn Reson Med, 1996. **36**(1): p. 7-12.

88. Mason, G.F., et al., *Detection of brain glutamate and glutamine in spectroscopic images at 4.1 T*. Magn Reson Med, 1994. **32**(1): p. 142-5.

89. Gruetter, R., et al., *Resolution Improvements inin Vivo1H NMR Spectra with Increased Magnetic Field Strength*. Journal of Magnetic Resonance, 1998. **135**(1): p. 260-264.

90. van Zijl, P.C. and C.T. Moonen, *In situ changes in purine nucleotide and N-acetyl concentrations upon inducing global ischemia in cat brain*. Magn Reson Med, 1993. **29**(3): p. 381-5.

91. Martinez-Hernandez, A., K.P. Bell, and M.D. Norenberg, *Glutamine synthetase: glial localization in brain*. Science, 1977. **195**(4284): p. 1356-8.

92. Kreis, R., N. Farrow, and B.D. Ross, *Localized 1H NMR spectroscopy in patients with chronic hepatic encephalopathy. Analysis of changes in cerebral glutamine, choline and inositols*. NMR in Biomedicine, 1991. **4**(2): p. 109-16.

93. Chamuleau, R.A., et al., *What the clinician can learn from MR glutamine/glutamate assays*. NMR in Biomedicine, 1991. **4**(2): p. 103-8.

94. Ross, B.D., E.R. Danielsen, and S. Bluml, *Proton magnetic resonance spectroscopy: the new gold standard for diagnosis of clinical and subclinical hepatic encephalopathy?* Dig Dis, 1996. **1**: p. 30-9.

95. Birken, D.L. and W.H. Oldendorf, *N-acetyl-L-aspartic acid: a literature review of a compound prominent in 1H-NMR spectroscopic studies of brain.* Neurosci Biobehav Rev, 1989. **13**(1): p. 23-31.

96. Urenjak, J., et al., *Proton Nuclear-Magnetic-Resonance Spectroscopy Unambiguously Identifies Different Neural Cell-Types.* Journal of Neuroscience, 1993. **13**(3): p. 981-989.

97. Patel, T.B. and J.B. Clark, *Lipogenesis in the brain of suckling rats. Studies on the mechansim of mitochondrial-cytosolic carbon transfer.* Biochem J, 1980. **188**(1): p. 163-8.

98. Pouwels, P.J.W. and J. Frahm, *Differential distribution of NAA and NAAG in human brain as determined by quantitative localized proton MRS.* NMR in Biomedicine, 1997. **10**(2): p. 73-78.

99. Tsai, G. and J.T. Coyle, *N-acetylaspartate in neuropsychiatric disorders.* Prog Neurobiol, 1995. **46**(5): p. 531-40.

100. Brulatout, S., et al., *A one-dimensional (proton and phosphorus) and two-dimensional (proton) in vivo NMR spectroscopic study of reversible global cerebral ischemia.* J Neurochem, 1996. **66**(6): p. 2491-9.

101. De Stefano, N., P.M. Matthews, and D.L. Arnold, *Reversible decreases in N-acetylaspartate after acute brain injury.* Magn Reson Med, 1995. **34**(5): p. 721-7.

102. Williamson P, D.D.S.J.C.T.M.S.M.H., *LOcalized phosphorus 31 magnetic resonance spectroscopy in chronic schizophrenic patients and normal controls.* Archives of General Psychiatry, 1991. **48**(6): p. 578-578.

103. Stanley, J.A., et al., *An in vivo study of the prefrontal cortex of schizophrenic patients at different stages of illness via phosphorus magnetic resonance spectroscopy.* Arch Gen Psychiatry, 1995. **52**(5): p. 399-406.

104. Stanley, J.A., et al., *An in vivo proton magnetic resonance spectroscopy study of schizophrenia patients.* Schizophr Bull, 1996. **22**(4): p. 597-609.

105. Wang, Z., et al., *Proton MR spectroscopy of pediatric cerebellar tumors.* AJNR Am J Neuroradiol, 1995. **16**(9): p. 1821-33.

106. Wittsack, H.J., et al., *Quantitative measurements with localized 1H MR spectroscopy in children with Canavan's disease*. J Magn Reson Imaging, 1996. **6**(6): p. 889-93.

107. Marcus, K.J., et al., *Predicting survival of children with CNS tumors using proton magnetic resonance spectroscopic imaging biomarkers*. Int J Oncol, 2007. **30**(3): p. 651-7.

108. Chang, K.H., et al., *In vivo single-voxel proton MR spectroscopy in intracranial cystic masses.* AJNR Am J Neuroradiol, 1998. **19**(3): p. 401-5.

109. Poptani, H., et al., *Characterization of intracranial mass lesions with in vivo proton MR spectroscopy*. AJNR Am J Neuroradiol, 1995. **16**(8): p. 1593-603.

110. Sappey-Marinier, D., et al., *Effect of photic stimulation on human visual cortex lactate and phosphates using 1H and 31P magnetic resonance spectroscopy.* J Cereb Blood Flow Metab, 1992. **12**(4): p. 584-92.

111. Posse, S., et al., *In vivo measurement of regional brain metabolic response to hyperventilation using magnetic resonance: proton echo planar spectroscopic imaging (PEPSI)*. Magn Reson Med, 1997. **37**(6): p. 858-65.

112. Seeger, U., et al., *Reliable detection of macromolecules in single-volume 1H NMR spectra of the human brain*. Magn Reson Med, 2001. **45**(6): p. 948-954.

113. Tkac, I., et al., *In vivo 1H NMR spectroscopy of rat brain at 1 ms echo time*. Magn Reson Med, 1999. **41**(4): p. 649-56.

114. Duyn, J.H., et al., *Multisection proton MR spectroscopic imaging of the brain.* Radiology, 1993. **188**(1): p. 277-82.

115. Shungu, D.C. and J.D. Glickson, *Sensitivity and localization enhancement in multinuclear in vivo NMR spectroscopy by outer volume presaturation.* Magn Reson Med, 1993. **30**(6): p. 661-71.

116. de Graaf, A.A., J.E. van Dijk, and W.M. Bovee, *QUALITY: quantification improvement by converting lineshapes to the Lorentzian type.* Magn Reson Med, 1990. **13**(3): p. 343-57.

117. Riddle, W.R., S.J. Gibbs, and M.R. Willcott, *Removing effects of eddy currents in proton MR spectroscopy.* Medical Physics, 1992. **19**(2): p. 501-9.

118. Zhu, G., D. Gheorghiu, and P.S. Allen, *Motional degradation of metabolite signal strengths when using STEAM: a correction method.* NMR in Biomedicine, 1992. **5**(4): p. 209-11.

119. Helms, G. and A. Piringer, *Restoration of motion-related signal loss and line-shape deterioration of proton MR spectra using the residual water as intrinsic reference.* Magn Reson Med, 2001. **46**(2): p. 395-400.

120. Vanhamme, L., et al., *MR spectroscopy quantitation: a review of time-domain methods.* NMR in Biomedicine, 2001. **14**(4): p. 233-46.

121. Mierisova, S. and M. Ala-Korpela, *MR spectroscopy quantitation: a review of frequency domain methods.* NMR in Biomedicine, 2001. **14**(4): p. 247-59.

122. Abildgaard, F., H. Gesmar, and J.J. Led, *Quantitative analysis of complicated nonideal fourier transform NMR spectra.* Journal of Magnetic Resonance (1969), 1988. **79**(1): p. 78-89.

123. Meyer, R.A., et al., *Evaluation of manual methods for integration of in vivo phosphorus NMR spectra.* Nmr in Biomedicine, 1988. **1**(3): p. 131-5.

124. Nelson, S.J. and T.R. Brown, *A Method for Automatic Quantification of One-Dimensional Spectra with Low Signal-to-Noise Ratio*. Journal of Magnetic Resonance, 1987. **75**(2): p. 229-243.

125. Marshall, I., et al., *Use of Voigt lineshape for quantification of in vivo 1H spectra*. Magn Reson Med, 1997. **37**(5): p. 651-7.

126. Petrakis, L., *Spectral Line Shapes - Gaussian and Lorentzian Functions in Magnetic Resonance*. Journal of Chemical Education, 1967. **44**(8): p. 432-6.

127. de Graaf, A.A. and W.M. Bovee, *Improved quantification of in vivo 1H NMR spectra by optimization of signal acquisition and processing and by incorporation of prior knowledge into the spectral fitting*. Magn Reson Med, 1990. **15**(2): p. 305-19.

128. Hennig, J., et al., *Direct absolute quantification of metabolites in the human brain with in vivo localized proton spectroscopy*. NMR in Biomedicine, 1992. **5**(4): p. 193-199.

129. Träber, F., et al., *1H metabolite relaxation times at 3.0 tesla: Measurements of T1 and T2 values in normal brain and determination of regional differences in transverse relaxation*. Journal of Magnetic Resonance Imaging, 2004. **19**(5): p. 537-545.

130. Schulte, R.F. and P. Boesiger, *ProFit: two-dimensional prior-knowledge fitting of J-resolved spectra*. NMR in Biomedicine, 2006. **19**(2): p. 255-63.

131. Walter, M., et al., *The Relationship Between Aberrant Neuronal Activation in the Pregenual Anterior Cingulate, Altered Glutamatergic Metabolism, and Anhedonia in Major Depression*. Archives of General Psychiatry, 2009. **66**(5): p. 478-86.

132. Srinivasan, R., et al., *A comparative study of myo-inositol quantification using LCmodel at 1.5 T and 3.0 T with 3 D H-1 proton spectroscopic imaging of the human brain*. Magnetic Resonance Imaging, 2004. **22**(4): p. 523-528.

133. Wright, S.M. and L.L. Wald, *Theory and application of array coils in MR spectroscopy*. NMR in Biomedicine, 1997. **10**(8): p. 394-410.

134. Press, W.H., et al., *Numerical recipes in C (2nd ed.): the art of scientific computing*1992: Cambridge University Press. 994.

135. Simmons, A., et al., *Serial precision of metabolite peak area ratios and water referenced metabolite peak areas in proton MR spectroscopy of the human brain*. Magn Reson Imaging, 1998. **16**(3): p. 319-30.

136. Hancu, I., et al., *1H MR spectroscopy using TE averaged PRESS: a more sensitive technique to detect neurodegeneration associated with Alzheimer's disease*. Magn Reson Med, 2005. **53**(4): p. 777-82.

137. Bertolino, A., et al., *Reproducibility of proton magnetic resonance spectroscopic imaging in patients with schizophrenia*. Neuropsychopharmacology, 1998. **18**(1): p. 1-9.

138. Brooks, W.M., S.D. Friedman, and C.A. Stidley, *Reproducibility of 1H-MRS in vivo*. Magn Reson Med, 1999. **41**(1): p. 193-7.

139. Duc, C.O., et al., *Quantitative H-1 MRS of the human brain in vivo based on the simulation phantom calibration strategy*. Magn Reson Med, 1998. **39**(3): p. 491-496.

140. Marshall, I., et al., *Reproducibility of metabolite peak areas in 1H MRS of brain*. Magn Reson Imaging, 1996. **14**(3): p. 281-92.

141. Ernst, R.R., G. Bodenhausen, and A. Wokaun, *Principles of nuclear magnetic resonance in one and two dimensions*. International series of monographs on chemistry, 1987, Oxford Oxfordshire; New York: Clarendon Press; Oxford University Press. xxiv, 610 p.

142. Canet, D., *Nuclear magnetic resonance : concepts and methods,* 1996, Chichester; New York: Wiley. x, 260 p.

143. Leary, S.M., et al., *A (1)H magnetic resonance spectroscopy study of aging in parietal white matter: implications for trials in multiple sclerosis.* Magn Reson Imaging, 2000. **18**(4): p. 455-9.

144. Helms, G., *The principles of quantification applied to in vivo proton MR spectroscopy.* European Journal of Radiology, 2008. **67**(2): p. 218-29.

145. Gustafsson, M.C., et al., *Low choline concentrations in normal-appearing white matter of patients with multiple sclerosis and normal MR imaging brain scans.* AJNR Am J Neuroradiol, 2007. **28**(7): p. 1306-12.

146. Soher, B.J., et al., *Quantitation of automated single-voxel proton MRS using cerebral water as an internal reference.* Magn Reson Med, 1996. **36**(3): p. 335-339.

147. Christiansen, P., et al., *In vivo quantification of brain metabolites by 1H-MRS using water as an internal standard.* Magn Reson Imaging, 1993. **11**(1): p. 107-18.

148. Maeda, H., et al., *An external reference for in vivo quantification of 1H spectroscopy.* Magn Reson Imaging, 1996. **14**(9): p. 1067-72.

149. Helms, G., *A precise and user-independent quantification technique for regional comparison of single volume proton MR spectroscopy of the human brain.* NMR in Biomedicine, 2000. **13**(7): p. 398-406.

150. Prantner, A.M., et al., *Magnetization transfer induced biexponential longitudinal relaxation.* Magn Reson Med, 2008. **60**(3): p. 555-63.

151. Schuff, N., et al., *Region and tissue differences of metabolites in normally aged brain using multislice 1H magnetic resonance spectroscopic imaging.* Magn Reson Med, 2001. **45**(5): p. 899-907.

152. Grasso, G., et al., *Assessment of human brain water content by cerebral bioelectrical impedance analysis: a new technique and its application to*

cerebral pathological conditions. Neurosurgery, 2002. **50**(5): p. 1064-72; discussion 1072-4.

153. Helms, G., *Volume correction for edema in single-volume proton MR spectroscopy of contrast-enhancing multiple sclerosis lesions.* Magn Reson Med, 2001. **46**(2): p. 256-63.

154. Laule, C., et al., *Water content and myelin water fraction in multiple sclerosis. A T2 relaxation study.* J Neurol, 2004. **251**(3): p. 284-93.

155. Ricci, P.E., et al., *Effect of voxel position on single-voxel MR spectroscopy findings.* AJNR American Journal of Neuroradiology, 2000. **21**(2): p. 367-74.

156. Jost, G., I. Harting, and S. Heiland, *Quantitative single-voxel spectroscopy: The reciprocity principle for receive-only head coils.* Journal of Magnetic Resonance Imaging, 2005. **21**(1): p. 66-71.

157. McLean, M.A., et al., *Quantitative analysis of short echo time 1H-MRSI of cerebral gray and white matter.* Magn Reson Med, 2000. **44**(3): p. 401-411.

158. Noworolski, S.M., et al., *High spatial resolution 1H-MRSI and segmented MRI of cortical gray matter and subcortical white matter in three regions of the human brain.* Magn Reson Med, 1999. **41**(1): p. 21-9.

159. Hetherington, H.P., et al., *Quantitative 1H spectroscopic imaging of human brain at 4.1 T using image segmentation.* Magn Reson Med, 1996. **36**(1): p. 21-9.

160. Ernst, T., R. Kreis, and B.D. Ross, *Absolute Quantitation of Water and Metabolites in the Human Brain. I. Compartments and Water.* Journal of Magnetic Resonance, Series B, 1993. **102**(1): p. 1-8.

161. Laule, C., et al., *Long T2 water in multiple sclerosis: what else can we learn from multi-echo T2 relaxation?* J Neurol, 2007. **254**(11): p. 1579-87.

162. Whittall, K.P., A.L. MacKay, and D.K. Li, *Are mono-exponential fits to a few echoes sufficient to determine T2 relaxation for in vivo human brain?* Magn Reson Med, 1999. **41**(6): p. 1255-7.

163. Whittall, K.P., et al., *Normal-appearing white matter in multiple sclerosis has heterogeneous, diffusely prolonged T2*. Magn Reson Med, 2002. **47**(2): p. 403-408.

164. Gussew, A., et al., *Absolute quantitation of brain metabolites with respect to the CSF fraction in 1H-MR spectroscopic volumes; World Congress on Medical Physics and Biomedical Engineering, September 7 - 12, 2009, Munich, Germany*, O. Dössel and W.C. Schlegel, Editors. 2009, Springer Berlin Heidelberg. p. 489-492.

165. Zhang, Y.Y., M. Brady, and S. Smith, *Segmentation of brain MR images through a hidden Markov random field model and the expectation-maximization algorithm*. IEEE Transactions on Medical Imaging, 2001. **20**(1): p. 45-57.

166. Kim, S.G., X. Hu, and K. Ugurbil, *Accurate T1 determination from inversion recovery images: application to human brain at 4 Tesla*. Magn Reson Med, 1994. **31**(4): p. 445-9.

167. Garber, H.J., et al., *Nuclear magnetic resonance study of obsessive-compulsive disorder*. Am J Psychiatry, 1989. **146**(8): p. 1001-5.

168. Bottomley, P.A., et al., *A review of normal tissue hydrogen NMR relaxation times and relaxation mechanisms from 1-100 MHz: dependence on tissue type, NMR frequency, temperature, species, excision, and age*. Medical Physics, 1984. **11**(4): p. 425-48.

169. Fischer, H.W., et al., *Nuclear relaxation of human brain gray and white matter: analysis of field dependence and implications for MRI*. Magn Reson Med, 1990. **16**(2): p. 317-34.

170. Drayer, B., et al., *MRI of brain iron*. American Journal of Roentgenology, 1986. **147**(1): p. 103-110.

171. Ye, F.Q., W.R.W. Martin, and P.S. Allen, *Estimation of the iron concentration in excised gray matter by means of proton relaxation measurements.* Magn Reson Med, 1996. **35**(3): p. 285-289.

172. Vymazal, J., et al., *The Quantitative Relation between T1-Weighted and T2-Weighted Mri of Normal Gray-Matter and Iron Concentration.*Journal of Magnetic Resonance Imaging, 1995. **5**(5): p. 554-560.

173. Vymazal, J., et al., *The relation between brain iron and NMR relaxation times: An in vitro study.* Magn Reson Med, 1996. **35**(1): p. 56-61.

174. Mlynárik, V., S. Gruber, and E. Moser, *Proton T1 and T2 relaxation times of human brain metabolites at 3 Tesla.* NMR in Biomedicine, 2001. **14**(5): p. 325-331.

175. Choi, C.G. and J. Frahm, *Localized proton MRS of the human hippocampus: metabolite concentrations and relaxation times.* Magn Reson Med, 1999. **41**(1): p. 204-7.

176. Sun, Y., et al., *Localisation, Registration and Visualisation of MRS Volumes of Interest on MR Images, XII Mediterranean Conference on Medical and Biological Engineering and Computing 2010*, P.D. Bamidis and N. Pallikarakis, Editors. 2010, Springer Berlin Heidelberg. p. 256-259.

177. Brooks, J.C., et al., *A proton magnetic resonance spectroscopy study of age-related changes in frontal lobe metabolite concentrations.* Cerebral cortex (New York, N Y : 1991), 2001. **11**(7): p. 598-605.

178. Engelbrecht, V., et al., *Age-dependent changes in magnetization transfer contrast of white matter in the pediatric brain.* American Journal of Neuroradiology, 1998. **19**(10): p. 1923-9.

179. van Buchem, M.A., et al., *Global Estimation of Myelination in the Developing Brain on the Basis of Magnetization Transfer Imaging: A Preliminary Study.* American Journal of Neuroradiology, 2001. **22**(4): p. 762-766.

180. Barker, G.J., P.S. Tofts, and A. Gass, *An interleaved sequence for accurate and reproducible clinical measurement of Magnetization Transfer Ratio.* Magnetic Resonance Imaging, 1996. **14**(4): p. 403-411.

181. Loevner, L.A., et al., *Microscopic disease in normal-appearing white matter on conventional MR images in patients with multiple sclerosis: assessment with magnetization-transfer measurements.* Radiology, 1995. **196**(2): p. 511-515.

182. Double, K.L., et al., *Topography of brain atrophy during normal aging and Alzheimer's disease.* Neurobiology of Aging, 1996. **17**(4): p. 513-521.

183. Hanyu, H., et al., *Magnetization transfer measurements of the hippocampus in the early diagnosis of Alzheimer's disease.* Journal of the Neurological Sciences, 2001. **188**(1–2): p. 79-84.

184. Dousset, V., et al., *Experimental allergic encephalomyelitis and multiple sclerosis: lesion characterization with magnetization transfer imaging.* Radiology, 1992. **182**(2): p. 483-491.

185. Mehta, R.C., G.B. Pike, and D.R. Enzmann, *Measure of magnetization transfer in multiple sclerosis demyelinating plaques, white matter ischemic lesions, and edema.* American Journal of Neuroradiology, 1996. **17**(6): p. 1051-5.

186. Erickson, B.J., *Imaging of Remyelination and Neuronal Health*, in *Advances in multiple Sclerosis and Experimental Demyelinating Diseases*, M. Rodriguez, Editor 2008, Springer Berlin Heidelberg. p. 73-92.

187. Srinivasan, R., et al., *Evidence of elevated glutamate in multiple sclerosis using magnetic resonance spectroscopy at 3 T.* Brain, 2005. **128**: p. 1016-1025.

188. Fernando, K.T.M., et al., *Elevated white matter myo-inositol in clinically isolated syndromes suggestive of multiple sclerosis.* Brain, 2004. **127**: p. 1361-1369.

189. Li, L.H., et al., *Proinflammatory role of aquaporin-4 in autoimmune neuroinflammation*. Faseb Journal, 2011. **25**(5): p. 1556-1566.

190. Emmer, B.J., et al., *Brain involvement in rheumatoid arthritis: a magnetic resonance spectroscopy study*. Arthritis Rheum, 2009. **60**(11): p. 3190-5.

191. van der Bijl, A.E., et al., *Advanced magnetic resonance imaging of the brain in patients treated with TNF-alpha blocking agents*. Clin Exp Rheumatol, 2007. **25**(2): p. 301-4.

192. Miller, A.H., V. Maletic, and C.L. Raison, *Inflammation and its discontents: the role of cytokines in the pathophysiology of major depression*. Biol Psychiatry, 2009. **65**(9): p. 732-41.

193. Huber, J.D., et al., *Inflammatory pain alters blood-brain barrier permeability and tight junctional protein expression*. American Journal of Physiology-Heart and Circulatory Physiology, 2001. **280**(3): p. H1241-H1248.

194. Vane, J. and R. Botting, *Inflammation and the mechanism of action of anti-inflammatory drugs*. The FASEB Journal, 1987. **1**(2): p. 89-96.

195. Taylor, M.J., et al., *Normal glutamate but elevated myo-inositol in anterior cingulate cortex in recovered depressed patients*. Journal of affective disorders, 2009. **119**(1-3): p. 186-9.

196. Sarchielli, P., et al., *1H-MRS in patients with multiple sclerosis undergoing treatment with interferon beta-1a: results of a preliminary study*. J Neurol Neurosurg Psychiatry, 1998. **64**(2): p. 204-12.

197. Wilkinson, I.D., et al., *Cerebral volumes and spectroscopic proton metabolites on MR: is sex important?* Magnetic Resonance Imaging, 1997. **15**(2): p. 243-8.

198. Ferrero-Miliani, L., et al., *Chronic inflammation: importance of NOD2 and NALP3 in interleukin-1beta generation*. Clinical and Experimental Immunology, 2007. **147**(2): p. 227-35.

199. Ahmed, A., *An overview of inflammation: mechanism and consequences.* Frontiers in Biology, 2011. **6**(4): p. 274-281.

200. Libby, P., *Inflammatory mechanisms: the molecular basis of inflammation and disease*. Nutr Rev, 2007. **65**(12 Pt 2): p. S140-6.

201. Cotran, R.S., et al., *Robbins pathologic basis of disease*. 6th ed 1999, Philadelphia: Saunders. xv, 1425 p.

202. Stedman, T.L., *Stedman's medical dictionary*. 25th ed 1990, Baltimore: Williams & Wilkins. xxxviii, 95, 1784 p.

203. D'Mello, C., T. Le, and M.G. Swain, *Cerebral Microglia Recruit Monocytes into the Brain in Response to Tumor Necrosis Factor alpha Signaling during Peripheral Organ Inflammation.* Journal of Neuroscience, 2009. **29**(7): p. 2089-2102.

204. Riazi, K., et al., *Microglial activation and TNF alpha production mediate altered CNS excitability following peripheral inflammation.* Proc Natl Acad Sci U S A, 2008. **105**(44): p. 17151-17156.

205. Stamatovic, S.M., et al., *Inflammation and brain edema: New insights into the role of chemokines and their receptors.* Brain Edema XIII, 2006. **96**: p. 444-450.

206. Siegle, G.J., C.S. Carter, and M.E. Thase, *Use of fMRI to predict recovery from unipolar depression with cognitive behavior therapy.* American Journal of Psychiatry, 2006. **163**(4): p. 735-738.

207. Videbech, P., et al., *The Danish PET/depression project: PET findings in patients with major depression.* Psychological Medicine, 2001. **31**(7): p. 1147-1158.

208. Ito, H., et al., *Hypoperfusion in the limbic system and prefrontal cortex in depression: SPECT with anatomic standardization technique*. Journal of Nuclear Medicine, 1996. **37**(3): p. 410-414.

209. Farchione, T.R., G.J. Moore, and D.R. Rosenberg, *Proton magnetic resonance spectroscopic imaging in pediatric major depression.* Biol Psychiatry, 2002. **52**(2): p. 86-92.

210. Gruber, S., et al., *Quantification of metabolic differences in the frontal brain of depressive patients and controls obtained by H-1-MRS at 3 Tesla.* Investigative Radiology, 2003. **38**(7): p. 403-408.

211. Coupland, N.J., et al., *Decreased prefrontal Myo-inositol in major depressive disorder.* Biological Psychiatry, 2005. **57**(12): p. 1526-1534.

212. Rosenberg, D.R., et al., *Reduced anterior cingulate glutamate in pediatric major depression: A magnetic resonance spectroscopy study.* Biological Psychiatry, 2005. **58**(9): p. 700-704.

213. Gabbay, V., et al., *Lateralized caudate metabolic abnormalities in adolescent major depressive disorder: A proton MR spectroscopy study.* American Journal of Psychiatry, 2007. **164**(12): p. 1881-1889.

214. Auer, D.P., et al., *Reduced glutamate in the anterior cingulate cortex in depression: an in vivo proton magnetic resonance spectroscopy study.* Biol Psychiatry, 2000. **47**(4): p. 305-13.

215. Sarchielli, P., et al., *Absolute quantification of brain metabolites by proton magnetic resonance spectroscopy in normal-appearing white matter of multiple sclerosis patients.* Brain, 1999. **122**: p. 513-521.

216. Saraceno, B., *The WHO World Health Report 2001 on mental health.* Epidemiologia e psichiatria sociale, 2002. **11**(2): p. 83-7.

217. Paez-Pereda, M. and M. Panhuysen, *Strategies to Identify Biomarkers for Depression*, in *Biomarkers for Psychiatric Disorders*, C. Turck, Editor 2009, Springer US. p. 299-314.

218. Korostil, M. and A. Feinstein, *Anxiety disorders and their clinical correlates in multiple sclerosis patients.* Multiple Sclerosis, 2007. **13**(1): p. 67-72.

219. Segal, D.L., M. Hersen, and V.B. Van Hasselt, *Reliability of the Structured Clinical Interview for DSM-III-R: an evaluative review.* Comprehensive psychiatry, 1994. **35**(4): p. 316-27.

220. Hamilton, M., *A rating scale for depression.* J Neurol Neurosurg Psychiatry, 1960. **23**: p. 56-62.

221. Moran, P.J. and D.C. Mohr, *The validity of Beck Depression Inventory and Hamilton Rating Scale for Depression items in the assessment of depression among patients with multiple sclerosis.* Journal of Behavioral Medicine, 2005. **28**(1): p. 35-41.

222. Dreher, W. and D. Leibfritz, *New method for the simultaneous detection of metabolites and water in localized in vivo H-1 nuclear magnetic resonance spectroscopy.* Magn Reson Med, 2005. **54**(1): p. 190-195.

223. Kempton, M.J., et al., *Effects of acute dehydration on brain morphology in healthy humans.* Human brain mapping, 2009. **30**(1): p. 291-8.

224. Greenleaf, J.E. and M.H. Harrison, *Water and Electrolytes.* Acs Symposium Series, 1986. **294**: p. 107-124.

225. Adolph, E.F., *Physiology of Man in the Desert*, 1947: Interscience Publishers.

226. Ham, B.J., et al., *Decreased N-acetyl-aspartate levels in anterior cingulate and hippocampus in subjects with post-traumatic stress disorder: a proton magnetic resonance spectroscopy study.* Eur J Neurosci, 2007. **25**(1): p. 324-9.

227. Olbrich, H.M., et al., *Frontolimbic glutamate alterations in first episode schizophrenia: evidence from a magnetic resonance spectroscopy study.* World J Biol Psychiatry, 2008. **9**(1): p. 59-63.

228. Komoroski, R.A., et al., *Effects of gender and region on proton MRS of normal human brain.* Magn Reson Imaging, 1999. **17**(3): p. 427-33.

229. Saunders, D.E., et al., *Aging of the adult human brain: in vivo quantitation of metabolite content with proton magnetic resonance spectroscopy.* Journal of Magnetic Resonance Imaging, 1999. **9**(5): p. 711-6.

230. Kaiser, L.G., et al., *Age-related glutamate and glutamine concentration changes in normal human brain: 1H MR spectroscopy study at 4 T.* Neurobiol Aging, 2005. **26**(5): p. 665-72.

231. Dixon, R.M., et al., *Longitudinal quantitative proton magnetic resonance spectroscopy of the hippocampus in Alzheimer's disease.* Brain, 2002. **125**(Pt 10): p. 2332-41.

232. Kim, Y.H., et al., *1H NMR spectroscopy: an approach to evaluation of diseased skin in vivo.* Journal of Investigative Dermatology, 1989. **92**(2): p. 210-6.

233. Chiaravalloti, N.D. and J. DeLuca, *Cognitive impairment in multiple sclerosis.* Lancet neurology, 2008. **7**(12): p. 1139-51.

234. Jose Sa, M., *Psychological aspects of multiple sclerosis.* Clinical neurology and neurosurgery, 2008. **110**(9): p. 868-77.

235. Feinstein, A., *Mood disorders in multiple sclerosis and the effects on cognition.* Journal of the Neurological Sciences, 2006. **245**(1-2): p. 63-6.

236. Charles, H.C., et al., *Brain choline in depression: in vivo detection of potential pharmacodynamic effects of antidepressant therapy using hydrogen localized spectroscopy.* Progress in neuro-psychopharmacology & biological psychiatry, 1994. **18**(7): p. 1121-7.

237. Hasler, G., et al., *Reduced prefrontal glutamate/glutamine and gamma-aminobutyric acid levels in major depression determined using proton magnetic resonance spectroscopy.* Arch Gen Psychiatry, 2007. **64**(2): p. 193-200.

238. Gudjonsson, J.E., et al., *HLA-Cw6-positive and HLA-Cw6-negative patients with psoriasis vulgaris have distinct clinical features.* Journal of Investigative Dermatology, 2002. **118**(2): p. 362-365.

239. Gudjonsson, J.E., et al., *Psoriasis patients who are homozygous for the HLA-Cw*0602 allele have a 2.5-fold increased risk of developing psoriasis compared with Cw6 heterozygotes.* British Journal of Dermatology, 2003. **148**(2): p. 233-235.

240. Devos, A., et al., *Classification of brain tumours using short echo time 1H MR spectra.* Journal of Magnetic Resonance (San Diego, Calif : 1997), 2004. **170**(1): p. 164-75.

241. Currie, S., et al., *Magnetic resonance spectroscopy of the brain.* Postgraduate medical journal, 2013. **89**(1048): p. 94-106.

242. Wilkinson, I.D., et al., *Cerebral proton magnetic resonance spectroscopy in asymptomatic HIV infection.* AIDS (London, England), 1997. **11**(3): p. 289-95.

243. Mukonoweshuro, W., I.D. Wilkinson, and P.D. Griffiths, *Proton MR spectroscopy of cortical tubers in adults with tuberous sclerosis complex.* AJNR American Journal of Neuroradiology, 2001. **22**(10): p. 1920-5.

244. Blockley, N.P., et al., *A review of calibrated blood oxygenation level-dependent (BOLD) methods for the measurement of task-induced changes in brain oxygen metabolism.* NMR in Biomedicine, 2012.

245. Malonek, D. and A. Grinvald, *Interactions between electrical activity and cortical microcirculation revealed by imaging spectroscopy: Implications for functional brain mapping.* Science, 1996. **272**(5261): p. 551-554.

246. Zhu, X.H. and W. Chen, *Observed BOLD effects on cerebral metabolite resonances in human visual cortex during visual stimulation: a functional (1)H MRS study at 4 T.* Magn Reson Med, 2001. **46**(5): p. 841-7.

247. Shih, Y.Y., et al., *INS-PRESS for functional MRS: simultaneous with-and without-water suppression spectral acquisition on visual cortex of human brains at 3T*. Proc Intl Soc Magn Reson Med, 17 (2009)

248. Hennig, T., et al., *Detection of Brain Activation Using Oxygenation Sensitive Functional Spectroscopy*. Magn Reson Med, 1994. **31**(1): p. 85-90.

249. Ernst, T. and J. Hennig, *Observation of a fast response in functional MR*. Magn Reson Med, 1994. **32**(1): p. 146-9.

250. Dymond, R., et al., *Application of double voxel functional spectroscopy to event-related cognitive experiments*. Magn Reson Med, 1999. **41**(2): p. 217-23.

251. Condon, B., et al., *Habituation-like effects cause a significant decrease in response in MRI neuroactivation during visual stimulation*. Vision Res, 1997. **37**(9): p. 1243-7.

252. DeYoe, E.A., et al., *Functional magnetic resonance imaging (FMRI) of the human brain*. Journal of Neuroscience Methods, 1994. **54**(2): p. 171-187.

253. Fox, P.T. and M.E. Raichle, *Stimulus Rate Determines Regional Brain Blood-Flow in Striate Cortex*. Annals of Neurology, 1985. **17**(3): p. 303-305.

254. Baslow, M.H., J. Hrabe, and D.N. Guilfoyle, *Dynamic relationship between neurostimulation and N-acetylaspartate metabolism in the human visual cortex: evidence that NAA functions as a molecular water pump during visual stimulation*. Journal of Molecular Neuroscience : MN, 2007. **32**(3): p. 235-45.

255. Mangia, S., et al., *Sensitivity of single-voxel 1H-MRS in investigating the metabolism of the activated human visual cortex at 7 T*. Magn Reson Imaging, 2006. **24**(4): p. 343-8.

256. Mangia, S., et al., *Sustained neuronal activation raises oxidative metabolism to a new steady-state level: evidence from 1H NMR spectroscopy in the human visual cortex*. Journal of cerebral blood flow and metabolism :

official journal of the International Society of Cerebral Blood Flow and Metabolism, 2007. **27**(5): p. 1055-63.

257. Smith, S.M., et al., *Advances in functional and structural MR image analysis and implementation as FSL*. NeuroImage, 2004. **23 Suppl 1**: p. S208-19.

258. Jenkinson, M., et al., *Improved optimization for the robust and accurate linear registration and motion correction of brain images.* NeuroImage, 2002. **17**(2): p. 825-41.

259. Smith, S.M., *Fast robust automated brain extraction.* Human brain mapping, 2002. **17**(3): p. 143-55.

260. Worsley, K., *Statistical analysis of activation images.* Functional MRI: an introduction to methods, 2001. **14**: p. 251-270.

261. Jenkinson, M. and S. Smith, *A global optimisation method for robust affine registration of brain images.* Medical Image Analysis, 2001. **5**(2): p. 143-156.

262. Woolrich, M.W., et al., *Temporal autocorrelation in univariate linear modeling of FMRI data.* NeuroImage, 2001. **14**(6): p. 1370-1386.

263. Ugurbil, K., et al., *Functional mapping in the human brain using high magnetic fields.* Philosophical Transactions of the Royal Society of London. Series B: Biological Sciences, 1999. **354**(1387): p. 1195-1213.

264. Weisskoff, R.M., et al., *Microscopic susceptibility variation and transverse relaxation: theory and experiment.* Magn Reson Med, 1994. **31**(6): p. 601-10.

265. Mangia, S. and I. Tkac, *Dynamic relationship between neurostimulation and N-acetylaspartate metabolism in the human visual cortex: evidence that NAA functions as a molecular water pump during visual stimulation.* Journal of Molecular Neuroscience : MN, 2008. **35**(2): p. 245-6; author reply 247-8.

266. Lin, Y., et al., *Investigating the metabolic changes due to visual stimulation using functional proton magnetic resonance spectroscopy at 7 T.* J Cereb Blood Flow Metab, 2012. **32**(8): p. 1484-95.

267. Sarchielli, P., et al., *Functional 1H-MRS findings in migraine patients with and without aura assessed interictally.* NeuroImage, 2005. **24**(4): p. 1025-31.

268. Taylor, D.L., et al., *Investigation into the Role of N-Acetylaspartate in Cerebral Osmoregulation.* Journal of Neurochemistry, 1995. **65**(1): p. 275-281.

269. Smith, A.T., K.D. Singh, and M.W. Greenlee, *Attentional suppression of activity in the human visual cortex.* Neuroreport, 2000. **11**(2): p. 271-277.

270. Harel, N., et al., *Origin of negative blood oxygenation level-dependent fMRI signals.* J Cereb Blood Flow Metab, 2002. **22**(8): p. 908-917.

271. Hancu, I., *Optimized glutamate detection at 3T.* Journal of Magnetic Resonance Imaging : JMRI, 2009. **30**(5): p. 1155-62.

272. Barker, P.B. and D.D.M. Lin, *In vivo proton MR spectroscopy of the human brain.* Progress in Nuclear Magnetic Resonance Spectroscopy, 2006. **49**(2): p. 99-128.

273. Sanacora, G., et al., *Reduced cortical gamma-aminobutyric acid levels in depressed patients determined by proton magnetic resonance spectroscopy.* Archives of General Psychiatry, 1999. **56**(11): p. 1043-7.

274. Rothman, D.L., et al., *Localized 1H NMR measurements of gamma-aminobutyric acid in human brain in vivo.* Proc Natl Acad Sci U S A, 1993. **90**(12): p. 5662-6.

275. Dreher, W., D.G. Norris, and D. Leibfritz, *Magnetization transfer affects the proton creatine/phosphocreatine signal intensity: in vivo demonstration in the rat brain.* Magn Reson Med, 1994. **31**(1): p. 81-4.

276. McLean, M.A., et al., *Magnetization transfer effect on human brain metabolites and macromolecules.* Magn Reson Med, 2005. **54**(5): p. 1281-5.

277. Helms, G. and J. Frahm, *Magnetization transfer attenuation of creatine resonances in localized proton MRS of human brain in vivo.* NMR in Biomedicine, 1999. **12**(8): p. 490-4.

278. Strauss, W.L. and S.R. Dager, *Magnetization transfer of fluoxetine in the human brain using fluorine magnetic resonance spectroscopy.* Biological Psychiatry, 2001. **49**(9): p. 798-802.

279. Perez-Ruiz, A., et al., *The INTERPRET Decision-Support System version 3.0 for evaluation of Magnetic Resonance Spectroscopy data from human brain tumours and other abnormal brain masses.* BMC Bioinformatics, 2010. **11**: p. 581.

280. Ott, D., J. Hennig, and T. Ernst, *Human brain tumors: assessment with in vivo proton MR spectroscopy.* Radiology, 1993. **186**(3): p. 745-52.

281. Go, K.G., et al., *Localized Proton Spectroscopy and Spectroscopic Imaging in Cerebral Gliomas, with Comparison to Positron Emission Tomography.* Neuroradiology, 1995. **37**(3): p. 198-206.

282. Meyerand, M.E., et al., *Classification of biopsy-confirmed brain tumors using single-voxel MR spectroscopy.* American Journal of Neuroradiology, 1999. **20**(1): p. 117-123.

283. Weis, J., et al., *Short Echo Time MR Spectroscopy of Brain Tumors: Grading of Cerebral Gliomas by Correlation Analysis of Normalized Spectral Amplitudes.* Journal of Magnetic Resonance Imaging, 2010. **31**(1): p. 39-45.